



# Introducing high strength and ductility twinning induced plasticity (TWIP) steels for European automotive applications through advanced material modeling (TWIP4EU)

**EUROPEAN COMMISSION**

Directorate-General for Research and Innovation  
Directorate D — Industrial Technologies  
Unit D.4 — Coal and Steel

E-mail: [rtd-steel-coal@ec.europa.eu](mailto:rtd-steel-coal@ec.europa.eu)  
[RTD-PUBLICATIONS@ec.europa.eu](mailto:RTD-PUBLICATIONS@ec.europa.eu)

Contact: RFCS Publications

European Commission  
B-1049 Brussels

# Research Fund for Coal and Steel

## Introducing high strength and ductility twinning induced plasticity (TWIP) steels for European automotive applications through advanced material modeling

### (TWIP4EU)

A. Butz

**Fraunhofer IWM**

Woehlerstrasse 11, 79108 Freiburg, GERMANY

M. Zapara

**Fraunhofer IWM**

Woehlerstrasse 11, 79108 Freiburg, GERMANY

A. Erhart, A. Haufe

**DYNAmore GmbH**

Industriestrasse 2, 70565 Stuttgart, GERMANY

M. Biasutti

**ESI GmbH**

Siemensstrasse 12, 63236 Neu-Isenburg, GERMANY

D. Croizet

**ESI Group**

101 Rue des Solets, 94150 Rungis, FRANCE

M. Kampczyk

**Faurecia Autositze GmbH**

Nordseher Straße 38, 31655 Stadthagen, GERMANY

J. Hagstrom, N. Stenberg

**Swerea KIMAB AB**

Isafjordsgatan 28 A, 164 40 Kista, SWEDEN

M. Schneider

**Salzgitter Mannesmann Forschung GmbH**

Eisenhüttenstrasse 99, 38239 Salzgitter, GERMANY

Grant Agreement RFSR-CT-2012-00019

1 July 2012 to 30 June 2015

### Final report

Directorate-General for Research and Innovation

## LEGAL NOTICE

Neither the European Commission nor any person acting on behalf of the Commission is responsible for the use which might be made of the following information.

The views expressed in this publication are the sole responsibility of the authors and do not necessarily reflect the views of the European Commission.

***Europe Direct is a service to help you find answers  
to your questions about the European Union***

**Freephone number (\*):  
00 800 6 7 8 9 10 11**

(\* ) Certain mobile telephone operators do not allow access to 00 800 numbers or these calls may be billed.

More information on the European Union is available on the Internet (<http://europa.eu>).

Cataloguing data can be found at the end of this publication.

Luxembourg: Publications Office of the European Union, 2017

Print	ISBN 978-92-79-65693-4	ISSN 1018-5593	doi:10.2777/146331	KI-NA-28-465-EN-C
PDF	ISBN 978-92-79-65694-1	ISSN 1831-9424	doi:10.2777/757375	KI-NA-28-465-EN-N

© European Union, 2017

Reproduction is authorised provided the source is acknowledged.



# Table of contents

- 1 FINAL SUMMARY .....5**

  - 1.1 WP1: TECHNICAL AND ADMINISTRATIVE PROJECT COORDINATION .....5
  - 1.2 WP2: MATERIAL PRODUCTION AND SUPPLY ..... 6
  - 1.3 WP3: MICROSTRUCTURE CHARACTERIZATION .....6
  - 1.4 WP4: MACROSCOPIC MATERIAL CHARACTERIZATION ..... 7
  - 1.5 WP5: MICROMECHANICAL MODELLING AND SIMULATION OF TWIP-STEELS.....9
  - 1.6 WP6: DEVELOPMENT OF A MACROSCOPIC ELASTIC PLASTIC MATERIAL MODEL FOR TWIP-STEELS .....9
  - 1.7 WP7: ALGORITHMIC TREATMENT AND NUMERICAL IMPLEMENTATION OF THE MACROSCOPIC MATERIAL MODEL .....11
  - 1.8 WP8: SIMULATION OF FORMING EXPERIMENTS AND VALIDATION OF THE CONSTITUTIVE FORMULATION .....11
  - 1.9 WP9: PROTOTYPE PRODUCTION AND VALIDATION .....12

- 2 SCIENTIFIC AND TECHNICAL DESCRIPTION OF THE RESULTS .....15**

  - 2.1 WP1: TECHNICAL AND ADMINISTRATIVE PROJECT COORDINATION .....16
  - 2.2 WP2: MATERIAL PRODUCTION AND SUPPLY .....19
  - 2.3 WP3: MICROSTRUCTURE CHARACTERISATION .....21
  - 2.4 WP4: MACRO CHARACTERIZATION OF THE MATERIAL AND FORMABILITY TESTS .....33
  - 2.5 WP5: MICROMECHANICAL MODELLING AND SIMULATION OF TWIP-STEELS.....58
  - 2.6 WP6: DEVELOPMENT OF A MACROSCOPIC ELASTIC-PLASTIC MATERIAL MODEL TO DESCRIBE THE DEFORMATION BEHAVIOR OF TWIP-STEELS .....67
  - 2.7 WP7: ALGORITHMIC TREATMENT AND NUMERICAL IMPLEMENTATION OF THE MACROSCOPIC MODEL.....81
  - 2.8 WP8: SIMULATION OF FORMING EXPERIMENTS AND VALIDATION OF THE CONSTITUTIVE FORMULATION .....96
  - 2.9 WP9: PROTOTYPE PRODUCTION AND VALIDATION .....115
  - 2.10 CONCLUSIONS.....137
  - 2.11 EXPLOITATION AND IMPACT OF THE RESEARCH RESULTS.....138

- LIST OF ABBREVIATIONS.....139**
- LIST OF FIGURES .....141**
- REFERENCES.....147**



# 1 Final summary

The aim of *TWIP4EU* is to promote the introduction of modern twinning induced plasticity (TWIP) steels as candidate material for production of lightweight automobile components. Therefore, a simulation framework was developed to model the complex deformation and forming behavior of TWIP-steels. Further sub-goals are the detailed experimental analysis on microstructure level and on macroscopic level, the validation of the developed model on standard experiments, complex forming processes and prototype production and the formulation of guidelines for the application of the developed simulation framework.

## 1.1 WP1: Technical and administrative project coordination

### 1.1.1 Structure of scientific and technical work program

The TWIP4EU project plan is divided into nine work packages that include experimental investigations, modelling and implementation, forming experiments and corresponding simulations as well as prototype production and validation. The work program has been assembled in three task groups, each of which contains two or three work packages:

- **TG (I) experimental group** is related to WP2, WP3, and WP4 includes the material characterization on micro and macro scale.
- **TG (II) modelling and implementation group** considers the work related to the development of the material model and its implementation into the finite element framework.
- **TG (III) application and validation group** contains the work packages WP8 and WP9. It is focused on the comparison and validation between experimental data and simulation.

### 1.1.2 Definition of material characterization procedure and definition of prototype component

The material characterization procedure considers micromechanical analyses as well as macroscopic test and also forming experiments. Different analyses and experiments were defined and designed in order to get a better understanding of the material behavior. Further, the experiments had to be suitable for validation and assessment of the developed material model. A backrest side member of a front seat was chosen as prototype component.

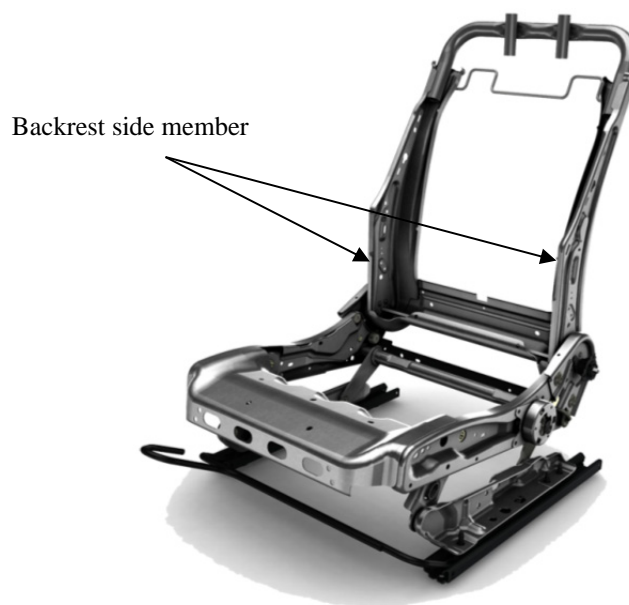


**Figure 1.1:** Seat frame including the backrest side member which was chosen as prototype component

### **1.1.3 Presentation and publication of the accomplished work**

The accomplished work was presented at different national and international workshops. Further, the results were published in journal and conference proceedings.

## **1.2 WP2: Material production and supply**

A pre-series TWIP-steel material was produced by SZMF with minimum yield strength of 600 MPa and an ultimate tensile strength of 1000 MPa. An ultimate elongation of more than 40% technical strain could be reached. The available sheet dimension is 300 mm x 1000 mm, the sheet thickness is 1.5 mm. The sheets were dispatched to the project partners for further microstructure analyses, material characterization, forming experiments and prototype production.

## **1.3 WP3: Microstructure characterization**

### **1.3.1 Characterization of the initial material**

The microstructure of the TWIP-steel material in the initial state was analyzed using SEM and EBSD analysis techniques. A weak fcc rolling texture was observed. Analyses over the sheet thickness (15% below surface and 35 % below surface) show no significant gradient with respect to the microstructure or texture. The grains show a globular shape. The grains size varies between 1  $\mu\text{m}$  and 20  $\mu\text{m}$ . Further, annealing twins could be detected using EBSD measurement. The available data were used to initialize the microstructure model in WP5.

### **1.3.2 Analysis of the material after deformation**

The microstructure of the material was analysed under different deformation conditions and levels of deformation. The following load cases were considered: Uniaxial tension, shear, biaxial tension and uniaxial load reversal. Since the macroscopic model is based on a physically motivated approach (see WP6), physical quantities like twin volume fraction and dislocation density and the evolution of these quantities during deformation were of high interest. The experimental analyses of these quantities provided valuable data which could be directly considered in the modelling part. Since the deformation twins are very small, the determination of the twin volume fraction using EDSB was not possible. For this reason, TEM analyses had to be done. Further, the development of the texture for different load cases was analysed.

For uniaxial tensile specimens, the experimental determination of the twin volume fraction was successfully completed for different levels of pre-straining. Due to the need of TEM analyses, the measurements have been very complex and time consuming. Considering some reasonable assumptions, the obtained evolution of the twin volume fraction is comparable with other measurements reported in literature. One important outcome of these analyses is the development of the twin volume fraction as function the applied strain for the uniaxial case. These data were directly used for the parameter identification of the developed macroscopic model.

The microstructure analyses of the material considering specimens from shear test, bulge test and from cyclic test were completed. Depending on the load case, the texture development showed significant differences, as expected. The analysis of the twin volume fraction for these stress states and also for load reversal is of high interest, since such data are currently not available in literature. Due to the complexity of the experimental analysis, the results had to be carefully interpreted. In case of the bulge test only a few grains could be analysed because of the crystallographic orientation of the twins with respect to the prepared TEM foils. Thus, these data are not useable from statistical point of view and should be carefully considered.

The obtained detailed information about the microstructure behavior (including texture development and twin volume fraction) during loading was provided for the further used in WP5 and WP6/WP7.

### 1.3.3 Microstructure characterization of samples obtained from formed automobile prototype component

While task 3.1 and task 3.2 are focused on the analysis of the initial state of the material and defined pre-strained specimens, it was initially planned to analyse the microstructure including the evolution of the twin volume fraction after typical sheet forming processes accompanied with complex loading history. Based on the experience of task 3.1 and task 3.2 it became clear that the experimental effort would be very high and that it is a priori unclear, if the results could be used (see Section 2.3.3). For this reason it was decided that the planned analysis of the twin volume fraction in the formed part had to be replaced by a micro-hardness measurement on defined section cut of the component. Since the hardness measurement can be correlated with the current strength of the material these quantities can also be used to estimate the current material state. Further, this method allows analyzing along complete section cuts which would not be possible with the initially planned microstructure analysis. The results of the experimental measurements are shown in Section 2.9.5.

## 1.4 WP4: Macroscopic material characterization

WP4 is concerned with the mechanical testing of the TWIP-steel material on macroscopic level. The main objectives of this WP are the determination of mechanical quantities which are commonly considered in sheet metal forming applications, the characterization of the spring back effect and the analysis of the forming behavior using typical forming experiments. The planned work could be successfully completed. The obtained data were analysed to get a better general understanding of the material behavior. Furthermore, the data were used to calibrate and validate the developed material model.

### 1.4.1 Mechanical tests for material characterization

Several different mechanical tests were performed to analyse the mechanical behavior of the TWIP-steel. From standard tensile test in  $0^\circ$ ,  $45^\circ$  and  $90^\circ$  with respect to rolling direction, the mechanical quantities as well as the flow curves were evaluated. The initial yield strength  $R_{p0.2}$  in rolling direction is about 630 MPa, the ultimate tensile strength  $R_m$  is 1035 MPa. With respect to the Lankford coefficients which are between 0.79 and 1.00, the material shows a relatively low anisotropy. The hardening behavior of the flow curves shows some dependence on the direction. The flow curve measured in  $90^\circ$  has a higher initial yield point but a lower ultimate strength. Thus, the flow curve in  $90^\circ$  crosses the one in  $0^\circ$  which is difficult to describe with standard material models.

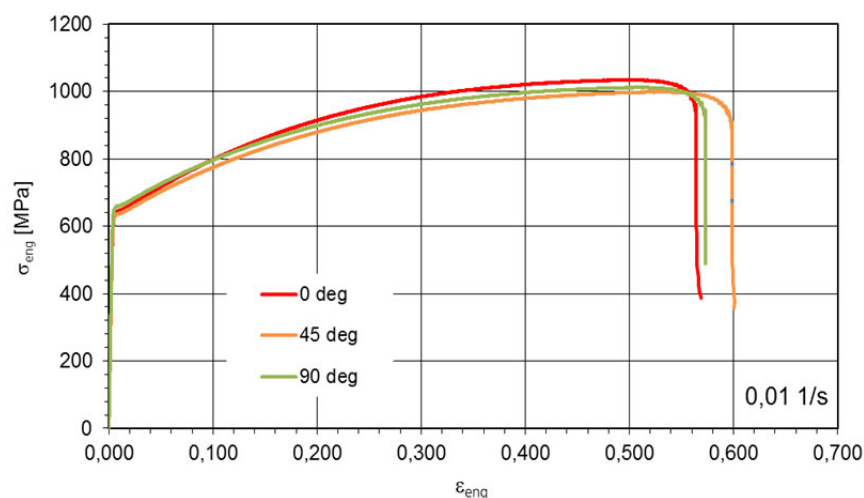


**Figure 1.2:** Engineering stress-strain-curves from uniaxial tensile tests for three different directions

Several experiments were carried out to analyse the Young's modulus in the initial state and after deformation. In the initial state, a relatively low Young's modulus of about 173GPa was determined. Measurements on pre-strained specimens for different strain levels did not show any statistically

significant change of the Young's modulus. Thus, the task 3.4 initially planned to analyse some non-linear elastic material behavior on micro structure level became obsolete and was omitted.

Tensile tests were performed for different strain rates ranging from 0.001 1/s up 20 1/s. An inverse strain rate sensitivity (stress strain curve decreases if the strain rate increases) curve could be observed which is typical for TWIP-steels.

For the evaluation of the material behavior under biaxial loading the bulge tests were carried out. Compared to the tensile tests, the initial yield strength is lower under biaxial loading. Values between 560 and 580 MPa were determined, however it should be mentioned that the evaluation of the initial yield point from the bulge test is not as precise as in the tensile test. Compared to the tensile test, the flow curve obtained from the bulge test shows a higher hardening rate. Thus, a stress dependent hardening can be observed with the analysed TWIP-steel material. This observation is in agreement with the results reported in literature [Renard2012]. Further, it was found that the ratio of major and minor strain in the centre of the bulge specimen develops from 1.0 to a value of 0.9. This means that the evolution of the strains under biaxial loading starts isotropic and continuously changes to an anisotropic behavior.

#### **1.4.2 Mechanical tests to identify kinematic hardening and Bauschinger effect**

It was expected that TWIP-steel would show a significant spring-back behavior due to the high strength of the material and a low Young's modulus at the same time. To identify kinematic hardening and Bauschinger effect, two different kinds of experiments were performed:

For the analysis of the Bauschinger effect (kinematic hardening) cyclic tension-compressions tests were done. Due to the high strength of the material, only small strain amplitudes could be realized without buckling of the specimen. For this reason it is difficult to make general statements concerning the kinematic hardening. Based on the available data, one can conclude that the material shows a significant Bauschinger effect. The yielding after load reversal starts at lower stresses. The kinematic hardening seems to be more significant than the isotropic hardening.

Further, the so-called bending under tension test (BUT-test) was carried out to evaluate the spring back behavior. Two different tool sizes and three load levels were chosen for the tests. Thus, the ratio between tensile loading and bending could be varied which significantly influenced the shape of the steel strip after spring back. The results of these tests were then used for comparison of the spring back prediction of numerical models.

#### **1.4.3 Tests to evaluate formability**

Nakajima tests and cup drawing tests were performed to evaluate the forming behavior of the TWIP-steel material. The Nakajima tests are useful to realize defined strain conditions (ratio between major and minor strain) while the cup drawing experiment is closer to typical deep drawing processes.

The Nakajima test was used to evaluate the forming limit diagram (FLC). Compared to other high strength steels, the TWIP-steel material shows a much better formability. Further, the Nakajima test was used to analyze the forming behavior for three defined loading conditions (uni-axial tension, close to plane strain and biaxial tension). Therefore the strains were evaluated at a strain level with sufficient distance to necking. A good reproducibility of the test could be reached. The obtained strain field were used to evaluate both the developed material model and the standard model.

Deep drawing tests of square cup were performed for three different drawing depths (20 mm, 40 mm and 60 mm). The drawing depth of 60 mm could be realized without any difficulty. After forming the strain fields were optically measured. The results show a good reproducibility.

## **1.5 WP5: Micromechanical modelling and simulation of TWIP-steels**

### **1.5.1 Creation of a microstructure model**

A crystal plasticity based full field microstructure model (unit cell model) was created to numerically analyse the material behaviour of the considered TWIP-steel on grain scale. The results from the microstructure simulations should be used as data in addition to the experimentally available data. With respect to the experimental data, microstructure morphology with approximately 1000 globular grains was created. The number of grains was sufficient to represent experimentally measured texture.

### **1.5.2 Parameter identification of the crystal plasticity based microstructure model**

A direct identification of the parameter is not possible for this class of material models. Therefore, an inverse parameter identification strategy was applied. Uniaxial stress-strain curve in rolling direction was used to fit the hardening parameter. The development of the twin volume fraction as function of uniaxial strain was used as additional objective function. It was possible to determine a set of parameter that accurately describes the stress-strain curve, the development of the twin volume fraction and also to Lankford coefficients in rolling direction and in transverse direction.

### **1.5.3 Evaluation of the initial yield surface**

The calibrated microstructure model was used to evaluate points on the initial yield surface. The number of calculated points is higher compared to the experimentally available number of points. These data were used to identify the parameter of anisotropic yield function YLD2000-2D which is used in the macroscopic model approach. Although the yield exponent of  $m=8$  is commonly used for metals with an fcc crystal structure, it was found that the exponent of  $m=6$  fits slightly better. This finding agrees also with the simulation results of the macroscopic tests. Here, the exponent  $m=6$  gives a better prediction of the strain fields.

## **1.6 WP6: Development of a macroscopic elastic plastic material model for TWIP-steels**

### **1.6.1 Assessment of commonly used material models**

Tensile tests as well as simple forming experiments considering different loading conditions were used to assess the applicability of a standard material model which is typically used in sheet metal forming simulations. An isotropic flow curve from the uniaxial tensile test and the Hill48 yield locus description were used as standard model. The Hill48 anisotropy parameters were determined using the Lankford coefficients.

For the uniaxial tensile test in 45 and 90 degree with respect to rolling direction, some significant deviations between experiment and simulation using the standard model can be observed. This is a known effect for the case that the Hill48 parameters were adjusted with respect to the Lankford coefficients. In case of the bulge-test the strains were overestimated with the numerical model. It is supposed that the experimentally observed stress-dependent hardening behavior is not correctly described with the standard model. Considering the Nakajima test, the 20 mm specimen which corresponds to the uniaxial tensile loading can be well predicted with the standard model while some more significant deviations are observed for the round specimen (200 mm). The standard model overestimates the strains, similar to the bulge test. The numerically predicted strains in the cup drawing test fit relatively good to the experiments for the lowest drawing depth of 20 mm, some more significant differences can be observed in the drawing depth of 60 mm. The punch-displacement curve is overestimated by the standard model.

It can be concluded that the considered standard model gives in principle reasonable results, but some significant deviations in the strain field and the force displacement curves could be observed. In order

to exploit the full forming capability of the TWIP-steel material, a more accurate description of the forming behavior is needed.

## 1.6.2 Formulation of a constitutive framework to describe the forming behavior of TWIP-steel

The physically-based Bouaziz-Allain approach [Bouaziz2001; Allain2004] for the description of flow behavior of TWIP-steels has been considered as a base model for the current research. This model considers some micromechanical quantities like the dislocation density, twin volume fraction and the flux of dislocations as internal state variables which develop depending from the current material state and the loading history. It was expected that the consideration of such a micromechanically motivated approach will give a better description of the macroscopic material behavior. Here a special consideration was on the effect of twinning. It is established that the high work hardening rate in TWIP-steels results from generation of deformation-nucleated twins. The dominant deformation mode in TWIP-steels is dislocation glide, while the deformation-nucleated twins gradually reduce the effective glide distance of dislocations which results in the “Dynamic Hall Petch” effect, see e.g. [DeCooman2012].

In order to include the influence of different loading conditions and kinematic hardening on the material behavior the original Bouaziz-Allain model has been modified and the extended three-dimensional finite elasto-plastic formulation has been developed. This model has been implemented into two commercial FE-codes LS-DYNA and PAM-STAMP. With respect to the experimental data and the needs of practical sheet forming simulations, the base model was extended in the following way:

- **Extension of the initially 1d-model to a 3d-model**  
Since the 1d-formulation of the base model is not suited for the implementation into a finite element formulation for sheet metal forming it was extended to a 3d-formulation. Therefore, several quantities and also the corresponding evolution equations had to be reformulated from scalar quantities to tensorial quantities.
- **Consideration of kinematic hardening**  
Extending the approach of Bouaziz et al. [Bouaziz2011] who presented the back-stresses in the 1d-formulation, the back-stress tensor  $\mathbf{X}$  has been introduced, which describes the kinematic hardening by incorporating the directional nature of the number of dislocations stored at an obstacle like a grain or twin boundary through the corresponding tensor  $\mathbf{n}$  of the flux of dislocations which have been arrived at a boundary.
- **Implementation of the anisotropic yield function Barlat YLD2000-2D to describe the initial yield surface of the material**  
Regarding the experimental results and in order to have sufficient flexibility to fit the behavior of TWIP-steels it was found that a simple isotropic von Mises based yield surface is not sufficient to accurately describe the deformation behavior of the considered material. Therefore, the model has been advanced by consideration of the Barlat YLD2000-2D yield condition [Barlat2003]. Since this yield condition is formulated for the plane stress state, it is only available in the shell formulation of the TWIP4EU model. Thus, anisotropic behavior of TWIP-steels can thus be captured precisely through 9 additional material parameters.
- **Consideration of a stress dependent twinning evolution**  
The evolution of twins and, consequently, strain hardening depend on the stress state applied. This has been revealed by comparison of uniaxial and biaxial flow curves and also by the available SEM/TEM analysis of twinning in different specimens. These findings agree with observations reported in literature [Renard2012]. An increase of the stress triaxiality leads to more pronounced twinning and thus more pronounced strain hardening. In order to account for stress dependent twinning effect, a factor  $k_{TWIN}$  which depends on the stress triaxiality has been introduced to the formulation of twin volume fraction.



## **1.7 WP7: Algorithmic treatment and numerical implementation of the macroscopic material model**

### **1.7.1 Algorithmic formulation of the developed macroscopic model for numerical implementation**

The algorithmic formulation of the macroscopic model developed in WP6 was successfully completed. This formulation is the basis for the implementation of the model into a finite element package.

### **1.7.2 Numerical implementation in for the 3D-case (solid) and 2D-case (shell formulation)**

The TWIP-steel material model was successfully implemented into two different finite element packages (LS-DYNA, PAM-STAMP) as solid formulation considering an isotropic yielding. Further, the TWIP-steel material model was successfully implemented into both the finite element packages for the use with shell elements. For this purpose, the original 3-dimensional solid formulation was constrained to fulfil the plane stress assumption. A comparison between the results obtained from the solid formulation and the shell formulation show the same behavior. The shell formulation of the developed model was used for the simulation of the forming experiments and the forming of the prototype. It should be noted that the aforementioned anisotropic yield function YLD2000-2D is only available for the shell formulation, since this yield functions is formulated for the plane stress condition.

### **1.7.3 Preliminary simulations to evaluate the numerical implementations**

The different implementations were extensively tested. Therefore, standard one-element numerical tests under consideration of different loading conditions were performed and different quantities like stress and strain components and internal variables were compared. The results show that the different implementations give the same results for one element tests and also for conventional tests like the uniaxial tensile test.

### **1.7.4 Simulation to validate the model formulation with a special focus on the development of internal state variables**

The first parameter identification procedure was performed in order to fit the macroscopic stress strain curve as well as the internal variables that describe the development of the twin volume fraction. Here, a two-step procedure was applied. In a first step, the parameters related to the twinning evolution were identified. For this purpose, the TEM data provided in task 3.2 were used. In the second step, the remaining parameters were fitted with respect to the stress-strain curve from the uniaxial tensile test. A good agreement between the experimental data and the simulation can be achieved for both the macroscopic behavior and the internal variables. Also the slope of the flow curve under biaxial loading can be modified independently from uniaxial behavior by consideration of the stress dependent hardening approach of the developed model.

## **1.8 WP8: Simulation of forming experiments and validation of the constitutive formulation**

### **1.8.1 Simulation of experimentally evaluated forming processes and comparison with experimental data**

The developed material model was validated by comparison of the obtained simulation result with both the experimental data and the results of the Hill48 standard model.

The uniaxial tensile test was considered in three directions to account for the anisotropic behavior of the TWIP-steel material. The TWIP4EU-model is able to precisely describe the stress-strain curve in all three directions while the results of the standard model significantly deviate for the stress-strain curves in 45 and 90 degrees to rolling direction.

The experimentally measured strain field of the bulge test can be described with good accuracy. The elliptic shape of the major and minor strain field is correctly predicted with the TWIP4EU-model. Further, the strains along the section cuts in rolling direction and in transverse direction were compared. The maximum strain levels predicted by the TWIP4EU model are in good agreement with the experiments. The Hill48 standard model overestimates the strain. Omitting the stress dependent hardening of the TWIP4EU model in the bulge test simulation leads to an overestimation of the strains. In this case the strain level is comparable to the strain level obtained by the Hill48 model.

For the Nakajima tests the major and minor strains predicted by the TWIP4EU-model along the section cuts in rolling direction are in good agreement with the experiments for the three considered specimens (20 mm, 130 mm and 200 mm). The prediction of the standard model was only for the 20 mm specimen in good agreement while some significant deviations were observed for the 130 mm specimen and the 200 mm specimen.

Compared to the aforementioned forming simulations some more significant differences in the strain field between experiment and the simulation were observed for the cup drawing test. The strains along the considered section cuts were underestimated. The same observation was found for the simulation results with the Hill48 standard model. The reason for these differences could not be clarified, but it is assumed that a more precise description of the Bauschinger effect could improve the results, see next paragraph.

The simulation of the bending under tension test (BUT-test) was considered to evaluate the spring back behavior of the developed material model. Using a standard parameter set which was identified by consideration of the micromechanical quantities as well as the tensile test and the bulge test lead to an overestimation of the spring back behavior. Using a modified parameter set with a larger part of kinematic hardening gives a better prediction. An exact prediction of the spring back behavior could not be achieved. It is expected that an improvement of the kinematic hardening approach (with respect to flexibility and accuracy) could lead to a more precise spring back prediction. This may also lead to an improved prediction of the strain field in the cup drawing simulation since kinematic hardening plays a role at the draw-in of the sheet as well. However, it should be mentioned that the spring back prediction is still being a big challenge not only for TWIP-steels but also for advanced high strength steels in general.

## **1.8.2 Formulation of guidelines for usage of the developed material model**

Guidelines for the determination of the parameters of the TWIP4EU material model were developed. Here the experiences from the forming simulation were taken into consideration. It is noted, that in total, the number of parameters which have to be defined is higher compared to standard material models. This is due to the fact that several different aspects were considered within the developed model: The micromechanical approach to describe the uniaxial isotropic-kinematic hardening of the material, the stress-state dependent hardening model and the anisotropic material description. A strategy for the identification of the parameters is proposed that takes into account microstructure related data as well as information from standard tensile test and the bulge test.

## **1.9 WP9: Prototype production and validation**

### **1.9.1 Definition of design specifications, fabrication of the automobile component and optical strain analysis of the formed components**

A backrest side member of a front seat was chosen as demonstrator part. As a load-bearing part directly positioned in the flow of forces, the backrest side member must provide a high degree of energy absorption during a potential car crash, while still maintaining a high degree of form stability.

Furthermore, the material must exhibit sufficient formability to produce the components. Finally, the maximum blank size must fit to the maximum dimensions of the available TWIP-steel material which is limited to 1000 mm x 300 mm. The chosen part fulfils all these requirements.

The punch of the tool had to be reworked in order to fit to the available sheet thickness of 1.5 mm. Two different blank shapes were used for forming of the prototype. Blank type 1 is close to the final part geometry. It has a high spring back sensitivity and moderate forming demands. Blank type 2 is characterized by a circular flange, a low spring back sensitivity and superior forming demands. Thus, blank type 2 is better suited to demonstrate the forming behavior of the TWIP-steel. Furthermore, two different drawing depths were realized with both blank types. The prototype component was successfully produced for both blank types and both drawing depths. The high formability of the TWIP-steel material could be demonstrated.



**Figure 1.3:** Prototype component made of TWIP-steel.

The strain fields of all four variants were optically measured after forming. It could be shown that there is a good reproducibility of the prototypes with respect to the deformation and the strain field. The data from optical strain measurements of the prototype component were used for comparison with the numerical results. Additionally, strain paths in defined sections cuts were evaluated for further comparison.

## **1.9.2 Model creation, forming simulation of the prototype component and comparison between experimental and numerical results**

A simulation model has been created based on the tool geometry, and experimental parameters according to the prototype tests. The numerical models for the forming simulation of the prototype are available for both commercial software packages LS-DYNA and PAM-STAMP. The strain fields (major and minor strain) of the simulations are in good agreement with the experimental data. The critical regions where the highest strains are measured are correctly predicted with the model. A more detailed evaluation of the strains along a section cut shows also a good agreement between the experimental data and the numerical results.

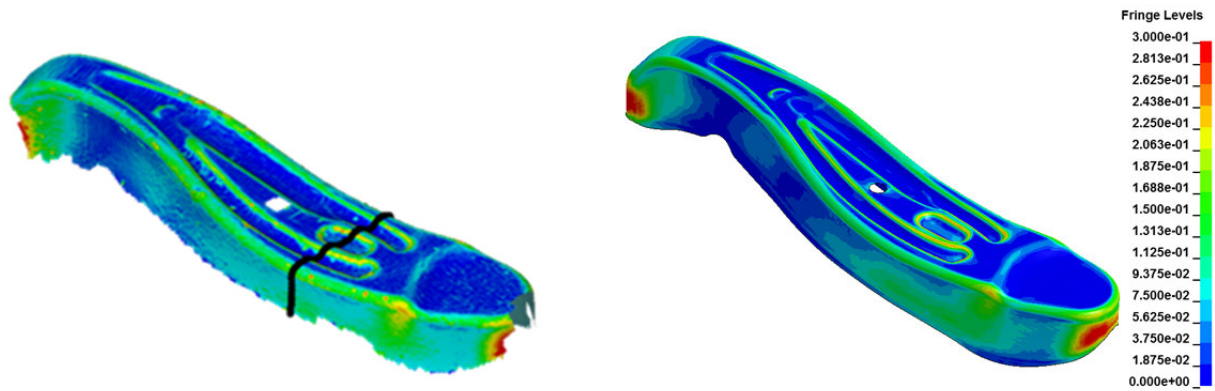


**Figure 1.4:** Major strain field after forming. Comparison between the experimental data (left) and the simulation results with the TWIP4EU-model (right). The colour scale of the legend is the same for experiment and simulation.

Under consideration of the standard set of parameters, the spring back of the prototype is overestimated, which corresponds to the results of the BUT-test simulation in WP8. Using a modified set of parameters leads to a better prediction of the spring back behavior, an effect that could also be observed in the BUT-test simulation.

## 2 Scientific and technical description of the results

### Motivation and objective of the project

In recent years the European steel industry has directed intensive research effort to the development of high manganese content steel grades which combine high strength and high ductility. During plastic deformation these steels typically undergo martensitic phase transformations (TRIP-effect: transformation induced plasticity) or mechanical twinning (TWIP-effect: twinning induced plasticity). Both types of displacive transitions are additional deformation mechanisms and introduce a strong dynamic microstructure refinement which governs a high hardening rate and superior ductility. The increased intensive research focused on these steels, of which European research has played a major part, has opened the doors for the introduction of TWIP-steels into the market. The most prospective market for TWIP-steels is the automotive industry as these steels offer a high flexibility for the production of unconventional shapes, in addition to the excellent properties that they present. Further, these steels offer a high lightweight potential through reduced materials usage due to the combination of high strength and high ductility and lower density (-5%) compared to conventional steels.

The automotive industry is very progressive in using numerical simulation tools all along the process chain, starting from first design steps up to the demonstration of crash worthiness. An integral part of the simulation concept mainly based on explicit or implicit finite element (FE) codes is the adequate description of the material behavior by efficient material models in all relevant phases of the process chain, complemented by practical concepts of material testing. Therefore, a new steel grade like TWIP-steel will only be accepted for large scale applications in the automotive industry if it will fit into the existing simulation concepts. This requires a thorough validation of the material behavior with easy to fit and easy to use material models to be included in commercial FE codes. At present, the superior deformation characteristic of TWIP-steels itself cannot be accurately described with available material model in commercial FE packages. This project, therefore, meets the requirements of the industry towards the development of predictive simulation techniques for the simulation of TWIP-steels in order to design innovative products on the basis of robust and stable production processes.

The aim of the project *TWIP4EU* is to develop a simulation framework to accurately model the complex deformation and forming behavior of TWIP-steels. The developed model will be implemented into commercial finite element codes to ensure its availability for industrial use. It is expected to go beyond the current state-of-the-art, thus facilitating the introduction of TWIP-steels in the automotive industry. Further sub-goals are the detailed experimental and simulative analysis of TWIP-steels with respect to the multiaxial material behavior, nonlinear loading paths and Bauschinger effect, as well as the validation of the developed model on complex forming processes including spring back behavior, the validation of the virtual design process and the formulation of guidelines for the application of the simulation framework.

## 2.1 WP1: Technical and administrative project coordination

### 2.1.1. Structure of scientific and technical work program

TWIP4EU comprises a well-structured work program divided into nine work packages that includes experimental investigations, micromechanical and macroscopic modelling, typical forming experiments and corresponding simulations as well as prototype production and validation. The interrelation between different work packages is illustrated in Figure 2.11. The work program has been assembled in three task groups, each of which contains two or three work packages:

**TG (I) experimental group** is related to WP2, WP3, and WP4. It provides the material needed for all experimental analysis and subsequent forming experiments and includes the material characterization on micro and macro scale.

**TG (II) modelling and implementation group** considers the development of the *Virtual Lab* for TWIP-steels as well as the macroscopic material model and its implementation into the finite element framework. The work packages WP5, WP6, and WP7 are related to this task group.

**TG (III) application and validation group** contains the work packages WP8 and WP9. It is focused on the comparison and validation between experimental data obtained for simple forming tests up to prototype testing and the corresponding predictions of the numerical simulations.

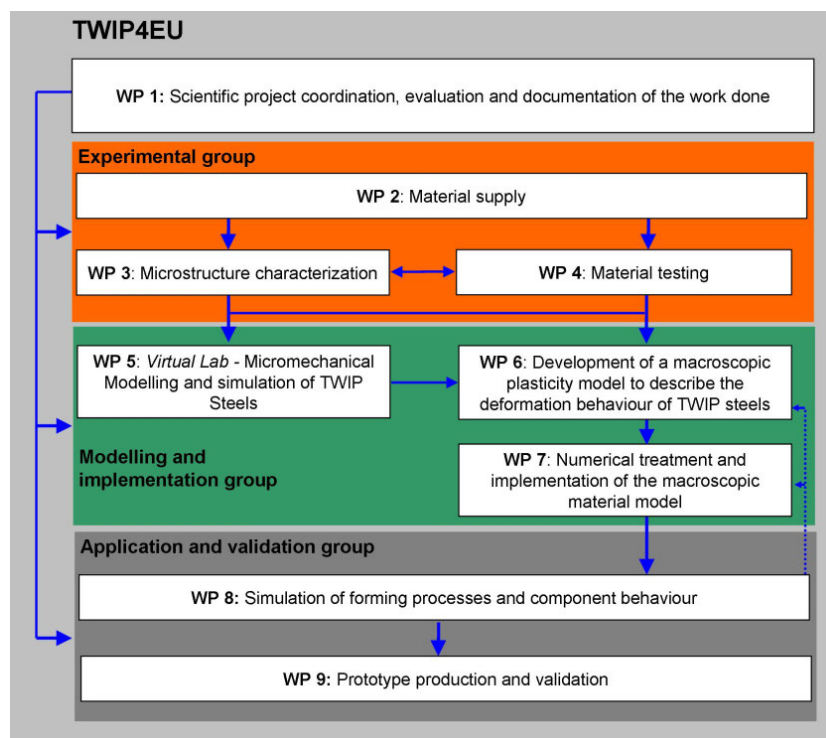


Figure 2.1.1: Work package overview

### 2.1.2 Definition of material characterization procedure and automobile prototype component

An experimental test program was elaborated for a detailed analysis of the TWIP-steel material. The experiments are given in the following overview, more details are given in the description of the corresponding work packages.

- Microstructure characterization – WP3

- Microstructure and texture analysis of material in the initial state
- Microstructure, texture analysis and TEM analysis of material after different deformation states.
- Fracture analysis
- Macroscopic material characterization – WP4
  - Tensile tests
  - Cyclic test
  - Bulge test
  - Nakajima test (FLC)
  - Bending under tension test
- Forming experiments – WP4
  - Nakajima tests (strain fields)
  - Cup drawing
- Component test – WP9
  - Prototype production (two different blank shapes)

A backrest side member of a front seat was chosen as prototype component. The component is relevant for crash safety, thus high strength steel is used for production. Due to shape of the component, the sheet material must have sufficient formability. These requirements can be fulfilled by TWIP-steel material.

### **2.1.3 Participation on national and international workshops and publication of the accomplished work**

#### **Presentations on national and international workshops:**

- A. Butz, M. Zapara, D. Helm, A. Erhart, A. Haufe, M. Biasutti, D. Croizet, M. Kampczyk, M. Schneider, N. Stenberg, J. Hagstrom: *On Constitutive Modelling of TWIP-Steels and its Application to Sheet Metal Forming Simulations*. 8<sup>th</sup> Forming Technology Forum, Zurich, Switzerland, 29.-30.06.2015.
- A. Erhart, A. Haufe, A. Butz: *A constitutive model for the simulation of the deformation behavior of TWIP-steels*. The 16th International Conference on Sheet Metal, March 16 - 18, 2015, Erlangen, Germany.
- A. Erhart, A. Haufe, A. Butz, M. Zapara, D. Helm: *Implementation of a constitutive model for the mechanical behavior of TWIP-steels and validation simulations*. 18th International ESAFORM Conference on Material Forming (ESAFORM 2015), April 15-17, 2015, Graz, Austria.
- A. Butz, M. Zapara, D. Helm, A. Erhart, A. Haufe, D. Croizet, M. Biasutti, N. Stenberg, J. Hagstrom, M. Kampczyk, M. Schneider: *Material Modeling of TWIP-Steels: Applications to Sheet Metal Forming Simulations*. LS-Dyna Forum 2014. Bamberg, Germany, 06.-08.10.2014.
- A. Haufe, A. Erhart: *Simulation of the Deformation Behavior of TWIP-steels*. Automotive Circle, 24.-25.09.2014, Bad Nauheim, Germany

- M. Zapara, A. Erhart, D. Croizet, A. Butz, A. Haufe, D. Helm, M. Biasutti, M. Schneider: *Macroscopic modelling and simulations of material behavior of modern twinning-induced plasticity steels*. 4<sup>th</sup> International Conference on Steels in Cars and Trucks. 15.-19.06.2014, Braunschweig, Germany.
- A. Butz, M. Zapara, A. Erhart, D. Croizet, N. Stenberg, J. Hagstrom, D. Helm, M. Schneider, M. Kampczyk, A. Haufe, M. Biasutti. *Deformation behavior of TWIP-steels: From experiments to constitutive modelling and simulations*. International Deep Drawing Research Group (IDDRG). 01.-04.06.2014, Paris, France.
- M. Zapara, A. Butz, D. Helm, A. Erhart, A. Haufe, D. Croizet, M. Biasutti, N. Stenberg, J. Hagstrom, M. Kampczyk, M. Schneider: *Modern TWIP-Steels: Constitutive modelling and Numerical Simulations*. Faurecia Seating Process Simulation Workshop, Brieres, France. May 21.-22.05.2014
- A. Haufe, A. Erhart, M. Zapara: *Ein Materialmodell für das Verfestigungsverhalten von TWIP-Stählen*. Presentation on the 20. Sächsische Fachtagung Umformtechnik. Dresden, Germany, 27.-28.11.2013.

### **Publications and Conference Proceedings**

- Butz, M. Zapara, D. Helm, A. Erhart, A. Haufe, M. Biasutti, D. Croizet, M. Kampczyk, M. Schneider, N. Stenberg, J. Hagstrom: *On Constitutive Modelling of TWIP-Steels and its Application to Sheet Metal Forming Simulations*. Proceedings of the 8<sup>th</sup> Forming Technology Forum, Zurich, Switzerland, 29.-30.06.2015, pp 35-40.
- Erhart, A. Haufe, A. Butz: *A constitutive model for the simulation of the deformation behavior of TWIP-steels*. Key Engineering Materials Vol 639 (2015) pp 411-418. doi:10.4028/www.scientific.net/KEM.639.411.
- Erhart, A. Haufe, A. Butz, M. Zapara, D. Helm: *Implementation of a constitutive model for the mechanical behavior of TWIP-steels and validation simulations*. Key Engineering Materials Vols 651-653 (2015) pp 539-544. doi:10.4028/www.scientific.net/KEM.651-653.539
- Butz, M. Zapara: *Modellierung Innovativer Blechwerkstoffe aus TWIP-Stahl*. Fraunhofer IWM Annual Report 2014, 22-23.
- M. Zapara, A. Erhart, D. Croizet, A. Butz, A. Haufe, D. Helm, M. Biasutti, M. Schneider: *Macroscopic modelling and simulations of material behaviour of modern twinning-induced plasticity steels*. Proceedings of the 4<sup>th</sup> International Conference on Steels in Cars and Trucks. 15.-19.06.2014, Braunschweig, Germany, pp 689-696.
- Butz, M. Zapara, D. Helm: *Modellierung von hochfesten und hochduktilen Blechwerkstoffen aus TWIP-Stahl*. Werkstattstechnik online Jahrgang 105, 2015. S. 47-48.
- Butz, M. Zapara, A. Erhart, D. Croizet, N. Stenberg, J. Hagstrom, D. Helm, M. Schneider, M. Kampczyk, A. Haufe, M. Biasutti. *Deformation behavior of TWIP-steels: From experiments to constitutive modelling and simulations*. International Deep Drawing Research Group (IDDRG). 01.-04.06.2014, Paris, France.
- Butz, M. Zapara, D. Helm: *Modellierung innovativer Blechwerkstoffe aus TWIP-Stahl*. Konstruktion 10-2014, IW10-IW11

### **Participation in a trade fair**

- Participation of Fraunhofer IWM at the *12th Blechexpo – International trade fair for sheet metal working*, 03.-06.11.2015 in Stuttgart, Germany



## 2.2 WP2: Material production and supply

This WP is focused on the production and supply of TWIP-steel material for the microstructure analysis of the material in WP3, the macroscopic material characterization in WP4, the forming experiments in WP4 and also for the production of the prototype component in WP9.

The main objectives of the WP are given as follows:

- Production of TWIP-steel material on a pilot plant
- Material supply for the experimental work in WP3, W4 and WP9

### 2.2.1 Production and supply of TWIP-steel material

The material was successfully produced on the small pilot plant for belt casting technology in Clausthal, Germany. 100 sheets of the produced TWIP-steel material with minimum yield strength of 600 MPa were provided for the material characterization and prototyping within the project. The sheet dimension is 300 x 1000 mm<sup>2</sup> with a thickness of 1.5 mm. The alloy composition is given in Table 2.2.1:

Mn	C	Al	Si
0,15	0,007	0,025	0,025

**Table 2.2.1:** Chemical composition in [%] of the considered TWIP-steel

The result of initial material characterization is shown in the following table considering tensile tests in longitudinal and transversal direction:

Test-Nr.	A <sub>0</sub> [mm]	B <sub>0</sub> [mm]	R <sub>p0.2</sub> [MPa]	R <sub>m</sub> [MPa]	A <sub>g</sub> [%]	A <sub>80</sub> [%]
1 - 0°	1.466	20.31	642	1039	40.6	41.4
2 - 0°	1.463	20.15	644	1044	44.8	48.9
3 - 0°	1.474	20.04	638	1049	48.5	53.5
4 - 0°	1.489	20.48	630	1025	39.0	39.9
1 - 90°	1.488	20.52	651	1014	40.8	41.6
2 - 90°	1.487	20.51	644	1019	42.3	43.1
3 - 90°	1.488	20.45	646	1019	43.7	44.7
4 - 90°	1.488	20.28	647	1023	47.5	51.7

**Table 2.2.2:** Mechanical properties of the TWIP-steel from initial characterization

In order to assess the influence of pre-straining on the mechanical properties, a portion of the available blanks from the TWIP4EU batch were pre-strained. The pre-straining was applied by an additional cold rolling procedure, where two different sheet thicknesses (1.35 mm and 1.19 mm) were realized. Due to the work hardening, blanks from the same initial processing route with significant higher yield strength, an increased ultimate tensile strength and a reduced elongation at fracture was obtained as shown in Table 2.2.3. Further, bulge test were carried out on the pre-strained material as described in WP4.

	Test-Nr.	A0 [mm]	B0 [mm]	Rm [MPa]	A80 [%]
Pre-strain level 1	3_10 - 0°	1.348	20.09	1148	35.6
	2_10 - 90°	1.346	20.08	1125	33.0
	3_10 - 90°	1.347	20.10	1121	31.5
Pre-strain level 2	2_20 - 0°	1.187	19.95	1323	19.5
	3_20 - 0°	1.189	20.03	1323	17.5
	2_20 - 90°	1.194	20.10	1325	12.0
	3_20 - 90°	1.189	20.13	1331	12.0

**Table 2.2.3:** Mechanical properties of the TWIP-steel after pre-straining.

In Figure 2.2.1 the engineering stress-strain curves for different two levels of pre-straining can be seen. The yield strengths are about 900 MPa and 1100 MPa. For the material that is pre-strained to a final sheet thickness of 1.19 mm, a significant difference in the ultimate elongation A80 can be observed.

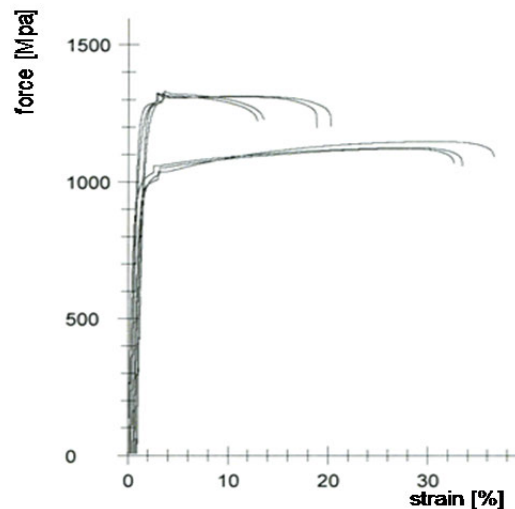


**Figure 2.2.1:** Engineering stress-strain curves of the pre-strained TWIP-steel from initial characterization

### 2.2.3 Production of supply of TWIP-steel material from commercial plant

Initially it was planned to use also serial material for the prototype production from a commercial plant which was built in Peine, Germany. This plant is the world first industrial-scale horizontal belt casting. The principle of this technology is illustrated in Figure 2.2.2.

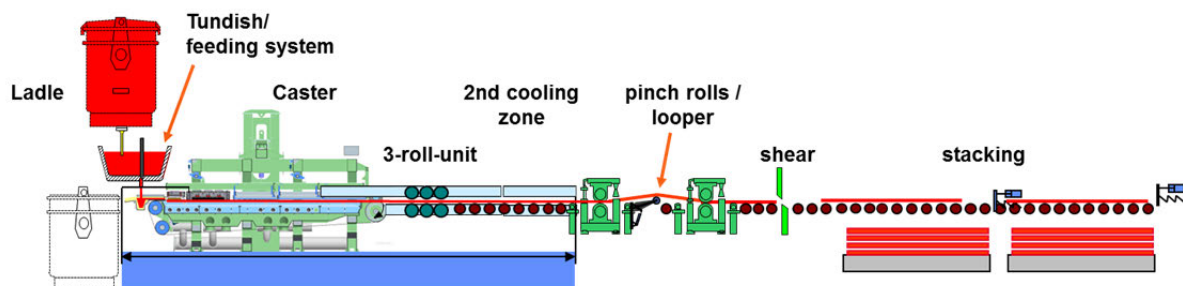


**Figure 2.2.2:** Belt casting plant to be installed in Peine

Since the TWIP-steel material was not available in required time, the prototype material was used instead for all experiments and forming tests as well as the prototype production carried out within this project.

## 2.3 WP3: Microstructure characterisation

WP3 is concerned with the experimental microstructure analysis of the TWIP-steel material. The main objectives of this work package can be summarized as follows:

- Microstructure characterization of the initial material, texture analysis using EBSD and analysis of the morphology of individual grains.
- Microstructure characterization using EBSD, SEM, TEM – to generate information on the effective grain size, twin volumes and to analyze their evolution during deformation.
- Fractography studies to determine fracture mechanisms and damage behavior.
- Analysis of non-linear elastic phenomena in TWIP-steel.

### 2.3.1 Microstructure analysis of the initial material

Materials characterisation of initial state was performed using EBSD and high resolution BSE imaging. The EBSD analyses were performed in a LEO Gemini 1530 FEGSEM. The EBSD hardware was HKL Fast detector and data was collected and analysed using software packages from Oxford Instruments (AZtech and Channel 5).

EBSD analysis was set-up for two kinds of analysis at two levels of resolution, one for grain size and texture analysis and one for detailed characterisation including twins, see Figure 2.3.1. On the left hand side of Figure 2.3.1 grain size and texture were the main targets. A step size of 0.25  $\mu\text{m}$  was used and 800 vs. 600 pixels were included in the analysis which gave almost 2000 grains. The  $\mu\text{m}$  bar is 50  $\mu\text{m}$ . On the right hand side of Figure 2.3.1 the twins and small details were the targets. Therefore 0.05  $\mu\text{m}$  step size was used and 1400\*1400 analysed points were included. The  $\mu\text{m}$  bar is 20  $\mu\text{m}$ . In the EBSD maps crystal orientations were coloured acc. to inverse pole figure. Grain boundaries larger than 2° misorientation and larger than 15° misorientation were coloured black (thin/thick), twin boundaries (annealing twins) were coloured in blue. The data for grain size and texture analysis included many grains in each analysis (>1900). Grain sizes varied quite a lot, from 1  $\mu\text{m}$  to 20  $\mu\text{m}$  in this analysis, see Table 2.3.1. Grains were close to equi-axed and annealing twins were frequent. Figure 2.3.2 shows images from the SEM/BSE detector.

Grain size (ECD, $\mu\text{m}$ )	Number of grains	Smallest grain* (ECD, $\mu\text{m}$ )	Largest grain* (ECD, $\mu\text{m}$ )
4.0	1907	0.9	19.7
* Grains were defined using 10° misorientation ** A limit on 10 pixels was set to define a grain.			

**Table 2.3.1:** Grain size statistics in the as-delivered material.

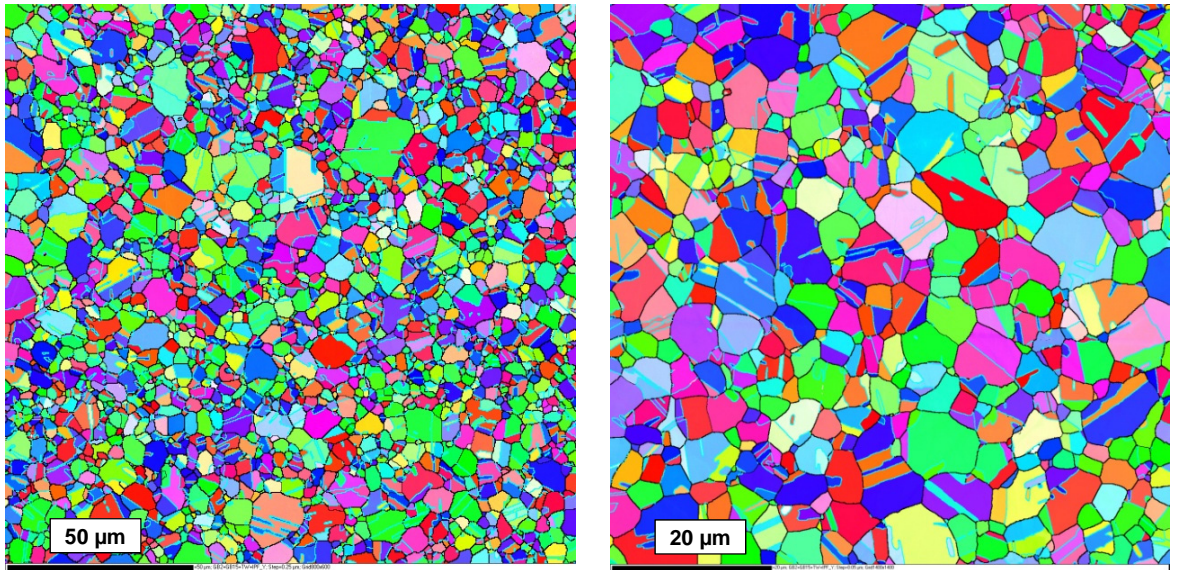


**Figure 2.3.1:** EBSD analysis on the initial material using two different set-ups, inverse pole figure map. Left: One with larger step size (0.25 μm) to cover a larger area and get texture information as well as grain size statistic. Right: A one with a finer step size (0.05 μm) to characterize twins and fine details in the microstructure.

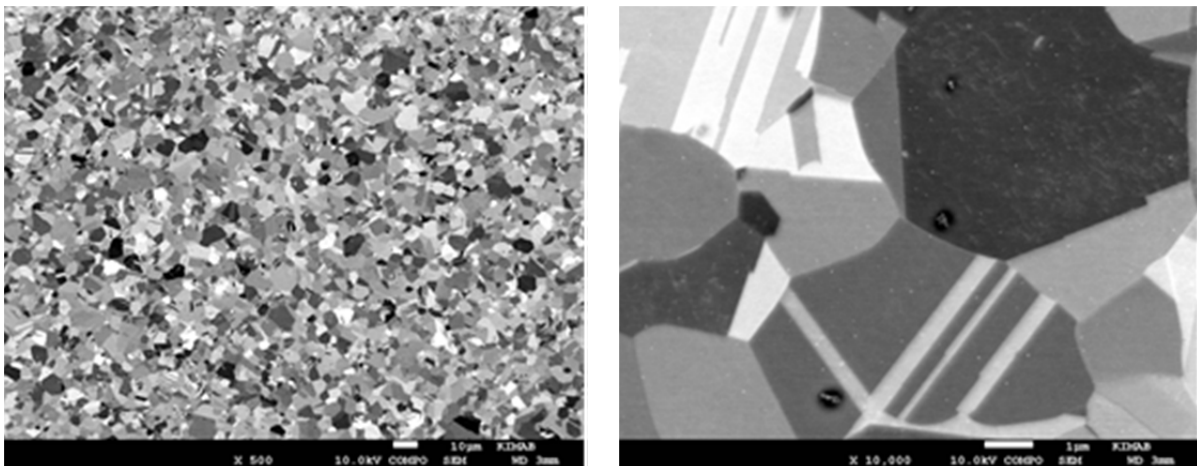


**Figure 2.3.2:** SEM/BSE images of the microstructure

Several EBSD analyses were performed for different positions and material state; this was done to ensure that the information of grain sizes and texture was statistically significant. Measurements were performed in several positions in the steel band; 15% depth (surface) and 35% depth (centre) and on both sides of the band. Figure 2.3.3 below shows examples of results from these EBSD analyses as pole figures. Texture analysis showed that the texture was similar on both sides of the steel band and that there were only small differences between surface (15% depth) and centre (35% depth). The texture was a weak retained rolling texture. From the evaluation of the misorientation profile in the material follows that twin boundaries ( $60^\circ$  around  $\langle 111 \rangle$ ) were frequent (annealing twins).



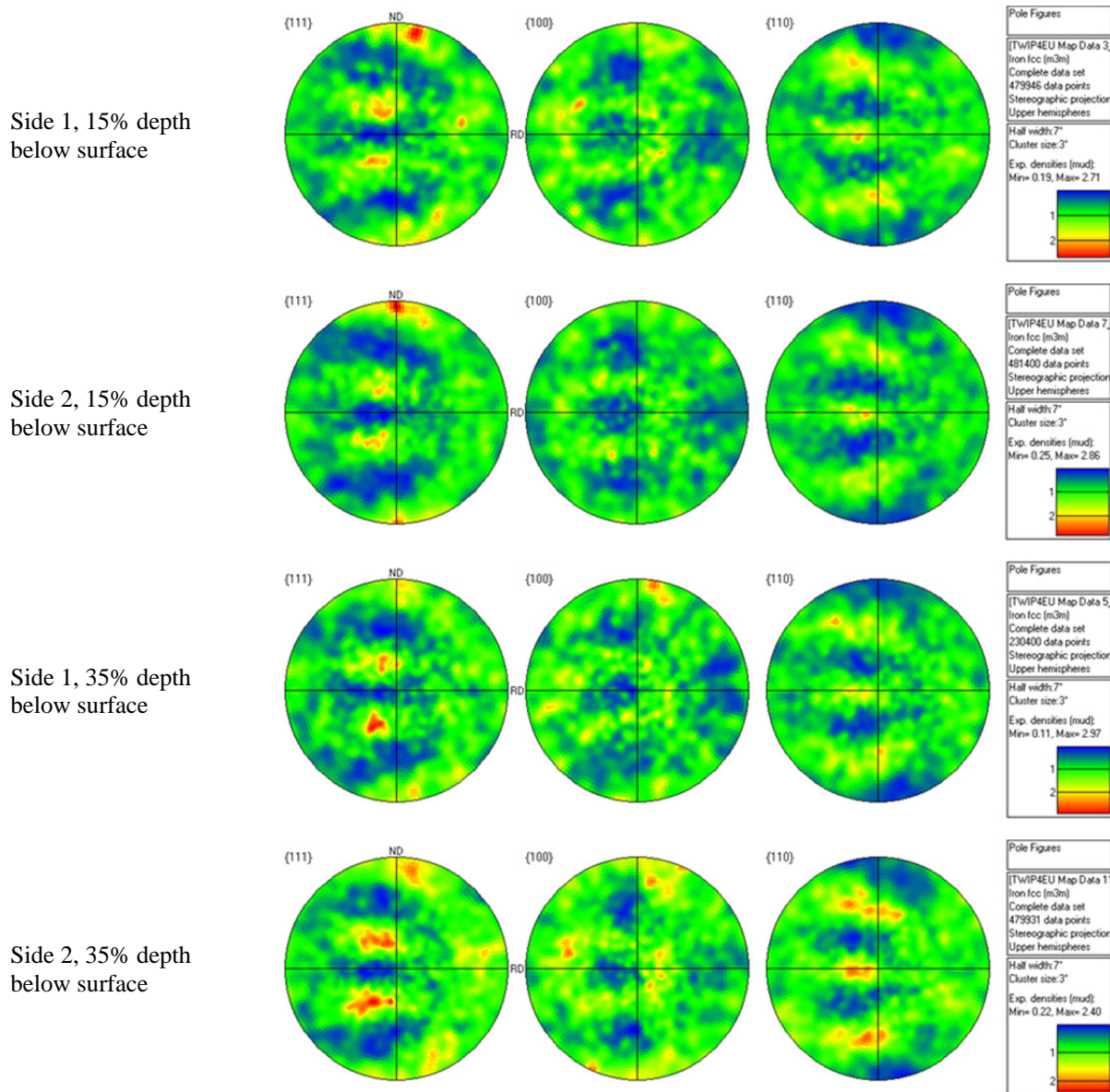


**Figure 2.3.3.:** Texture analysis from EBSD measurement. The extensive analyses showed that texture was similar on both sides and that there were small differences between surface (15% depth) and centre (35% depth). The texture was a weak retained fcc rolling texture.

## 2.3.2 Microstructure analysis of pre-strained material

Since the macroscopic model is based on a physically motivated approach (see WP6), physical quantities like twin volume fraction and dislocation density and the evolution of these quantities during deformation are of high interest. The experimental analyses of these quantities provide valuable data which were directly considered in the modelling part. The evolution of the twin volume fraction and the dislocation density at different strain levels were used to validate the material model as described in Section 2.7.

It was also analysed if the applied stress state during deformation influences the amount of the twin volume fraction during deformation. For this purpose, macroscopic tensile tests were interrupted at different strain levels and the smaller samples were cut out from these specimens for further microstructure analysis. Furthermore, specimens from shear test and from bulge test (biaxial stress state) were analysed. The evolution of the twin volume under load reversal was also analysed for one selected case.

Different macroscopic tests were interrupted at different strain levels, see below. Smaller samples were cut out from these pre-strained specimens for further microstructure analysis. The main instrument for determination of twinning (area fraction and thickness) and dislocation densities was transmission electron microscopy (TEM) due to the fact that SEM based methods do not have the resolution to do the work properly. A combination of TEM and SEM, where SEM was used to analyse how many grains (fraction of) which actually contained twins, and TEM was used to characterise the twins, was the best way to get both details and statistics. SEM-EBSD was also used for characterisation of the crystallographic texture evolution during deformation. The TEM work was performed on a TEM JEOL 2100F (HR).

The deformation states chosen for characterisation were:

- Tensile straining using macro tensile specimens; 5%, 10%, 15%, 25% and 45% (engineering strains parallel to the rolling direction). Additionally, samples strained to 5% and 10% in the transverse direction were included.
- In-situ SEM tensile strain: Series of SEM-EBSD analyses were made.
- In-situ SEM shear strain: A series of SEM-EBSD analyses were made. Additionally TEM specimens were extracted from two shear strained materials (about 5% and 15% strain).
- Specimens that were first strained to 10% tensile strain and then compressed back close to zero strain.
- Specimens from bulge tests which were interrupted at three different loading levels (15, 25 and 40 %) to analyse the microstructure development under biaxial stress state.

Characterisation of several different deformation modes was performed; shear tests, tensile-compression tests and bulge tests as described above. EBSD was used for characterisation of texture evaluation and TEM was used for analysis of twins and dislocation densities. Table 2.3.2 with data from all the TEM analyses is provided; this table contains data from the studies of tensile tests as well as the data on shear tests and bulge tests. Some more details are given in the following subsections.

Sample	Deformation mode	Deformation (%)	Twin Area in twinned grains (%)	Twin Area, total (%) <sup>*</sup>	Disl. Density in Twins ( $10^{14} \text{ m}^{-2}$ )	Disl. Density in Matrix ( $10^{14} \text{ m}^{-2}$ )	Mean twin distance (matrix, nm)	Mean twin thickness (nm)
0-5	Tensile	5	2.5	0.25	12.3	1.5	793	20
0-10	Tensile	10	8.8	1.7	24.1	2.4	431	20
90-5	Tensile	5	3.2	0.32	-	1.6	672	22
90-10	Tensile	10	7.6	1.5	-	2.5	425	17
6B 15	Tensile	15	10.4	2.6	-	3.5	218	12
6B 25	Tensile	25	18.4	9.2	-	-	148	15
4-01 45	Tensile	45	21	20	-	-	162	19
S 0.11	Shear		0.6	<<0.1	-	2.4	>>1000	-
S 0.22	Shear		10.4	6.4	-	4.0	147	17
Tensile	Tensile	5.8	5.9	0.59	-	2.7	204	13
Tensile/comp.	Tensile/compress	7.7/2.2	2.8	0.42	-	3.3	665	23
Bulge1		15**	(17)***	-	-	5.6	104	22
Bulge2		25**	(15)***	-	-	-	106	18
Bulge3		40**	(10)***	-	-	Disl. Cell****	167	19

\* Calculated according to Ref. [Gutierrez2011].

\*\* Equivalent engineering strain (%) according to Salzgitter-Mannesman.

\*\*\* Twins in bulge tests develop preferentially on crystallographic planes 45° away from the sheet surface, this makes analysis difficult and only very few observations could be done.

\*\*\*\* Bulge3, 40% eq. strain; Dislocation cells developed, diameter = ca. 80 nm including half dislocation wall.

**Table 2.3.2.:** Summary of data extracted from TEM analysis

### 2.3.2.1 Uniaxial tensile straining using macro tensile specimens

#### SEM characterisation

All specimens were characterised using EBSD to get data for the evaluation and modelling of crystallographic texture evolution. The EBSD analyses were performed in a LEO Gemini 1530 FEG-SEM. The EBSD hardware was HKL Fast detector and data was collected and analysed using software packages from Oxford Instruments (AZtech and Channel 5).

## TEM characterisation

The twinned area was preferably imaged in the dark field mode. By using the (200) diffraction spot of the twins when the (111) plane from the matrix was diffracted it was possible to measure the true twin cross section and the distance between the twins with high resolution in a large part of the grain without much disturbance compared what is obtained in the bright field mode. The images were then analysed by using image analysis tools and extracting the intensity along lines perpendicular to the twins. In this way the intensities from the (200) spot of the twins were separated from the matrix contrast and thus possible to be measured with a very high resolution,  $\pm 2$  nm.

Bright field imaging was used for the measurements of dislocation densities and dark field imaging was used in order to show the complex lattice structure in the matrix and twinned area of the material having a large degree of deformation. The densities of dislocations were measured in the samples having up to 15 % degree of deformation. At higher strain it was too difficult to resolve single dislocations. Here the bright field mode was used when the dislocations on the (111) plane were visible in high contrast. The method used for these measurements was the line intersection which gives the number of dislocations expressed as number/m<sup>2</sup>. For these analyses it was necessary to know the thickness of the foil at each occasion, and for this reason the thicknesses of the individual grains in the specimens were measured by means of electron energy loss spectroscopy (EELS).

For the materials having 5-10 % deformation the dislocation density in the twins was measured and compared with the dislocation density in the matrix. The difference in dislocation density between the area in the centre of grains and the area close to grain boundaries was quantified in some of the grains.

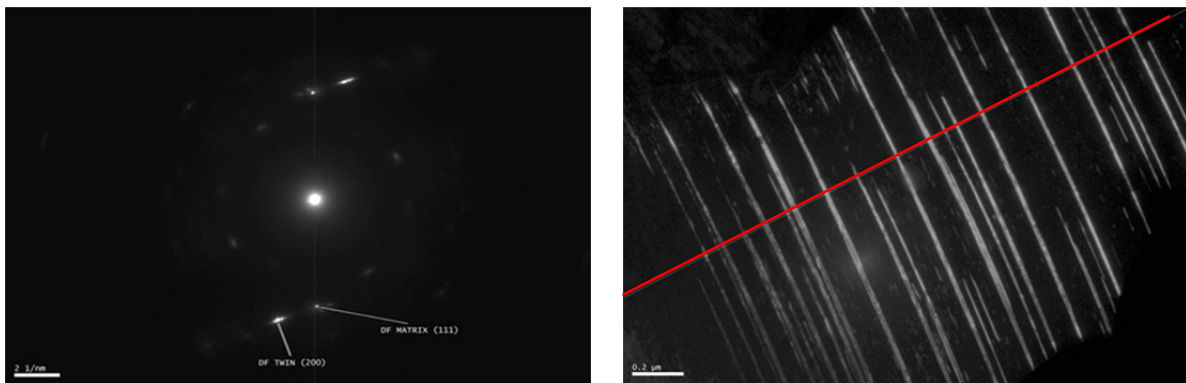


**Figure 2.3.4.:** Left: Diffraction pattern from a crystal grain showing the spots from matrix respectively twin lattices. The (111) plane is the twinning habitus plane and is here close to parallel to the electron beam. Right: Dark field image showing bend twins by using the (200) reflection as indicated in the diffractogram above. Deformation degree was 25 % (engineering strain). The diagram below represents the intensity along the indicated line

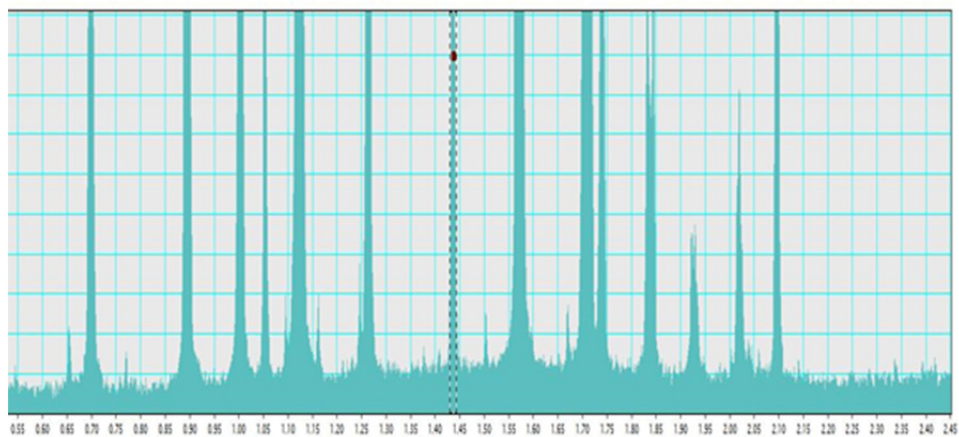


**Figure 2.3.5.:** Intensity diagram showing the intensity from the (200) spot along the red line in the dark field shown in Figure 2.3.4.

Approximately 20-25 different grains were investigated carefully for each type of material. Not all grains contained twins, especially at low strains. Kim et. al. [Kim2013] present data for the fraction of twinned grains, and at 5% strain about 10% of the grains contain twins according to this paper. The present study by TEM confirms these findings but for the analysis of the fraction of twinned grains it is recommended to use SEM/EBSD to gain more statistics. SEM/EBSD has on the other side limited resolution and at low magnifications it is not possible to obtain reliable data on 20 nm thick twins, however, by using high resolution band contrast images and angle/axis misorientation relationship it is possible to see twins using SEM/EBSD and it is a convenient way to achieve statistical information about the fraction of grains containing twins.

The final estimation of the total twin area fractions and dislocation densities in the material was made by using the following rough approximations:

For material with 5% deformation, the figures are based on only one operating twinning system and for the other higher degrees of deformation the calculations were based on twinning systems developed on two different twinning planes in 60% of the grains containing twins. This is again referring to Kim et. al. [Kim2013] where it was found that the possibility for the operation of two twinning system in the same grain is likely when the planes (111)//TA. The dislocation density calculations were based on the assumption that two different slip planes were activated for all strain levels. Dislocations in FCC crystal structures operate on two equivalent crystal planes with respect to the direction of the applied strain and the orientation factor of the active slip planes (111). In the twins it is expected that only one slip plane is active.

The results of the quantitative measurements are summarised in Table 2. The Figures 2.3.6 and 2.3.7 illustrate the development of the twin volume fraction and the mean twin spacing, respectively as function of the applied strain.

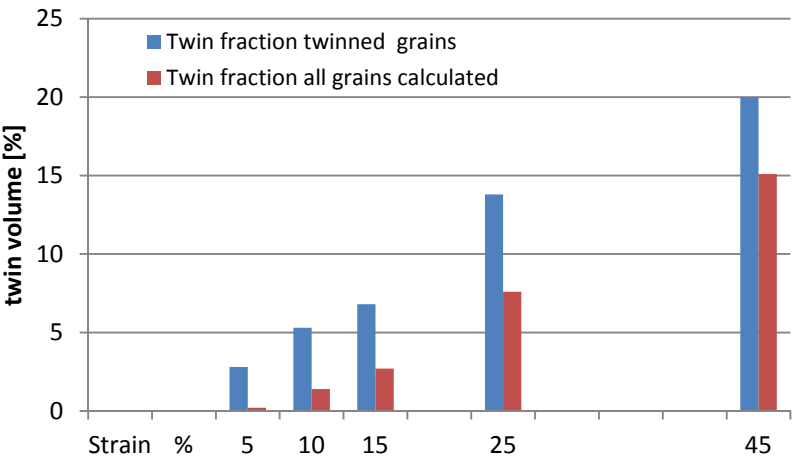


Figure 2.3.6: Twin volume fraction [%] as functions of strain

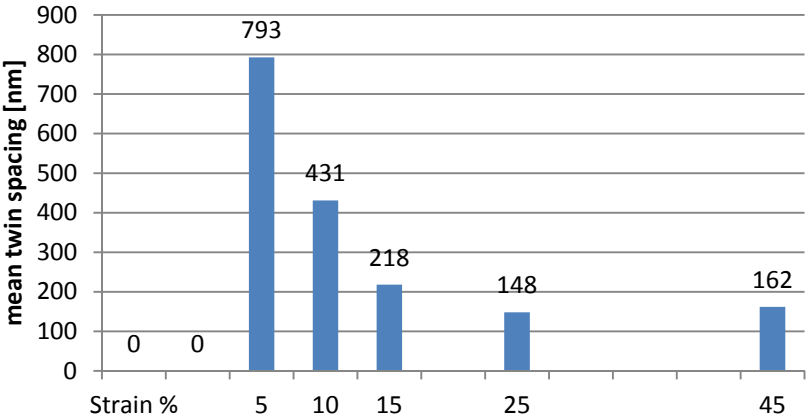
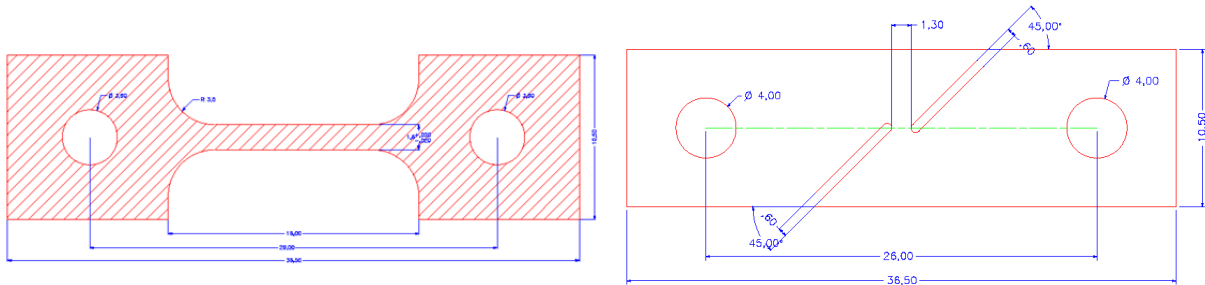


Figure 2.3.7: Mean twin spacing in nm as function of the applied strain



### 2. 3.2.2 In-situ SEM tensile and shear strain

In-situ SEM mechanical testing provides an effective tool for repeated analysis at different strains. In this case in-situ mechanical testing was used for two purposes: One was simply to produce material with a specific, well defined, shear strain for subsequent TEM analysis. The other was to study texture development during increasingly higher plastic deformation. Mechanical deformation of specimens inside the SEM was performed for tensile as well as for shear specimens, Figure 2.3.8. shows the different specimen geometries that were used to realize different stress states.



**Figure 2.3.8:** The specimens used for in-situ tensile test and shear test.

EBSD was used to analyse the crystallographic texture at different strains. Figure 2.3.9 shows pole figures after different degrees of tensile deformation (initial state, 8% strain and 26% strain) and Figure 2.3.10 shows the same for shear strained specimens. The pole figures are plotted in the RD-TD-plane.

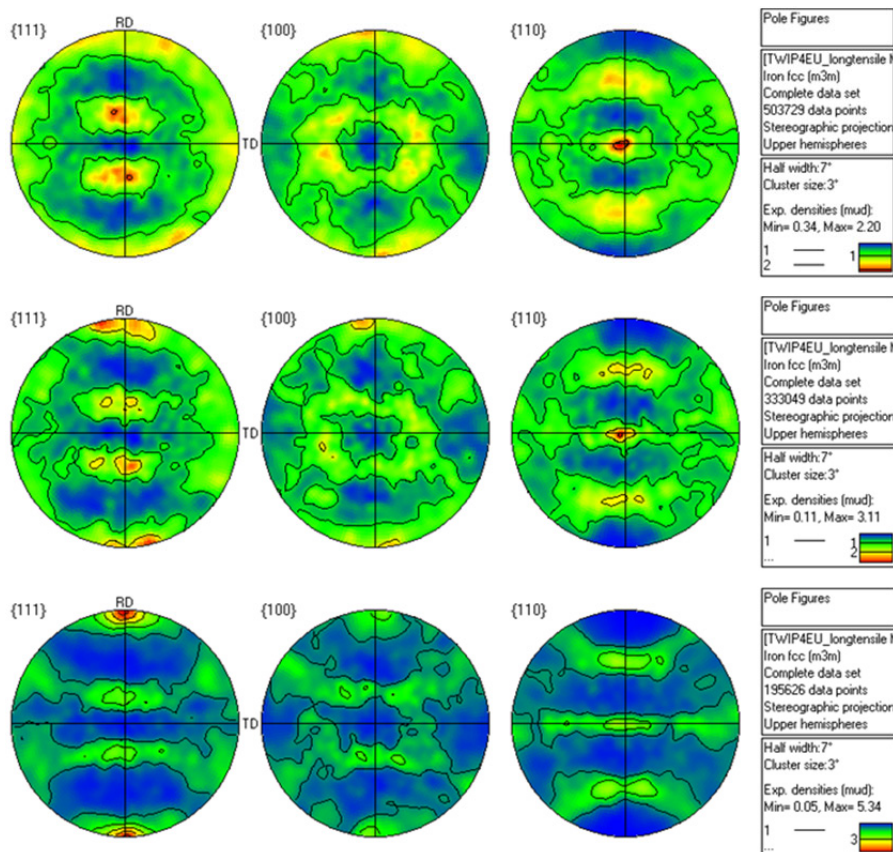


**Figure 2.3.9:** Texture of the TWIP-steel after different degrees of tensile deformation. The first set of pole-figures was without any deformation. The second set was collected after 8% plastic deformation and the third set after 26% plastic deformation (elongation in X direction as measured on the specimen).

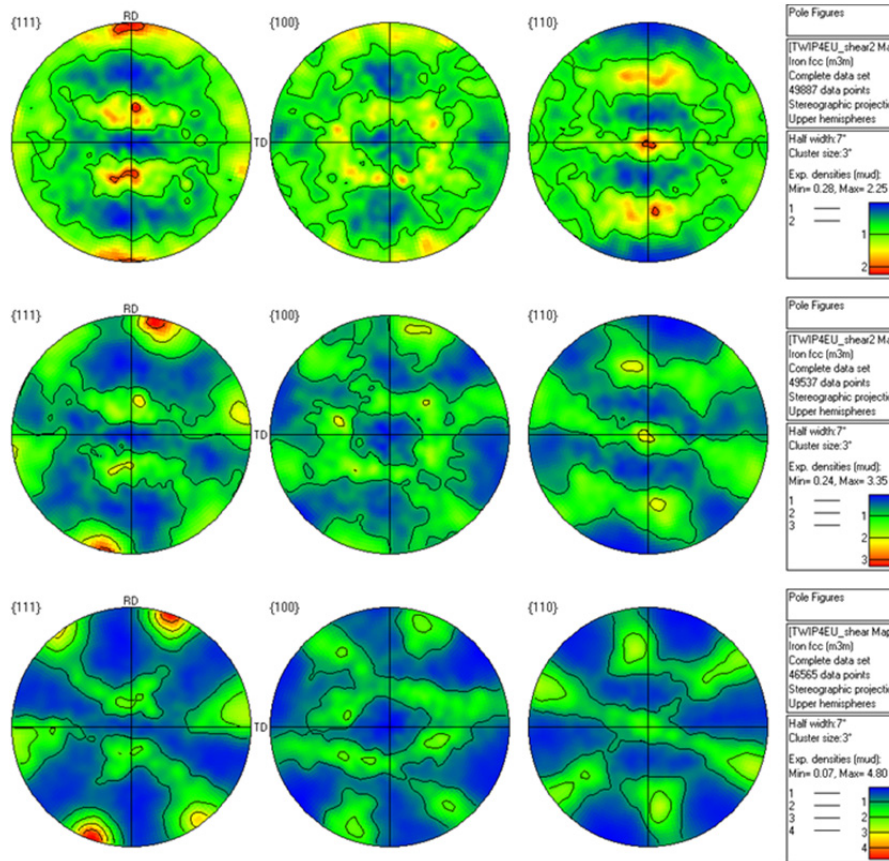


**Figure 2.3.10:** Texture of the TWIP-steel after different degrees of shear deformation.

The fraction and thicknesses of twins and the mean distance between the twins in twin deformed grains in shear- tested TWIP-steel was measured by means of Transmission Electron Microscopy. Two levels of deformation was characterised, 0.11 and 0.22 corresponding to 0.05 and 0.1 equivalent plastic strain (EPS).

It was found that twinning was less pronounced in shear at low strains compared to uniaxial strain but dislocation density was higher at comparable equivalent plastic strains (5%). Shear strain of 0.11 (0.05 EPS) resulted in a dislocation density of  $2.4 (10^{14} \text{ m}^{-2})$  similar to the dislocation density in axial tensile specimens deformed 10%. The twin area fraction was negligible,  $<0.1\%$ , compared with around 3% twin area fraction for the axial tensile specimens deformed 5%. At higher strain the twinning was instead higher compared to uniaxial tension, at a shear strain of 0.22 (0.1 EPS) the twin fraction was 17% compared to 8-9% in the uniaxial test with 10% strain. 17% was reached at a strain of about 25% in uniaxial tension. The dislocation density was also higher in the shear test in this case ( $4 \times 10^{14} \text{ m}^{-2}$ ) similar to the dislocation density in axial tensile specimens deformed 20%.

The twinned area was preferable imaged in the dark field mode. By using the (200) diffraction spot of the twins when the (111) plane from the matrix was diffracted it was possible to measure the true twin cross section and the distance between the twins with high resolution in a large part of the grain without much disturbance compared what is obtained in the bright field mode (Fig.5). The images were then analysed by using image analysis tools and extracting the intensity along lines perpendicular to the twins. In this way the intensities from the (200) spot of the twins were separated from the matrix contrast and thus possible to be measured with a very high resolution,  $\pm 2 \text{ nm}$  (Fig. 6).

### 2.3.2.3 Tensile deformation and deformation by tension and reversed compression

The fraction and thicknesses of twins and the mean distance between the twins in twin deformed grains in TWIP-steel subjected to tension followed by compression was measured by means of Transmission Electron Microscopy (TEM). The evolution of the dislocation density and substructure was also characterized and measured. The material was deformed in a tensile testing machine. One specimen was deformed only by tension at 5.8%, and one specimen was at first deformed by tension to 7.7% and then subjected to reversed strain in compression by 2.2%. It was found that the specimen,

which was compressed by 2.2% subsequent to tension, showed a decreased density of twins and fraction of twined area. Probably, the compression with reversed stress caused “untwining” after tension, in the fraction of twins that have the most favourable orientation factor for the movements of dislocations involved in this process.

Approximately 15 different grains were investigated carefully for each type of material. The final estimation of the total twin area fractions and dislocation densities in the material was made by the following rough approximations: For the strain levels 5.8% and 7.7% the figures are based on the assumption that, at these low strains, twinning takes place on only one twinning planes in the grains containing twins. This is referring to [Guitierrez2011], who showed that the possibility for the operation of two twinning system in the same grain is likely at higher degree of deformation when the texture is developed and planes (111)//TA. The following factors were used for the fraction of twins in the entire population of grains in the material: 0.099 for the tensile specimen with the strain 5.8% and 0.153 for the strain of 7.7% in the tensile-compressed specimen. The dislocation density calculations were based on the assumption that two different slip planes were activated for all strain levels, thus a factor of two was used. Dislocations in FCC crystal structures operate on two equivalent crystal planes with respect to the direction of the applied strain and the orientation factor of the active slip planes (111).

### 2.3.2.4 Specimens from bulge tests

Bulge tests were done externally, see Section 2.4. Three tested specimens were sent to KIMAB for examination. The specimens had experienced equivalent strains of 15%, 25% and 40%. Major and minor strains are shown in Figure 2.3.11.

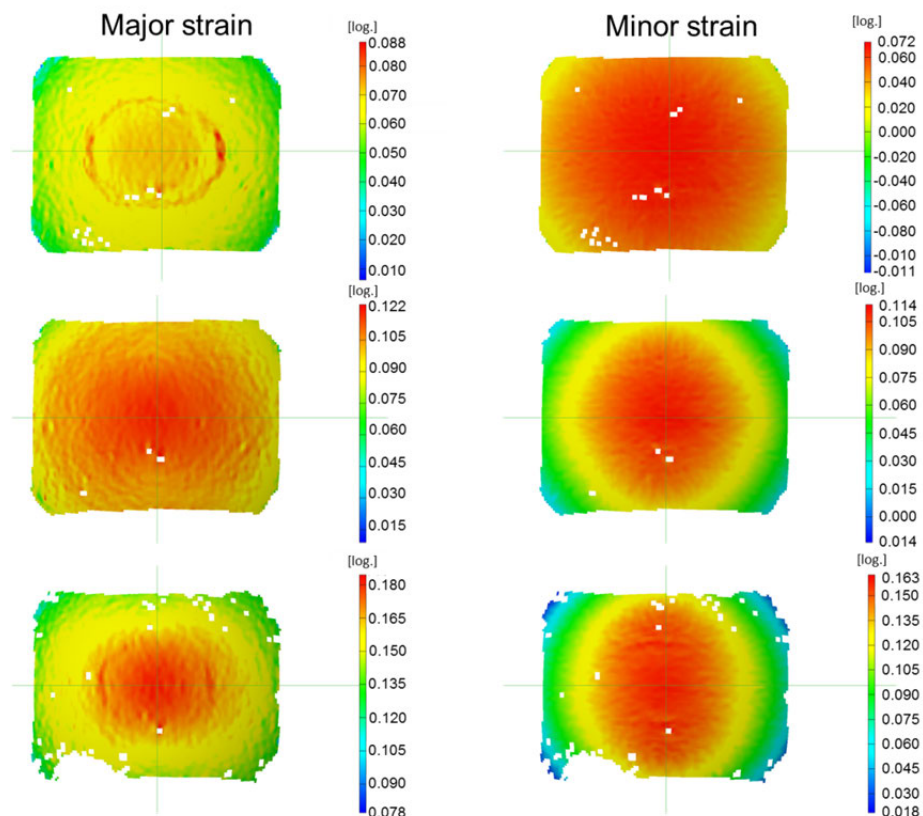


**Figure 2.3.11:** Major and minor strain in the 3 bulge tests (OBS scales are different in the strain bars)

### Texture evolution in TWIP-steel deformed by bulge testing

EBS analysis was performed on the initial material (not deformed) and the three bulge tested materials with different strains. Figure 2.3.12 shows pole figures for different levels of biaxially strained material. A comparison with Figure 2.3.9 and Figure 2.3.10 shows that the applied deformation mode (uniaxial tension, shear, biaxial tension) significantly influences the resulting pattern of the pole figure.



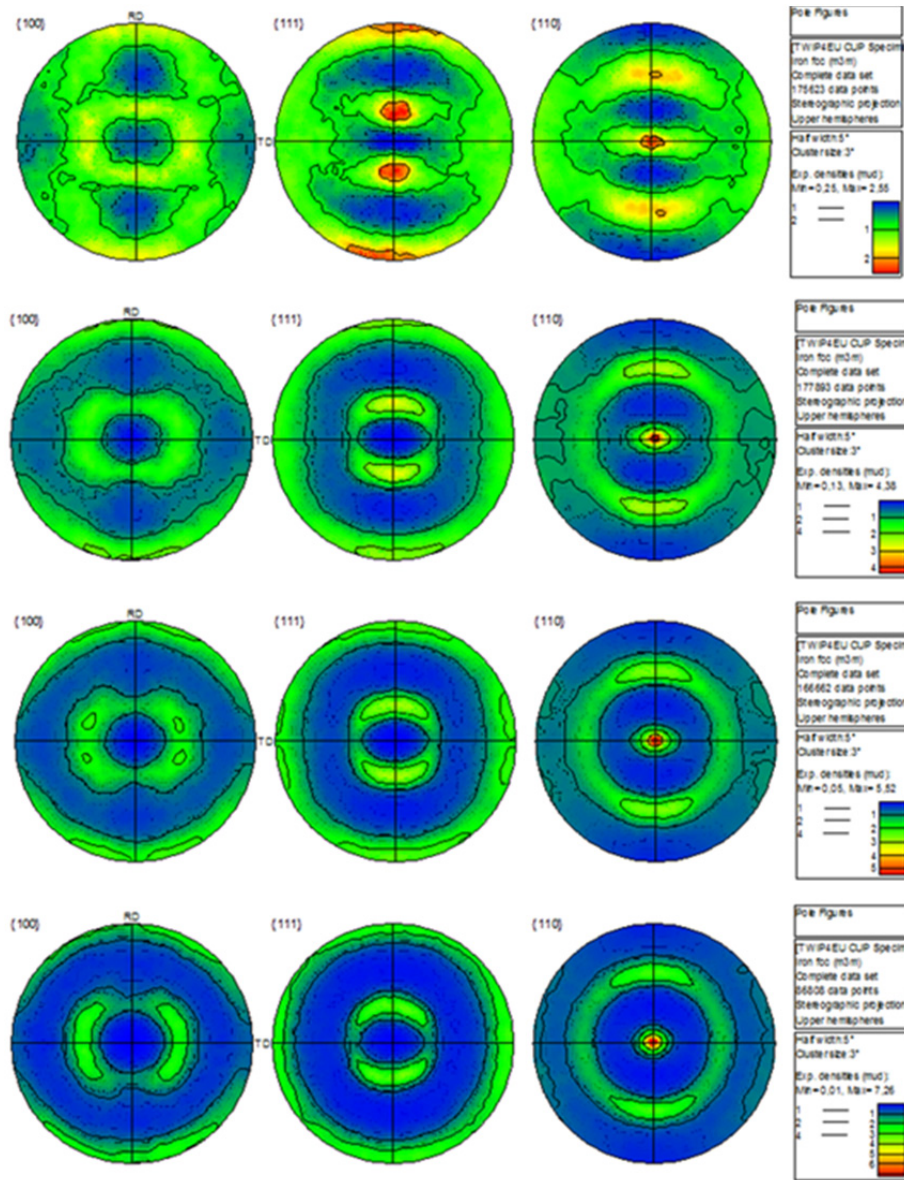


**Figure 2.3.12:** Pole figures for the starting material and the 3 bulge tests at different strains. Not deformed (a), 15% (b), 25% (c), and 40% (d). The step during EBSD analysis was  $2.5\mu\text{m}$  and the matrix was  $489 \times 366$  pixels ( $1.2 \times 0.9$  mm).

In Figure 2.3.13 the microstructure evolution can be seen with increasing deformation during the bulge test. It was not possible to characterise the twins using EBSD. The spatial resolution is not high enough, it must be remembered that the twin thicknesses were only a few tenths of nanometers.

### TEM characterization in TWIP-steel deformed by bulge testing

It was found that the majority of the twins form on crystallographic planes  $45^\circ$  away from the sheet surface and this showed to be devastating for the analysis. TEM foils were made parallel to the sheet surface and the maximum tilt in the TEM was  $20^\circ$ . It was therefore not possible to tilt the twins to become parallel to the beam. Due to these circumstances very few grains could be analysed and the data in Table 2.3.2 is therefore not statistically well. The available data on twins and dislocations are also presented in Table 2.3.2 but they have to be carefully interpreted.

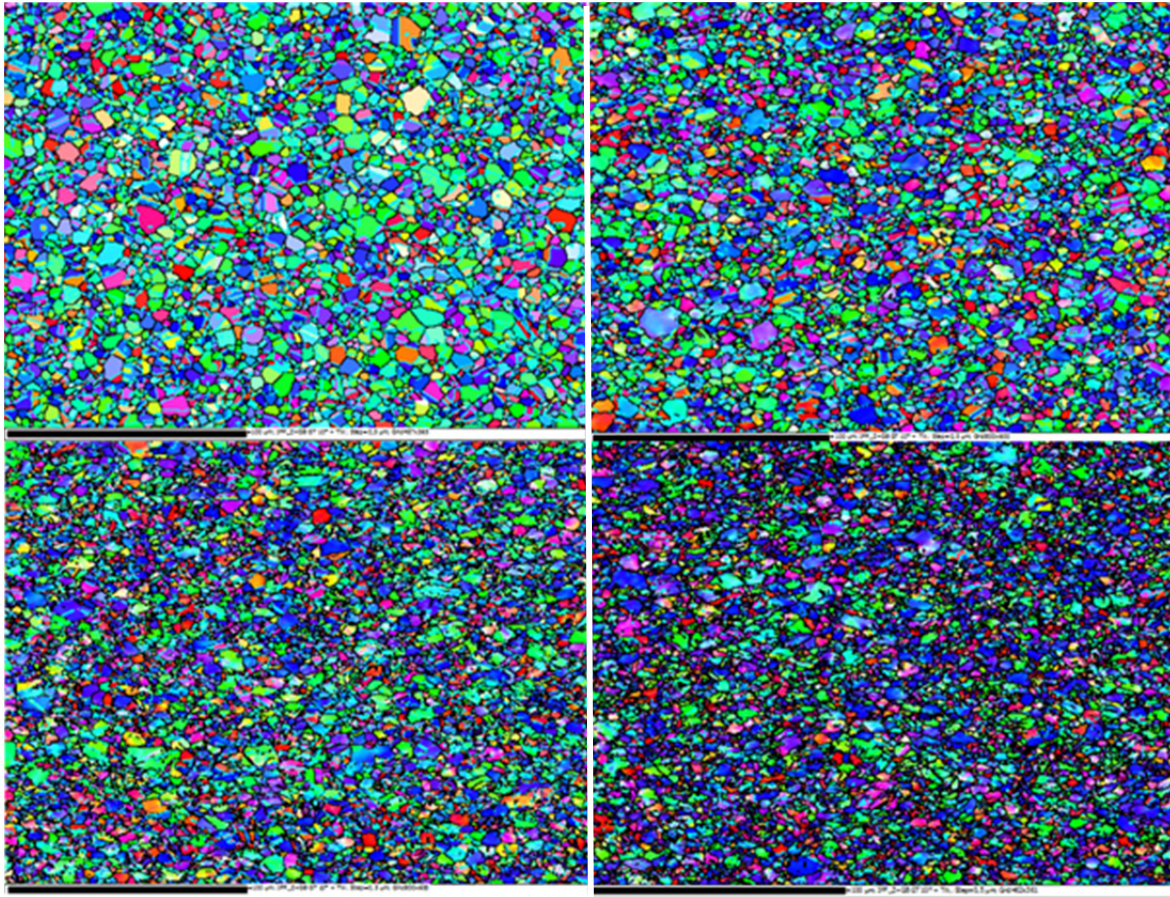
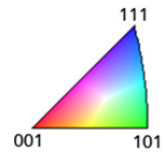


**Figure 2.3.13:** Bulge test: EBSD orientation maps with colours according to IPF colouring in the rolling direction. Not deformed (top left), 15% (top right), 25% (bottom left), and 40% (bottom right). The step during analysis was  $0.5\mu\text{m}$  and the matrix was  $432 \times 361$  pixels. The scale bar is  $100\mu\text{m}$ .



### 2.3.3 Fractography studies

Fracture surfaces from ten specimens were analysed and documented. Eight specimens were of the standard type macro tensile specimens that were used in the project for mechanical testing and two were smaller specimens commonly used for cyclic tests.

All specimens showed ductile fracture behaviour with shear deformation as a dominating component. Large flat surfaces with close to  $45^\circ$  inclination to the load direction with micro dimples were dominating to a certain extent in all cases. The mechanism was ductile fracture; dislocations have moved along shear planes and created micro voids that have grown to dimples and finally caused plastic instability and fracture. Inclusions and large particles were commonly found in the large dimples. In most specimens a stripe pattern was visible which probably was inherited from the rolling process, see Figure 2.3.14. The microstructure is not banded in the final condition but during the processing route a banded structure was probably developed, there is also segregation of Mn in a banded manner.



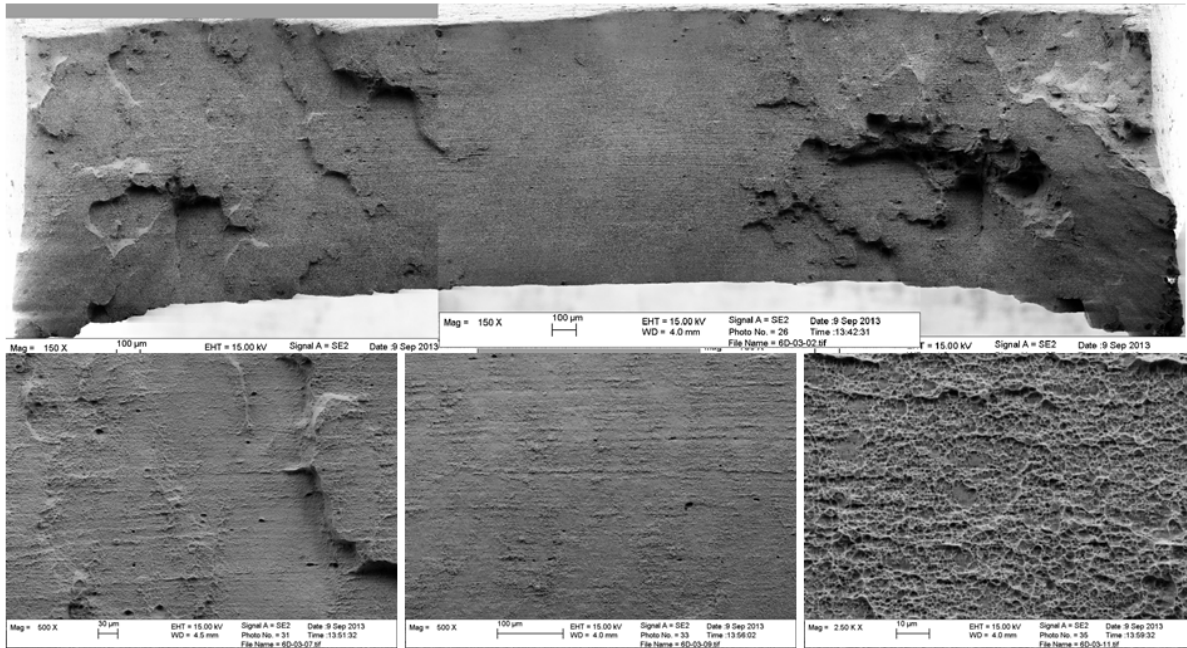


**Figure 2.3.14:** Example of specimen with clear stripes; Specimen 4-03, tensile specimen from macroscopic test. The fractured surface was dominated by shear, mostly flat surfaces with  $\mu$ -dimples. The final (residual) rupture surface was small. The surface contained large dimples and visible inclusions/large particles

### 2.3.4 Non-linear elastic material behavior

In the macroscopic tests it was concluded that the Young's modulus does not change with plastic deformation cannot be statistically verified for the TWIP-steel considered in this project, see Section 2.4.2.6. Therefore, microscopic investigations of this behaviour are redundant. The planned man hours for this WP were used to do additional work to characterise twinning behaviour.

### 2.3.5 Microstructure characterization of samples obtained from formed automobile component prototype

While task 3.1 and task 3.2 are focused on the analysis of the initial state of the material and defined pre-strained specimens, it was planned to analyse the microstructure incl. twin volume fraction after typical sheet forming processes accompanied with complex loading history in this task. Several microstructure analyses were done in task 3.1 and 3.2 including TEM-analyses to determine for the twin-volume fraction. Based on this experience the following drawback of the initially planned detailed microstructure analysis becomes obvious:

- Although the determination of the twin volume fraction at some locations of the deformed part would be helpful for the validation of the macroscopic model, it is stated that the effort is too high. Only a very few analyses could be performed.
- The information about the twin volume fraction would be very local.
- Due to the high plastic deformation in some areas of the prototype component, it is unclear if the analysis of the twin volume fraction would be successful.
- The orientation of the twins after complex deformation is unclear. Thus, the same problem as in the bulge test could occur.

For the aforementioned reasons it was decided that the planned analysis of the twin volume fraction on the deformed part will be replaced by a micro-hardness measurement on defined section cut of the component. Since the hardness measurement can be correlated with the current strength of the material these quantities can also be used for comparison with the numerical model. Further, this method allows analyzing complete section cuts which would not be possible with the initially planned microstructure analysis. The results of the experimental measurements are shown in Section 2.9.5.

## **2.4 WP4: Macro characterization of the material and formability tests**

WP4 is concerned with the mechanical tests of the TWIP-steel material on macroscopic level. The following objectives were defined for this WP

- Determination of the mechanical quantities commonly used in sheet metal forming applications
- Analysis of the thermo-mechanical and strain rate dependent behavior of the considered material
- Characterization of the spring back behavior
- Evaluation of the formability of the material
- Performing of simple experiments for validation with simulations

The results of these analyses were used in the modelling part of the project to initialize, calibrate and validate the numerical models in WP7 and WP8 and also in WP6 for the assessment of a standard material model commonly used for sheet metal forming simulations. Further, the data will be used for calibration and validation of the micromechanical model in WP5.

### **2.4.1 Mechanical tests for material characterization**

In this task, typical macroscopic tests were performed to analyse the material behavior of the considered TWIP-steel under different loading conditions. The loadings include, tension, compression, non-linear loading, temperature and rate.

- Tensile tests in different orientations of the sheet: 0°, 45°, 90°
- Tensile tests at seven different strain rates between 0.001 1/s and 20 1/s.
- Tensile tests at three different temperatures
- Tension – compression tests with different amplitudes
- Tensile tests on pre-deformed specimens
- Tensile tests for determination of elastic properties
- Shear tests
- Bulge tests

#### **2.4.1.1 Test specimen for tensile tests**

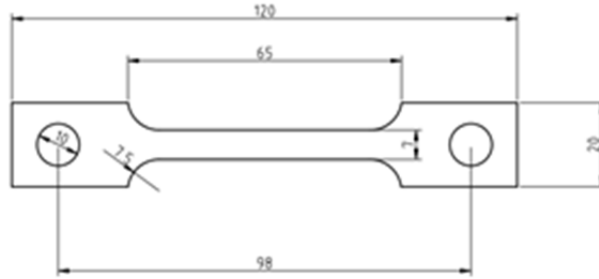
For the tensile tests three distinctly different test specimen were used.

Specimen no. 1 (Figure 2.4.1) was used in the majority of the tensile tests. The design has a relatively long straight area which gives a controlled stress state. This specimen is also used in the test at elevated temperature. The holes in the thicker part of the design are used for attachment then. Ordinary clamping does not suffice once the temperature goes up.

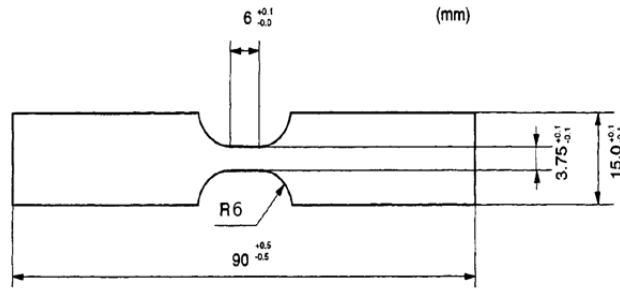
Specimen no. 2 (Figure 2.4.1) has a thinner waist than specimen no. 1. It is used for tests where size influence is investigated. But the main purpose of this specimen is to reduce the free length and thus reduce the risk for buckling when the material is tested in compression. Specimen no. 2 primarily is used in tension-compression tests.

Specimen no. 3 (Figure 2.4.1) is an ISO-standard design. In this project it is primarily used for filming of the deformation. It is also the base design for the shear test specimen.

Specimen number 1



Specimen number 2



Specimen number 3

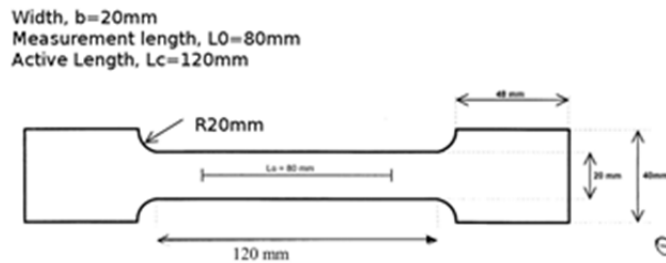


Figure 2.4.1: Test specimen used for the tensile testing in TWIP4EU

### 2.4.1.1 Standard tensile tests

Tensile tests in three directions were done. The directions were rolling direction (0 degree), transverse direction (90 degree) and 45 degrees to rolling direction (45 degree). During these tests the lateral contraction for the extraction of the Lankford-Coefficients (r-values) was measured. Table 2.4.1 gives an overview over the mechanical properties obtained from the uniaxial tensile test. The data are in good agreement with the initial material characterization described in WP 2.

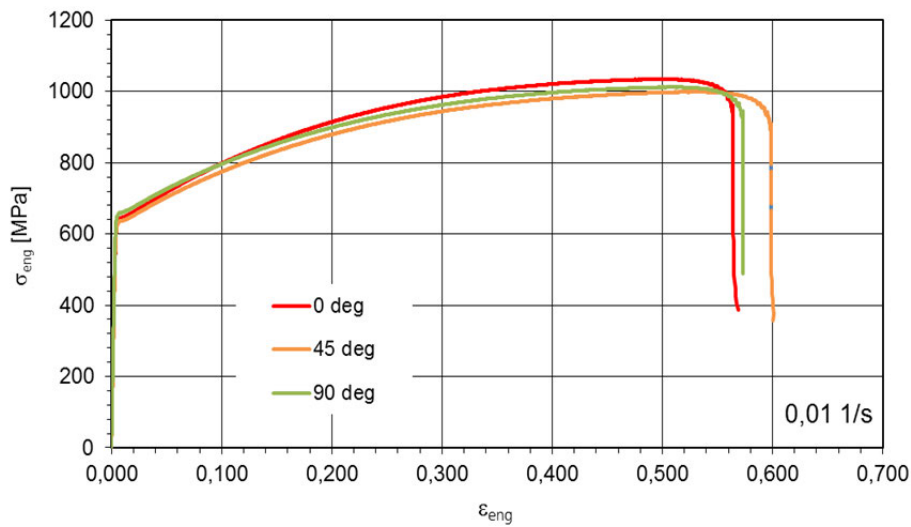
	Orientation		
	0 degree	45 degree	90 degree
$R_{p0,05}$ [MPa]	572	590	628
$R_{p0,2}$ [MPa]	633	630	652
$R_m$ [MPa]	1035	999	1012
$A_{25}$ [-]	56,7	59,9	57,1
$A_g$ [-]	49,2	52,3	51,2
r-value ( $r_{incr}$ )	0,787	0,962	0,997
E [MPa]	172952	168000	175000

Table 2.4.1: Mechanical properties of the TWIP-steel material.

In Figure 2.4.2 the results of the tensile tests are compared. There seems to be little anisotropy in the material. However, for the cross direction there seems to be a slightly higher initial yield stress. The



Lankford coefficient in 0 degree with respect to the rolling direction is less than one, see Table 2.4.1. Thus, an anisotropic flow of material is expected.



**Figure 2.4.2:** Engineering stress-strain-curves from uniaxial tensile tests for three different directions

The flow curves in Figure 2.4.3 show the typical hardening behaviour of twip-steels. Compared to conventional steels, a significant higher hardening for large strains can be observed. It can be noticed that the flow curve transverse direction (90 deg) crosses the flow curve in rolling direction (0 deg) since it has a higher initial yield strength but a lower ultimate yield strength.

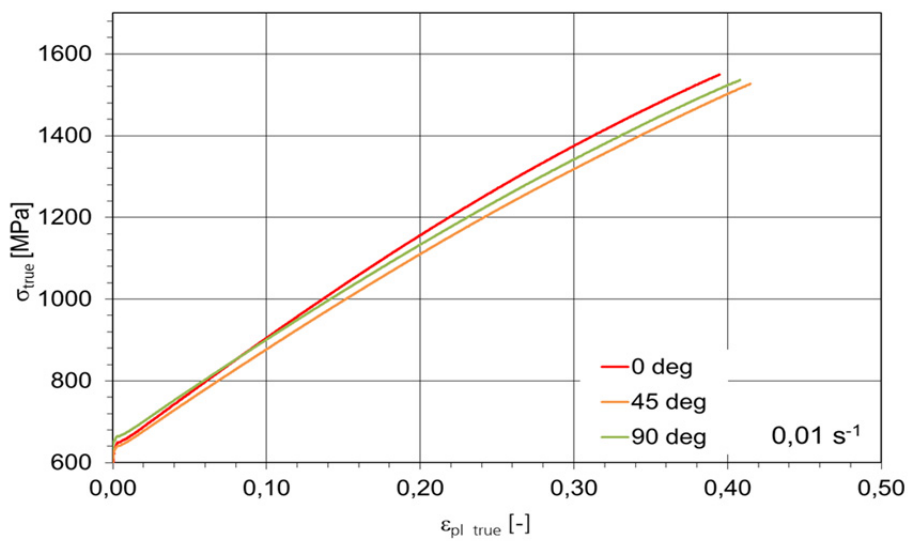


**Figure 2.4.3:** Flow-curves from uniaxial tensile tests for three different directions.

The Lankford coefficients for the three considered orientations are plotted as a function of the true strain in Figure 2.4.4. The values for the Lankford coefficients given in Table 2.4.1 are evaluated according to the DIN ISO 10113 2008-8 standard (incremental Lankford coefficient).

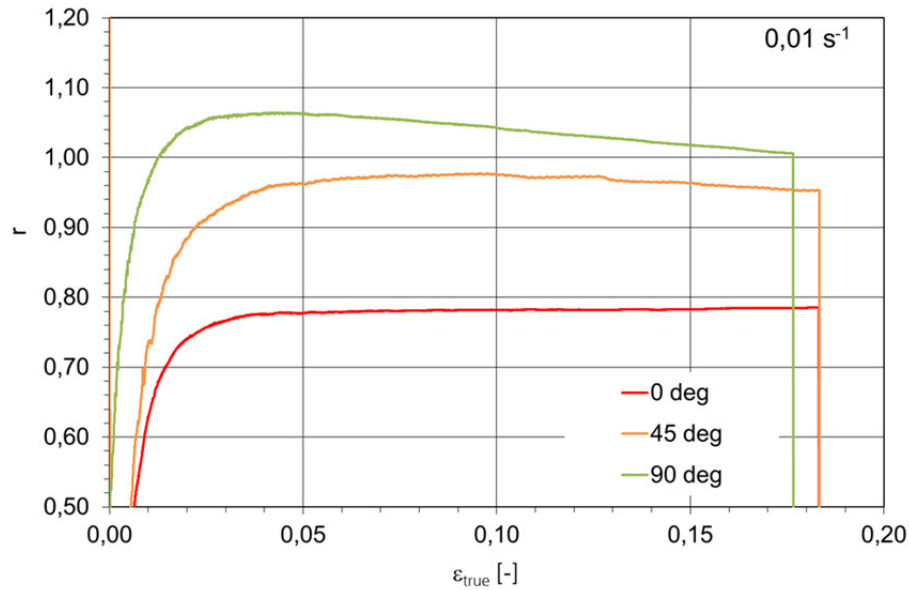


**Figure 2.4.4:** Lankford coefficients (r-values) for three different directions.

### 2.4.1.2 Strain rate dependency

The strain rate usually has an impact on the yield stress and the hardening of a material. Therefore, several tensile tests were performed with strain rates varying from 0.001 to 20 1/s. In Figure 2.4.5 the curves for strain rates up to 0.3 1/s are given. In Figure 2.4.6 further test with strain rates up to 20.0 1/s are added. The high strain rate tensile curves have a slightly lower hardening modulus than in the slowly deformed tests.

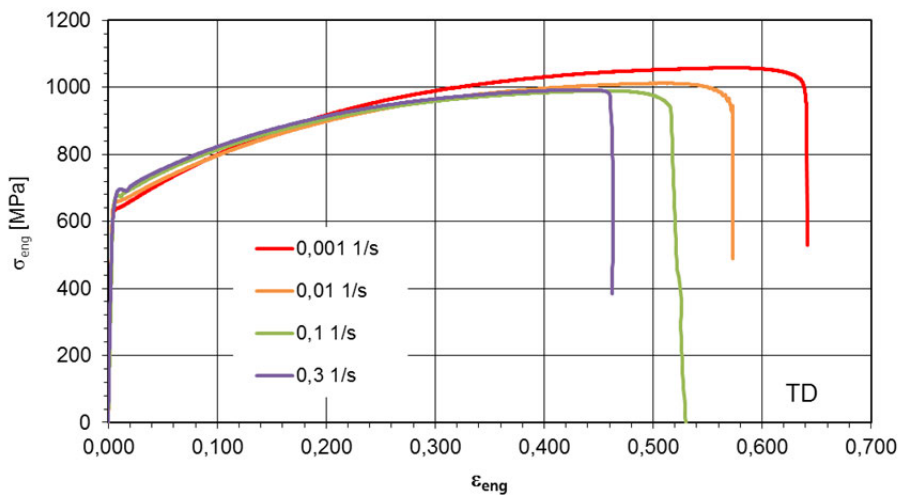


**Figure 2.4.5:** Tensile tests under several different strain rates.

It seems that the strain rate does not affect the initial yield stress much. But, the hardening modulus is reduced with increased strain rate. For lower strain rates up to 0.3 1/s one can see a crossing of the stress-strain curves at about 20 percent engineering strain. This effect is already known as inverse strain rate sensitivity which means that lower strain rates lead to higher stresses.

However, the temperature increases significantly with plastic deformation, see Figure 2.4.7. It might be that effect that shows up as a reduction of the hardening modulus. With this standard experiment it is difficult to decouple the effect of strain rate dependence and temperature effects.

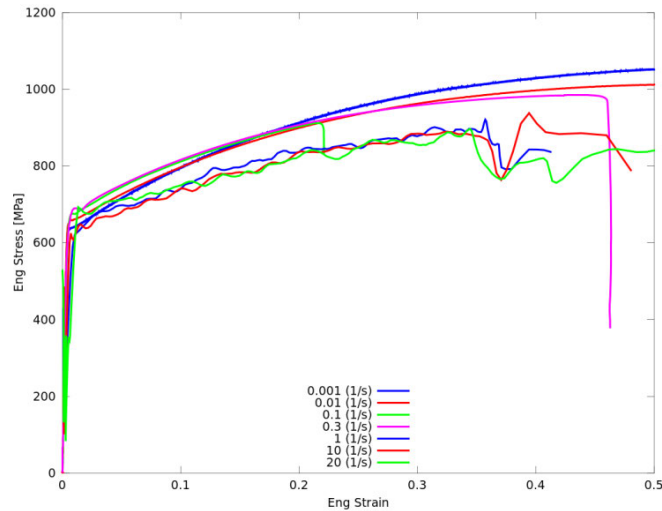


**Figure 2.4.6:** Tensile tests under several different strain rates. The three lower curves for the highest strain rates are from testing in a different machine where strain measurement was made with a laser extensometer. The scatter can be attributed to the difficulties in measuring the strain at these rates.

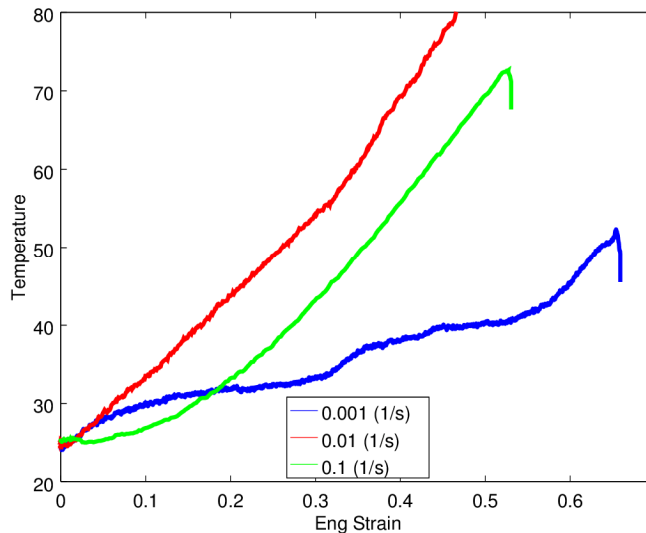


**Figure 2.4.7:** Temperature increase as function of applied deformation for three different strain rates

### 2.4.1.3 Bulge tests to determine and quantify hardening behavior at large strains

The hydraulic bulge test is a proper method to test a sheet in balanced biaxial tension. Within this project, the bulge test is performed for different purposes:

- to evaluate the forming behavior of the TWIP-steel material at higher strains and under biaxial loading
- to evaluate the biaxial forming behavior of pre-strained material
- to apply a defined biaxial pre-strain on the material for further analysis of the microstructure
- to evaluate the applicability of commonly used yield functions
- to determine two parameters of the Barlat YLD2000-2D yield function ( $\sigma_{\text{biax}}$  and  $r_{\text{biax}}$ )

The bulge tests have been externally assigned to the institute IFUM at the University Hannover. The test principle is illustrated in Figure 2.4.8. The correlation between pressure and strain can be determined from experimental data. The sketch in Figure 2.4.8 gives information about the interrelation of the measurement variables.

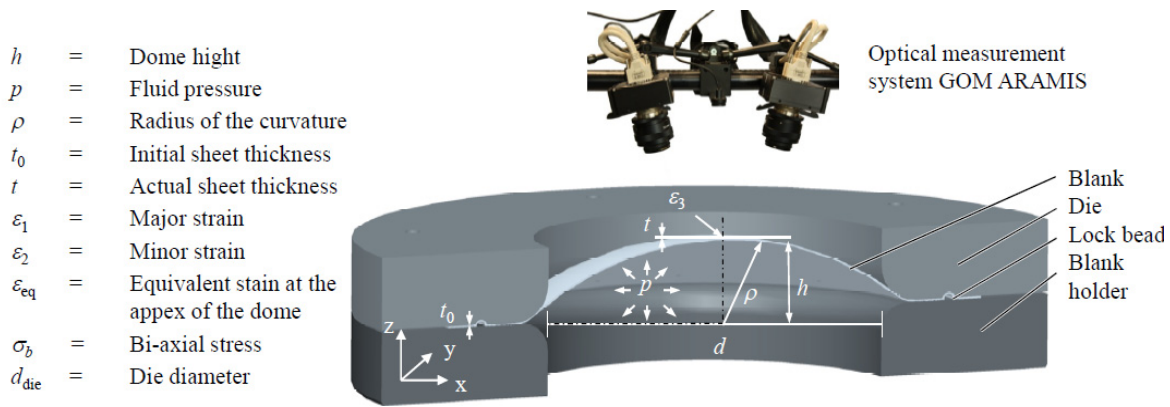


**Figure 2.4.8:** Test principle bulge test [Vucetic2012]

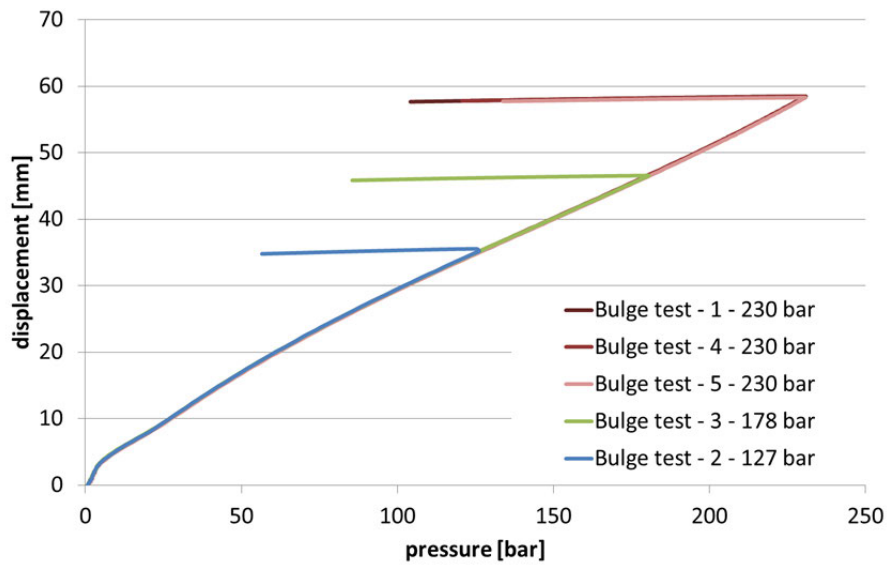
The detailed test program is given in Table 2.4.1. Due to the process of pre-straining (cold rolling) the thickness of the material decreases.

	Yield strength [MPa]	Initial sheet thickness [mm]	Number of valid tests [-]
Standard material – up to max. pressure	600	1.50	3
Standard material – interrupted tests at approx. 15% (127 bar) and 25%, strain (178 bar)	600	1,50	1 for each strain level
Pre-strained (cold rolled) material, see task 2.1 of the mid-term report	900	1.35	3
Pre-strained (cold rolled) material, see task 2.1 of the mid-term report	1100	1.20	3

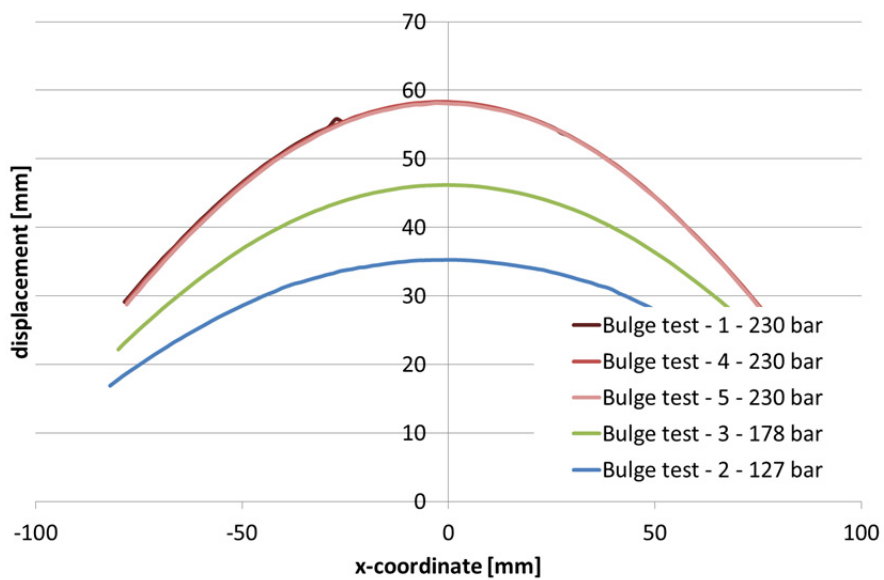
**Table 2.4.2:** Material definition and test program for the bulge test

Figure 2.4.9 show the pressure-displacement curve of the centre of the bulge specimen. The shape of the deformed sheet along a cut parallel to the rolling direction is illustrated in Figure 2.4.10. In both diagrams, the three tests with a maximum pressure of 230 bar show a good reproducibility. Additionally, the experimental data of the two interrupted test are also given. The analysis of interrupted bulge tests of the standard material will provide detailed information about the material behavior and the microstructure evolution during the test. Therefore, bulge specimens with the strains of 15% (127 bar), 25% (178 bar) and 45% (230 bar) in the region near the dome are produced. These specimens were sent to the project partner KIMAB for further microstructure analyses. The results are described in Section 2.3.2.4. The strain distribution of the interrupted tests is given in Figure 2.3.11.

The flow curves of the three different material states (standard material TWIP600 and cold rolled to two different levels, see Section 2.2.1) are given in Figure 2.4.11. Since the specimen width of the pre-series material was limited to 300 mm, only the small bulge tool set be used. This caused the drawback of a pressure limitation. Only the thinnest specimens with a thickness of 1.20 mm could loaded until crack. For the determination of result scattering all experiments were done three times. The curves show a good agreement. This was also confirmed by the optical strain measurements. As an example Figure 2.4.12 shows the strain distributions of the TWIP-steels with yield strength of about 600 MPa.



**Figure 2.4.9:** Pressure-displacement curves of the center of the bulge specimen.



**Figure 2.4.10:** Displacement in z-direction for different pressure levels, cut parallel to the rolling direction.

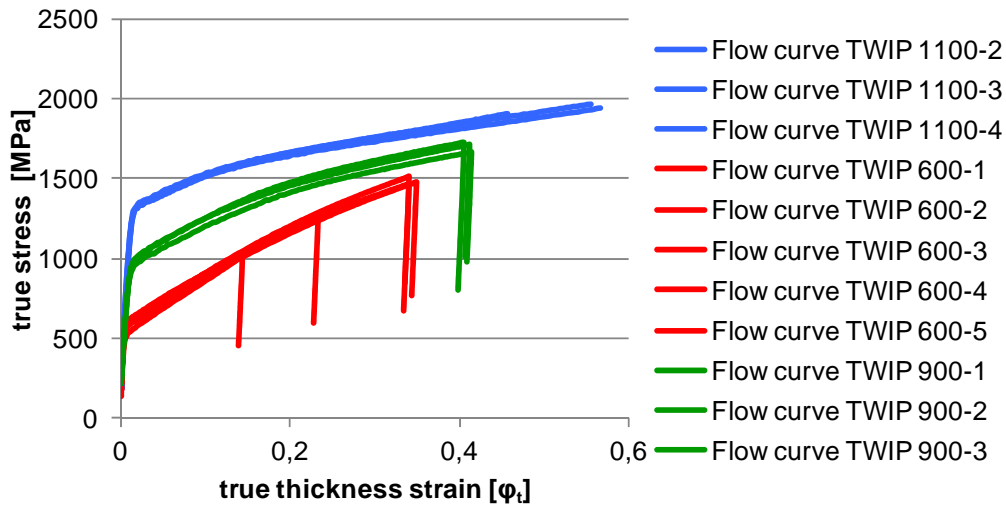


**Figure 2.4.11:** True strain - true thickness strain curves of 3 different TWIP-steel batches

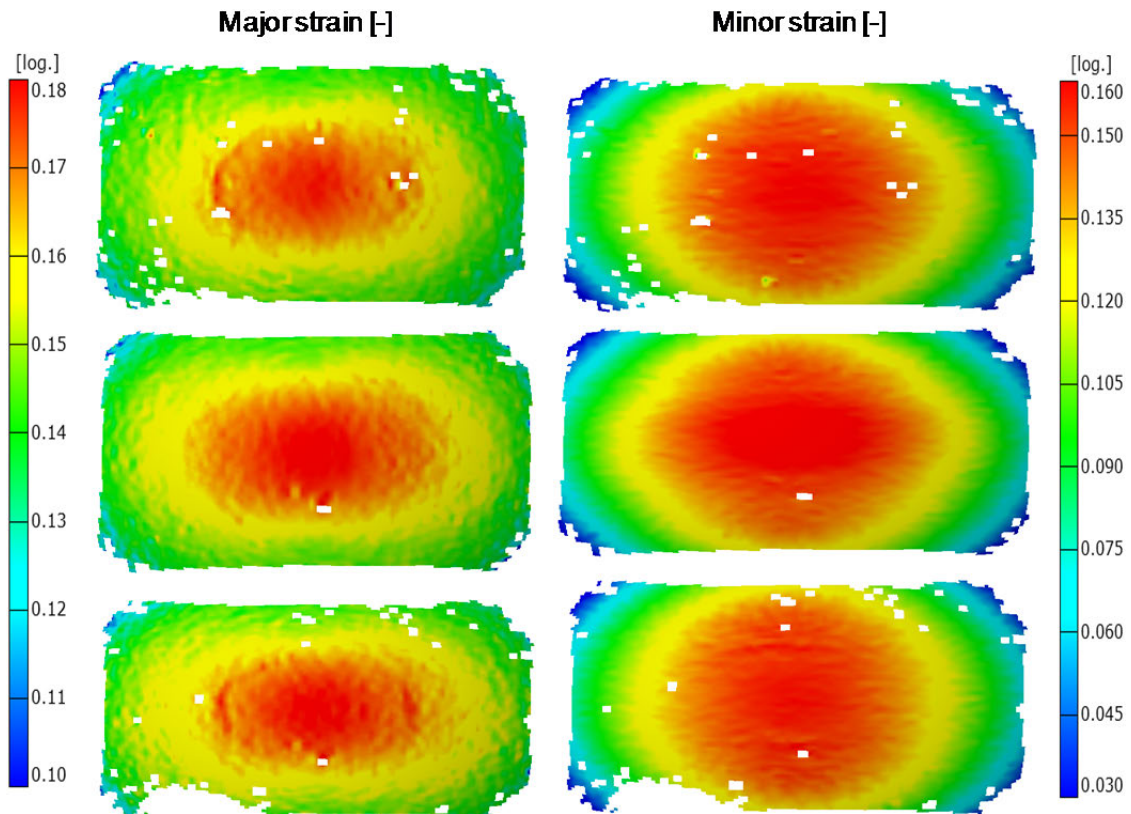


**Figure 2.4.12:** Major and minor strain distribution of three different bulge tests for the standard TWIP-steel material at a pressure of 230 bar.

The archived strain states of the analysed bulge specimens are plotted into the forming limit diagram (described in Section 2.4.3.1), see Figure 2.4.13. Even with the maximum pressure that could be realized with the available experimental set up, the strain state was far away from the forming limit.

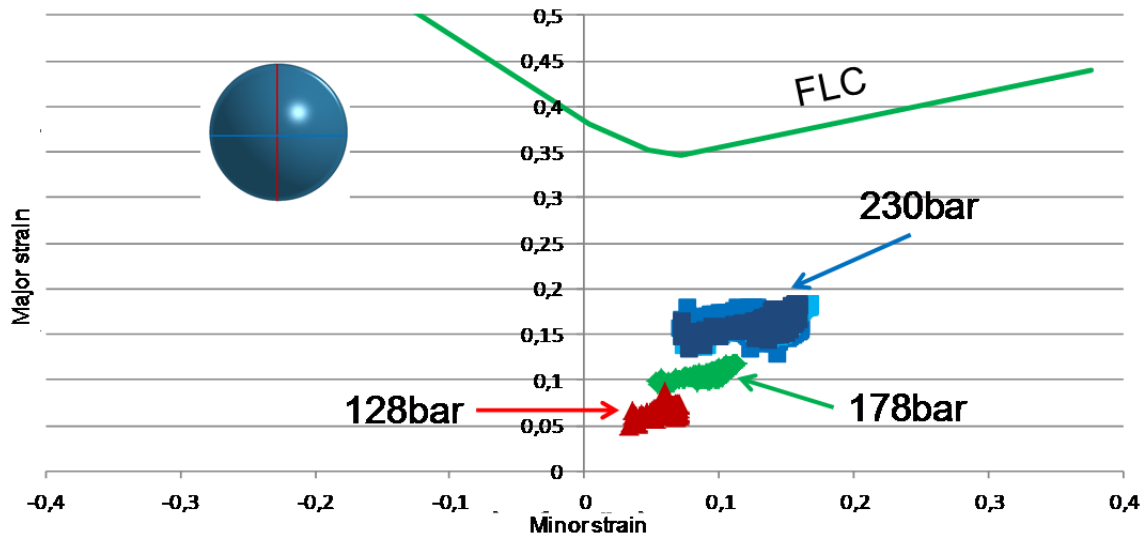


Figure 2.4.13: Strain states achieved by the bulge tests for different pressure levels

Compared to the flow curves from uniaxial tensile tests, the flow curves from the bulge test show lower initial yield strength and a higher hardening rate, see Figure 2.4.14. Thus, the flow curves from tensile test and bulge test will cross each other. Obviously the hardening rate depends on the stress state. Similar observations for other stress state were also reported in literature [Renard2012].

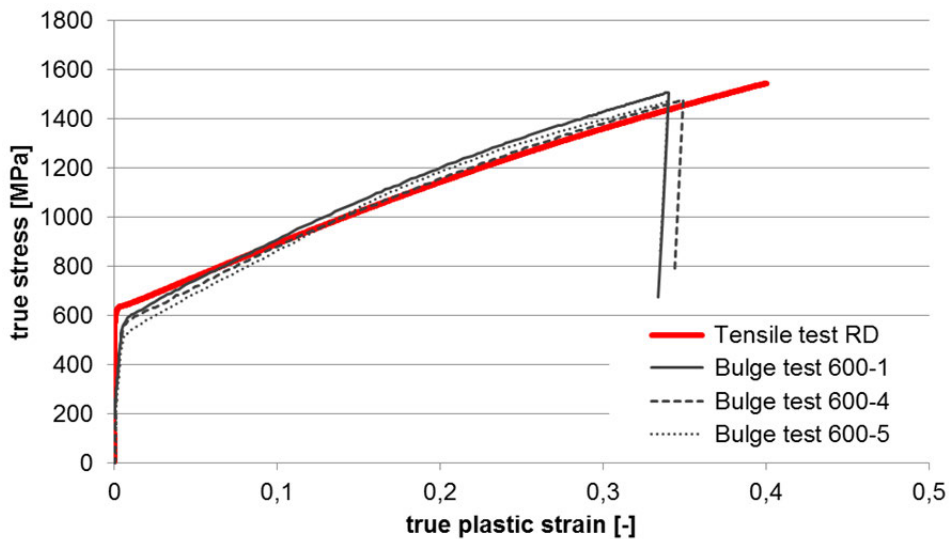


Figure 2.4.14: Comparison of the flow curves from uniaxial tensile test and bulge test.

Furthermore, the evolution of the major strain and minor strain under equi-biaxial stress conditions was analysed. Figure 2.4.15 illustrates the development of the major and minor strains at the dome as function of the vertical displacement of the dome.

In Figure 2.4.16 the minor strain is plotted as a function of the major strains. It can be seen that the slope of the curve is close to one for lower strains up to approximately 0.08. For higher strains the slope decreases to a value of about 0.9. Thus, the straining is not isotropic under equi-biaxial stress.

From further analyses follows that the direction of the minor strain is parallel in rolling direction while the major strain is parallel to the transverse direction of the sheet. This observation can be explained with the differences of the flow curves in rolling direction and transverse direction. As illustrated in Figure 2.4.3 the flow curve in transverse direction is lower than in rolling direction, this will lead to higher strains compared to the strains in rolling direction. Further, the strain level in Figure 2.4.16 at which the curves start to deviate from  $m=1$  fits well with the strain level in Figure 2.4.3 at which the flow curves start to deviate.

This effect will be considered to define the value for  $r_b$  of the Barlat YLD2000-2D yield model, see Section 2.7.6.



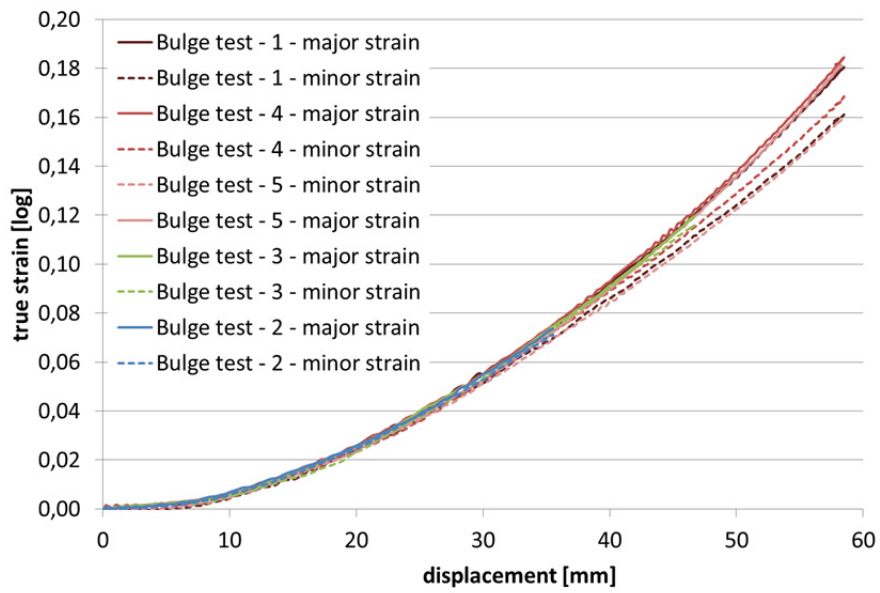


**Figure 2.4.15:** Comparison of major and minor strains at the dome of the bulge specimen as function of the dome height.

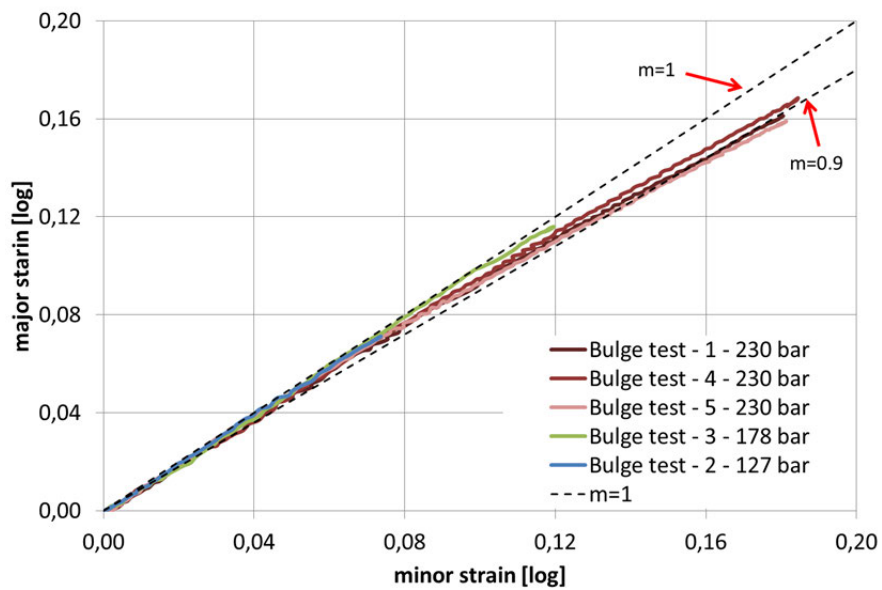


**Figure 2.4.16:** Development of the major strain as function of the minor strain at the centre of the bulge specimen.



#### 2.4.1.4 Tests and analysis for evaluation of the change of Young's modulus with plastic deformation

With respect to the planned modelling approach, it was necessary to analyse if the Young's modulus shows a significant change with plastic deformation and if it is needed to take this effect into account within the model. Under consideration of the available results no visible proof of any change of Young's modulus has been detected. Here are the observations.

##### The initial Young's modulus

Several of the tension compression tests in rolling direction were analysed. In Figure 2.4.17 the first part of the stress-strain curves are shown. This represents the natural spread in tests. From these data the mean Young's modulus is 182150MPa with a mean deviation of 7191MPa.

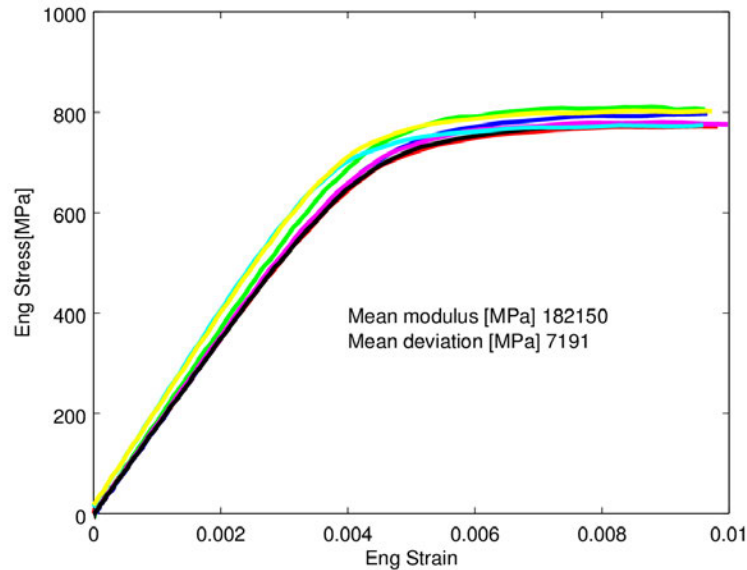


**Figure 2.4.17:** The first part of tensile tests. The mean Young's modulus is 182150 MPa with a mean deviation of 7191 MPa. The moduli are extracted from true stress-strain data.

From the tensile tests on Specimen no. 1 the mean value of the Young's modulus is 178100 MPa with a mean deviation of 8148 MPa.

##### The Young's modulus after plastic deformation

Figure 2.4.18 shows the strain levels where the unloading-loading sequences were applied on the test specimens. From this three tangent moduli for each sequence are extracted. These moduli are shown in Table 2.4.3. The apparent Young's modulus is defined in this case as the mean tangent modulus in the unloading-loading sequence. The values of the moduli are extracted from true stress-strain data. From these data the mean Young's modulus is 173650 MPa with a mean deviation of 5778 MPa.

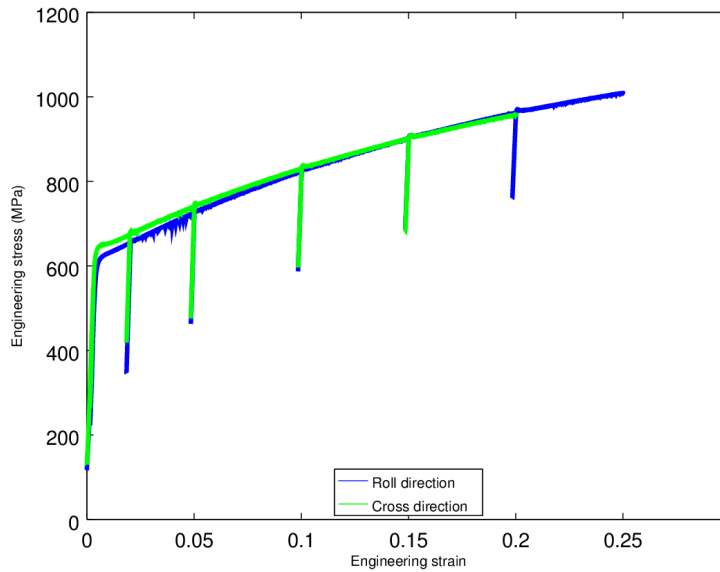


**Figure 2.4.18:** The mean Young's modulus for all these load-unloading sequences is 173650 MPa with a mean deviation of 5778 MPa. There is no apparent reduction due to plastic deformation.

Strain level at unloading [-]	0.02	0.05	0.10	0.15	0.20
Mean tangent modulus [MPa]	180400	167800	183800	174000	176800

**Table 2.4.3:** The mean tangent modulus at different states of plastic deformation. In the table the strain level is shown as the level of engineering strain where each unloading-loading sequence starts. The values of the moduli are extracted from true stress-strain data.

In Figure 2.4.19 the instantaneous tangent modulus of every loading-unloading sequence can be seen. It is apparent that the tangent modulus is not constant, but it is clear that the level of plastic deformation does not influence that

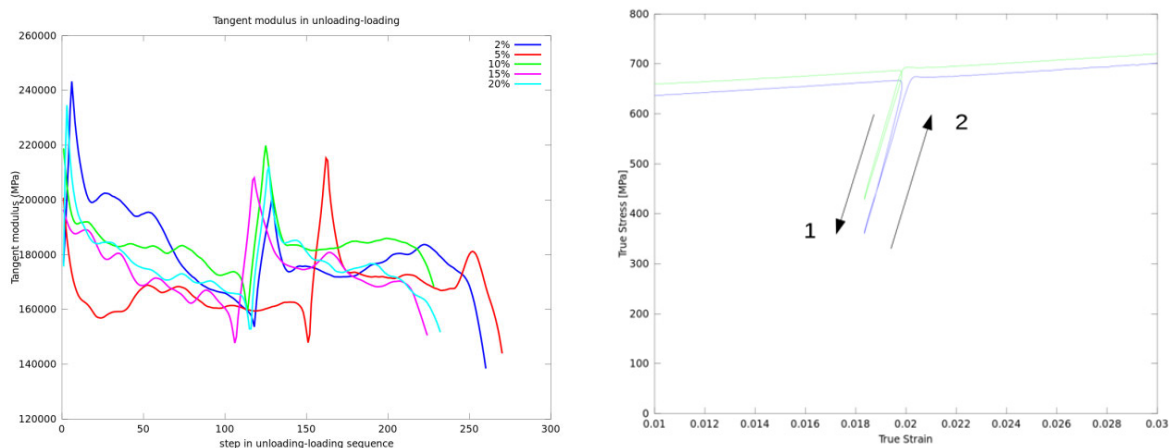


**Figure 2.4.19:** The instantaneous tangent modulus of every loading-unloading sequence. The mean value represents each level of plastic deformation in Table 2.4.1. To the right the direction of the x-axis in the left figure is shown.

## Conclusion

Initially the Young's modulus is approximately 180000 MPa with a mean deviation of approximately 8000MPa. This shall be put in contrast with the mean Young's modulus from the unloading-loading sequences of 173650 MPa with a mean deviation of 5778 MPa.

If there is a change of Young's modulus as a result of plastic deformation it cannot be statistically verified by the measurements here. Measuring Young's modulus is known to be very difficult, and in the testing for the TWIP4EU project the Young's modulus was extracted from three distinct different measurements. All these measurements, with deviations, point at a constant Young's modulus. As seen in Figure 2.4.21 the difference in the three apparent modulus measurements cannot be determined, the span of the deviation of each measurement gives that there is no trend. This can also be seen in Figure 2.4.20 where it is shown that there is no dependency on the plastic deformation. The mean value of the Young's modulus from these three sets of measurements is 178000 MPa.

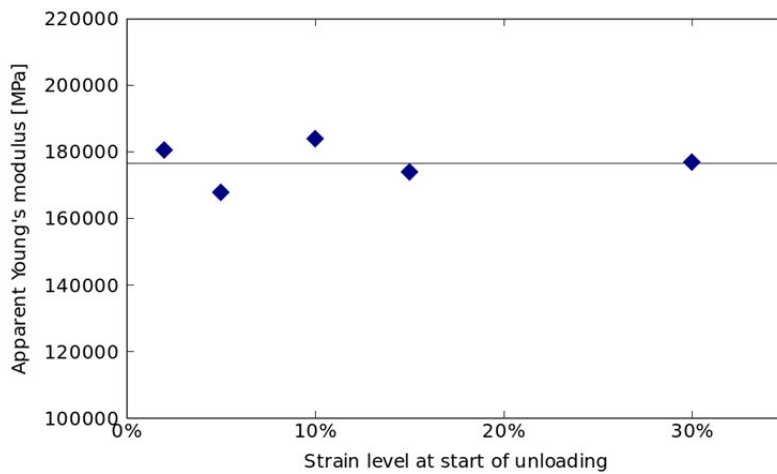


**Figure 2.4.20:** The apparent moduli from the measurements presented in Figures 2.4.17 and 2.4.18. The points show the modulus at increasing plastic deformation.

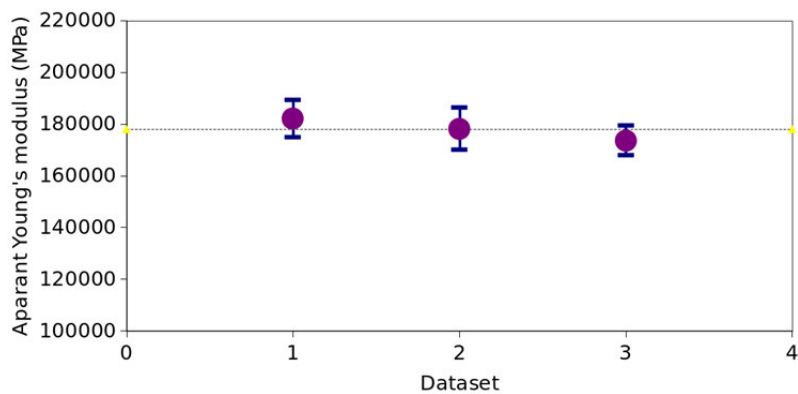


**Figure 2.4.21:** The three measurements of the apparent Young's moduli. The two first are values for the initial modulus. The last one represents the mean average apparent moduli from Figure 2.4.17.

## 2.4.2 Experiments to identify kinematic hardening and spring back behavior

In the simulation of sheet metal forming processes the prediction of spring back behavior plays an important role. In the considered TWIP-steel material, the combination of a relatively low Young's modulus and the high strength of the material leads to significant spring back behavior. Here, two different types of tests were performed. The tension-compression test is typically used to determine the Bauschinger effect. From a modelling point of view, the obtained cyclic stress-strain curves allow to differentiate between isotropic and kinematic hardening. Further, the bending under tension (BUT) test is performed to evaluate the spring back behavior. Since the setup of the test is relatively simple, this test is also very useful to validate the numerical model with respect to spring back prediction.

### 2.4.2.1 Tension-compression tests

Tension-compression tests are important in determining the Bauschinger effect. Changing the loading direction gives a good visualisation of the effect. The interpretation of the effect into a kinematic hardening is seen by the approximately uniform size of the elastic region both in loading and unloading.

Tension-compression tests with different amplitudes have been performed. The testing direction was parallel to the transverse direction of the sheet. An overview over the different tests is given in Table 2.4.4. Due to the high strength of the TWIP-steel material, a relatively large force was needed to reach the demanded strains in compression. For this reason, the buckling tendency became problematic for larger strain amplitudes. For this reason, only small strain amplitudes could be realized, as also reported in Table 2.4.4.

Min Strain	Max strain	Outcome
-1%	1%	OK
-1.5%	1.5%	OK
-2%	2%	usually buckle
4%	6%	OK
3%	7%	buckle

**Table 2.4.4:** Overview of performed tension-compression tests

In Figure 2.4.22a, tension-compression tests with different strain amplitudes are shown. As already mentioned, the Bauschinger effect is very significant: During load reversal, the plastic deformation starts at significantly lower stresses compared to the maximum stress reached at the point of load reversal. This observation is independent from the applied strain amplitude. The cyclic stress-strain curve after several load cycles with a strain amplitude of  $\pm 1\%$  is illustrated in Figure 2.4.22b. At least for these small strain amplitudes, practically no isotropic hardening can be observed. If this observation is also valid for higher strain could not be analyzed.

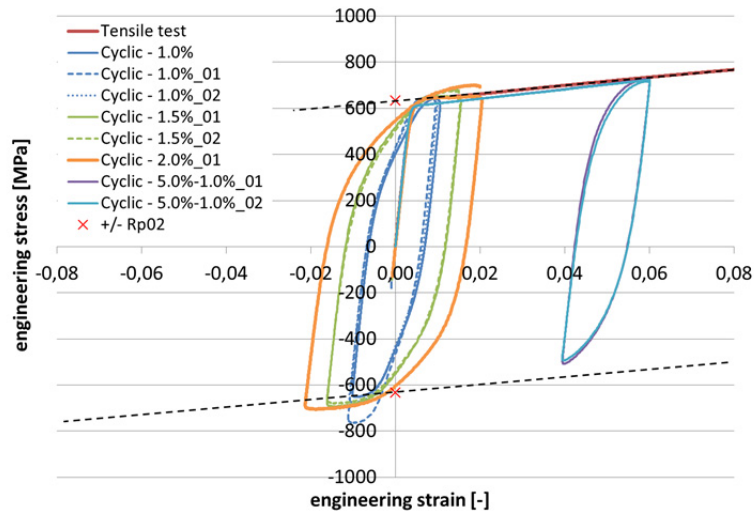


Figure 2.4.22a: Results of cyclic tension-compression tests with different strain amplitudes.

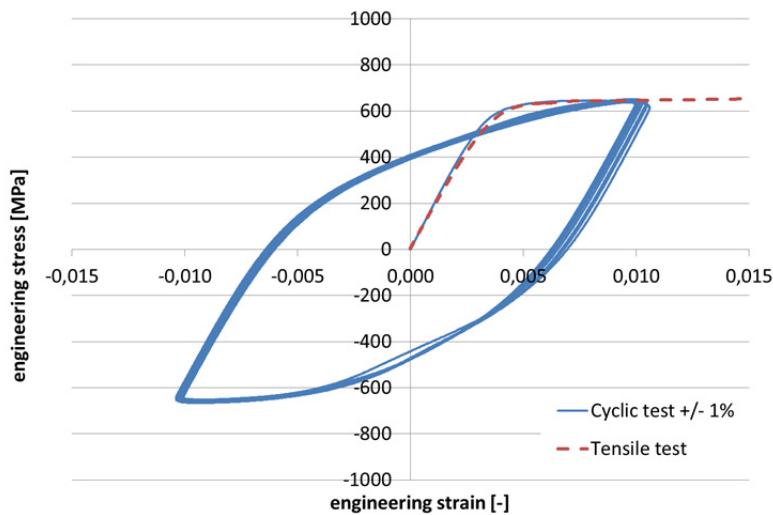


Figure 2.4.22b: Results of cyclic tension-compression tests after several cycles. The strain amplitude is  $\pm 1\%$ .

### 2.4.2.2 Tensile test on differently pre-strained specimens to analyze non-linear strain paths

The material behaviour under nonlinear loading histories can also be used to analyse kinematic hardening. Therefore 90 mm wide test pieces were pre-strained to two different levels. Smaller test pieces were cut out from these deformed sheets and tested. Three pre-strains in each direction and deformation level were made. The levels of pre-strains were:

Test-Nr.	Prestraining: Orientation-level of pre-strain			
	0deg-5p	0deg-10p	90deg-5p	90deg-10p
1	0.042	0.053	0.021	0.063
2	0.032	0.053	0.042	0.084
3	0.032	0.053	0.032	0.042

Table 2.4.5: Overview over pre-strained specimens

The stress-strain-curves of the initial material before pre-straining as well as the stress-strain-curves after pre-straining are shown in Figure 2.4.15. As expected, a higher amount of pre-strain leads to a higher initial yield stress. It is noted that the 5% and 10% pre-strain have been target levels. The distance between the clamps was used for applying the target strain. From the overview Table 2.4.5 follows that the strain that could be attained was lower than the target strain.

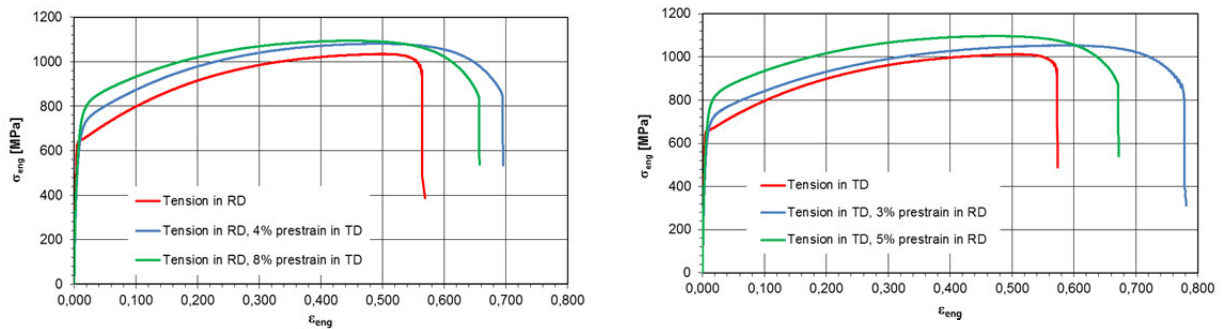


**Figure 2.4.23:** Stress-strain curves from the pre-strained specimens

### 2.4.2.3 Bending under tension test

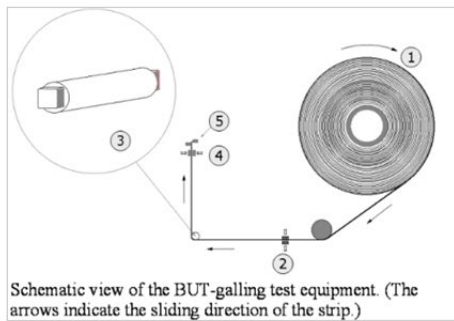
The lay out of the BUT machine is illustrated in Figure 2.4.24. The strip can be supplied as a coil (1) which is fed automatically into the machine and successively cut off by the strip cutter (6). The test material was however provided as strips of 1000 mm length and 50 mm width which were loaded by hand. The strip is initially placed under the tool cylinder (3) and fixed to the brake force grip (4). It is then manually bent around the cylindrical tool (3) and fed into the hydraulic pulling force grip (5). A constant brake force is applied at position 3 and the strip is pulled 215 mm with a speed of 100 mm/s over the tool by the pulling cylinder. The pulling force is measured at position 5. All the strips were lubricated with drawing oil (Quakerdraw 250L). The brake force was increased in steps for each successive new strip. The cylindrical die is rotating freely with the aid of roller bearings which connect the cylinder to the machine frame. In a real situation in a forming tool the friction will take a finite value. For the present purpose it is however favourable to have negligible friction with a freely rotating cylindrical tool. It is still true that a slight relative motion will occur between the strip and the rotating cylinder surface. This friction effect is significantly smaller than the friction over a fixed tool. A small relative motion occurs both in the drawing direction and in the transverse direction.

The shape of the strip was evaluated by photographing the strips as in Figure 2.4.25 and digitizing the coordinates of the curved strips. Figure 2.4.26 (left) illustrates such an evaluation. Based on these numerical data, the local curvature of the strip can be calculated, Figure 2.4.26 (right). It shows that an almost constant curvature is obtained over the section of the strip which has passed over the cylinder in the BUT test. In this work the average of this curvature was used as a measure of the sheet shape after spring back.

For the TWIP4EU test two sizes of the tool and three load levels were chosen. The strip was 50mm wide and all strips were cut in the 0deg direction (rolling direction). The results are given in Table 2.4.6.



Fig 1a BUT machine. (1) coil, (2) grip for brake force, (3) tool holder, (4) grip for pulling



Schematic view of the BUT-galling test equipment. (The arrows indicate the sliding direction of the strip.)

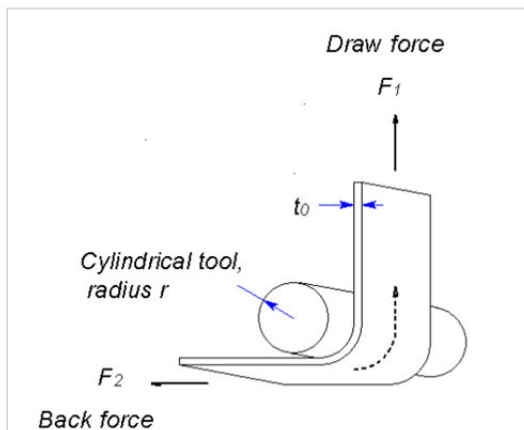
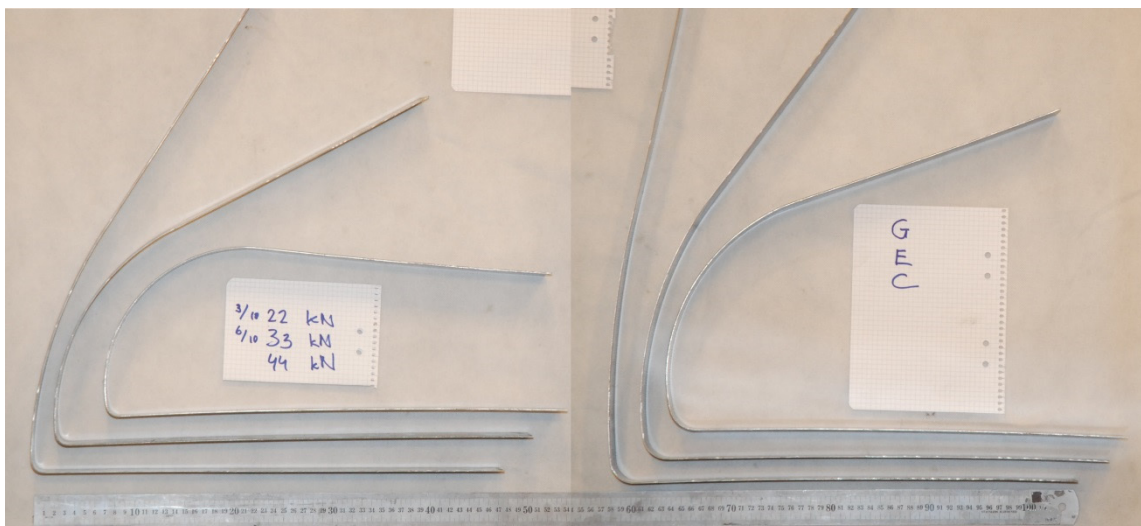


Fig 1b. Principal sketch of BUT machine and 1c. tool configuration.

**Figure 2.4.24:** The Bending Under Tension (BUT) machine.



**Figure 2.4.25:** The shape of the strips after they have been drawn in the BUT machine. The curvature of the strip is a measure for spring-back.



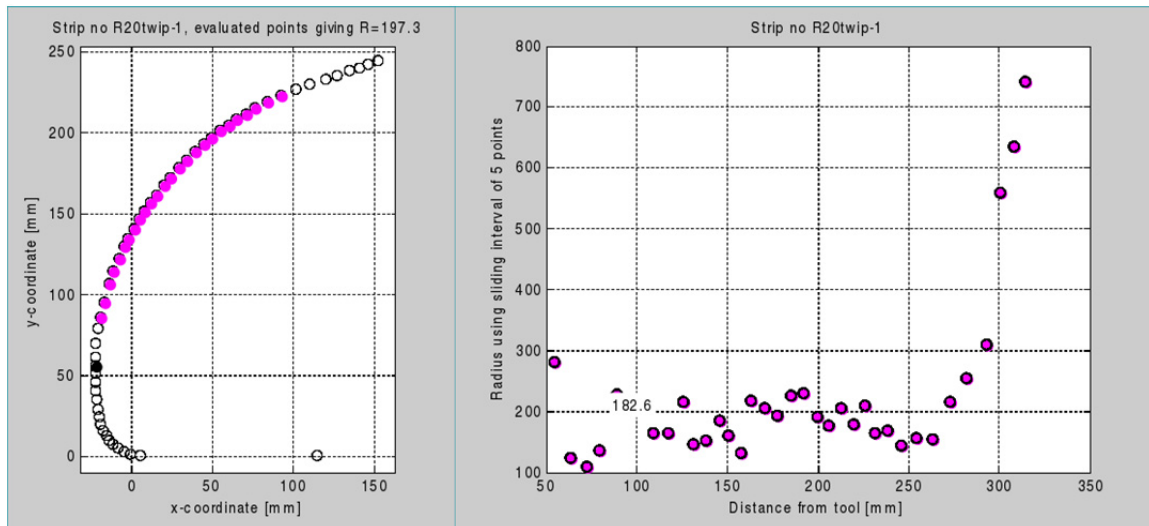


**Figure 2.4.26:** The curvature is evaluated in a continuous row of points. When a locally accepted deviation is reached the set of points all contribute to a global radius with a least square approach.

Radius of tool (mm)	Brake force (kN)	Evaluated radius (mm)
20	22.7	197.3
20	33.6	355.1
20	44.5	759.3
10	22.7	146.2
10	33.6	218.3
10	44.4	435.3

**Table 2.4.6:** The evaluated radii of the strip after the BUT-test.

## 2.4.3 Tests to evaluate formability

To evaluate the formability, Nakajima tests and deep drawing of square cups were conducted. The experiments with the Nakajima specimen were used to determine the forming limit diagram of the material. Further, Nakajima experiments which were stopped before the onset of necking were used as forming experiment under defined strain conditions. To come one step closer to a deep drawn industrial part, square cups were formed and analyzed:

### 2.4.3.1 Nakajima tests to generate forming limit curves

The determination of the forming limit curve (FLC) that describes the forming limit for sheet metal materials is standardized in accordance to ISO 12004-2. The forming limits are described in the range from uniaxial to biaxial stress conditions depending on the ratio of major and minor strain. FLCs are typically used for problems concerning sheet metal forming application like deep drawing and stamping applications. In combination with forming analyses critical regions of the component part can be identified.

According to DIN EN ISO 12004-2 [DIN EN ISO 12004-2] two different experimental tools can be employed to determine the FLC. The Nakajima test setup uses a hemispherical punch with a diameter of 100 mm whereas a flat-bottom punch is applied in case of the Marciniak test setup. By means of this punch sheet metal blanks having different widths are stamped until failure. The punch velocity has



to be set between 1.0 mm/s and 2.0 mm/s. The ISO standard limits the determination of FLCs to sheet thicknesses in the range of 0.3 mm till 4 mm. A complete FLC is described by at least five different geometries with three valid samples for each geometry, see Figure 2.4.25. In order to obtain valid samples, cracks must initiate within a range of 15 mm from the dome centre and must not start from the edge. The level of the FLC is given by the lowest major strain in the FLC. For this reason it is important to identify the corresponding sample geometry.

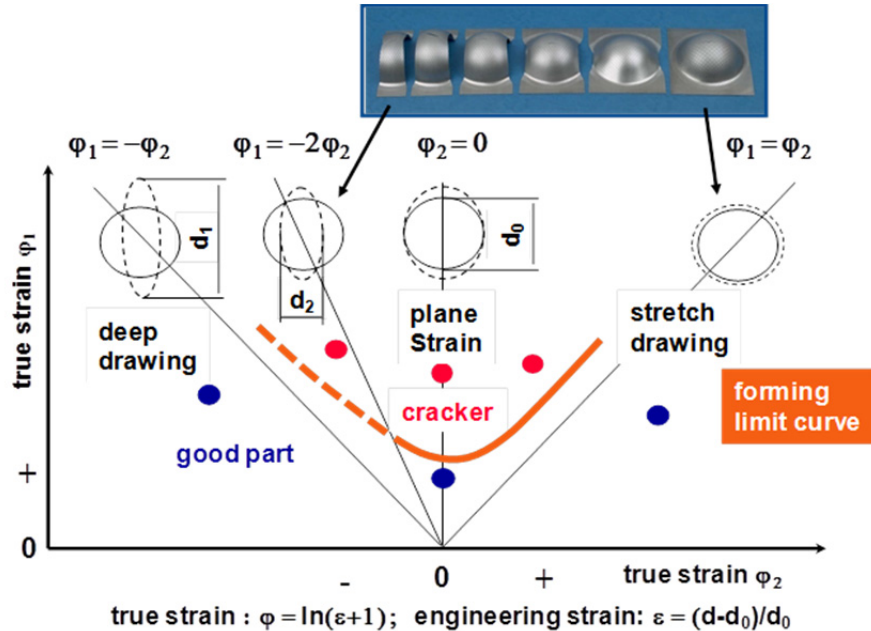


**Figure 2.4.27:** Schematic forming limit curve

Optical 3D measurement systems like ARAMIS are used to determine the FLC by capturing the deformations that develop while stamping. There exist different methods for evaluating the strains. Up to now the only standardized method is the so called cross section method in accordance to ISO 12004-2. Major and minor strain values along predefined sections lines that run perpendicular to the crack are used. The strain distribution just before the onset of necking is reconstructed in the necking area by fitting an inverse parabola. The forming limits as pair of value of major and minor strain are taken from the corresponding crack position.

Another evaluation method that is still in development is called time dependent method. This method is used for materials which show multiple local necking or strain distributions that do not match to an inverse parabola. Considering the highest value of thinning rate two stages before fracture the necking zone is defined. In order to calculate the forming limit at least 40 images before fracture are taken into account. By fitting the thinning rate for both in the area of stable and instable necking using the linear best fit method the point of instable necking is determined. The corresponding mean values of major and minor strain at this point represent the forming limit for the FLC.

In Figure 2.4.26 the FLCs for TWIP-steel with a sheet thickness of 1.5 mm are shown for both cross section method according to ISO 12004-2 and time dependent linear best fit evaluation method. It is obviously that both evaluation methods lead to almost identical forming limit curves. Due to this fact it can be concluded that an evaluation of the TWIP-steel using the conventional cross section method is sufficient [DIN EN ISO 12004-2], [GOM2014].

Due to the high ductility of TWIP-steel, the forming limit curve reaches higher strains compared to other high strength steels (e.g. dual phase steels).

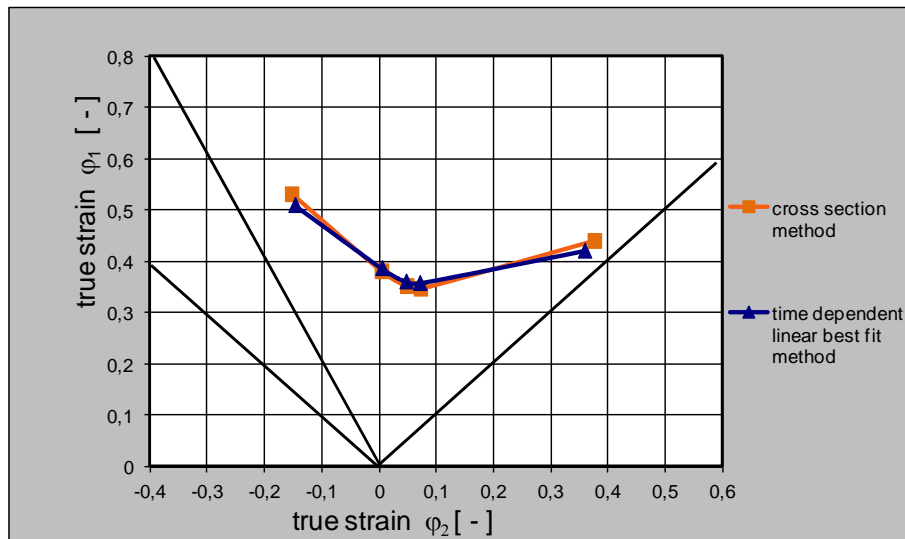


**Figure 2.4.28:** FLCs determined by means of cross section method and time dependent linear best fit method

### 2.4.3.2 Nakajima-test: Forming experiment

Besides the determination of the forming limit curve, the Nakajima tests were also considered as simple forming experiments since it fulfils the following requirements for a useable experimental set up:

- Geometrical data has to be accessible.
- Clamping conditions have to be defined.
- The tribological conditions should be homogeneous and known.
- If an intermediate layer is used, its thickness should be insignificant.
- The forming process should be at least at a few states detectable by an optical strain measurement system.

To achieve different loading conditions three different blank widths (20 mm, 130 mm and 200 mm) are tested. The reproducibility of the results is guaranteed by three parallel forming trials. The punch velocity is about 1 mm/s. Therefore, the experiment can be considered as quasi-static. During the whole experiment the material strain distribution is captured by an ARAMIS system.

Figure 2.4.29 gives an impression of the reproducibility of the forming of the specimen with widths of 20 mm. All ARAMIS data were transformed in a consistent coordinate system. The punch displacement is used for the synchronization of the projects. The transformation and the synchronization are done manually. This might cause some small deviations which can be seen when comparing the results of the three parallel specimens. Figure 2.4.30 shows the results from the three specimens with a width of 130 mm. The strain distributions are also very similar.

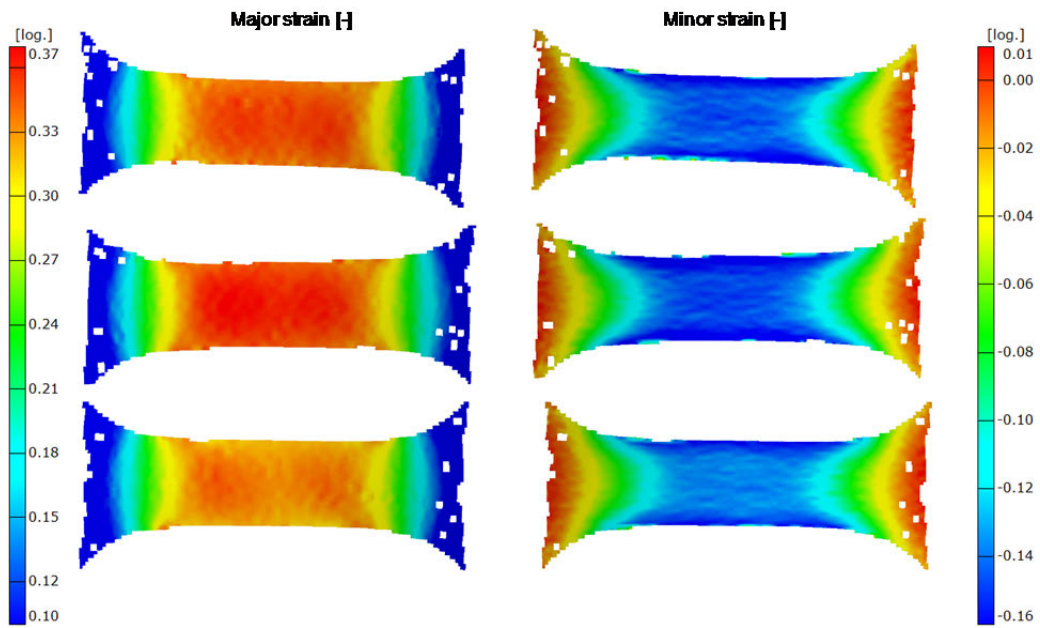


Figure 2.4.29: Comparison of 3 parallel specimen – 20 mm

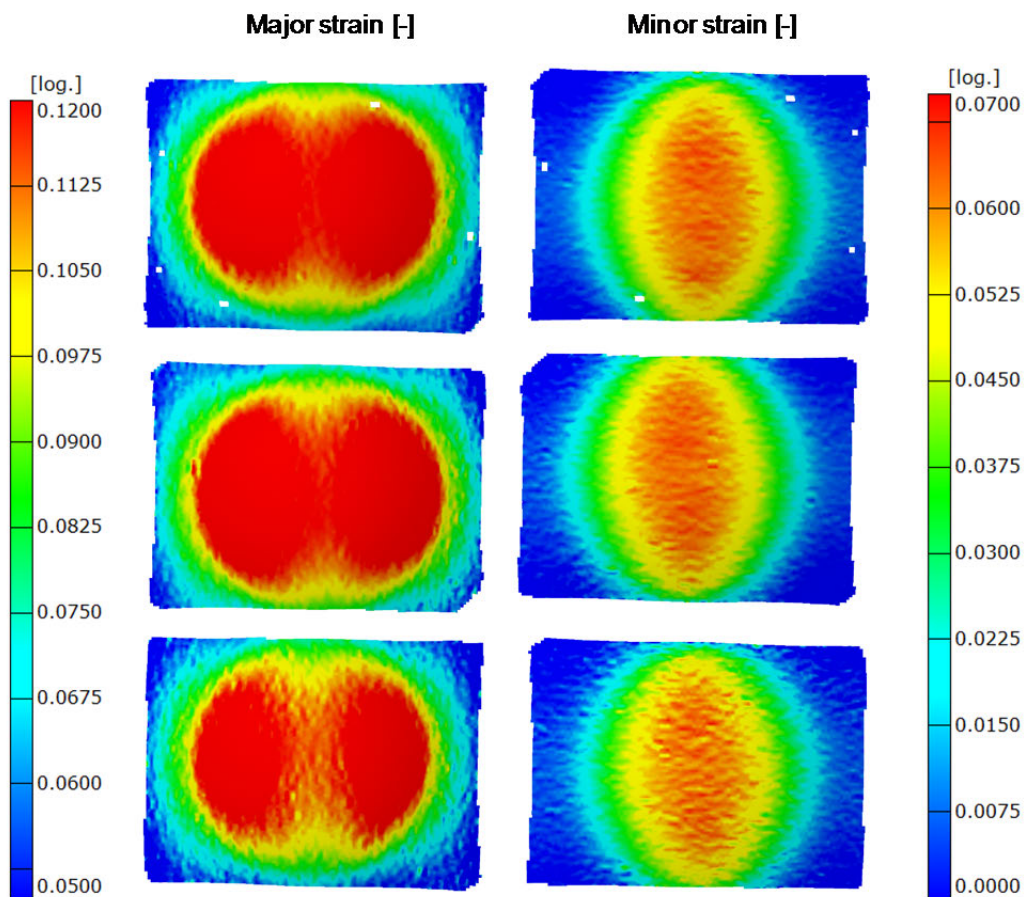
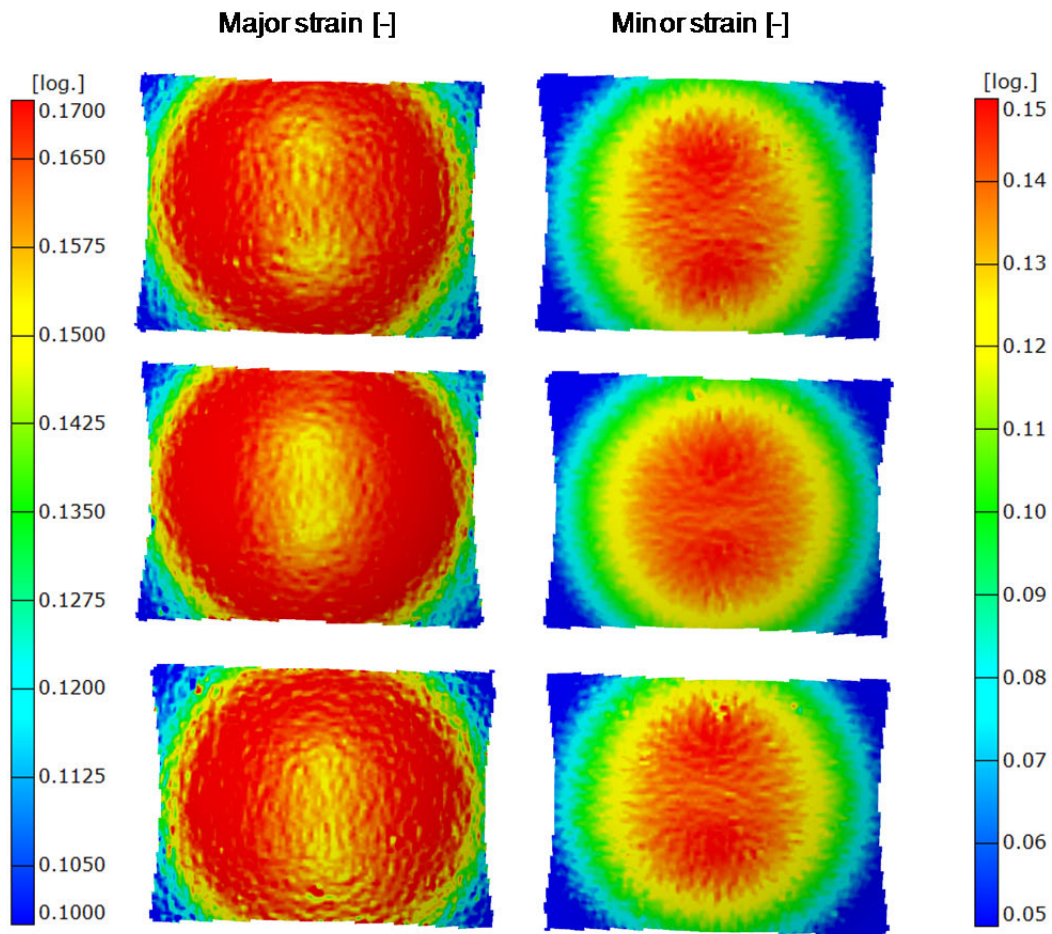


Figure 2.4.30: Comparison of 3 parallel specimen – 130 mm

The same good agreement is achieved with the square specimens. Figure 2.4.31 shows a rotational symmetrical strain distribution. The deviation from ideal symmetry is caused by the anisotropic flow behavior of the TWIP-steel due to its milling process.



**Figure 2.4.31:** Comparison of 3 parallel specimen – 200 mm

The contour plots in the previous figures give a good impression of the strain distribution at each specimen. Besides that one aim of the Nakajima forming experiment was to achieve different loading conditions. Therefore the major and minor strains in the middle of each specimen have been determined. The nine result pairs are shown in the forming limit diagram in Figure 2.4.32. It is noted that the plotted strains states are evaluated for defined punch displacements which do not represent the onset of failure. This explains the lower strains compared to the FLC in Figure 2.4.28. The experiments were analysed before a local necking has occurred. To achieve stable and comparable conditions a safety margin was respected. It can be seen that the strains are below the forming limit of the material.

Figure 2.4.32 shows also that the experimental data has only a little scattering. For the comparison with the numerical simulation one representative specimen is selected. It is mentioned that these tests are well suited for the evaluation of loading conditions between uniaxial and biaxial stress state. Loading conditions considering shear components cannot be realized with these tests. For this reason, simple deep drawing experiments were performed as described in Section 2.4.4.3.

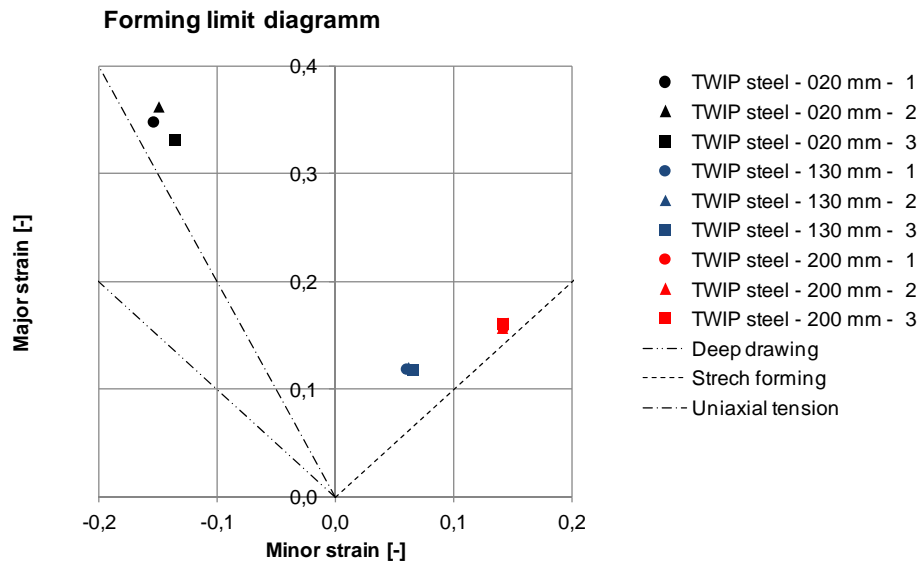


**Figure 2.4.32:** Comparison of all nine specimens. It is noted that the plotted strains states are evaluated for defined punch displacements which do not represent the onset of failure.

### 2.4.3.3 Deep drawing of square cups

Considering the aforementioned forming experiments like Nakajima-test and bulge test only monotonic strain paths and stress states between uniaxial and biaxial tension can be realized. On the way to typical industrial part geometry a more complex forming experiment is reasonable. Therefore, deep drawing of square cups is also considered since this forming experiment allows different forming states and different strain relations. Figure 2.4.33 shows the tool geometries of the cup. This experiment is close to the industrial part because of its bending and unbending effect at the draw in radius and because of the deep drawing conditions.

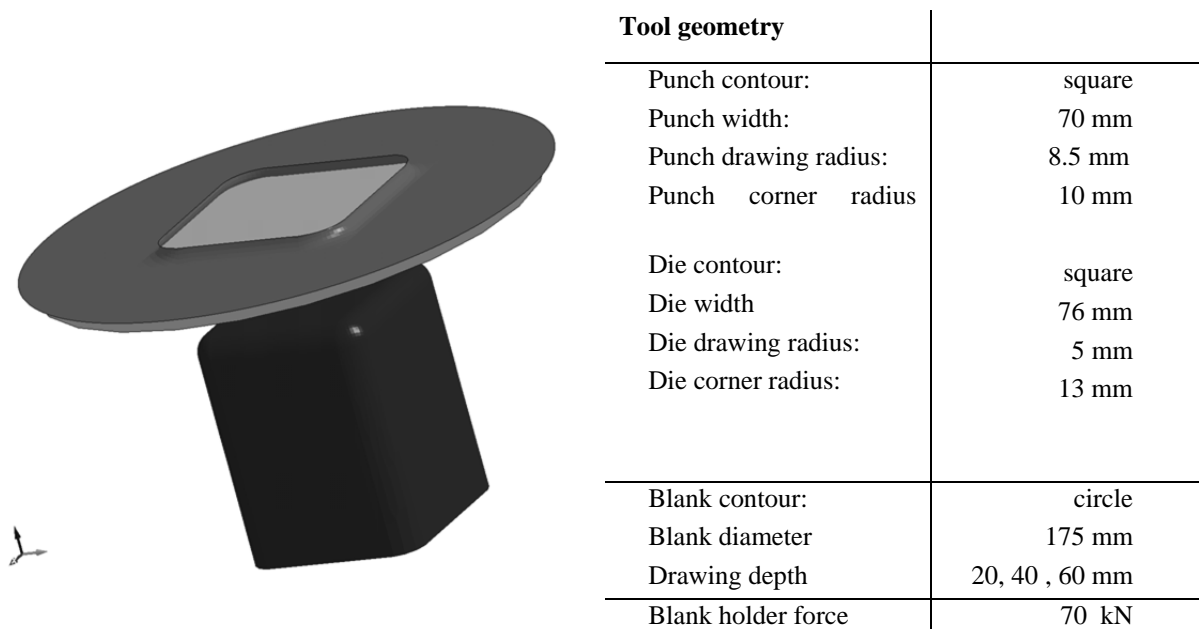


**Figure 2.4.33:** Tools for forming experiment

The considered square cups have a drawing depth of 20 mm, 40 mm and 60 mm. All drawing depths were tested three times to ensure reproducibility. Figure 2.4.34 shows the distribution of major and minor strain on the outer surface of a 60 mm cup. In Figure 2.4.35 the obtained strains for defined cuts are plotted into the FLC diagram. In addition to the local strain distribution the global punch force was determined. The measured curves are shown in Fig. 2.4.36.



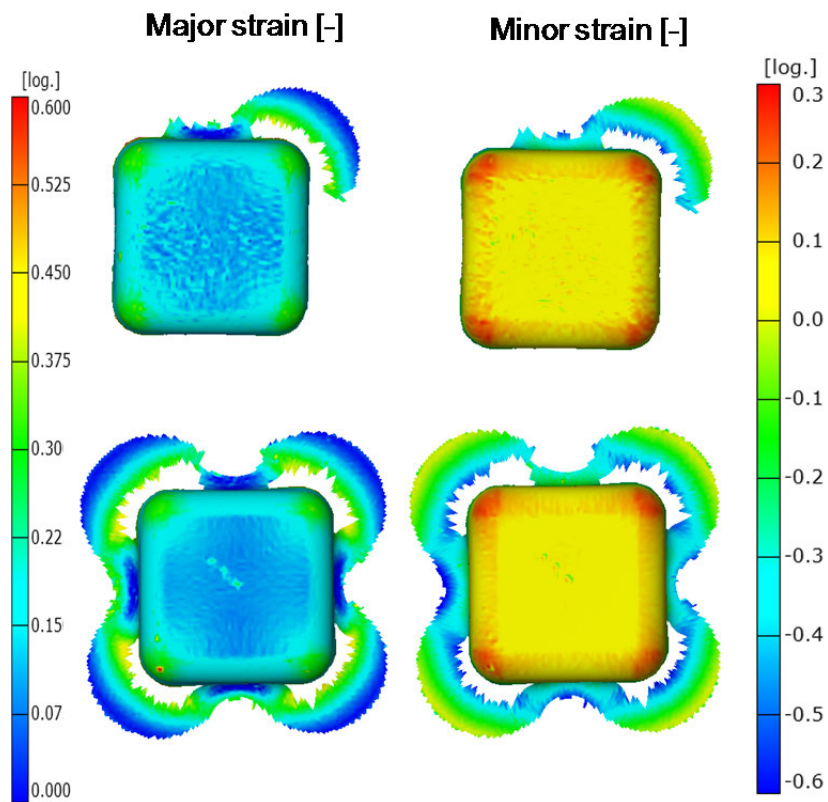


Figure 2.4.34: Major and minor strain distribution of a square cup with 60 mm drawing depth.

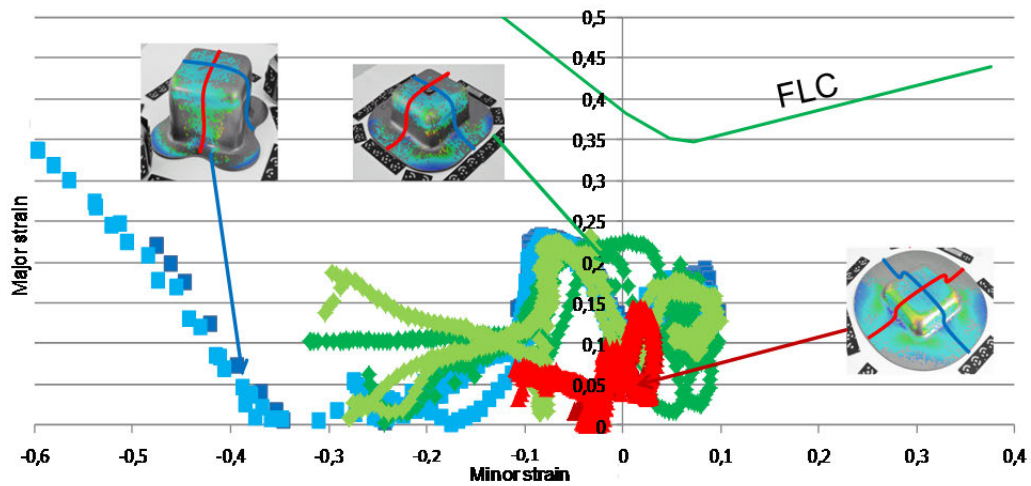


Figure 2.4.35: Strain states experimentally achieved by forming of square cups with three different drawing depths.



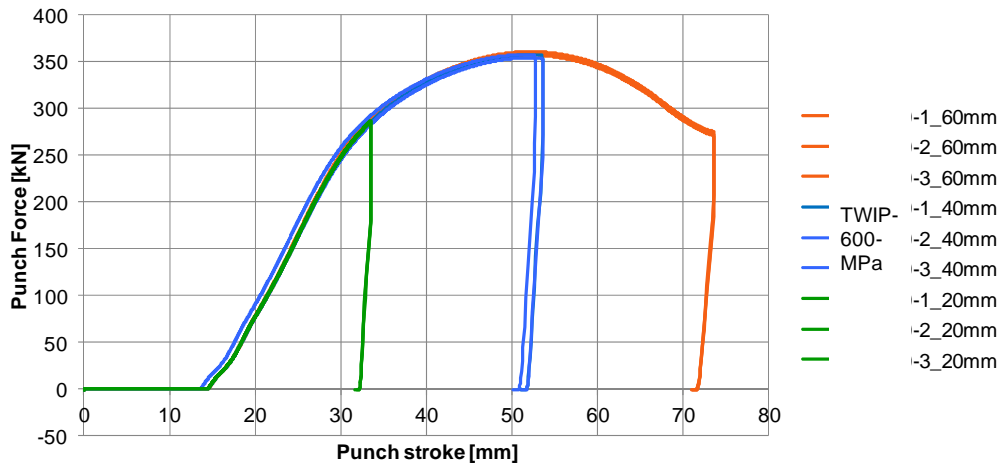


Figure 2.4.36: Global punch force vs. punch stroke of the formed square cups.

## 2.5 WP5: Micromechanical modelling and simulation of TWIP-steels

The objective of WP5 is the micromechanical modelling and simulation of TWIP-steels on grain scale. The microstructure model represents grain structure and texture of TWIP-steels in a sufficiently large representative volume element (RVE). Based on a crystal plasticity constitutive model, microstructural quantities like twin volume fraction will be calculated for prescribed stress and strain paths. These virtual experiments are not meant to replace real experiments, but rather complement them by generating additional data.

### 2.5.1 Crystal plasticity finite element framework to incorporate twinning

A description of the used single crystal plasticity model and the main aspects considering the parameter of the model is given in this section.

Following [Prakash2009] the model to describe the micromechanical behavior of TWIP-steels is given as follows: In the framework of large deformation, the deformation gradient  $\mathbf{F}$  is multiplicatively decomposed into an elastic part  $\mathbf{F}_e$  and a plastic part  $\mathbf{F}_p$ . In the context of single crystal plasticity,  $\mathbf{F}_p$  describes the part of local deformation due to plastic slip on crystallographic planes which are assumed to leave the crystal lattice unchanged. The part  $\mathbf{F}_e$  contains the lattice deformation and local rigid body rotations, see e.g. [Miehe1999]

$$\mathbf{F} = \mathbf{F}_e \mathbf{F}_p \quad (2.5.1)$$

The plastic part of the spatial velocity gradient  $\mathbf{L}^p$  is well suited to introduce a constitutive equation for representing dislocation glide: Following for example [Hutchinson1970] and [Mandel1973] and neglecting twinning effects, multi-slip phenomena can be represented effectively as a sum of shear rates on all slip systems by introducing

$$\mathbf{L}_p = \sum_{\alpha=1}^n \dot{\gamma}^{(\alpha)} \mathbf{s}^{(\alpha)} \otimes \mathbf{n}^{(\alpha)} \quad (2.5.2)$$

In Equation (5.2)  $\dot{\gamma}$  represents the shear rate of the slip system  $(\alpha)$ ,  $\mathbf{s}^{(\alpha)}$  and  $\mathbf{n}^{(\alpha)}$  represent the slip direction and the slip plane normal of the slip plane  $(\alpha)$ . In rate-dependent crystal plasticity theories, different constitutive relations have been proposed for representing the slip rate in accordance with experimental observations [Baiker2014]. In the applied model, the slip rate is given by a power law

$$\dot{\gamma}^{(\alpha)} = \dot{\gamma}_0 \text{sign} [\tau^{(\alpha)}] \left| \frac{\tau^{(\alpha)}}{g^{(\alpha)}} \right|^{1/n} \quad (2.5.3)$$

Here,  $\dot{\gamma}_0$  represents a reference shear rate. The resolved shear stress  $\tau^{(\alpha)}$  on a slip plane follows from Schmid's law

$$\tau^{(\alpha)} = \mathbf{s}^{(\alpha)} \cdot \boldsymbol{\sigma} \mathbf{n}^{(\alpha)} \quad (2.5.4)$$

In Equation (2.5.3) the expression  $g^{(\alpha)}$  describes the current strength of the slip system. The current strength depends on the hardening function  $\hat{\tau}^{(\alpha)}$ . In the considered model, the hardening function is expressed in terms of a modified Voce-hardening law:

$$\hat{\tau}^{(\alpha)} = \tau_0^{(\alpha)} + \left[ \tau_1^{(\alpha)} + \theta_1^{(\alpha)} \Gamma \right] \left[ 1 - \exp \left( - \frac{\theta_0^{(\alpha)} \Gamma}{\tau_1^{(\alpha)}} \right) \right] \quad (2.5.5)$$

The quantities  $\tau_0$ ,  $\tau_1$ ,  $\theta_0$ ,  $\theta_1$  are material parameter which have to identified separately for each slip / twin system family. A typical hardening curve together with an interpretation of the material parameter is illustrated in Figure 2.5.1.

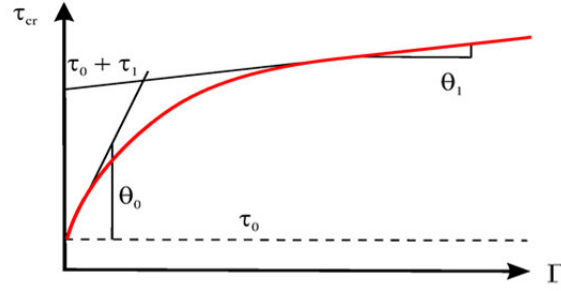


**Figure 2.5.1:** Typical hardening curve of a slip system and interpretation of the material parameter according to Equation 2.5.5.

The hardening function itself is expressed in a differential equation

$$\dot{g}^{(\alpha)} = \frac{d\hat{\tau}^{(\alpha)}}{d\Gamma} \sum_{\beta}^N h_{\alpha\beta} \dot{\gamma}^{(\beta)} \quad (2.5.6)$$

The expression  $h_{\alpha\beta}$  represents the hardening matrix. While the diagonal term represents the self-hardening of the slip systems, the off diagonal terms describe the latent hardening. This topic will be discussed more in detail at the end of this section.  $\Gamma$  represents the cumulative shear over all slip systems ( $\alpha$ ), given in the following equation

$$\dot{\Gamma} = \sum_{\alpha}^N |\dot{\gamma}^{(\alpha)}| \quad (2.5.7)$$

For the consideration of twinning effects, equation (2.5.2) is modified as follows, see e.g. [Roters2010]

$$\mathbf{L}_p = (1 - f_{twin}) \sum_{\alpha=1}^{N_{slip}} \dot{\gamma}^{(\alpha)} (\mathbf{s}^{(\alpha)} \otimes \mathbf{m}^{(\alpha)}) + \sum_{\beta=1}^{N_{twin}} \dot{f}^{\beta} \gamma_{twin} (\mathbf{s}^{(\beta)} \otimes \mathbf{m}^{(\beta)}) \quad (2.5.8)$$

In the first, simple approximation, the twinning can be interpreted as additional slip planes with a characteristic twin shear  $\gamma_{twin}$ . For fcc and bcc crystal structures, the value for  $\gamma_{twin}$  is typically set to  $\sqrt{2}/2$ .  $f_{twin}$  describes the total twin volume fraction.

In the single crystal plasticity model considered, the interaction between the plastic deformation due to slip and due to twinning plays an important role. In the model, this interaction can be defined by the hardening matrix  $h_{\alpha\beta}$  which is the part of equation (2.5.6). TWIP-steel material has an fcc crystallographic lattice. Thus, the slip system family  $\{110\}\langle 111 \rangle$  and the twin system family  $\{11-2\}\langle 111 \rangle$  are considered. From physical point of view, the latent hardening can be explained as an additional hardening of a slip or twin system due to lattice distortion that was caused by other slip or twin systems. In the model, this additional hardening is described by the parameters  $q_1$  and  $q_2$ . Here,  $q_1$  denotes the latent hardening within the same slip system family while  $q_2$  denotes the latent hardening of slip systems between different families, (between slip system family and twin system family). A more detailed description of the hardening matrix is illustrated in Figure 2.5.2.

The existing single crystal plasticity model is used to describe the plastic deformation due to plastic slip and twinning on grain level. A simple approach to describe twinning effects is considered in the model. The interaction between plastic slip and twinning can be described by adjusting the hardening matrix.

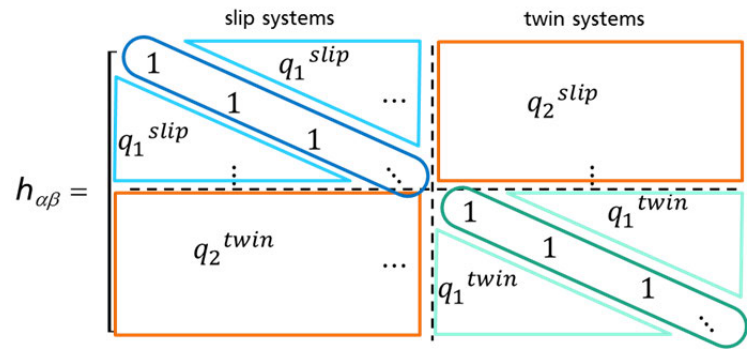


Figure 2.5.2: Detailed description of the hardening matrix  $h_{\alpha\beta}$

## 2.5.2 Parameter identification and calibration of the micro-structure model

The objective of this task is the parameter identification for crystal plasticity simulations and calibration and validation of the microstructure model with data generated from experimental investigations in WP3 and WP4. The principal procedure is illustrated in Figure 2.5.3.

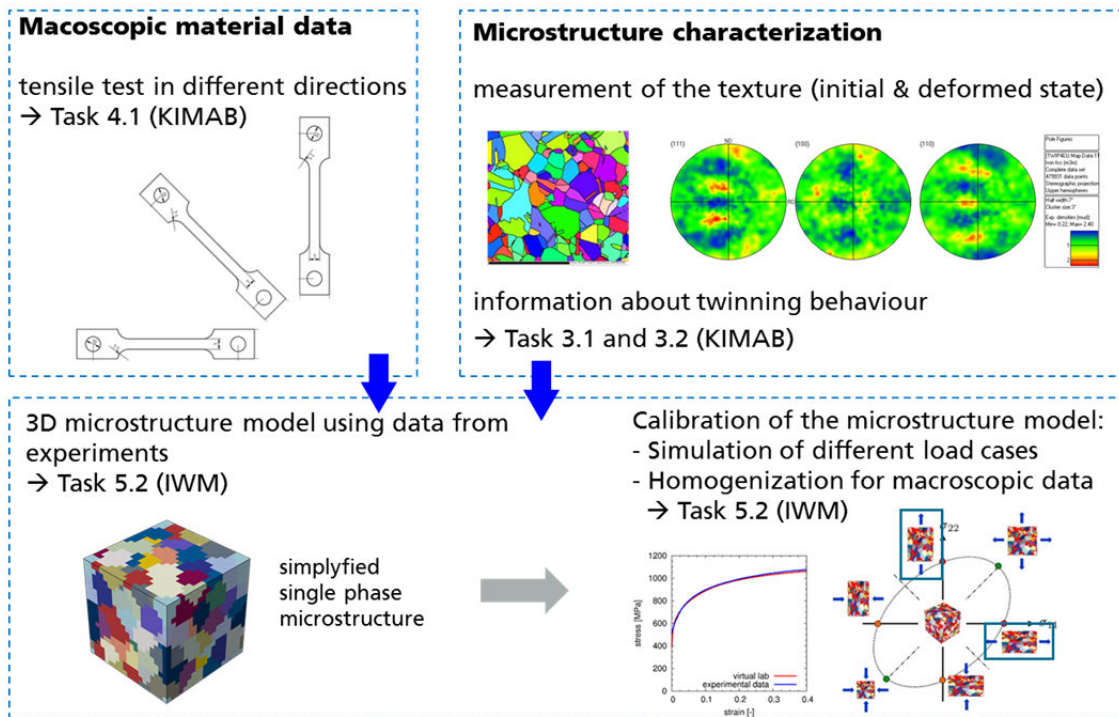


Figure 2.5.3: Procedure for creating the microstructure model and the parameter identification.

As mentioned in Section 2.5.1, the microstructure model considers different grains with different orientations. The single crystal plasticity based material model accounts for the plastic deformation due the slip of predominant slip systems as well as plastic deformation due to twinning of the crystal lattice. Therefore, the following three aspects have to be considered to complete the numerical model:

- Morphology of the microstructure, spatial resolution of single grains
- Consideration of a representative texture
- Identification of the material parameter

These three aspects will be described on the following subsections.

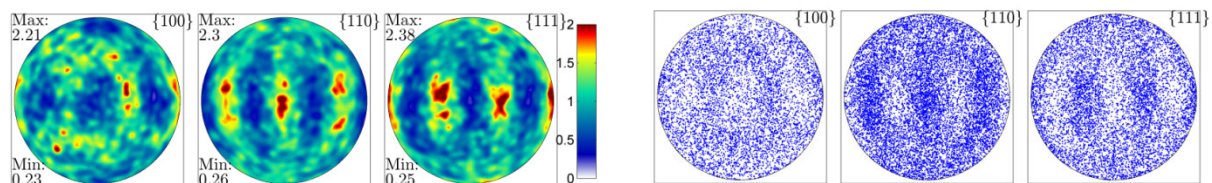
### 2.5.2.1: Generation of the microstructure morphology.

Since it was found in Section 2.3.1 (task 3.1) that the initial morphology can be described by globular grains with an aspect ratio close to one, it was concluded that a microstructure model with globular grains should be sufficient to represent the real morphology. Further, it was assumed that the observed annealing twins can be neglected for the representation of the microstructure. Based on these assumptions, it was possible to use a simple Voronoi tessellation scheme in order to create the microstructure model.

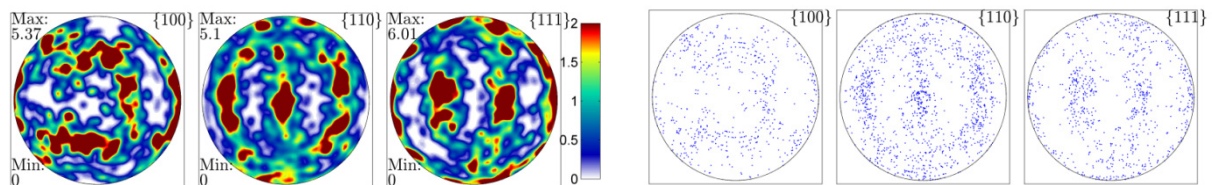
### 2.5.2.2: Texture

In the initial state of the numerical model, one crystal lattice orientation is assigned for each single grain. The initial orientations for the grains are different and must be chosen in order to represent the initial texture of the material. Experimental data of the initial state of the material were obtained in WP3, see Section 2.3.1. Since the number of grains which are considered in the microstructure model is significantly less than the number of orientations obtained from EBSD measurement, the number of experimentally measured orientations must be reduced. However, the reduced number of orientations must be able to represent a texture which is nearly equivalent compared to the one experimentally measured. Therefore, two different strategies were applied and the results were compared. In the first case, the scheme proposed in [Eisenlohr2008] was used to reduce the number of orientations. A comparison with the experimental texture has shown that this scheme was not able to create an equivalent texture. It seems that this procedure works well for strong textures but it cannot be applied for relatively weak textures. In the second approach, the following strategy was applied to reduce the number of experimentally measured orientations: The measured orientations were clustered with a step size of five degree in order to create an odf (orientation distribution function). These orientations were sorted with respect of the corresponding area fraction. The  $n$  orientations with the highest weight were used for the microstructure model. Here,  $n$  represents the number of grains which were used in the model. Figure 2.5.4 shows the comparison of the experimentally measured pole figure (see task 3.1) and the pole figure obtained from the initial state of the microstructure model. One can see that both pole figures are similar, although the number of grains in the pole figure obtained from measurement is much larger. The maximum intensities are found on the same positions. The maximum values of the intensities increase with decreasing number of considered orientations because in this case, weight of each single orientation is higher.

Experimental data



Reduced texture considering 1000 orientations



Reduced texture considering 100 orientations

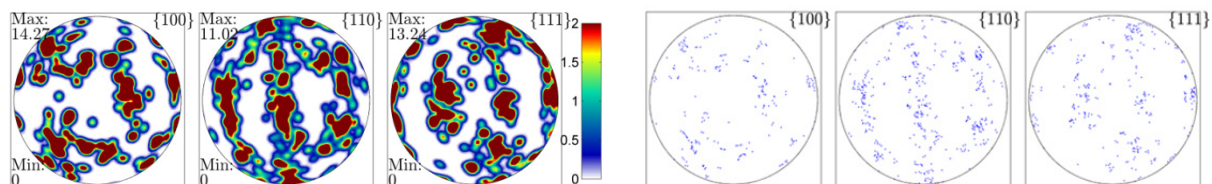


**Figure 2.5.4:** Comparison between the experimentally measured texture and texture with reduced number of orientations to be used as input for the microstructure model (left) Illustration of the discrete orientations (right). The orientations are projected in the RD-TD-plane of the sheet.

### 2.5.2.3. Parametric study

The crystal plasticity based constitutive model is already explained in Section 2.5.1. The focus of this section is on the discussion of the material parameter under special consideration of the parameters which define the latent hardening inside the slip system family and between different slip system families. For a first parametric study, a simplified but numerically efficient model considering 100 different orientations and  $12^3$  elements was considered. An overview over the material parameter of the single crystal plasticity model is given in Table 2.5.1

Parameter	Explanation
$E = 173000$	Young's modulus
$\nu = 0.3$	Poisson number
$\tau_0^{\text{slip}}, \tau_1^{\text{slip}}, \theta_0^{\text{slip}}, \theta_1^{\text{slip}}$	Hardening parameter of the slip system family
$\tau_0^{\text{twin}}, \tau_1^{\text{twin}}, \theta_0^{\text{twin}}, \theta_1^{\text{twin}}$	Hardening parameter of the twin system family
$q_1^{\text{slip}}$	Coefficient of self to latent hardening inside the slip system family
$q_2^{\text{slip}}$	Coefficient of self to latent hardening between the slip system family and the twin system
$q_1^{\text{twin}}$	Coefficient of self to latent hardening between twin system and slip system
$q_2^{\text{twin}}$	Coefficient of self to latent hardening between twin systems
$\dot{\gamma}_0 = 0.01$	reference shear rate
$N = 28$	Strain rate sensitivity (nearly rate independent material behavior is assumed)

**Table 2.5.1:** Overview over parameter of the used single crystal material model.

Here, the parameter  $E$ ,  $\nu$ ,  $N$  and  $\dot{\gamma}_0$  were defined a priori. The hardening parameter and the coefficients of self to latent hardening are essential to describe the plastic deformation with respect to slip and twinning. These parameters have to be calibrated under consideration of experimental data. To evaluate the principle behavior of the material model, a pre-study was performed. Therefore, uniaxial tensile loading was applied to the representative volume element with different sets of material parameter. An overview over the considered parameter sets is given in Table 2.5.2.

Parameter	Unit	Set-1	Set-2	Set-3	Set-4	Set-5
<b>Slip-system</b>						
$\tau_0$	[MPa]	230,6	230,6	230,6	230,6	230,6
$\tau_1$	[MPa]	36,7	36,7	36,7	36,7	36,7
$\theta_0$	[MPa]	1878	1878	1878	1878	1878
$\theta_1$	[MPa]	758	758	500	500	500
$q_1^{\text{slip}}$	[-]	0,5	0,5	0,5	0,5	0,5
$q_2^{\text{slip}}$	[-]	0,5	0,5	0,5	0,5	2,0
<b>Twin-system</b>						
$\tau_0$	[MPa]	275	275	275	275	275
$\tau_1$	[MPa]	35,3	35,3	35,3	35,3	35,3
$\theta_0$	[MPa]	10000	1000	1000	1000	1000
$\theta_1$	[MPa]	333	333	333	100	333
$q_1^{\text{twin}}$	[-]	2	1	2	2	2
$q_2^{\text{twin}}$	[-]	1,3	1,3	1,3	1,3	1,3

**Table 2.5.2:** Used sets of parameter for the first parametric studies



The stress-strain data as well as the twin volume fraction were numerically homogenized. The homogenized stress-strain curve and the corresponding twin volume fraction as function of true strain are illustrated in Figure 2.5.5. Depending on the chosen values for the parameters significant differences in the numerical results can be found. Parameter-sets which lead to a high amount of twin volume fraction (set 2 and set 4) show an s-shaped stress-strain curve. Parameter sets which show an intermediate evolution of the twin volume fraction show also a linear hardening behavior. Comparing the numerical results with the experimental data, it follows that parameter set-3 is the closest to the experimental data. The twin volume fraction is too high in all considered cases. It is noted that this parametric study was done without quantitative consideration of the twin volume fraction.

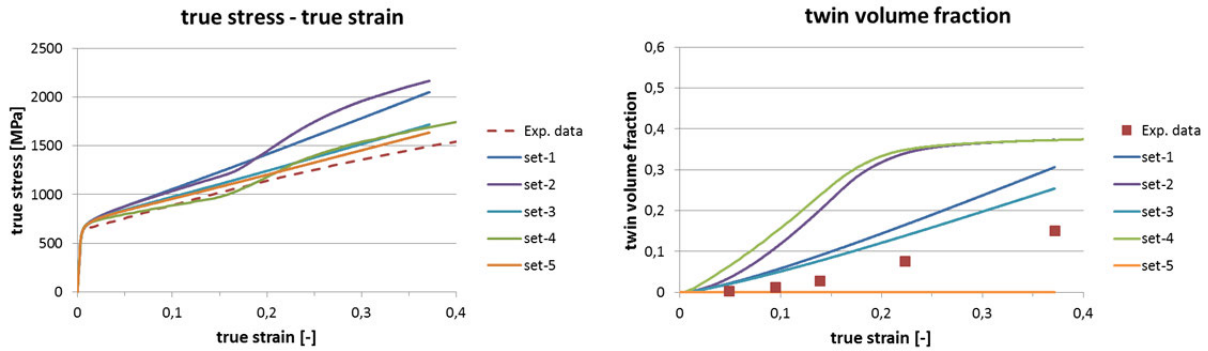


**Figure 2.5.5:** Results of the first pre-study of the stress-strain curve (left) and the twin volume fraction evolution (right) for different combinations of hardening parameter.

Further, the Lankford coefficients calculated from the homogenized results of the microstructure simulation for different set of parameters are compared with the experimental values (task 4.1). The results are given in Table 2.5.3.

	$r_0$ [-] at 20% strain	$r_{90}$ [-] at 20% strain
Experimental data	0,79	1,00
Parameter set		
Set-1	0,725	1,13
Set-2	0,805	1,10
Set-3	0,720	1,14
Set-4	0,850	1,13
Set-5	0,700	1,13

**Table 2.5.3:** Comparison of the Lankford coefficients obtained from different simulations with experimental data.

Here two aspects are mentioned: In the model, parameter sets which yield higher twin volume fraction also leads to a higher Lankford coefficient  $r_0$ . Further, in case 3 which gave the best fit to the experimental stress strain curve and the twin volume evolution, the quantity  $r_0$  is underestimated while  $r_{90}$  is overestimated. A possible reason could be a more pronounced texture due to reduced number of orientations in the simulation (see Section 2.5.3.2). Although it is known that the number 100 grains or orientations, respectively is usually too low to archive a good prediction of the anisotropic behavior, the prediction of the Lankford coefficients is relatively close to the experimental values. The principal trend ( $r_0 < r_{90}$ ,  $r_0 < 1$ ,  $r_{90} \geq 1$ ) is correctly predicted by the simple microstructure model, independently from the set of hardening parameter. Further it can be observed that the choice of the hardening parameter have much more influence on the stress strain curve and on the development of the twin volume fraction while the influence on the r-values is less significant. The prediction of the r-values is mainly influenced by the given texture.

### 2.5.3 Evaluation of the yield surface, calculation of Lankford coefficients, evaluate the macroscopic hardening

For the evaluation of the yield surface a microstructure model with 1000 grains was used. An optimized set of parameter could be determined that gives a good agreement with the available data. The hardening parameter as given in Table 2.5.4:

	$\tau_0$ [MPa]	$\tau_1$ [MPa]	$\theta_0$ [MPa]	$\theta_1$ [MPa]	$q_1$ [-]	$q_2$ [-]
slip system	220	10.0	5000	285	1.0	1.0
twin system	280	35.3	1000	196	2.0	1.0

**Table 2.5.4:** Final parameter set of the crystal plasticity based material model.

The comparison between the experimental data and the simulation results is illustrated in Figures 2.5.6 – 2.5.8. with respect to the true stress-strain curve, the Lankford coefficients and the evolution of the twin volume fraction. The results of the micromechanical model are in good agreement with the experimental data for all three considered quantities.

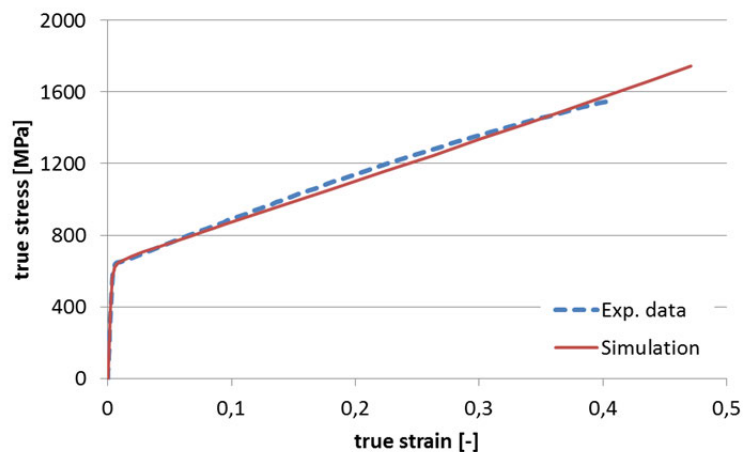


**Figure 2.5.6:** True stress strain curve in rolling direction. Comparison between experimental data and the prediction of the microstructure model.

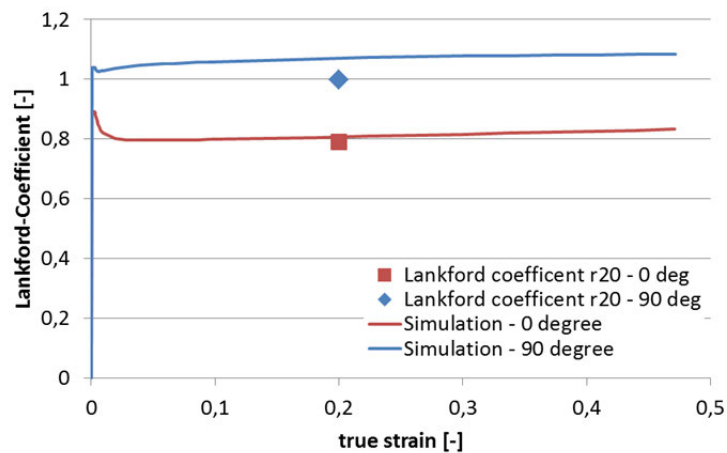


**Figure 2.5.7:** Lankford coefficients in rolling direction (0 deg.) and transverse direction (90 deg). Comparison between experimental value at 20 % strain and the prediction of the microstructure model.

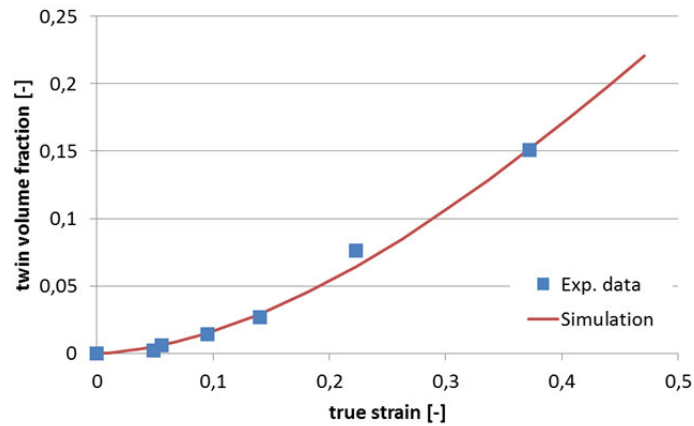


**Figure 2.5.8:** Development of the twin volume fraction. Comparison between experimental data obtained from WP3 and from the simulation of the microstructure model.

Further, several points of the initial yield surface in the first quadrant of the  $\sigma_{11}$ - $\sigma_{22}$  stress space were calculated using the microstructure model. To evaluate the points on the initial yield surface, the following procedure was used.

- Application of biaxial loading conditions. Therefore, displacements boundary conditions with different, pre-defined ratios of the displacements  $u_1$  and  $u_2$  were applied in rolling and transverse direction of the microstructure model.
- Homogenization of the components of the stress and strain tensor.
- Calculation of the initial yield strength according to the  $R_{p0.2}$  criterion under consideration of the von Mises equivalent stress-strain curve.

Although the used model is relatively simple, the determined points of the initial yield surface in the first quadrant are reasonable, see Figure 2.5.1.

Since it is very difficult to evaluate the initial yield under biaxial tension directly from experimental bulge data, the biaxial yield point was determined on two different ways:

- Via inverse simulation of the bulge test and the Nakajima test (consideration of the round specimen).
- Using the micromechanical approach described in this task.

Both strategies give very similar results for the equi-biaxial yield point which is approximately 580 MPa in the case of inverse simulation (red dot in the first quadrant in Figures 2.5.9) and 590 MPa from microstructure simulation.

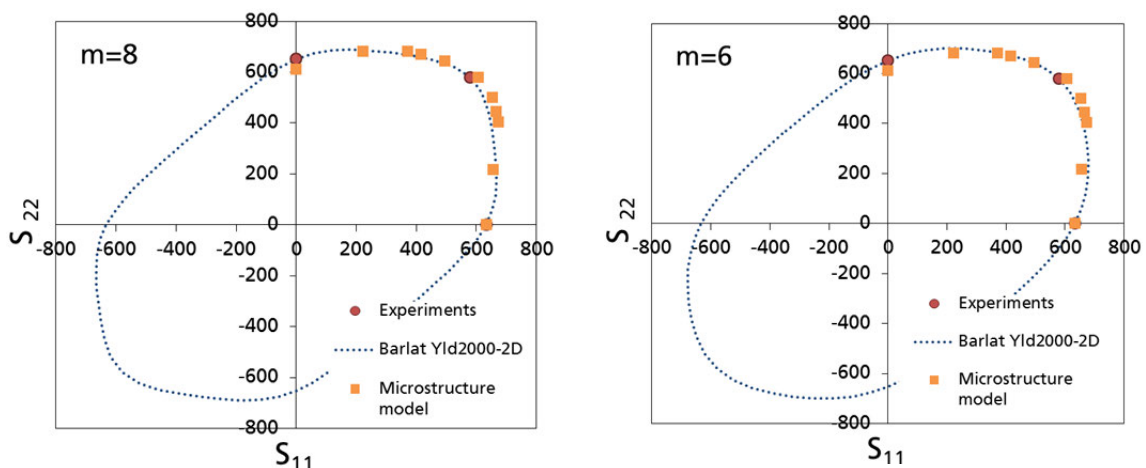


**Figure 2.5.9:** Comparison of the initial yield surface based on the Barlat YLD2000-2D model and some initial yield points based on micromechanical simulations.

Further, the Barlat yield function YLD2000-2D [Barlat2003] was adjusted to the available data from experiment and micromechanical simulation. The yield function exponent  $M$  (see Section 2.7.2) was analysed under consideration of the available data points of the initial yield surface. For fcc material like TWIP-steel,  $M=8$  is commonly used, but from Figure 2.5.1 follows that an exponent  $M=6$  fits slightly better to the data from microstructure simulation. The corresponding sets of parameters are given in Table 2.5.4 and Table 2.5.5.

a1	a2	a3	a4	a5	a6	a7	a8	M
1,005	0,981	1,229	1,020	1,048	1,183	1,055	0,720	6

**Table 2.5.4:** Set of  $\alpha_i$ -values of the Barlat YLD2000-2D yield function for  $M = 6$ .

a1	a2	a3	a4	a5	a6	a7	a8	M
1,016	0,966	1,219	1,023	1,048	1,188	1,036	0,767	8

**Table 2.5.5:** Set of  $\alpha_i$ -values of the Barlat YLD2000-2D yield function for  $M = 8$ .

In principle, these data can be used directly in the macroscopic simulations. However, from macroscopic simulations it was found that a better prediction of the tensile test in 0, 45 and 90 degree can be obtained, if an additional calibration of  $\sigma_{45}$  and  $\sigma_{90}$  is done with respect to the flow curve at higher strains. This calibration procedure leads to minor deviations of the initial yield point in the case of tensile test in 45 and 90 degree direction, but to a much better agreement of the whole flow curves, as given in Figures 2.8.1 – 2.8.3. From this point of view, the benefit of the microstructure simulations is related to the prediction of the biaxial yield point and to the estimation of the exponent  $M$ .

## 2.6 WP6: Development of a macroscopic elastic-plastic material model to describe the deformation behavior of TWIP-steels

The main topic of WP6 is the development of macroscopic elasto-plastic material model that is able to describe the deformation behavior of TWIP-steel in sheet metal forming application. The results of this WP will be the basis for the algorithmic treatment and the numerical implementation of the material model to be done WP7. The following main objectives are defined for WP6:

- Assessment of commonly used yield criteria in the industry and comparison with experimental data.
- Formulation of a constitutive framework to describe the material behavior of the considered TWIP-steel material during forming.

### 2.6.1 Assessment of yield criteria commonly used in industrial sheet metal forming applications.

An important aspect in sheet metal forming simulation is the accurate prediction of the flow of material during the forming process. Due to the production process, sheet metal usually shows anisotropic material behavior. In the numerical model, this anisotropy of sheet metal is usually considered by anisotropic yield functions. Since the deformation mechanism of high strength TWIP-steels differs from conventional steels, it is unclear whether conventional yield functions can be used. For this reason, this task assesses the applicability of a standard material model which is typically used for sheet metal forming simulations.

#### 2.6.1.1: Calibration of the standard model

As standard material model an elasto-plastic material model that considers a uniaxial flow curve obtained from tensile test in rolling direction and the Hill'48 yield locus as input was chosen. The model parameters are given in the following table:

Item	Value	Unity	Remark
Material model	Mat36	-	*MAT_3-PARAMETER_BARLAT
Density	7.40	GPa	-
Young's modulus	180	GPa	constant value
Poisson ratio	0.3	-	-
r 0°	0.787	-	constant value
r 45°	0.962	-	constant value
r 90°	0.997	-	constant value
m	2	-	Barlat exponent for yield curve, 2 causes Hill48

**Table 2.6.1:** Parameters for LS-Dyna forming simulation using the standard model.

The chosen material model uses the yield locus according to “Barlat89” [Barlat1989] which can be adjusted to the needed shape by the exponent m. If 2 is used for the parameter the yield locus is identical with the well-known Hill48 yield locus [Hill1948] as shown in Figure 2.6.1

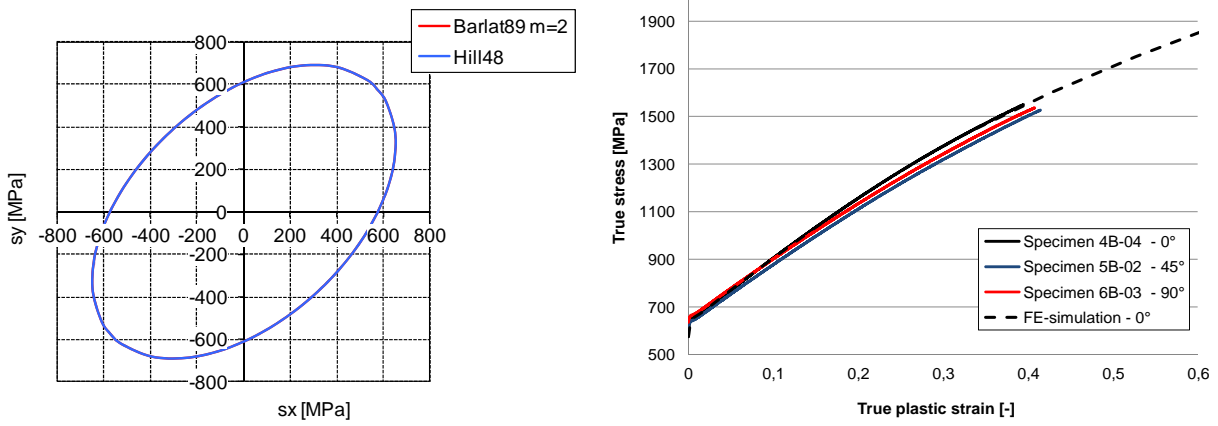


**Figure 2.6.1:** Yield locus for the TWIP-steel (left) and true plastic strain - true stress curves from experiment and simulation (right)

The evaluation of this standard material model (isotropic hardening + Hill48 yield surface) will be directly compared with experimental data in the following subsection. Some more details and also a direct comparison with the developed TWIP4EU-model will be given in Section 2.8.

### 2.6.1.2: Tensile test

- The Hill48 yield model is adjusted with the flow curve in rolling direction and under consideration of the three  $r$ -values. It is expected that the predicted strain distribution in the principal directions of the sheet is in relatively good agreement with experimental data. Comparing the uniaxial flow curves in Figure 2.6.2, one can see that the flow curve in rolling direction is well described (since it is directly included to the material card) while some significant differences can be observed in transverse direction.

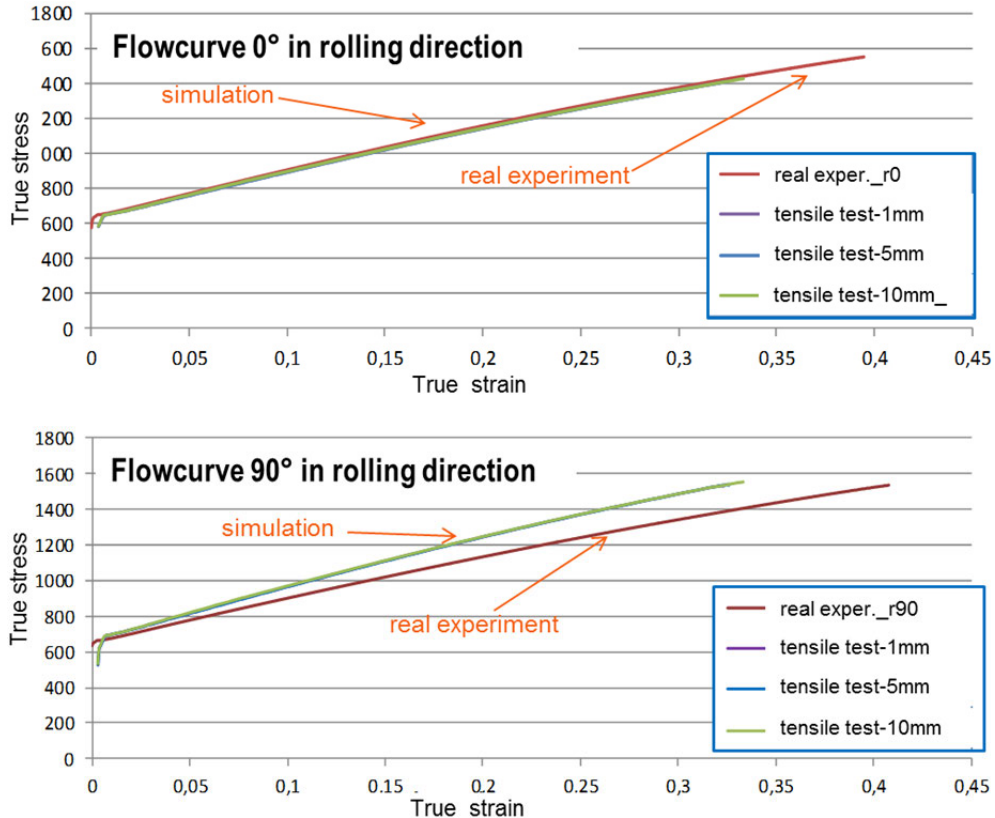


**Figure 2.6.2:** Comparison of the flow curve in rolling direction and in transverse direction: Measurement versus simulation.



There are two reasons that can explain the deviation:

- The Hill48 yield locus slightly overestimates the initial yield in transverse direction. This is a known drawback in the case that the Hill48 model is calibrated with respect to the r-values.
- The hardening behavior of the TWIP-steel material is different in both directions. In transverse direction, a lower hardening can be observed, see Figure 2.4.3. Since the Hill48 model considers the same hardening rate in both directions, the flow curve in transverse direction is overestimated from the simulation.

### 2.6.1.3: Nakajima-test

For the comparison of experimental results and commonly used yield criteria Nakajima specimens with three different specimen shapes (Nakajima specimens with 20 mm, 130 mm and 200 mm width) had been formed. In the following figures the comparison between experiments and simulation along section cuts are reported. Figure 2.6.3 shows the deviation of the major strains along section cuts in specimen direction and perpendicular. The analysis for the minor strains delivers comparable results.

The results from LS-DYNA and PAM-STAMP are both close to the ARAMIS measurements in the center of the specimen. The deviations increase with increasing distance to the centre. With the increase of the specimen's width the deviations also grow. The stretch forming specimens shows the largest deviation which can be seen in Figure 2.6.4.

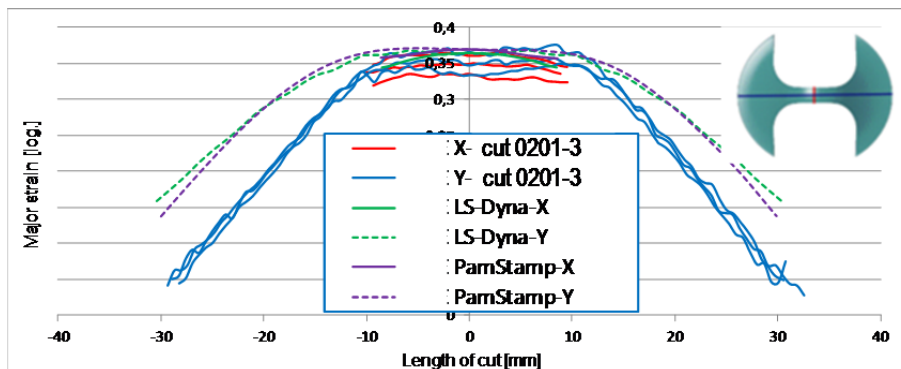


Figure 2.6.3: Major strain on section cuts through Nakajima specimen with width of 20 mm

The increase of deviation is on the one hand caused by a more complex strain state (compared to the uniaxial tension) and on the other hand by friction effects.

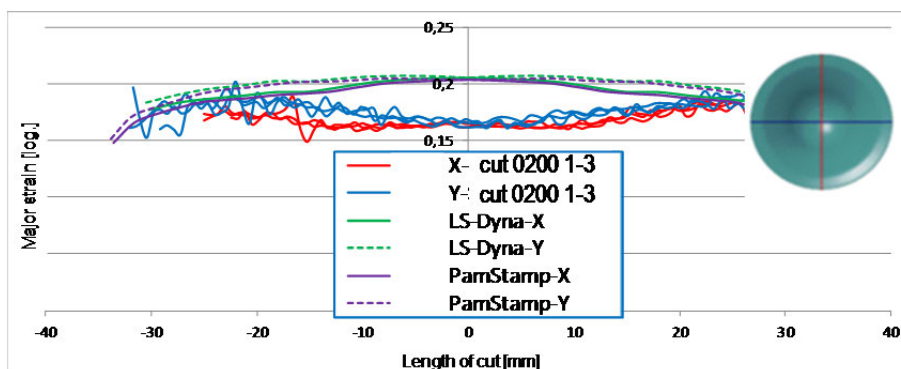


Figure 2.6.4: Major strain on section cuts through Nakajima specimen with width of 200 mm

#### 2.6.1.4: Bulge-test

The bulge test allows analysing the material behavior under equi-biaxial tension. Due to the oil as active fluid medium the effect of friction is eliminated. Figure 2.6.5 shows a good accordance between experiment and simulation for low strains.

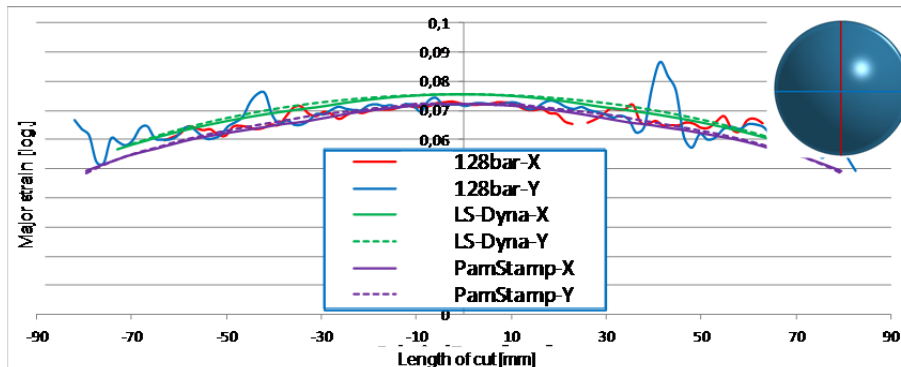


Figure 2.6.5: Major strain on section cuts through bulge test at low pressure

Unfortunately the deviations between experiment and simulation results increase significantly with the increase of pressure, which can be seen in Figure 2.6.6.

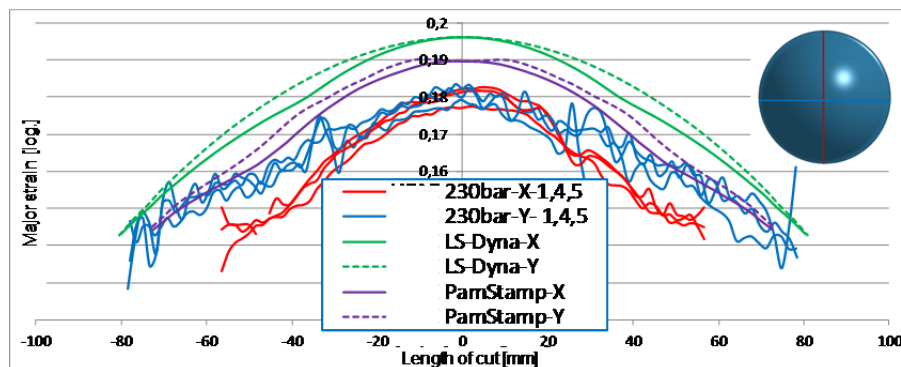
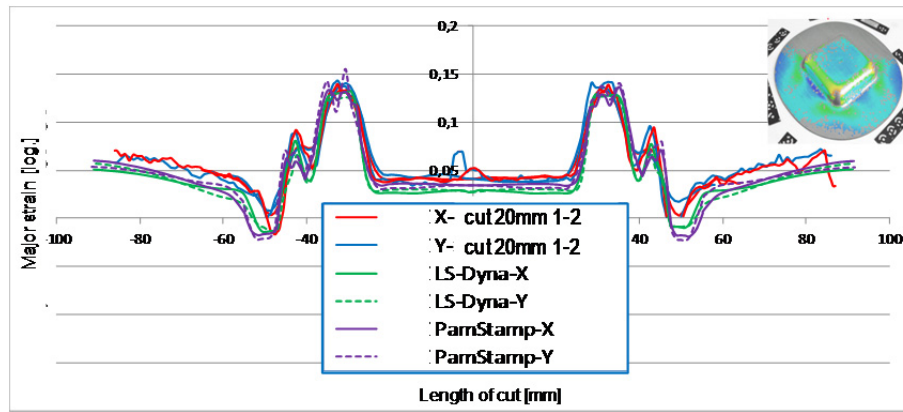


Figure 2.6.6: Major strain on section cuts through bulge test at high pressure

#### 2.6.1.5: Cup-drawing

To investigate the accuracy of a commonly used material model under deep drawing conditions, square cups with three different drawing depths were formed.

The cups with the lowest drawing depth show only small deviations in comparing simulations to optical strain measurement. But as already seen in the bulge test, the deviations grow with increasing strains. This can be seen in Figure 2.6.7 and Figure 2.6.8 for the square cups with a drawing depth of 20 mm and 60 mm.



**Figure 2.6.7:** Major strain on section cuts through square cup with 20 mm drawing depth

Due to the deviations in the middle of the specimen the remaining curve ends look like shifted horizontally.

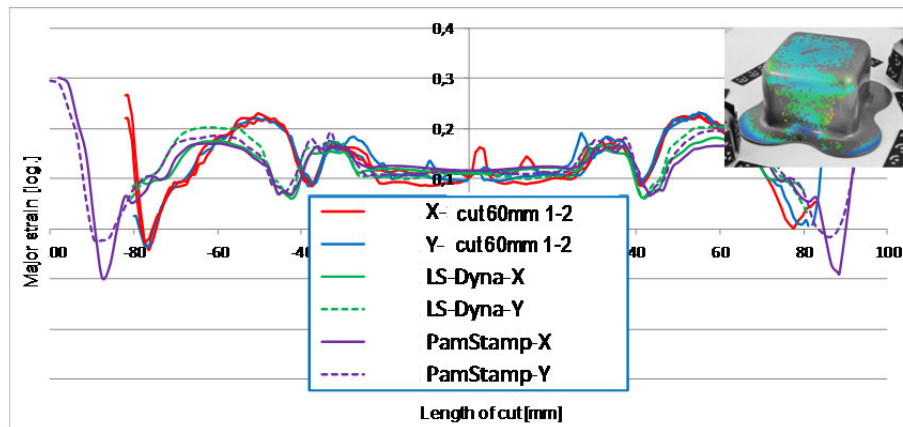


**Figure 2.6.8** Major strain on section cuts through square cup with 60 mm drawing depth

## 2.6.2 Formulation of a constitutive framework to model the forming behavior of TWIP-steels

The physically-based Bouaziz-Allain approach [Bouaziz2011] for the description of flow behavior of TWIP-steels has been considered as a base model for the current research. In order to include the influence of different loading conditions and kinematic hardening on the material behavior the original Bouaziz-Allain model has been modified and an extended three-dimensional finite elasto-plastic formulation has been developed.

### 2.6.3.1 Introduction

Experimental investigations (WP3 and WP4) and additional simulation results of the micromechanical constitutive framework (WP5) represent the basis for a phenomenological formulation of a macroscopic constitutive model for TWIP-steel. The interrelations between the physical phenomena of TWIP-steel require an advanced theoretical model. Such an elasto-plastic constitutive model has to account for the aspects of elastic behavior, anisotropy (yield surface), isotropic and kinematic hardening (Bauschinger effect). Further, it seems that the dependency of strain hardening on the twin volume fraction has to be reflected within the formulation. It is established that a high rate of work hardening in TWIP-steels results from the generation of deformation-nucleated twins. The dominant deformation mode in TWIP-steel is dislocation glide, and the deformation-induced twins gradually reduce the effective glide distance of dislocations which results in the “Dynamical Hall-Petch effect” illustrated schematically in Fig. 2.6.9.

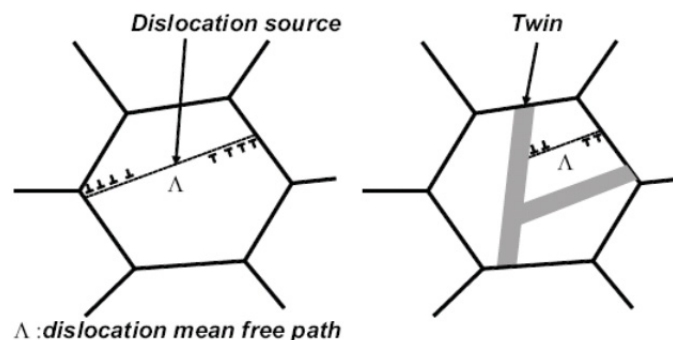


**Figure 2.6.9** Illustration of the dynamical Hall-Petch effect [De Cooman2012]. Mechanical twins are formed due to the low stacking fault energy. They gradually reduce the effective glide distance of dislocations, resulting in the very high strain hardening observed in TWIP-steel.

The impressive strain hardening is the most studied mechanical characteristic of TWIP alloys. Among all the possible mechanisms (twinning, pseudo-twinning, deformation strain ageing (DSA), bundles of Lomer-Cottrell locks) suitable to explain the strain-hardening of TWIP alloys, only the role of twins as obstacles to gliding dislocations has been seriously taken into account and quantified. Following Bouaziz et al. [Bouaziz2011], this aspect is mainly due to the fact that:

- in absence of twinning the work-hardening is much lower as illustrated in Fig. 2.6.10 for the alloy Fe–30Mn deforming only by dislocation glide up to the uniform elongation
- even in the absence of carbon in solid solution, an alloy which twins exhibits an important strain-hardening.

Various models have been proposed to model the TWIP-effect in high manganese steel in order to understand the parameters controlling their pronounced work-hardening. The role of twins on the strain-hardening was originally proposed by Rémy [Rémy1978]. In order to take into account large dislocation pileups against the twin boundaries, Rémy developed a microstructural based behaviour

law using a similar approach to that developed by Hall and Petch to describe the effect of grain refinement in metals.

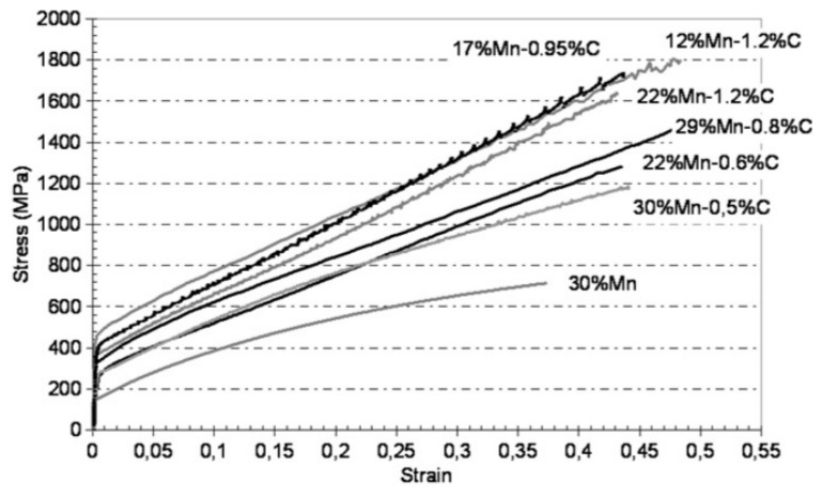


**Figure 2.6.10** Tensile behaviour of TWIP-steels with coarse grains (between 20  $\mu\text{m}$  and 40  $\mu\text{m}$ ) for a wide range of carbon and manganese contents [Bouaziz2011]

Bouaziz et al. [Bouaziz2001] and Allain et al. [Allain2004] were probably the first to attempt to model the effect of the strain-induced twinning on the work-hardening of TWIP-steel on a physical basis using the Kocks-Mecking approach [Mecking1981]. In their description the twins act as impenetrable obstacles. The model computes uniaxial tensile stress-strain curves on the basis of the evolution of the dislocation density and the twin volume fraction.

Recently Steinmetz et al. [Steinmetz2013] have developed a new multiscale dislocation density-based constitutive model for the strain-hardening behaviour in TWIP-steels. Compared to the Bouaziz-Allain model, the Steinmetz model allows more complex microstructural information to be included in the model without losing the ability to identify reasonable initial values and bounds for all parameters. Particular attention is placed on the mechanism by which new deformation twins are nucleated, and a new formulation for the critical twinning stress is presented. However, it seems to be quite a challenge to reproduce in frames of the ongoing project all experiments which are required for accurate fitting of sophisticated input parameters of the Steinmetz model.

Since the literature survey has shown that the Bouaziz-Allain model has been proved as an adequate model for the description of the flow behavior of TWIP alloys it has been selected as a “base” model for the current project. In order to include the influence of different loading conditions and kinematic hardening (Bauschinger effect) on the material behaviour the original Bouaziz-Allain model has been substantially modified and an extended three-dimensional (tensorial) finite elasto-plastic formulation has been developed and implemented computationally in frames of WP7 in the commercial FE codes ABAQUS/Explicit, LS-Dyna and PAM-STAMP as user subroutines, see Section 2.7.

### 2.6.3.2 Constitutive framework

To represent the macroscopic behaviour of sheet metals in complex forming processes, an adequate material model should at least account for isotropic and kinematic hardening as well as the plastic anisotropy. In the present context, the macroscopic plastic behaviour is represented on the basis of the additive decomposition of the symmetric second order strain rate tensor,

$$\mathbf{D} = \mathbf{D}_e + \mathbf{D}_p \quad (2.6.1)$$

into an elastic part  $\mathbf{D}_e$  and a plastic part  $\mathbf{D}_p$ . The stress state is modelled by means of a hypoelastic relation

$$\overset{\circ}{\boldsymbol{\sigma}} = \overset{4}{\mathbf{C}} \mathbf{D}_e = \overset{4}{\mathbf{C}} [\mathbf{D} - \mathbf{D}_p] = K \operatorname{tr}(\mathbf{D} - \mathbf{D}_p) \mathbf{I} + 2\mu(\mathbf{D}^D - \mathbf{D}_p^D), \quad (2.6.2)$$

wherein  $\overset{\circ}{\boldsymbol{\sigma}}$  is an appropriate objective time derivative of the Kirchhoff stress  $\boldsymbol{\sigma} = (\det \mathbf{F}) \mathbf{T}$  ( $\mathbf{T}$  denotes the Cauchy stress tensor), the elastic constants are a part of the fourth order tensor  $\overset{4}{\mathbf{C}}$ ,  $\mu = \frac{E}{2(1+\nu)}$  is the shear modulus,  $K = \frac{2\mu(1+\nu)}{3(1-2\nu)}$  is the bulk modulus,  $\mathbf{I}$  is the identity tensor,  $E$  is the Young's modulus,  $\nu$  is the Poisson ratio, and upper index D denotes the deviatoric part of a tensor. The accumulated plastic strain rate  $\dot{s}_p$  is defined by:

$$\dot{s}_p = \sqrt{\frac{2}{3}} \|\mathbf{D}_p\|, \quad (2.6.3)$$

where  $\|\mathbf{D}_p\| = \sqrt{\mathbf{D}_p : \mathbf{D}_p}$  denotes the tensor norm. The isotropic plastic yielding can be described by different yield functions. For simplicity, only a von Mises type yield function is considered:

$$f = \|\boldsymbol{\sigma}^D - \mathbf{X}^D\| - \sqrt{\frac{2}{3}} (\sigma_0 + \sigma_f). \quad (2.6.4)$$

Here  $\mathbf{X}$  is the back-stress tensor,  $\sigma_0$  is the initial yield radius, and  $\sigma_f$  the isotropic hardening function. In contrast to the von Mises like yield function, also other yield functions (*e.g.*, a Hill type yield function) can be easily incorporated in order to represent observed anisotropies, as described in Section 2.7.1. The plastic flow is modelled by a normality rule

$$\mathbf{D}_p = \gamma \frac{\partial f}{\partial \boldsymbol{\sigma}}. \quad (2.6.5)$$

with  $\gamma = \sqrt{3/2} \dot{s}_p$  being a plastic multiplier which follows from the consistency condition for plastic flow:

$$f = 0, \quad df = 0. \quad (2.6.6)$$

Now, the stress terms  $\sigma_0$ ,  $\sigma_f$ , and  $\mathbf{X}$  of the yield function  $f$  (2.6.4) have to be described. As reported by Bouaziz *et al.* [Bouaziz2011] the initial yield radius  $\sigma_0$  is related to the lattice friction stress due to solid solution hardening depending only on the chemical composition. In high Mn austenitic steels it can be mathematically expressed as:

$$\sigma_0 \text{ (MPa)} = 228 + 187 \text{ wt.\%C} - 2 \text{ wt.\%Mn}. \quad (2.6.7)$$

The isotropic hardening function is simply assumed to obey the classical relation with the statistical stored dislocation density  $\rho$ :

$$\sigma_f = \alpha M \mu b \sqrt{\rho}. \quad (2.6.8)$$

with  $\alpha$  constant,  $M$  the average Taylor factor, and  $b$  the burgers vector. Extending the approach of Bouaziz *et al.* [Bouaziz2011] who presented the back-stresses  $\sigma_b$  in the one-dimensional formulation:

$\sigma_b = M \frac{\mu \cdot b}{L} n$ , we introduce the back-stress tensor  $\mathbf{X}$  which describes the kinematic hardening:



$$\mathbf{X} = M \frac{\mu \cdot b}{L} \mathbf{n}, \quad (2.6.9)$$

with  $L$  being the geometrical length scale of the microstructure, and  $\mathbf{n}$  is the tensor of the flux of dislocations which have been arrived at a twin or grain boundary. This tensorial quantity  $\mathbf{n}$  allows us to incorporate the directional nature of the number of dislocations stored at an obstacle like a grain boundary.

Eqs. (2.6.8) and (2.6.9) contain the internal variables which can be defined as shown below. Following Mecking and Kocks [Mecking1981] and Sinclair *et al.* [Sinclair2006] the statistical stored dislocation density evolution with plastic strain resulting from the competition between accumulation and annihilation by dynamic recovery is

$$\frac{d\rho}{ds_p} = M \cdot \left( \frac{1-n/n_0}{b \cdot L} + \frac{k}{b} \sqrt{\rho} - f \cdot \rho \right), \quad (2.6.10)$$

where  $k$  and  $f$  are parameters directly linked to the athermal work hardening limit and dynamic recovery,  $n_0$  is the maximum number of dislocation loops at the boundaries, and  $n$  can be considered in view of Eq. (2.6.8) as the von Mises invariant  $J(\mathbf{n}) = \sqrt{(3/2)\mathbf{n} : \mathbf{n}}$  of the tensor  $\mathbf{n}$ . In the present case grain and twin boundaries are assumed the main microstructural obstacles for gliding dislocations. Thus  $L$  can be written as:

$$\frac{1}{L} = \frac{1}{d} + \frac{1}{t}. \quad (2.6.11)$$

with  $d$  the grain size and  $t$  the mean distance between adjacent twins. According to the stereological analysis [Bouaziz2001],  $t$  is linked to the twin volume fraction  $F$  and the twin thickness  $e$  (assumed constant) by the relation:

$$\frac{1}{t} = \frac{1}{2e} \frac{F}{(1-F)}. \quad (2.6.12)$$

In the absence of a valid physical expression, Bouaziz *et al.* [Bouaziz2011] have proposed an empirical law:

$$\text{for } s_p \geq \varepsilon_{\text{init}}, F = F_0 \left( 1 - e^{-\beta(s_p - \varepsilon_{\text{init}})} \right)^m, \quad (2.6.13)$$

where  $\varepsilon_{\text{init}}$  is the critical plastic strain at which twinning begins,  $F_0$  is the maximum volume fraction of twins,  $m$  is the stacking fault energy parameter,  $\beta$  is the fitting coefficient. The critical strain at which twinning begins,  $\varepsilon_{\text{init}}$ , should evolve linearly with the grain size [Bouaziz2008]. The relation between  $\varepsilon_{\text{init}}$  and grain size in  $\mu\text{m}$ ,  $d$ , can be linearly fitted as:

$$\varepsilon_{\text{init}} = 0.0038d + 0.023. \quad (2.6.15)$$

Bouaziz *et al.* [Bouaziz2011] considered a one-dimensional evolution law for the strain dependence of the number of dislocations ( $n$ ) stopped at a grain and a twin boundary. The flux of dislocations arriving at a boundary per slip band can be calculated:

$$\frac{dn}{ds_p} = \frac{\lambda}{b} \left( 1 - \frac{n}{n_0} \right), \quad (2.6.16)$$

where  $\lambda$  is the mean spacing between slip bands. The ratio  $\lambda/b$  gives the number of dislocations per slip band geometrically necessary to provide the deformation, and the corrective term  $(1 - n/n_0)$  accounts

for the finite number of sites available for dislocations at the boundary. The maximum number of dislocation loops at the boundaries,  $n_0$ , depends only on chemical composition of a TWIP-steel and can be defined as the linear function (see Fig. 2.6.11) of the lattice friction stress,  $\sigma_0$  [Bouaziz2011]:

$$n_0 = 0.02\sigma_0. \quad (2.6.17)$$

The reason why  $n_0$  increases with  $\sigma_0$  can be explained in as follows: a TWIP-steel with a higher friction stress due to solid solution hardening may exhibit stronger twins which are more effective as obstacles for dislocation movement as supported by the recent TEM study showing that the dislocation pile-ups at twin boundaries are much more larger in a TWIP-steel hardened by carbon in solid solution compared to a TWIP-steel without carbon [Idrissi2010; Bouaziz2011].

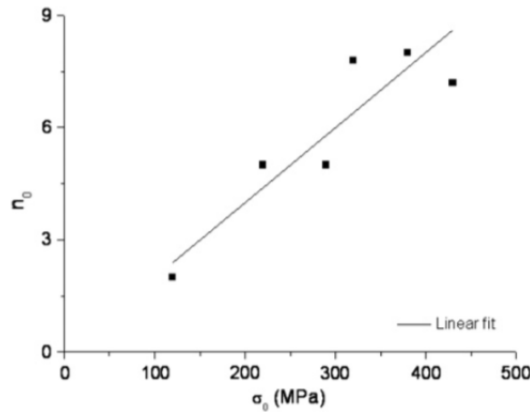


**Figure 2.6.11** Identified evolution of the maximum number of dislocations stored at twin boundaries and the lattice friction stress [Bouaziz2011]

Modifying the Bouaziz model [Bouaziz2011] the evolution equation (2.6.16) has been introduced as a tensorial extension of the Bouaziz model:

$$\overset{\circ}{\mathbf{n}} = \frac{\lambda}{b} \left( \frac{2}{3} \mathbf{D}_p - \dot{\gamma}_p \frac{\mathbf{n}}{n_0} \right), \quad (2.6.18)$$

with  $\overset{\circ}{\mathbf{n}}$  being an appropriate objective time derivative of the tensor  $\mathbf{n}$ . The idea behind this extension is related to the kinematic hardening model of [Armstrong1966]. With this concept, the reversible nature of the dislocation flux at a boundary under cyclic loading is taken into account. A summary of this first extension of the base model is given in Figure 2.6.12.

Due to the recent experimental results obtained and with respect to the needs of practical sheet forming simulations, the current model approach has been further extended. The following modifications have been performed:

- Implementation of an anisotropic yield function.
- Consideration of a stress dependent twinning
- Kinematic hardening

### Implementation of an anisotropic yield function

Regarding the experimental results, see Section 2.4.1 and in order to have sufficient flexibility to fit the behavior of modern TWIP-steels (see Section 2.6.2), the hitherto isotropic, von Mises based TWIP4EU-model has been advanced by integrating the Barlat YLD2000-2D yield condition (see [Barlat2003]) in the current shell formulation. Anisotropic behavior of TWIP-steels can thus be captured precisely through 9 additional material parameters. Details concerning the formulations of the Barlat YLD2000-2D yield condition are given in Section 2.7.2.

<u>Kinematics</u>	$\mathbf{D} = \mathbf{D}_e + \mathbf{D}_p$ (1)	<u>The initial yield radius</u>	$\sigma_0(\text{MPa}) = 228 + 187 \text{wt}\% \text{C} - 2 \text{wt}\% \text{Mn}$ (8)
<u>Hypoelasticity</u>	$\overset{\circ}{\boldsymbol{\sigma}} = \mathbf{C} \mathbf{D}_e = \mathbf{C} [\mathbf{D} - \mathbf{D}_p]$ (2)	<u>The isotropic hardening function</u>	$\sigma_f = \alpha M \mu b \sqrt{\rho}$ (9)
<u>Yield function</u>	$f = \ \boldsymbol{\sigma}^D - \mathbf{X}^D\  - \sqrt{\frac{2}{3}}(\sigma_0 + \sigma_f)$ (3)	<u>The back-stress tensor</u>	$\mathbf{X} = M \frac{\mu \cdot b}{L} \mathbf{n}$ (10)
<u>Normality rule</u>	$\mathbf{D}_p = \gamma \frac{\partial f}{\partial \boldsymbol{\sigma}}$ (4)	<u>The statistical stored dislocation density</u>	$d\rho = M \cdot \left( \frac{1 - J(\mathbf{n})/n_0}{b \cdot L} + \frac{k}{b} \sqrt{\rho} - f \cdot \rho \right) ds_p$ (11)
<u>Accumulated plastic strain</u>	$\dot{s}_p = \sqrt{\frac{2}{3}} \ \mathbf{D}_p\ $ (5)	<u>The twin volume fraction</u>	$F = F_0 \left( 1 - e^{-\beta(s_p - \varepsilon_{init})} \right)^m$ (12)
<u>Consistency condition</u>	$f = 0, df = 0$ (6)	<u>Length scale of microstructure</u>	$\frac{1}{L} = \frac{1}{d} + \frac{1}{2e} \frac{F}{(1-F)}$ (13)
<u>Plastic multiplier</u>	$\gamma = \sqrt{\frac{3}{2}} \dot{s}_p$ (7)	<u>Flux of dislocations arriving at a boundary</u>	$\overset{\circ}{\mathbf{n}} = \frac{\lambda}{b} \left( \frac{2}{3} \mathbf{D}_p - \dot{s}_p \frac{\mathbf{n}}{n_0} \right)$ (14)

**Figure 2.6.12:** Summary of the twip-steel material model considering the extension from 1d formulation to a 3d tensorial formulation..

### Stress-dependent twinning

The twinning evolution and, consequently, the strain hardening depend on the applied stress state, that has been revealed by comparison of uniaxial and biaxial flow curves and also by the SEM/TEM analysis of the twinning evolution in different specimens subjected to tensile, shear, biaxial and cyclic loading, see Section 2.3.2. It is assumed that the increase of stress triaxiality leads to more pronounced twinning and thus more pronounced strain hardening. In order to account for stress dependent twinning effect, a factor  $k_{TWIN}$  has been introduced to the formulation of twin volume fraction (12), which can now be expressed in the following rate form:

$$\dot{F} = F_0 m \left[ 1 - e^{-\beta(s_p - \varepsilon_{init})} \right]^{m-1} \left[ -e^{-\beta(s_p^t - \varepsilon_{init})} \right] [-\beta] \dot{s}_p k_{twin} , \quad (12a)$$

where the factor  $k_{TWIN}$  is defined in its simplest form as a linear function of the stress triaxiality  $\eta$ :

$$k_{TWIN} = r \text{ abs}(\eta) - \frac{r}{3} + 1 , \quad (15)$$

with  $r$  being the slope of the linear function  $k_{TWIN}$  allowing for more twinning with increasing stress triaxiality (see Fig. 2.6.9). In case of uniaxial tension:  $\eta = 1/3$  and  $k_{TWIN} = 1.0$ . The definition of the function in Eq. (15) ensures that the state of uniaxial tension remains unaffected by the variation of  $r$ .

Thus, the identification of the parameters to describe the uniaxial flow curve and the determination of the function for  $k_{TWIN}$  can be done separately. The stress triaxiality  $\eta$  is defined as the ratio of the hydrostatic stress and the equivalent stress:

$$\eta = \frac{\sigma_H}{\sigma_V} .$$

The parameter  $r$  can be then fitted by means of experiments with triaxiality that differs significantly from 1/3. This might be biaxial tension dominated tests, e.g. a bulge test (triaxiality  $\approx 2/3$ ) and shear dominated tests with triaxiality  $\approx 0.0$ .

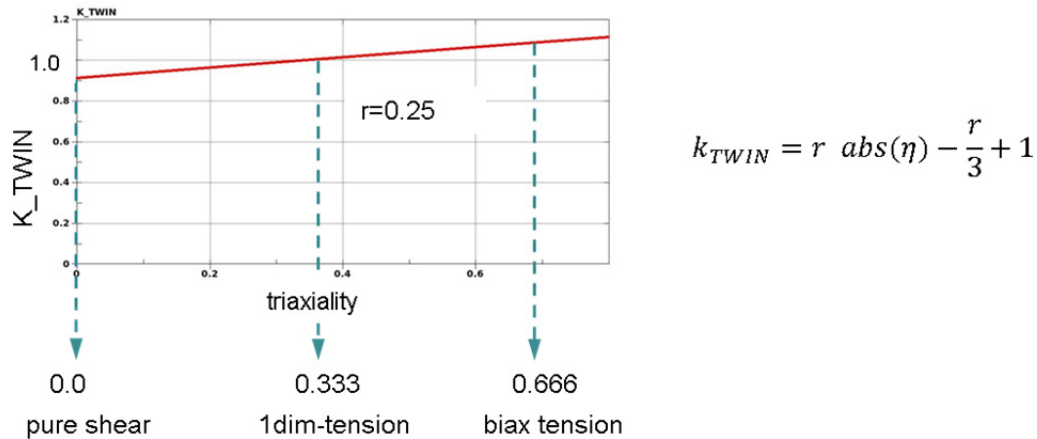


**Figure 2.6.13:** Factor  $k_{TWIN}$  to account on stress state dependent twinning

The effect of stress-dependent twinning is demonstrated on the results of one-solid-element tests, see Figure 2.6.14. The results for the twin volume evolution as a function of the effective plastic strain for different stresses, with triaxiality varying from 0.0 (pure shear) to 0.666 (biaxial loading) are given in Figure 2.6.14. For this,  $r$  has arbitrarily been chosen to be  $r=0.25$ , just in order to show the triaxiality dependent twin evolution effect. In the case of pure shear the twin volume evolution is decreases while it increases in the case of biaxial tension. As already mentioned, uniaxial tension remains unaffected, independently from the chosen value of  $r$ .

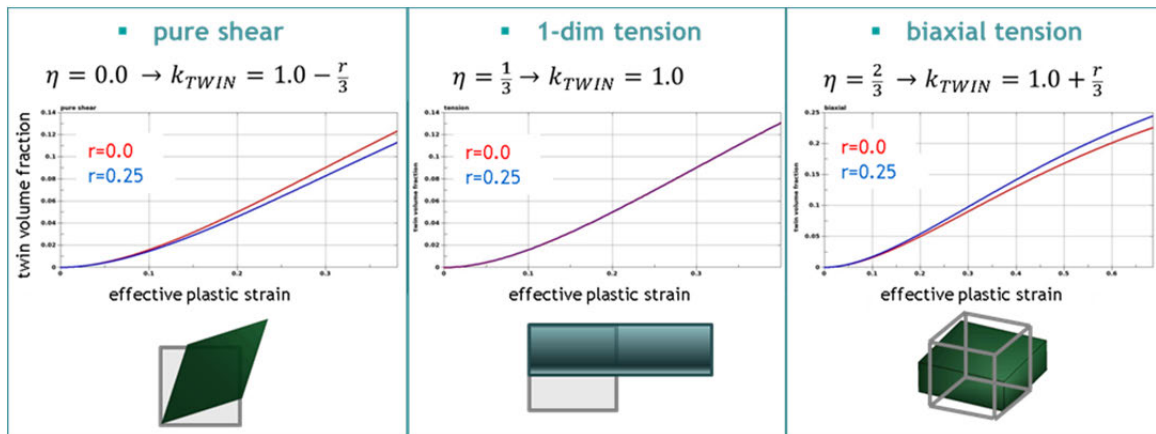


**Figure 2.6.14:** Influence of triaxiality on the twin volume fraction.

More complex functions to describe the triaxiality dependences of  $k_{TWIN}$  will be discussed in Section 2.7.1.3. The aim is to better describe the material behavior under compression and shear conditions, respectively which is important for deep drawing simulation.

### Kinematic hardening and spring back behavior

In the simulation of sheet metal forming processes the prediction of spring back behavior plays an important role. In the considered TWIP-steel material, significant spring back behavior is expected due to

the combination of a low Young's modulus and a high strength of the material. In order to determine Bauschinger effect tension–compression tests with different amplitudes have been performed. An overview over the tests is given in Table 2.4.4. From these results follows that the strong Bauschinger effect in TWIP-steels should be accurately considered in a constitutive model.

The simulation results have shown that the cyclic behavior of the TWIP-steel cannot be described accurately within the current formulation (see Figure 2.6.15 left, red curve). It should be mentioned that the back-stress tensor  $\mathbf{X}$  (Eq. 10) describing the kinematic hardening is a function of the tensor  $\mathbf{n}$  (Eq. 14) which represents a flux of dislocations arriving at a grain or a twin boundary (for details see mid-term report, p. 79-81). Eq. (14) takes the reversible nature of the dislocation flux at boundaries under cyclic loading into account and is related to the well-known Frederick–Armstrong kinematic hardening model [Armstrong1966]. Chaboche and Rousselier observed that, the hardening behavior of the steel material can be more accurately approximated by the sum of different Frederick–Armstrong terms [Chaboche1983]. The characteristics of the Frederick-Armstrong-type Eq. (14) are determined by the values  $\frac{\lambda_i}{b}$  and  $\frac{\lambda_i}{bn_{0i}}$ ; different value pairs result in different characteristics. Thus, one may obtain the following Chaboche-type formulation of Eq. (14):

$$\overset{\circ}{\mathbf{n}} = \sum_{i=1}^k \overset{\circ}{\mathbf{n}}_i = \sum_{i=1}^k \frac{\lambda_i}{b} \left( \frac{2}{3} \mathbf{D}_p - \dot{\gamma}_p \frac{\mathbf{n}_i}{n_{0i}} \right). \quad (14a)$$

Therefore, based on (10) the combined back-stress tensor can be expressed as the following sum:

$$\mathbf{X} = \sum_{i=1}^k \mathbf{X}_i = M \frac{\mu \cdot b}{L} \sum_{i=1}^k \mathbf{n}_i. \quad (10a)$$

This Chaboche-type extension has been implemented by Fraunhofer IWM into the Abaqus-Version of the TWIP4EU model for further analyses. Therefore, the tension-compression test was simulated using two terms of the back-stress  $\mathbf{X}$ . The results presented in Fig. 2.6.14. show that a cyclic curve can be fitted with the Chaboche-type approach better than within the previous formulation. The drawback of this approach is that the uniaxial monotonic stress-strain curve deviates from the experimental data for strains up to 5% (see Figure 2.6.10). Since an accurate description of the uniaxial monotonic stress-strain curve is essential for forming simulations, this approach was not further considered for forming simulations. However, experimental data from the bending-under-tension tests allow to validate this model with respect to spring-back prediction and to identify the possible potential for further improvement see Section 2.8.3. It is noted that implementation in LS-DYNA and PAM-STAMP consider only one back-stress component.

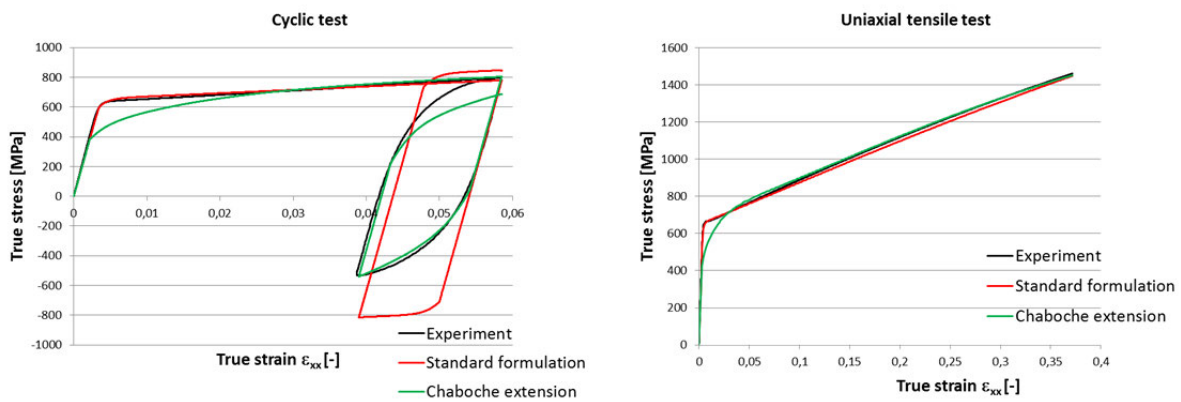


**Figure 2.6.15:** Cyclic test (left) and tensile test (right): Experiments and simulations with Chaboche extension (green curves) and within the standard formulation (red curves)

## Summary of the extended constitutive model

Figure 2.6.16 gives an overview of the extended constitutive model. Extensions with respect to the overview given in Figure 2.6.12 are highlighted in red.

<u>Kinematics</u>		<u>The initial yield radius</u>	
$\mathbf{D} = \mathbf{D}_e + \mathbf{D}_p$	(1)	$\sigma_0 \text{ (MPa)} = 228 + 187 \text{ wt\% C} - 2 \text{ wt\% Mn}$	(8)
<u>Hypoelasticity</u>		<u>The isotropic hardening function</u>	
$\overset{\circ}{\boldsymbol{\sigma}} = \mathbf{C} \mathbf{D}_e = \mathbf{C} [\mathbf{D} - \mathbf{D}_p]$	(2)	$\sigma_f = \alpha M \mu b \sqrt{\rho}$	(9)
<u>Anisotropic yield function</u>		<u>The back-stress tensor</u>	
$f = \sigma_{\text{eff}}^{\mathbf{D}}(\boldsymbol{\sigma}^{\mathbf{D}}, \mathbf{X}^{\mathbf{D}}) - (\sigma_0 + \sigma_f)$	(3a)	$\mathbf{X} = M \frac{\mu \cdot b}{L} \sum_{i=1}^k \mathbf{n}_i$	(10a)
<u>Normality rule</u>		<u>The statistical stored dislocation density</u>	
$\mathbf{D}_p = \gamma \frac{\partial f}{\partial \boldsymbol{\sigma}}$	(4)	$d\rho = M \cdot \left( \frac{1 - J(\mathbf{n})/n_0}{b \cdot L} + \frac{k}{b} \sqrt{\rho} - f \cdot \rho \right) ds_p$	(11)
<u>Accumulated plastic strain</u>		<u>The evolution of twin volume fraction</u>	
$\dot{s}_p = \sqrt{\frac{2}{3}} \ \mathbf{D}_p\ $	(5)	$\dot{F} = F_0 m \left[ 1 - e^{-\beta(s_p - \varepsilon_{\text{init}})} \right]^{m-1} \times$ $\times \left[ -e^{-\beta(s_p^t - \varepsilon_{\text{init}})} \right] [-\beta] \dot{s}_p k_{\text{twin}}$	(12a)
<u>Consistency condition</u>		<u>Length scale of microstructure</u>	
$f = 0, df = 0$	(6)	$\frac{1}{L} = \frac{1}{d} + \frac{1}{2e} \frac{F}{(1-F)}$	(13)
<u>Plastic multiplier</u>		<u>Flux of dislocations arriving at a boundary</u>	
$\gamma = \sqrt{\frac{3}{2}} \dot{s}_p$	(7)	$\overset{\circ}{\mathbf{n}} = \sum_{i=1}^k \frac{\lambda_i}{b} \left( \frac{2}{3} \mathbf{D}_p - \dot{s}_p \frac{\mathbf{n}_i}{n_{0i}} \right)$	(14a)

Figure 2.6.16: Extended TWIP-steel material model.

### 2.6.4 Task 6.3: Transformation of Virtual Lab generated quantities for incorporation in the macroscopic plasticity material model

As described in Section 2.5.3 it was possible to determine the biaxial yield point and to give an estimation concerning the exponent  $m$  auf YDL2000-2D yield function and the corresponding anisotropy parameter. These data were considered for the parameter identification of the macroscopic model. The provision of additional quantities from microstructure simulations, especially the evolution of twin volume fraction for different loading conditions has to be critically considered: Although it was possible to accurately calibrate the development of the twin volume fraction for the case of uniaxial tension (see Figure 2.5.8), additional data to validate the microstructure mode for other load cases were not available in sufficient quality. Thus, it could not be ensured that additional data obtained from the microstructure simulation represent the material behavior in sufficient accuracy. For this reason, not further quantities were transferred from microstructure simulation to the macroscopic material model. It is noted that this decision was not critical for the continuation of the project.



## 2.7 WP7: Algorithmic treatment and numerical implementation of the macroscopic model

Subject of WP7 is the algorithmic treatment and numerical implementation of the macroscopic constitutive model for TWIP-steels, formulated in WP6. DYNAmore has been carrying out the implementation of this material model into LS-DYNA<sup>®</sup>, ESI has performed the implementation into PAM-STAMP<sup>®</sup>.

The following objectives were defined for WP7:

- Algorithmic formulation of the developed macroscopic plasticity model for numerical implementation.
- Numerical implementation of the algorithm for the formulated macroscopic plasticity model in a commercial finite element package for 3-D case (solid formulation); effective error handling and reworking of code for improved efficiency and general purpose usage.
- Numerical implementation of the algorithm for the formulated macroscopic plasticity model in a commercial finite element package for 2-D case (shell formulation); effective error handling and reworking of code for improved efficiency and general purpose usage.
- Preliminary simulations to evaluate the numerical implementation.
- Simulations to validate the model formulation and numerical implementation with a special focus on the evaluation of internal state variables used in the macroscopic model.

In Section 2.7.1, the algorithmic formulation and numerical implementation issues will be described. For results of preliminary simulations, the determination of material parameters for the underlying TWIP-steel grade and validation simulations it is referred to Sections 2.7.2 and 2.7.3.

### 2.7.1 Algorithmic realization and numerical implementation

The TWIP4EU-model, described in Section 2.6.2 had - for first investigations - been realized in combination with the isotropic von Mises yield surface for the 3D (solid) as well as for the 2D (shell) case. The model has then been advanced for anisotropic effects through embedding the TWIP4EU-formulation in the Barlat YLD2000-2D plasticity model [Barlat2003], which is naturally a plane stress (shell) formulation. Some users might be interested in the von Mises based version of the material model, either if they would like to use a solid element discretization (the BarlatYLD2000 model is a 2-dimensional formulation and restricted to shell elements) or if they don't have the possibility to determine the 8 anisotropy material parameters  $\alpha_i$ . For all cases the twinning evolution is formulated and implemented as stress dependent quantity, as described later. For the realization of the 2D-case (shell), see Section 2.7.1.4.

#### 2.7.1.1 Algorithmic realization of the von Mises type formulation:

The nonlinear coupled constitutive equations, see chapter 2.6.2, Figure 2.6.15 are solved in a *predictor-corrector-procedure* considering one time step  $n \rightarrow n + 1$  with incremental variation of the variables:  $(\cdot)^{n+1} = (\cdot)^n + \Delta(\cdot)$ . An additive split of the stain increment  $\Delta\boldsymbol{\varepsilon}$  into elastic ( $\Delta\boldsymbol{\varepsilon}^{el}$ ) and plastic ( $\Delta\boldsymbol{\varepsilon}^{pl}$ ) part is assumed:  $\Delta\boldsymbol{\varepsilon} = \Delta\boldsymbol{\varepsilon}^{el} + \Delta\boldsymbol{\varepsilon}^{pl}$ . In the predictor *trial step* elastic behavior is assumed for the given strain increment, i.e:

$$\boldsymbol{\varepsilon}^{el,n+1,tr} = \boldsymbol{\varepsilon}^{el,n} + \Delta\boldsymbol{\varepsilon}$$

For this assumption the associated deviatoric trial stress is evaluated

$$dev \boldsymbol{\sigma}^{n+1,tr} = \mathbb{C}^{el} : (dev \boldsymbol{\varepsilon}^{el,n} + dev \Delta\boldsymbol{\varepsilon}) = dev \boldsymbol{\sigma}^n + 2\mu dev \Delta\boldsymbol{\varepsilon}$$

leading to a trial relative stress:

$$\boldsymbol{\xi}^{n+1,tr} = dev \boldsymbol{\sigma}^{n+1,tr} - \boldsymbol{X}^n$$

Then it is tested, whether the trial state is valid, i.e. the assumption of an elastic step is true, evaluating the yield condition.

$$f^{n+1,tr} = \sqrt{\xi^{n+1,tr} : \xi^{n+1,tr}} - \sqrt{2/3} (\sigma_{y,0} + \sigma_f^n)$$

If the yield condition is fulfilled, i.e. if  $f^{n+1,tr} \leq 0$  is true, the current strain increment is indeed an elastic step and thus the trial stress state is the real stress state and the history variables remain unchanged, as there are the plastic strains  $s$ , the twin volume fraction  $F$ , the stored dislocation density  $\rho$  and the number of stopped dislocations  $\mathbf{n}$ .

$$\boldsymbol{\sigma}^{n+1} = \boldsymbol{\sigma}^{tr,n+1}$$

$$s^{pl,n+1} = s^{pl,n}, F^{n+1} = F^n, \rho^{n+1} = \rho^n, \mathbf{n}^{n+1} = \mathbf{n}^n$$

Does, however, the trial state breach the yield condition, the corrector step, a *return projection* of the stress state onto the yield surface is necessary. To this, the nonlinear coupled material equations have to be solved for the real plastic strain increment, and accordingly for the new history variables and the actual stress state.

The deviatoric stresses are given by

$$dev\boldsymbol{\sigma}^{n+1} = dev\boldsymbol{\sigma}^{n+1,tr} - 2\mu \Delta\gamma \mathbf{N}^{n+1}$$

and the relative stress can be evaluated by:

$$\begin{aligned} \boldsymbol{\xi}^{n+1} &= dev\boldsymbol{\sigma}^{n+1} - \mathbf{X}^{n+1} = dev\boldsymbol{\sigma}^{n+1,tr} - 2\mu \Delta\gamma \mathbf{N}^{n+1} - (\mathbf{X}^n + \Delta\mathbf{X}) \\ &= \boldsymbol{\xi}^{n+1,tr} - 2\mu \Delta\gamma \mathbf{N}^{n+1} - \Delta\mathbf{X} \end{aligned}$$

Following the notes of [Simo & Hughes 1998] the current normal to the yield surface can be evaluated from the known trial relative stress by

$$\mathbf{N}^{n+1} = \boldsymbol{\xi}^{n+1,tr} / \|\boldsymbol{\xi}^{n+1,tr}\| = \text{known}$$

and the norm of relative stress is given by

$$\|\boldsymbol{\xi}^{n+1}\| = \|\boldsymbol{\xi}^{n+1,tr}\| - 2\mu \Delta\gamma - \|\Delta\mathbf{X}\|$$

Insertion into the yield condition leads to one nonlinear equation for this case, which can be solved for the plastic multiplier  $\Delta\gamma$ :

$$\begin{aligned} f^{n+1} &= \|\boldsymbol{\xi}^{n+1}\| - \sqrt{2/3} (\sigma_{y,0} + \sigma_{yf}) = \|\boldsymbol{\xi}^{n+1,tr}\| - 2\mu \Delta\gamma - \|\Delta\mathbf{X}(\Delta\gamma)\| - \sqrt{2/3} (\sigma_{y,0} + \sigma_f(\Delta\gamma)) \\ &= 0 \end{aligned}$$

From the plastic multiplier  $\Delta\gamma$  the actual stress state can be evaluated and the internal history variables: Number of stopped dislocations  $\mathbf{n}^{n+1}$ , twin volume fraction  $F^{n+1}$ , stored dislocation density  $\rho^{n+1}$  and internal length scale  $L^{n+1}$  can be updated, as well as the plastic strain  $s^{pl,n+1} = s^{pl,n} + \Delta s^{pl}$ .

This predictor-corrector procedure is summarized in Figures 2.7.1 and 2.7.2. Herein,  $b$  denotes the burgers vector,  $k$  the forest hardening parameter,  $n_0$  the threshold number of stopped dislocation,  $\lambda$  the mean space between slip bands,  $F_0$  the maximum twin volume fraction,  $\beta$  a fitting coefficient,  $\varepsilon^{init}$  the threshold strain, from which twinning begins,  $d$  the grain size,  $e$  the twin mean thickness,  $M$  the Taylor factor,  $\mu$  the shear modulus and  $\alpha$  a fitting material constant, and the material parameter  $m$  is related to the stacking fault energy.

trial step at time $t^{n+1}$ :		$\Delta \varepsilon^{el} = \Delta \varepsilon$
➤ 1 <sup>st</sup> evaluate trial stress:	$dev \sigma^{tr} = dev \sigma^n + 2\mu dev \Delta \varepsilon$	
	$\xi^{tr} = dev \sigma^{tr} - X^n$	
➤ 2 <sup>nd</sup> check yield condition:	$f^{tr} = \sqrt{\xi^{tr} : \xi^{tr}} - \sqrt{2/3} (\sigma_{y,0} + \sigma_f^n)$	
➤ A) if yield condition fulfilled ( $f^{tr} \leq 0$ ):		
	$dev \sigma^{n+1} = dev \sigma^{tr}$	stress
	$s^{pl,n+1} = s^{pl,n}$	history
	$F^{n+1} = F^n, \rho^{n+1} = \rho^n, \mathbf{n}^{n+1} = \mathbf{n}^n$	
	exit	
➤ B) else if $f^{tr} > 0$ : goto radial return		

Figure 2.7.1: Elastic trial step for the TWIP4EU von Mises based material model.

radial return at time $t^{n+1}$ :	
stress:	$\sigma = \sigma^{tr} - 2\mu \Delta \gamma N$
hardening:	$\sigma_f = \alpha M \mu b \sqrt{\rho + \Delta \rho(\Delta \gamma)}$
	$X = M \mu b \left( \frac{\mathbf{n}(\Delta \gamma)}{L(\Delta \gamma)} \right)$
internal variables:	$\Delta \rho = M \left( \frac{1 - \frac{\sqrt{3} \ \mathbf{n}^n\ }{n_0}}{b L^n} + \frac{k}{b} \sqrt{\rho^n} - f \rho^n \right) \sqrt{\frac{2}{3}} \Delta \gamma$
	$\Delta \mathbf{n} = \frac{\lambda}{b} \left( \frac{2}{3} \Delta \gamma N^{n+1} - \sqrt{\frac{2}{3}} \Delta \gamma \frac{\ \mathbf{n}^n\ }{n_0} \mathbf{n}^n \right)$
	$\Delta \frac{1}{L} = \frac{\Delta F((\Delta \gamma))}{2e(1 - F^n)^2}$
➤ 1 <sup>st</sup> solve yield condition for $\Delta \gamma$ :	$f = \ dev \sigma(\Delta \gamma) - X(\Delta \gamma)\  - \sqrt{\frac{2}{3}} (\sigma_{y,0} + \sigma_f(\Delta \gamma)) = 0 \rightarrow \Delta \gamma$
➤ 2 <sup>nd</sup> update stress and history using equations above	
➤ 3 <sup>rd</sup> exit	

Figure 2.7.2: Radial return for the TWIP4EU von Mises based material model.

### 2.7.1.2 Algorithmic realization within the Barlat - YLD2000 formulation:

Alternatively, the TWIP4EU- model was integrated in the Barlat - YLD2000 yield condition. The anisotropic effects of TWIP-steel sheets can thus be captured precisely through 9 additional material parameters.

Starting point for the algorithmic realization of the material model for TWIP-steel is the Barlat YLD2000 yield condition (see [Barlat et al. 2003]), that reads:

$$f = \sigma_{eff} (s_{xx} - 2X_{xx} - X_{yy}, s_{yy} - 2X_{yy} - X_{xx}, s_{xy} - X_{xy}) - (\sigma_{y0} + \sigma_{yf}) \leq 0$$

The effective stress is hereby defined as:

$$\sigma_{eff} = \left( \frac{1}{2}(\Phi' + \Phi'') \right)^{1/M}$$

with

$$\Phi' = |X'_1 - X'_2|^M \quad \text{and} \quad \Phi'' = |2X''_1 + X'_2|^M + |X''_1 + 2X'_2|^M.$$

The exponent M is a material parameter, depending on the crystal structure, see for example [Banabic 2010]. For TWIP-steel M=8.0 is recommended due to its FCC (Face Centered Cubic) crystal structure. The stress eigenvalues for the determination of the effective stress are given by:

$$X'_1 = \frac{1}{2} \left( X'_{11} + X'_{22} + \sqrt{(X'_{11} - X'_{22})^2 + 4(X'_{12})^2} \right)$$

$$X'_2 = \frac{1}{2} \left( X'_{11} + X'_{22} - \sqrt{(X'_{11} - X'_{22})^2 + 4(X'_{12})^2} \right)$$

$$X''_1 = \frac{1}{2} \left( X''_{11} + X''_{22} + \sqrt{(X''_{11} - X''_{22})^2 + 4(X''_{12})^2} \right)$$

$$X''_2 = \frac{1}{2} \left( X''_{11} + X''_{22} - \sqrt{(X''_{11} - X''_{22})^2 + 4(X''_{12})^2} \right)$$

$$X''_1 = \begin{bmatrix} X'_{11} \\ X'_{22} \\ X'_{12} \end{bmatrix} = \begin{bmatrix} L'_{11} & L'_{12} & 0 \\ L'_{21} & L'_{22} & 0 \\ 0 & 0 & L'_{33} \end{bmatrix} \begin{bmatrix} \xi_{xx} \\ \xi_{yy} \\ \xi_{xy} \end{bmatrix} \quad \text{and} \quad \begin{bmatrix} X''_{11} \\ X''_{22} \\ X''_{12} \end{bmatrix} = \begin{bmatrix} L''_{11} & L''_{12} & 0 \\ L''_{21} & L''_{22} & 0 \\ 0 & 0 & L''_{33} \end{bmatrix} \begin{bmatrix} \xi_{xx} \\ \xi_{yy} \\ \xi_{xy} \end{bmatrix}$$

The matrix  $L$  contains 10 material parameters and the vector  $\xi = dev \sigma - X$  denotes the relative stress, i.e. the deviatoric stress  $s := dev \sigma$  minus the back stress  $X$ . These 10 material parameters can be reduced to 8 independent material parameters  $\alpha_i$  through:

$$\begin{pmatrix} L'_{11} \\ L'_{12} \\ L'_{21} \\ L'_{22} \\ L'_{33} \end{pmatrix} = \frac{1}{3} \begin{pmatrix} 2 & 0 & 0 \\ -1 & 0 & 0 \\ 0 & -1 & 0 \\ 0 & 2 & 0 \\ 0 & 0 & 3 \end{pmatrix} \begin{bmatrix} \alpha_1 \\ \alpha_2 \\ \alpha_7 \end{bmatrix} \quad \begin{pmatrix} L''_{11} \\ L''_{12} \\ L''_{21} \\ L''_{22} \\ L''_{33} \end{pmatrix} = \frac{1}{9} \begin{pmatrix} -2 & 2 & 8 & -2 & 0 \\ 1 & -4 & -4 & 4 & 0 \\ 4 & -4 & -4 & 1 & 0 \\ -2 & 8 & 2 & -2 & 0 \\ 0 & 0 & 0 & 0 & 9 \end{pmatrix} \begin{bmatrix} \alpha_3 \\ \alpha_4 \\ \alpha_5 \\ \alpha_6 \\ \alpha_8 \end{bmatrix}$$

The anisotropic yield surface is thus determined by those remaining 8 material parameters  $\alpha_i$  in addition to the exponent M.

In the following, the implementation of the extended Bouaziz hardening model in combination with the Barlat YLD2000 yield condition is described.

The constitutive model is formulated for plane stress applications (stress component  $\Delta\sigma_{33} = 0$ ). It is assumed, that the related unknown out-of-plane strain increment  $\Delta\varepsilon_{33}$ , that fulfills the plane stress condition, is determined, described in section 2.7.1.4.

Within a time step and for a given strain increment  $\Delta\varepsilon$ , the constitutive equations are – as for the von Mises implementation – solved iteratively by a “elastic-predictor”– “plastic-corrector” scheme. An associated flow rule is used, i.e. the plastic strain is normal to the yield surface:  $\Delta\varepsilon^{pl} = \sqrt{3/2} \Delta s^{pl} N$ .

$N$  denotes the normal to the yield surface and  $\Delta s^{pl}$  is the plastic multiplier, which serves as primary variable. In the following, the index k denotes the iteration counter. Every time step starts with the initialization of the plastic multiplier  $\Delta s^{pl,k=0} = 0$  and the history variables (internal variables), as there are the number of stopped dislocations  $n^{n+1,k=0} = n^n$ , the geometrical internal length scale  $L^{n+1,k=0} = L^n$ , the twin volume fraction  $F^{n+1,k=0} = F^n$  and the dislocation density  $\rho^{n+1,k=0} = \rho^n$ .

With these initialized values the trial step is realized by assuming elastic behavior, i.e.  $\Delta\boldsymbol{\varepsilon}^{pl} = \mathbf{0}$ ; and the trial deviatoric stress increment  $\Delta\mathbf{s}^{tr}$ , the trial back stress increment  $\Delta\mathbf{X}^{tr} = \mathbf{0}$  and the trial isotropic hardening  $\sigma_{yf}^{tr} = \sigma_{yf}^n$  and thus the trial Barlat yield function  $f^{tr}$  (as given above) are evaluated for this assumption, see Figure 2.7.3. For the case, the trial yield function fulfills the yield condition, i.e.  $f^{tr} \leq 0$ , the current time step is indeed an elastic step: The trial stresses are the real stresses ( $\Delta\boldsymbol{\sigma} = \Delta\boldsymbol{\sigma}^{tr}$ ) and the history variables don't change.

Initialization at time $t^{n+1}$ :			
history:	$\mathbf{n}^{n+1,k=0} = \mathbf{n}^n$	$F^{n+1,k=0} = F^n$	$\rho^{n+1,k=0} = \rho^n$
trial step at time $t^{n+1}$ : $\Delta\boldsymbol{\varepsilon} = \Delta\boldsymbol{\varepsilon}^{el}$			
➤ 1 <sup>st</sup> evaluate deviatoric trial stress:	$\mathbf{s}^{tr} = \mathbf{s}^n + 2\mu \text{dev}\Delta\boldsymbol{\varepsilon}$		
relative trial stress:	$\boldsymbol{\xi}^{tr} = \mathbf{s}^{tr} - \mathbf{X}^n$		
➤ 2 <sup>nd</sup> check yield condition:	$f^{tr} = \sigma_{eff}(\boldsymbol{\xi}^{tr}) - (\sigma_{y0} + \sigma_{yf})$		
➤ A) if yield condition fulfilled ( $f^{tr} \leq 0$ ):			
	$\mathbf{s}^{n+1} = \mathbf{s}^{tr}$		stress
	$\Delta s^{pl,n+1} = \Delta s^{pl,n}$		plastic multiplier
	$F^{n+1} = F^n, \rho^{n+1} = \rho^n, \mathbf{n}^{n+1} = \mathbf{n}^n$		history
	exit		
➤ B) else if $f^{tr} > 0$ : goto return mapping			

**Figure 2.7.3:** Initialization and trial step for the TWIP4EU-Barlat-YLD2000-2D version.

For the case, the trial yield function violates the yield condition, i.e. for  $f^{tr} > 0$  an iterative stress return map is performed. For this, the increments or residual changes respectively of the internal variables, following from the continuous equations given in chapter 2.6, are listed, with the material parameters described above for the von Mises implementation.

Increments / residual changes of the internal variables:

$$\text{Dislocation density:} \quad \Delta\rho = M \left( \frac{1 - n_{eff}/n_0}{bL} + \frac{k}{b} \sqrt{\varrho} - f\varrho \right) \Delta s^{pl} \quad (1)$$

$$\text{Number of stopped dislocations: } \Delta\mathbf{n} = \lambda/b \left( \frac{2}{3} \Delta\boldsymbol{\varepsilon}^{pl} - \mathbf{n}/n_0 \Delta s^{pl} \right) \quad (2)$$

$$\begin{aligned} \text{Twin volume fraction:} \quad \Delta F &= \frac{\partial F}{\partial s^{pl}} \Delta s^{pl} \quad (3) \\ &= m\beta F_0 e^{-\beta(s^{pl} - \varepsilon^{init})} \left( 1 - e^{-\beta(s^{pl} - \varepsilon^{init})} \right)^{m-1} \Delta s^{pl} \end{aligned}$$

### 2.7.1.3 Effect of stress triaxiality dependent twinning

From the experimental results under uniaxial tension, shear and biaxial loading, it could be observed, that twinning and thus the hardening of TWIP-steels seems to be dependent on the loading situation: More pronounced twinning and thus more pronounced hardening can be observed for stress states with increasing triaxiality. For being able to capture this observed effect within the simulation, the twin volume evolution equation has been enhanced by the factor  $k_{TWIN}$ , in order to have the possibility, to account for stress dependent twinning effects, see Section 2.6.2:

$$\text{New formulation for twin volume fraction: } \Delta F = \frac{\partial F}{\partial s^{pl}} \Delta s^{pl} k_{TWIN} \quad (4)$$

An initial assumption for the implementation was a linear dependence of the factor  $k_{TWIN}$  on the triaxiality (case 1) for the simulation of the tensile tests, the bulge test and the nakajima test, all of them with positive triaxiality. The drawback if this simple assumption is that the factor  $k_{TWIN}$  can become negative for lower triaxialities, depending on the chosen value for the slope  $m_t$ . It seems to be more plausible to define a symmetric function for  $k_{TWIN}$ . Case 2 allows defining a symmetric tension-compression behavior for the factor  $k_{TWIN}$ . By consideration of case 3 it is possible to define a trilinear dependence of  $k_{TWIN}$  as a function of the triaxiality. Further, case 3 allows for values  $m_t$  larger than 3.0 without receiving negative values for  $k_{TWIN}$  for triaxialities varying from 0.0 to 0.333. The three different cases are illustrated in Figure 2.7.4.

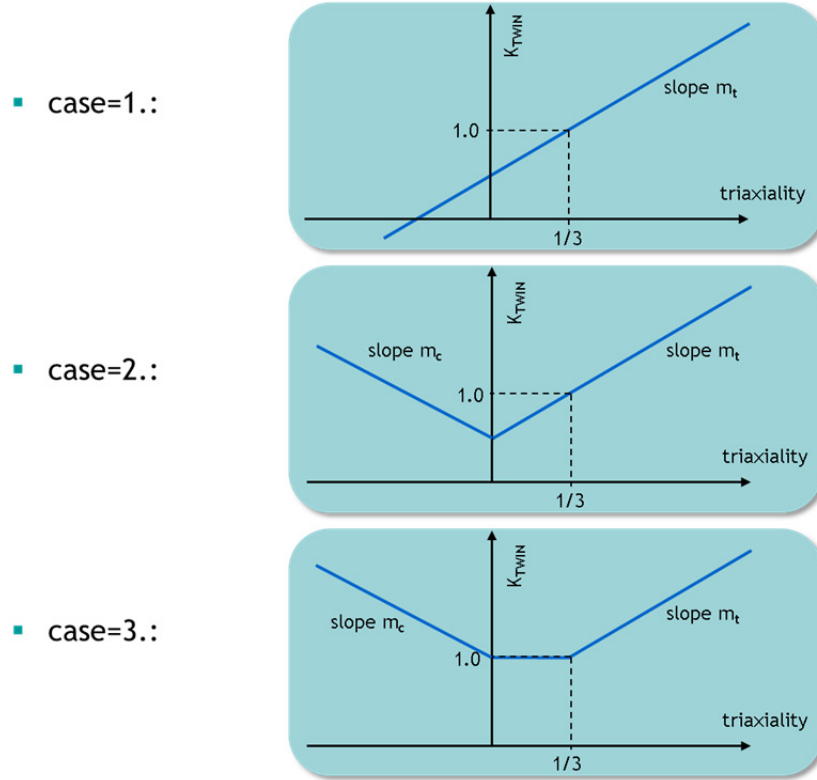


**Figure 2.7.4:** Implemented versions for stress state dependent twinning.

The internal length scale  $L$  – a characteristic measure for the microstructure - is given by

$$\frac{1}{L} = \frac{1}{d} + \frac{F}{2e(1-F)}. \quad (5)$$

The internal micromechanical motivated variables are updated by  $(\cdot)^{k+1} = (\cdot)^k + \Delta(\cdot)$  and they control the back stress through:

$$\mathbf{X} = M \frac{\mu b}{L} \mathbf{n} \quad (6)$$

and the isotropic hardening through:

$$\sigma_{yf} = \alpha M \mu b \sqrt{\bar{\rho}}. \quad (7)$$

The stress return algorithm (see Figure 2.7.5) is based on the iterative solution of the nonlinear yield condition  $f = 0$ , with residual update of the internal history variables until an appropriate convergence criterion is met. The converged stress state and the updated history variables are stored.

The aforementioned ability to account for triaxiality dependent twinning has been implemented in the von Mises based TWIP4EU-Model as well.



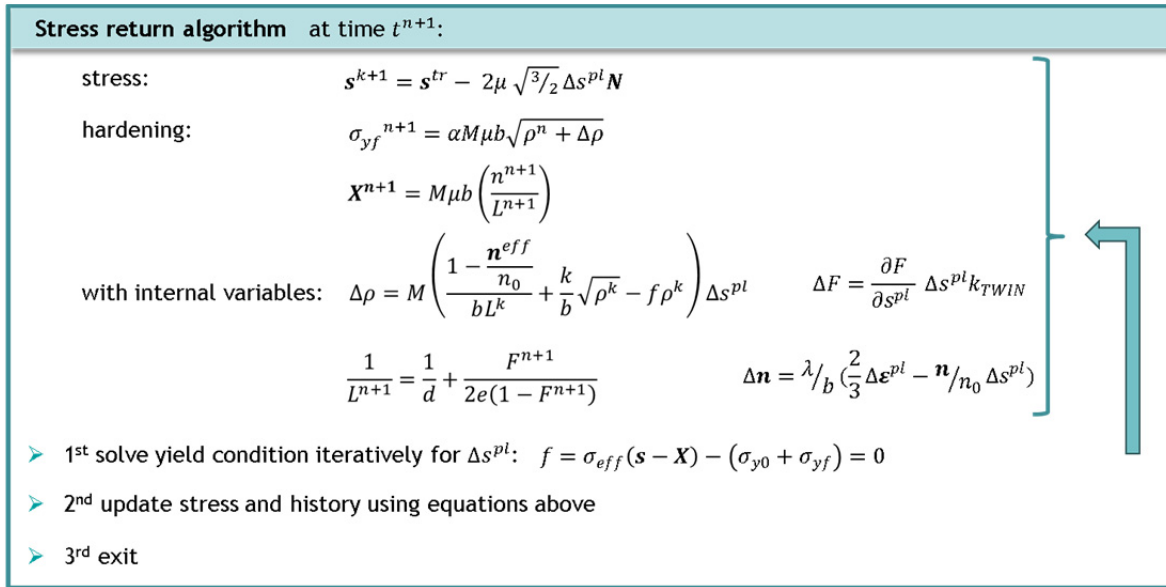


**Figure 2.7.5:** Stress return algorithm for the TWIP4EU-Barlat-YLD2000 version.

### 2.7.1.4 Numerical implementation 2D

The plane stress assumption is typically introduced in the analysis of bodies, in which one of the dimensions (the thickness) is much smaller than the others and is subjected to loads that generate dominant stresses perpendicular to the thickness direction, as for example thin sheets as they are under investigation within this project. In practice, shell elements are usually used for sheet metal forming simulation. For this reason, it is necessary to numerically implement the algorithm for the formulated macroscopic elasto-plasticity model for the 2-D case, i.e. for a plane stress shell formulation. This implementation was realized for both LS-DYNA<sup>®</sup> and PAM-STAMP<sup>®</sup>.

The concept is, to constrain the original 3-dimensional constitutive equation in order to obtain its plane stress counterpart. Only the in-plane and out-of-plane shear strain components are known (given) in the 3-dimensional equation and the plane stress constraint is used as an additional condition to determine the in-plane stresses and the out-of-plane strain. One possibility is to use the original 3-dimensional predictor / return mapping algorithm and introduce an outer iteration loop to find the appropriate out-of-plane component of the strain increment  $\Delta \varepsilon_{zz}$ , which is appropriate to the plane stress constraint

$$\sigma_{zz}^{n+1} = 0$$

This iterative approach is realized in LS-DYNA<sup>®</sup> for the TWIP-steel material model and described in Figure 2.7.6.

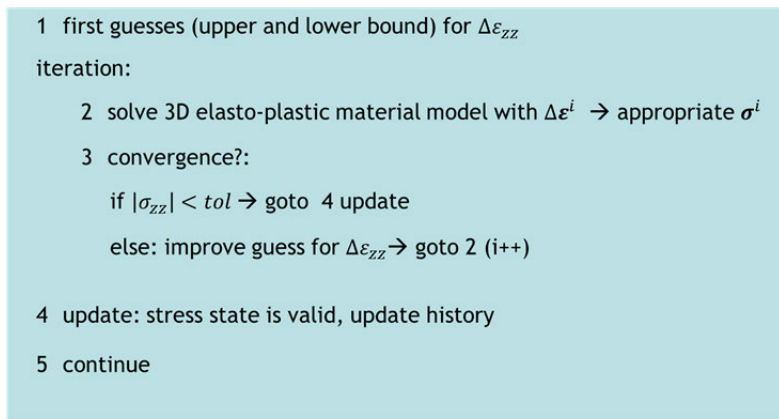


**Figure 2.7.6:** Iterative procedure for the plane stress condensation of the constitutive law

Another possibility is to add the constraint equation for the out-of-plane-stress component

$$\sigma_{zz}^{n+1} = 0$$

to the system of return-mapping equations and the out-of-plane component of the strain increment  $\Delta\varepsilon_{zz}$  becomes a new unknown of the system. I.e. the original 3-dimensional elastic-predictor / return mapping algorithm has to be modified, leading to an augmented algebraic system of equations. This 2D radial return is realized in PAM-STAMP<sup>®</sup> for the TWIP-steel material model. Hereby, the integration of the constitutive equations is made under the plane stress assumption. At every time the plane stress equation has to be complied:

$$\sigma_{zz} = 0$$

The trial stress  $\boldsymbol{\sigma}^{tr,n+1}$  is calculated by treating the total strain increment as elastic:

$$\boldsymbol{\sigma}^{tr,n+1} = \boldsymbol{\sigma}^n + \mathbf{A} : \Delta\boldsymbol{\varepsilon}$$

where  $\mathbf{A}$  is the elasticity tensor under the plane stress assumption, see for example [de Souza 2008]. From the additive decomposition of strain rate tensor into an elastic part and a plastic part, the stress tensor is written as:

$$\boldsymbol{\sigma}^{n+1} = \boldsymbol{\sigma}^{tr,n+1} - \Delta s^{pl} \mathbf{A} : \left\{ \frac{\partial f}{\partial \boldsymbol{\sigma}} \right\}_t$$

Herby  $f$  denotes the yield function. Under the plane stress assumption, the yield function definition is taken as  $f = f(\xi_{xx}, \xi_{yy}, \xi_{xy}, \sigma_f)$  with  $\boldsymbol{\xi} = \boldsymbol{\sigma} - \mathbf{X}$  being the effective stress.  $\left\{ \frac{\partial f}{\partial \boldsymbol{\sigma}} \right\}_{t^n}$  is the plastic flow direction evaluated at the time  $t^n$  and  $\Delta s^{pl}$  the equivalent plastic strain increment. This equivalent plastic strain increment  $\Delta s^{pl}$  can be seen as the main unknown. Indeed, if knowing its value, we can deduce all values of the variables involved in the constitutive equations at the time  $t^{n+1}$ . First we can calculate the dislocation density increment  $\Delta\rho$  and the “dislocation loops” increment  $\Delta\mathbf{n}$ :

$$\Delta\rho = \left\{ \frac{d\rho}{ds_p} \right\}_{t^n} \Delta s^{pl}$$

$$\Delta\mathbf{n} = \left\{ \frac{2\lambda}{3b} \frac{\partial f}{\partial \boldsymbol{\sigma}} - \frac{\lambda}{bn_o} \mathbf{n} \right\}_{t^n} \Delta s^{pl}$$

Where:  $\left\{ \frac{d\rho}{ds_p} \right\}_t$  is the derivative of the dislocation density with respect to the equivalent plastic strain evaluated at the time  $t^n$ . Its expression is directly given by the model.  $\left\{ \frac{2\lambda}{3b} \frac{\partial f}{\partial \boldsymbol{\sigma}} - \frac{\lambda}{bn_o} \mathbf{n} \right\}_{t^n}$  is the “flow direction” of the tensor  $\mathbf{n}$  evaluated at the time  $t^n$ . Its expression is given by the evolution law of  $\mathbf{n}$ : in which the plastic strain rate has been substituted by its expression coming from the plastic flow equation.

Then one can update:

$$s^{pl,n+1} = s^{pl,n} + \Delta s^{pl}$$

$$\rho^{n+1} = \rho^n + \Delta\rho$$

$$\mathbf{n}^{n+1} = \mathbf{n}^n + \Delta\mathbf{n}$$

$$\sigma_f^{n+1} = \alpha M \mu b \sqrt{\rho^{n+1}}$$

$$\mathbf{X}^{n+1} = M \mu b \frac{\mathbf{n}^{n+1}}{L(s^{pl,n+1})}$$

where  $L$  is the characteristic length of the material which can be seen as a function of  $s^{pl}$ . The yield condition written at the time  $t^{n+1}$ . leads to an equation with one unknown  $\Delta s^{pl}$

$$f(\Delta s^{pl}) = 0 .$$

## 2.7.2 Preliminary simulations

Several preliminary simulations to assess the numerical implementation of the macroscopic elastoplastic constitutive model for TWIP-steel have been performed, starting from one-element tests in order to study the behavior under monotonic and cyclic uniaxial loading, pure shear, biaxial loading and for a changing loading path. For these simulations, the material parameters published in [Bouaziz 2011] have been used. And concurrently the accordance of the simulation results between the implementations in LS-DYNA and PAM-STAMP has been controlled.

### 2.7.2.1 Comparison with 1d monotonous hardening model for TWIP-steel of [Bouaziz 2011]

By means of a one-dimensional monotonic tensile loading test, the results of the 1-dimensional hardening model for TWIP-steel of [Bouaziz 2011] and of the 3D cyclic TWIP4EU model, that is based on the 1-D Bouaziz model, are compared.

For that purpose the results, published by [Bouaziz 2011] for the true stress – true strain behavior in a one-dimensional monotonic tensile test, are compared to simulation results with the implemented 3D material model in the von Mises based version, using just one solid element, see Figure 2.7.7. The material parameters for this study are given in [Bouaziz 2011].

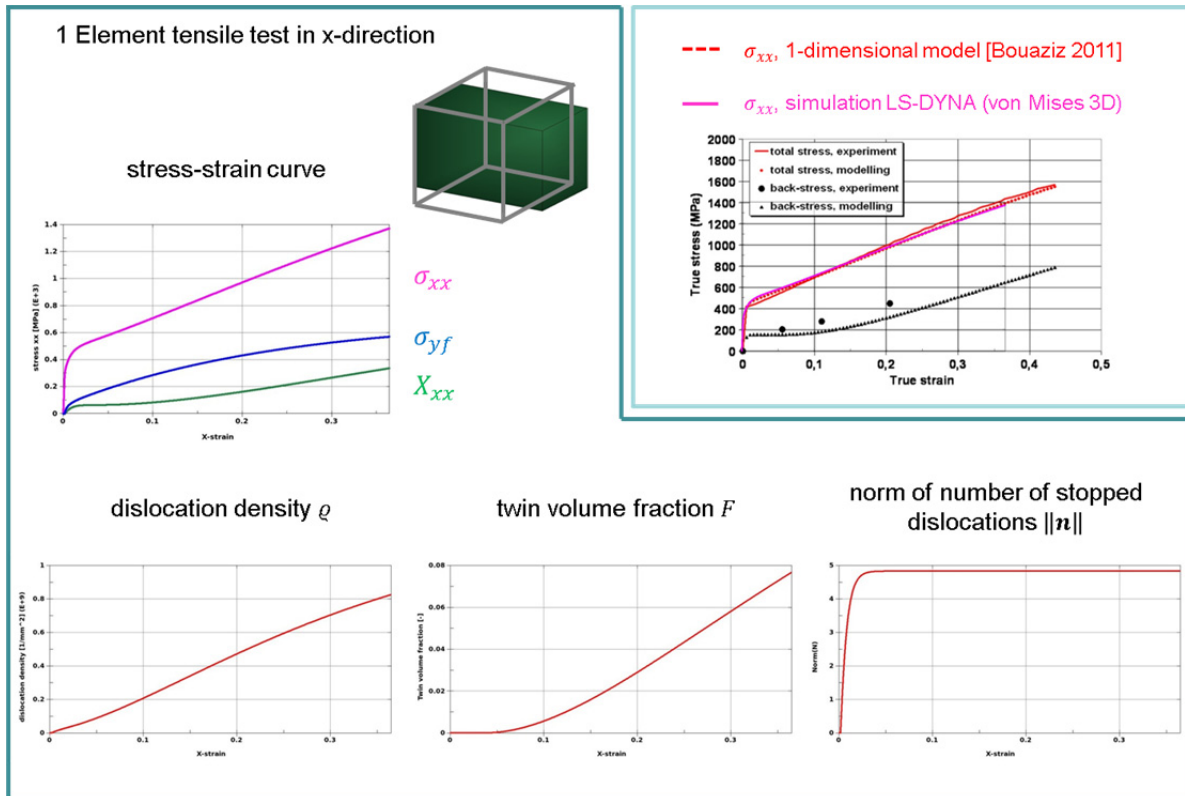


**Figure 2.7.7:** Stress-strain behavior in tensile test: 1D-hardening model Bouaziz vs. 3D-von Mises based TWIP4EU implementation in LS-DYNA (top right), and evolution of internal variables (below).

It should be noted, that - in contrast to the TWIP4EU model – [Bouaziz 2011] does not take elastic strains into account but on the other hand splits the plastic deformation into a contribution due to dislocation glide and one due to twinning. Therefore no exact accordance is expected between the models but very close results. And, indeed, the differences between the hardening curve of [Bouaziz 2011] and the TWIP4EU-simulation results are very small, see Figure 2.7.7 top right.

### 2.7.2.2 Comparison between implementation in PAM-Stamp and LS-DYNA by means of the 90° tensile test conducted by KIMAB

For a further comparison of the implementations in PAM-STAMP and LS-DYNA of the von Mises based 3D (solid) TWIP4EU material model, the results for the 90° tensile test of KIMAB have been used. The material parameters, that are given in Table 2.7.1 are in this case fitted to this 90° tensile test

(as the von Mises based version is isotropic), i.e. they do not comply the final hardening parameters. In Figure 2.7.8, the load-displacement results of the simulations with both codes, an Abaqus test implementation and the experimental results are contrasted. The load-displacement curves show a good agreement between the three implementations in different codes.

Material parameters for the TWIP alloy Fe-15%Mn-0.7%C-2.5%Al-2.5%Si (SCT 2014 paper)			
Notation	Value	Unit	Physical meaning
$E$	175000,8	MPa	Young's Modulus
$\nu$	0,3		Poisson's Ratio
Density	7,85E-09	tonne/mm <sup>3</sup>	Material density
$\mu$	67308	MPa	Shear modulus
$b$	2,50E-07	mm	Burgers vector
$M$	3,06		Taylor factor
$\alpha$	0,25		Mean dislocation strength parameter
$k$	0,028		Forest (latent) hardening parameter
$f$	2,7		Parameter of dynamic recovery of dislocations
$\Lambda$	3,17E-04	mm	Mean spacing between slip bands
$F_0$	0,15		Maximum volume fraction of twins
$e$	2,20E-05	mm	Twin mean thickness
$\varepsilon_{init}$	0,00E+00		The critical strain at which twinning begins
$\beta$	2,5		Fitting coefficient
$m$	1,81		Parameter of stacking fault energy (SFE)
wt%C		%	C content
wt%Mn		%	Mn content
$d$	3,00E-03	mm	Grain size
$\rho_0$	0,00E+00	mm <sup>-2</sup>	The initial dislocation density
$\sigma_0$	530	MPa	The initial yield radius
$n_0$	5,4		The maximum number of dislocation loops at the boundaries

**Table 2.7.1:** Test version of material parameters for Fe-15%Mn-0.7%C-2.5%Al-2.5%Si TWIP-steel.

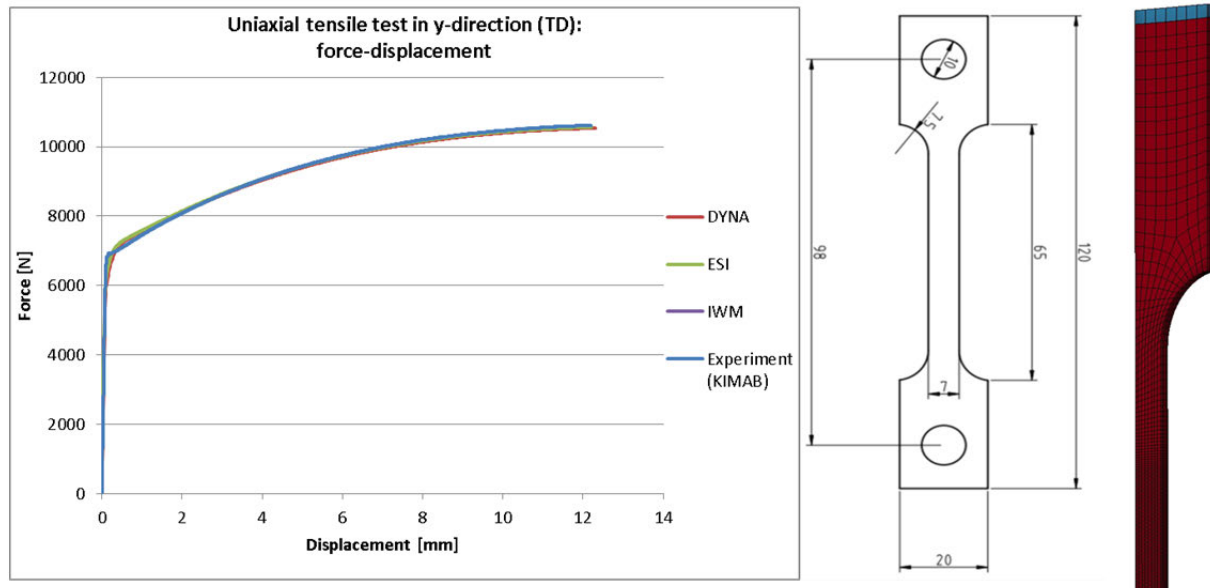


**Figure 2.7.8:** Load-displacement curve 90°-tensile test (left): Experimental results vs. TWIP4EU-model implemented in LS-DYNA (red), implemented in PAM-STAMP (green), IWM-Abaqus implementation (violet), geometry (middle), discretization of an eighth of the specimen with solid elements (right).

### 2.7.2.3 Implementation test of the Barlat YLD2000 version of the TWIP4EU model on basis of the shear test performed by KIMAB

In order to test the implementation of the Barlat YLD2000 based TWIP4EU-model, the shear test, experimentally performed by KIMAB, has been simulated with the BarlatYLD2000-2D based implementation on the one hand and with the von Mises based (2D-) implementation on the other hand. For following choice of the anisotropy material parameters:  $\alpha_i = 1.0$  and exponent  $M=2.0$ , the formulation of the Barlat YLD2000-2D yield surface coincides with the von Mises yield surface. I.e. we expect the same system response of both models for this choice. Thereby no triaxiality dependence is taken into account, i.e.  $m_c=m_t=0.0$ , as this simulations just serve as an implementation test. The specimen has been discretized with under-integrated stabilized 4-noded shell elements and 5 integration points over the sheet thickness of 1.5mm. The material parameters, listed in Table 2.7.1, have been used. In Figure 2.7.9 the load – relative-displacement responses of the shear test are shown: The simulation results of the von Mises based TWIP4EU-model (in 2D) and the Barlat YLD2000-2D based TWIP4EU-model agree with each other for this special choice of anisotropy material parameters, just the way it should be. And, in addition, there's a good correlation of the simulation results with the experimental results.

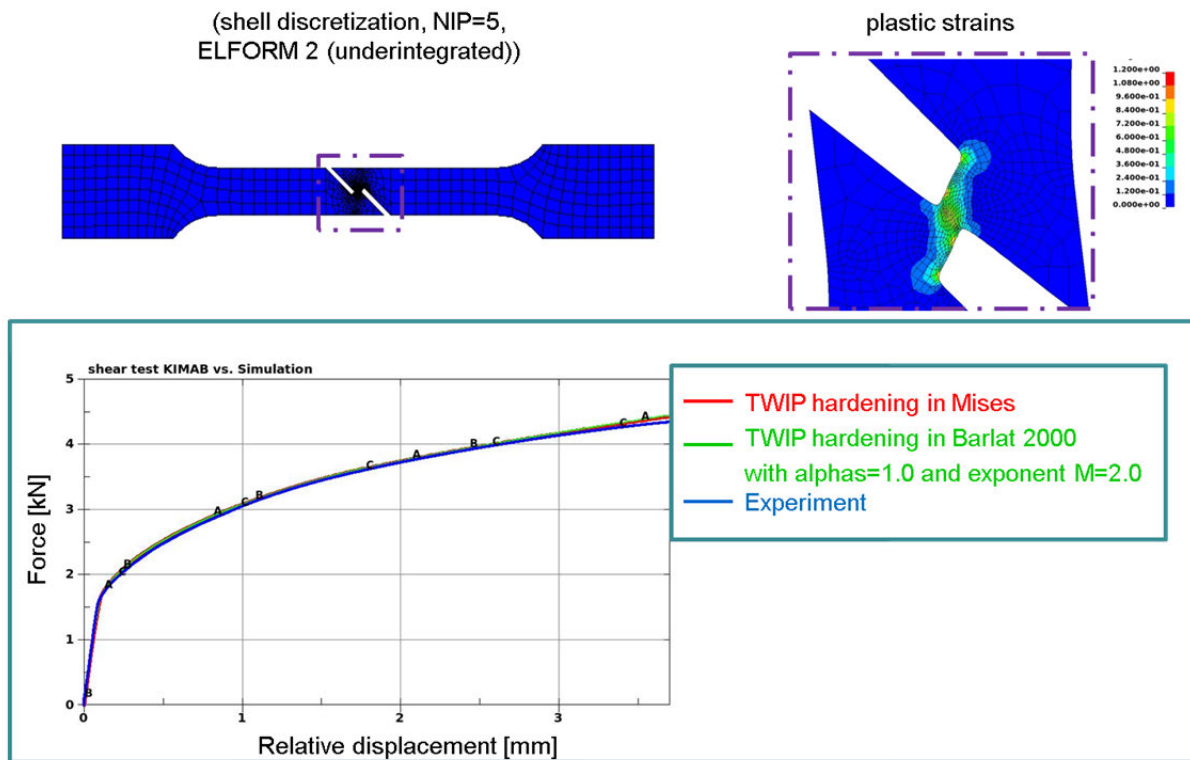


**Figure 2.7.9:** Shear Test (KIMAB): Load-relative Displacement curve experimental results vs. TWIP4EU-Model implemented in LS-DYNA: von Mises version vs. Barlat YLD2000-2D version.

### 2.7.2.4 Comparison between simulation with 3D-solids and 2D-shells

By means of a tensile test, simulation results using the 3D and 2D shell implementation for the TWIP4EU constitutive model are compared. The isotropic von Mises model was used since it is available for both formulations. The tensile specimen is discretized with solid elements on the one hand and shell elements on the other hand, see Figure 2.7.10.

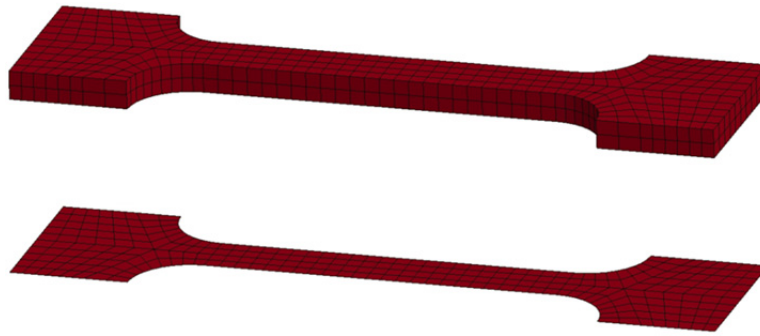


**Figure 2.7.10:** Solid vs. shell discretization of a tensile test

The simulations show a good agreement, as can be seen from the deformations, distribution of plastic strain (Figure 2.7.11) and the system response (see Figure 2.7.12). As reference, the load displacement curve obtained from the MAT24 models is added in Figure 2.7.12. Here, a simple isotropic material model with a tabulated flow curve of the TWIP-steels material was used. The load-displacement curves of the 2D (shell)- and the 3D (solid)- simulation fit until the point of proportional elongation. The difference in the load-displacement curve in Figure 2.7.12 after the point of proportional elongation can be explained by the use of different element formulations.

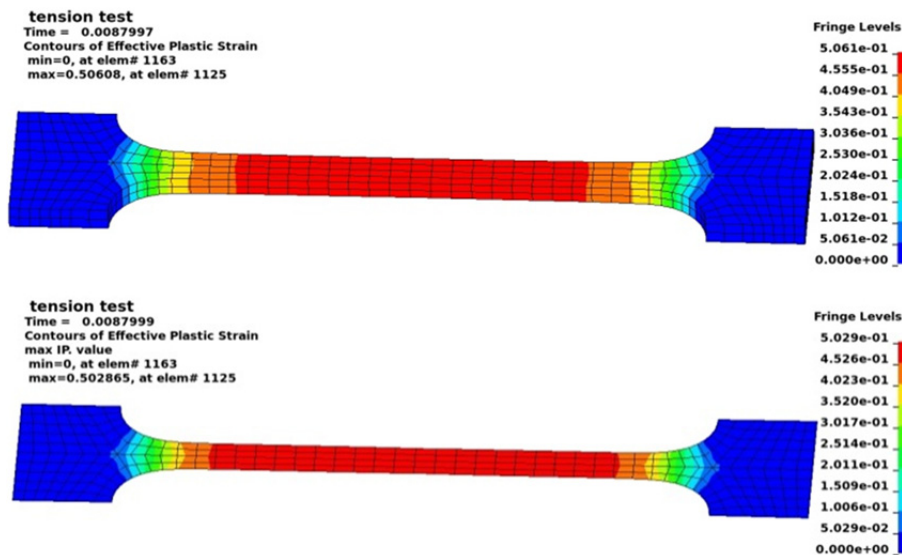


**Figure 2.7.11:** Deformed tensile specimen and equivalent plastic strain: Solid vs. shell formulation

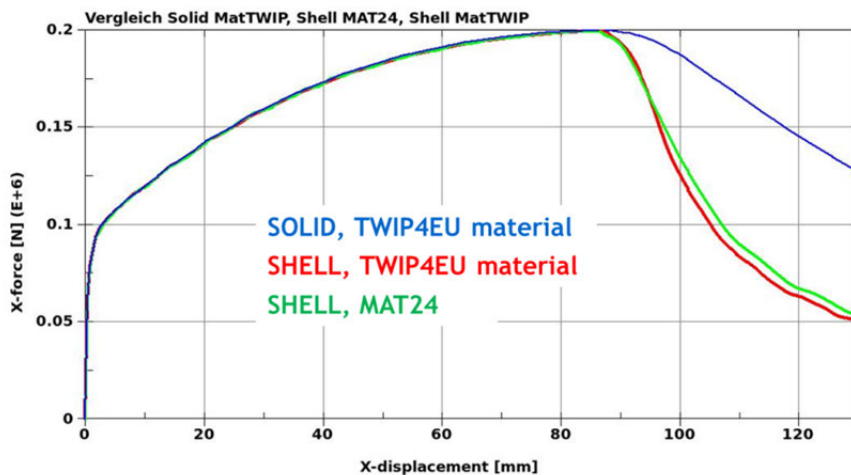


**Figure 2.7.12:** Load-Displacement curve solid vs. shell



### 2.7.3 Validation of the numerical model

Precise material parameters for the TWIP-steel grade Fe-15%Mn-0.7%C-2.5%Al-2.5%Si have been determined. The hardening material parameters, describing the onset of yielding as well as the isotropic and kinematic hardening behavior, were found by optimization of the stress-strain behavior of the 0°-tensile test results under monotonous loading, varying the appropriate material parameters. The resulting elastic and hardening material parameters are given in Table 2.7.2. For the 0°-tensile test, anisotropy parameters as well as the triaxiality dependence don't influence the results. These parameters will be defined in Section 2.8.

Notation	Value	Unit	Physical meaning
$E$	175000	MPa	Young's Modulus
$\nu$	0,3	---	Poisson's Ratio
Density	7,40E-09	ton/mm <sup>3</sup>	Material density
$\mu$	67307,6923	MPa	Shear modulus
$b$	2,50E-07	mm	Burgers vector
$M$	3,06	---	Taylor factor
$\alpha$	0,296	---	Mean dislocation strength parameter
$k$	0,03	---	Forest (latent) hardening parameter
$f$	1,295	---	Parameter of dynamic recovery of dislocations
$\lambda$	3,17E-04	mm	Mean spacing between slip bands
$F_0$	0,36	---	Maximum volume fraction of twins
$e$	2,20E-05	mm	Twin mean thickness
$\epsilon_{init}$	0,00E+00	---	The critical strain at which twinning begins
$\beta$	2,26	---	Fitting coefficient
$m$	1,95	---	Parameter of stacking fault energy (SFE)
$d$	3,00E-03	mm	Grain size
$\rho_0$	0,00E+00	mm <sup>-2</sup>	The initial dislocation density
$\sigma_0$	592,14	MPa	The initial yield radius
$n_0$	1	---	The max. number of dislocation loops at the boundaries
$m_t$	t.b.d.	---	Slope of $k_{TWIN}$ -function in tension
$m_c$	t.b.d.	---	Slope of $k_{TWIN}$ -function in compression
case	t.b.d.	---	Selection of stress dependent hardening case (1 - 3)

**Table 2.7.2:** Elastic and hardening material parameters for Fe-15%Mn-0.7%C-2.5%Al-2.5%Si TWIP-steel for the first validation of the TWIP4EU model.

The material model parameters (see Section 2.6.2) have been fitted in order to describe as accurately as possible the experimental results for this steel. The calibration procedure was done carefully in order to have the correct order of magnitude given by the physical basis for each parameter.

#### 2.7.3.1 Fit of twin volume fraction

Evolution of twin volume fraction was used as a fitted material function due to amount of available and expected experimental data. Twinning evolution function (Equation 2.6.13) originally presented in [Bouaziz2011] was fitted to the TEM experimental data from a uniaxial tensile test, see Section 2.3.2, using MS EXCEL Solver by varying the values of  $b$ ,  $e_{init}$ ,  $m$ , and  $F_0$ . Figure 2.7.13 shows the comparison between the experimental data and the results obtained from the TWIP4EU-model.

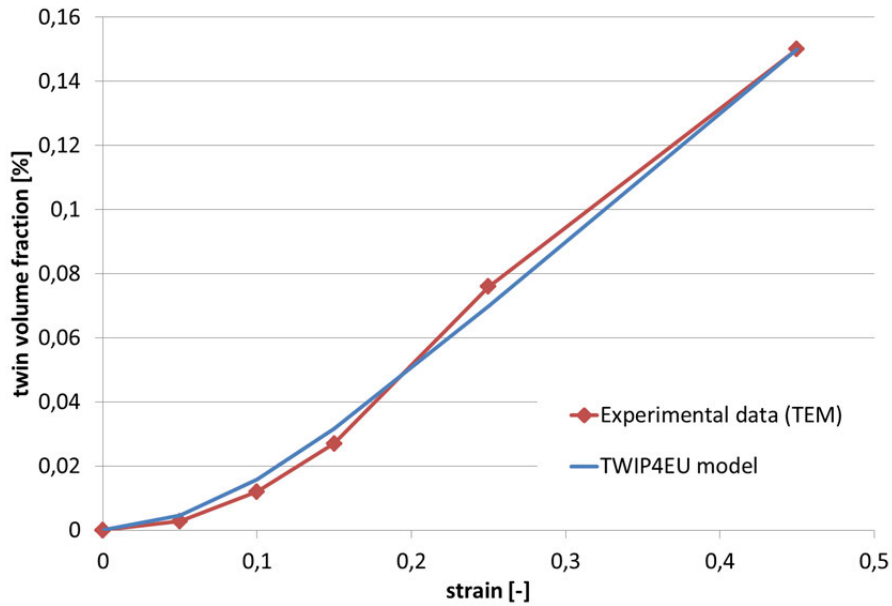


**Figure 2.7.13:** Twinning evolution of the considered TWIP-steel under uniaxial tension. The experimental data correspond to the data given in Table 2.3.2

### 2.7.3.2 Tensile tests in 0° with respect to rolling direction

For the simulation of the tensile tests, the structure has been discretized by under-integrated hourglass stabilized shell elements with 5 integration points over the thickness, see Figure 2.7.14. The material parameters are given in Table 2.7.2.



**Figure 2.7.14:** Numerical model for the simulation of the tensile test. Discretization of the specimen with shell elements, an element size of 1 mm was used.

The resulting stress strain curve shown in Figure 2.7.15 is in good agreement with the experimental data as well as with a commercially available standard model. Thus, the parameter set given in Table 2.7.2 is able to describe the micromechanical base twinning behavior and also the macroscopic stress-strain curve for uniaxial tension.

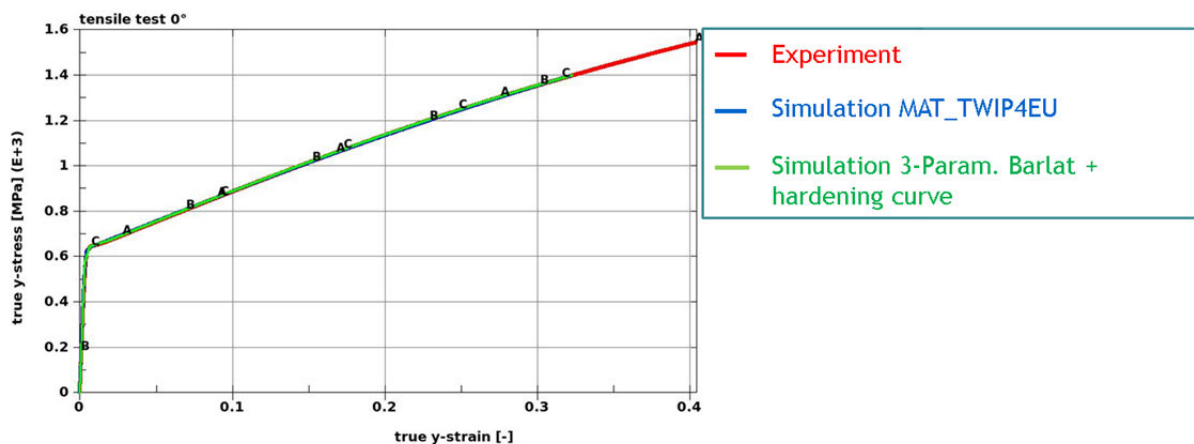


**Figure 2.7.15:** Tensile test 0°: Stress-strain behavior: Experimental vs. simulation results (TWIP4EU-model based and 3-Parameter Barlat in combination with a hardening curve).

### 2.7.3.3 Bulge test – hardening behavior

The bulge test, described in Section 2.4.1.3, may be used to calibrate the implemented TWIP4EU-material model with stress dependent twinning, and to fit the stress dependence parameter  $m_t$ . To this end, test simulations under biaxial loading have been performed for varying stress dependence parameter  $m_t$ . Figure 2.7.15 shows the experimental results for the hardening behavior in the bulge test, and corresponding simulation results. As described in Section 2.6.2, the stress depended hardening scales the uniaxial flow curve as a function of the stress state. Since the biaxial flow curve is more curved than the uniaxial flow curve, it is difficult to exactly fit the biaxial flow curve. The best fit to the experimental results is found for  $m_t$  in the range of 3.0 - 4.0. It becomes clear that the flow curve will be underestimated if the stress dependent hardening is omitted. For a more detailed discussion of the bulge test and the evaluation of major and minor strains it is referred to chapter 2.8.3.1.

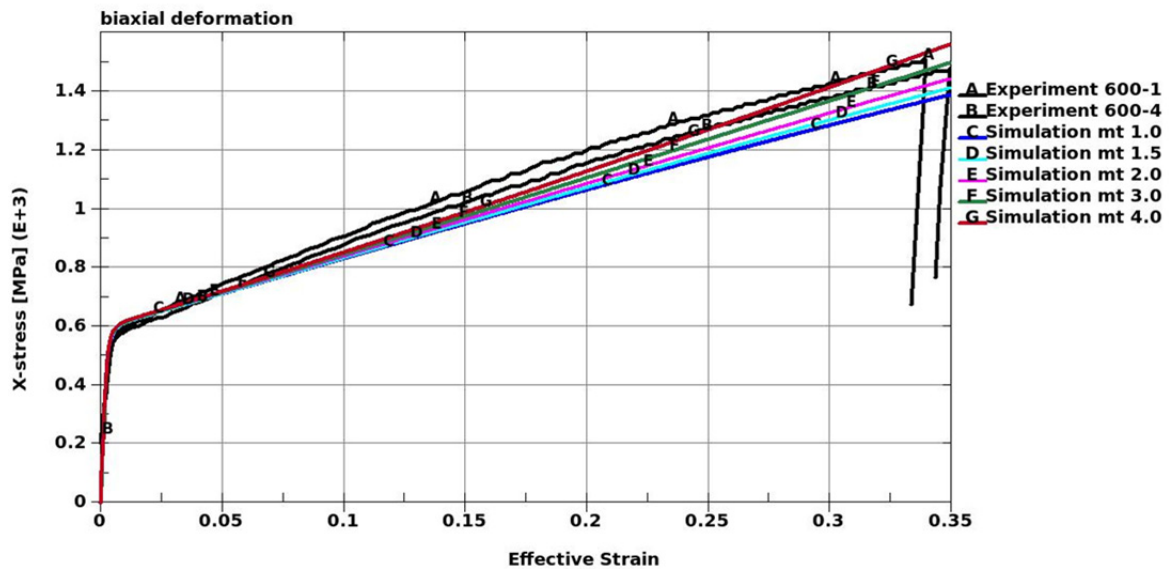


**Figure 2.7.16:** Biaxial flow curve of bulge test vs. TWIP4EU-model hardening curve under biaxial loading for varying stress dependence parameters  $m_t$ .

The first comparisons between numerical results and experimental data are in good agreement. It shows the principle applicability of the TWIP4EU model with respect to monotonic hardening, stress dependent hardening and representation of microstructural quantities. A more detailed evaluation of the model under consideration of typical forming experiments will be given in Section 2.8.2.

## 2.8 WP8: Simulation of forming experiments and validation of the constitutive formulation

The main objective of this work package is the validation of the developed material model by means of comparison of simulation models results to the experimental tests results. The experiments are described in Section 2.4 and provide a wide database of raw data, which have to be further evaluated and thus compared with the results of the simulation models. The objectives of this WP are summarized as follows:

- Transfer of raw data obtained from forming experiments in WP 4 and evaluation of local strain distribution using optical strain analysis tools
- Comprehensive evaluation of the capability of the formulated constitutive model by simulation of the forming experiments performed in WP4
- Comparison and validation of the predicted numerical results with experimental investigations
- Formulation of guidelines for usage of the new constitutive framework for forming simulations

### 2.8.1 Evaluation of local strain distributions from forming experiments using optical measurements

The test specimens obtained from simple forming experiments performed in tasks 4.1, 4.2 and 4.3 will be considered to evaluate the local strain distribution using optical strain analysis tools. The results from the Nakajima specimen, the bulge test and the square cup drawing will be compared with the numerical simulation using the software SVIEW. This allows a 3D comparison of the geometry and the strain distribution. Since this type of comparison is very time consuming it cannot be done for every single modification of the numerical model or set of material parameter. For this, section cuts through the specimen in two perpendicular directions are made for frequently needed comparisons.

#### 2.8.1.1 Preparing the sheets for optical measurement

The forming experiments as well as the forming of the prototype were documented using the optical strain measurement system ARGUS. It was found that the standard chemistry for the electrolytic dot pattern does not work for the surface of the TWIP-steel since the achievable contrast of the dots is not sufficient. By using a laser beam the contrast of the dots can significantly be improved, see the right hand side of Figure 2.8.1. Here the dots are not black; they have a white metallic appearance. Depending on the beam intensity whitish dots are applied that can optically be analyzed.

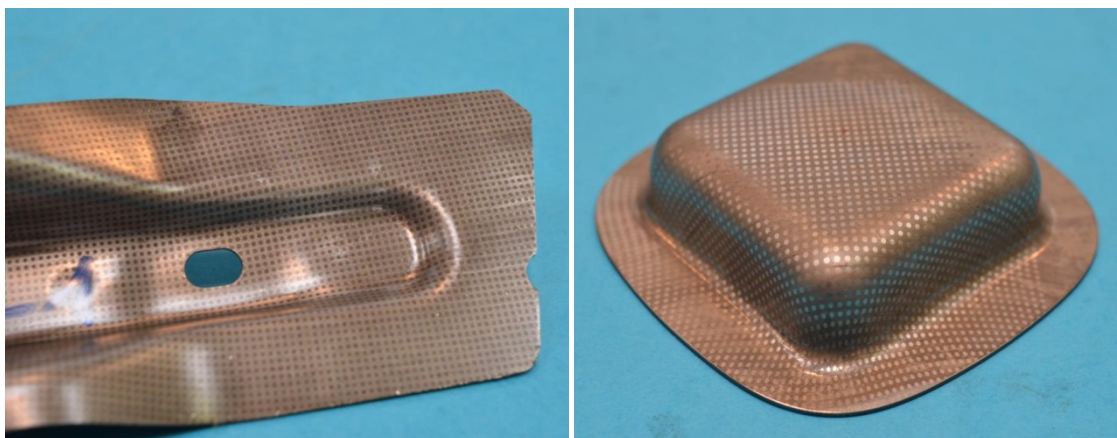
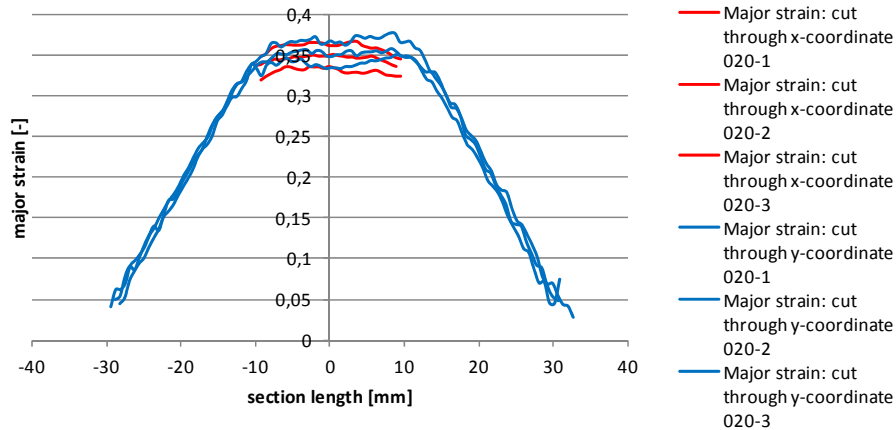


**Figure 2.8.1:** Specimen with an electrochemically etched pattern (left). Improved pattern with laser beam applied (right).

### 2.8.1.2 Strain data from Nakajima-Specimens

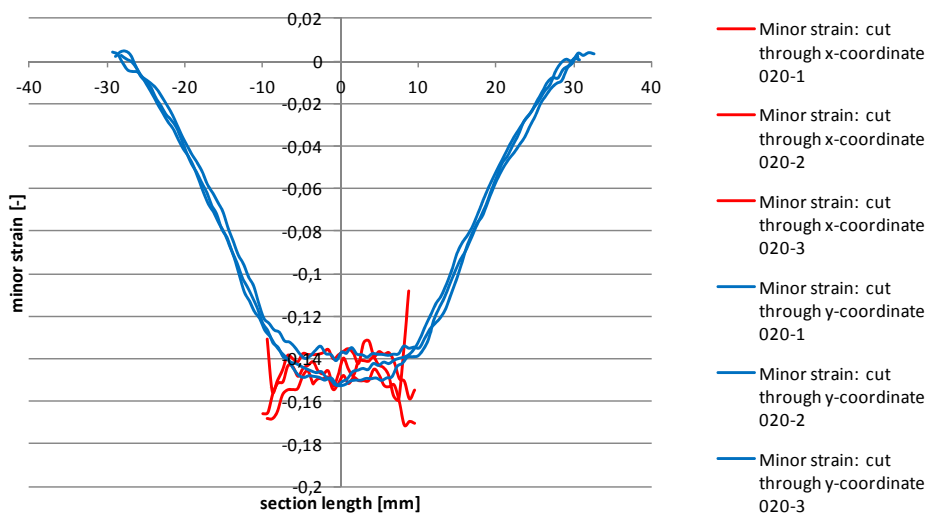
The major and minor strains were printed in a single diagram. The y direction is always the long side of the specimen and parallel to the rolling direction. The x direction stands for the short side of the specimen and is perpendicular to the rolling direction.

Figure 2.8.2 documents the major strains in the narrow Nakajima specimen with a width of 20 mm. The corresponding minor strains are shown in Figure 2.8.3. The strains in both diagrams are typical for a uniaxial loading of the specimens.



**Figure 2.8.2:** Major strain data from section cut of 20 mm Nakajima specimen

At the edges of the specimen the optical measurement system generates a big scattering. This is a result of an improper drawn mask for zone on the specimen that is used for the strain calculation. In these areas the pixels from the background lead to non-physical results.



**Figure 2.8.3:** Minor strain data from section cut of 20 mm Nakajima specimen

The results from the Nakajima specimen with widths of 130 mm are shown in Figures 2.8.4 and 2.8.5. The middle of the specimen has lower strains due to friction than the lateral areas.

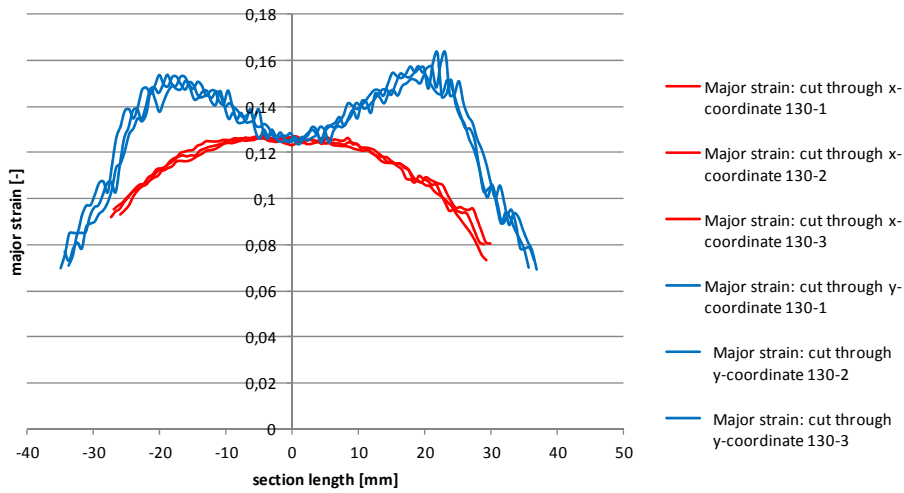


**Figure 2.8.4:** Major strain data from section cut of 130 mm Nakajima specimen

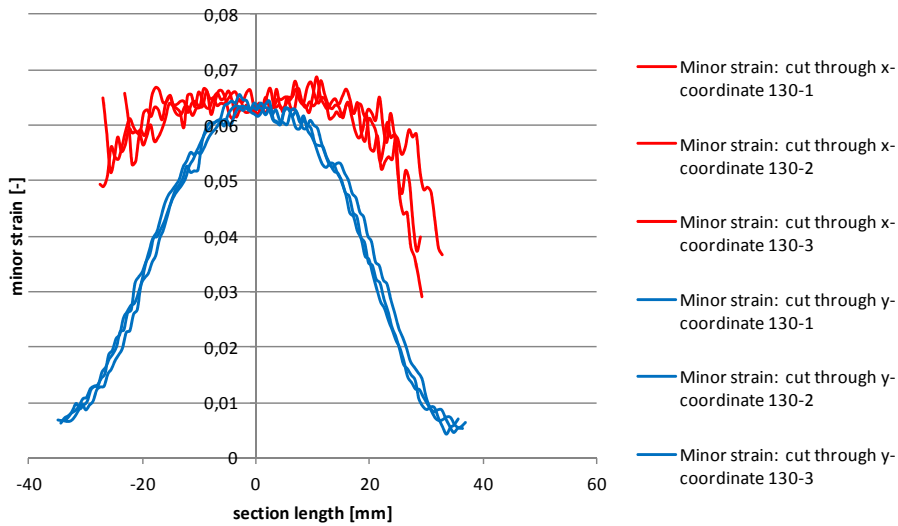


**Figure 2.8.5:** Minor strain data from section cut of 130 mm Nakajima specimen

This effect is also visible at the result of the stretch forming specimen. The major strains are shown in Figure 2.8.6 and the minor strains in Figure 2.8.7.

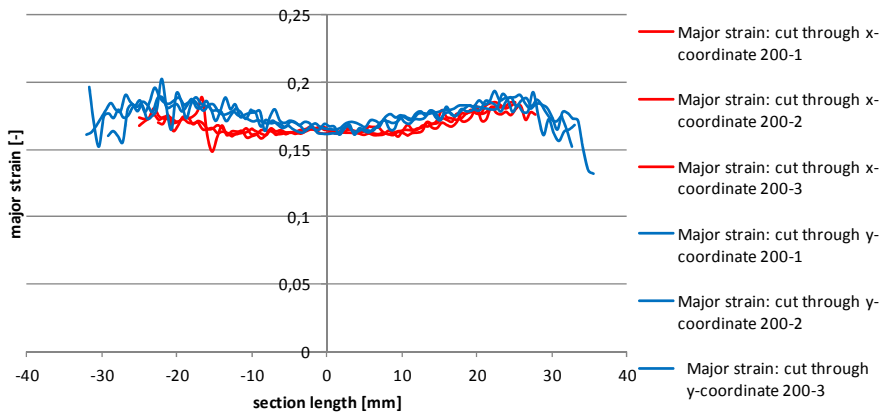


**Figure 2.8.6:** Major strain data from section cut of 200 mm Nakajima specimen



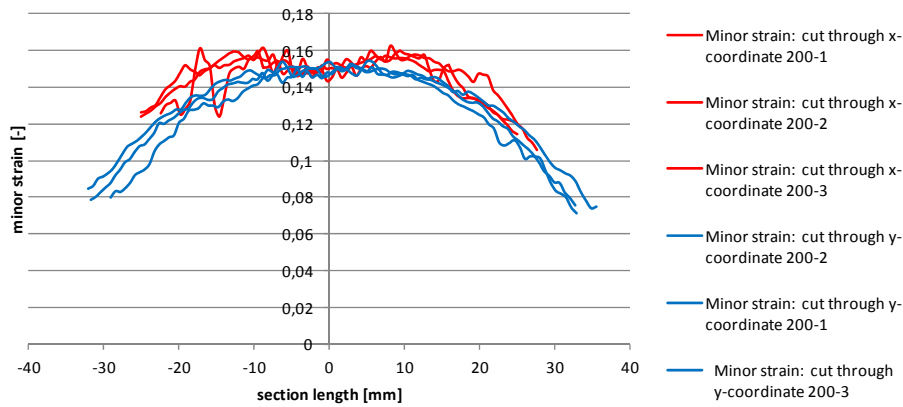


**Figure 2.8.7:** Minor strain data from section cut of 200 mm Nakajima specimen

### 2.8.1.3 Strain data from bulge test

The advantage of the bulge test is that no friction has to be considered. The pressure displacement curves of the dome are already shown in Figure 2.4.9. The scattering of these curves is very low. As described in Section 2.4.2.1, the maximum pressure was limited by the experimental set-up. The corresponding results from the Aramis strain analysis are plotted in Figure 2.8.8.

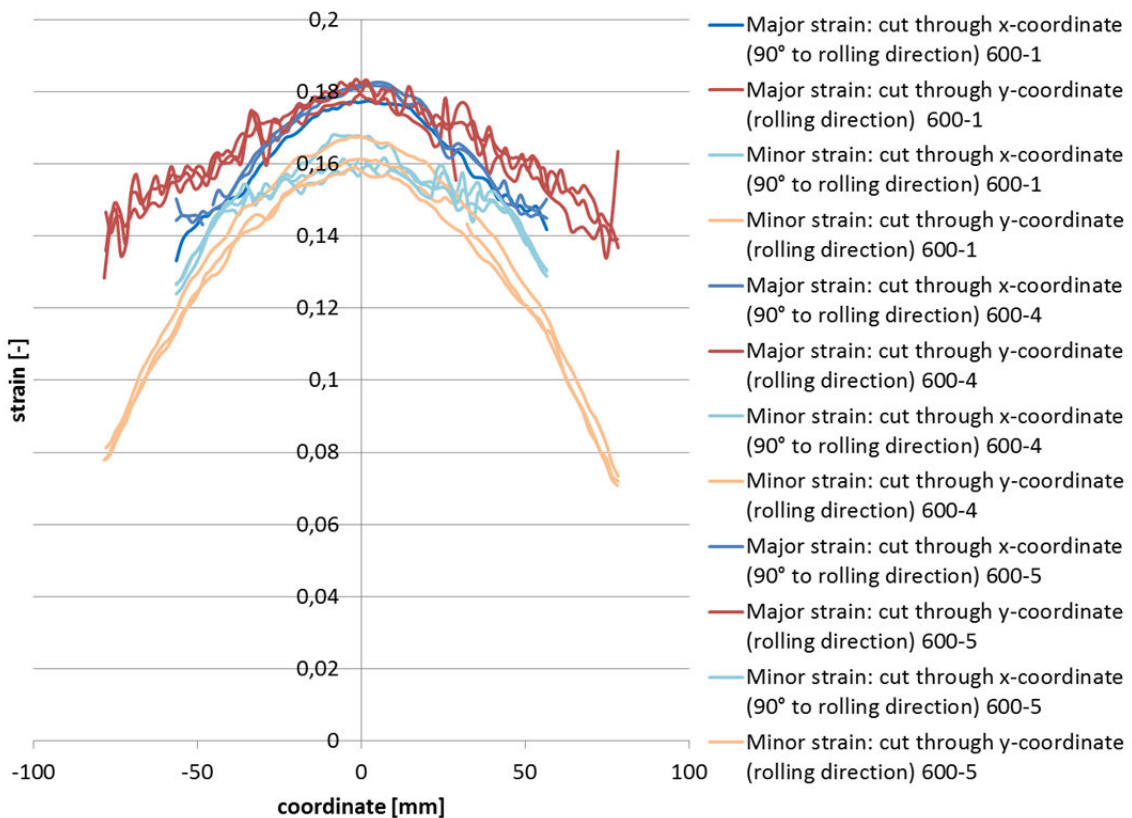


**Figure 2.8.8:** Major and minor strains of the bulge test performed with 240 bar

The major and minor strains are not on the same level. This means that the material reacts on a equibiaxial loading with an anisotropic deformation. At lower pressures this effect is not visible. It starts with some delay at higher strain. This strain dependent effect can also be seen in Figure 2.4.16. Here minor and major strains in the centre of the dome were analysed during the whole test.

### 2.8.1.4 Strain data from square cup forming experiment

The Nakajima specimen and the bulge tests should provide data for more or less defined monotonic strain states. To complete the experiments, square cups were formed to account for a deep drawing strain state and also with a more complex geometry. To provide different strain levels, cups with a drawing depth of 20, 40 and 60 mm were formed, see Section 2.4.4.3. The square cups were also analysed with an optical strain measurement system and the strain on section cuts were plotted. Figure 2.8.9 shows the strains of the flattest cup. The increase of drawing depth from 20 to 40 mm the strains also grow which can be seen in Figure 2.8.10, Fig. 2.8.11 shows the strains of the cup with the highest drawing depth.

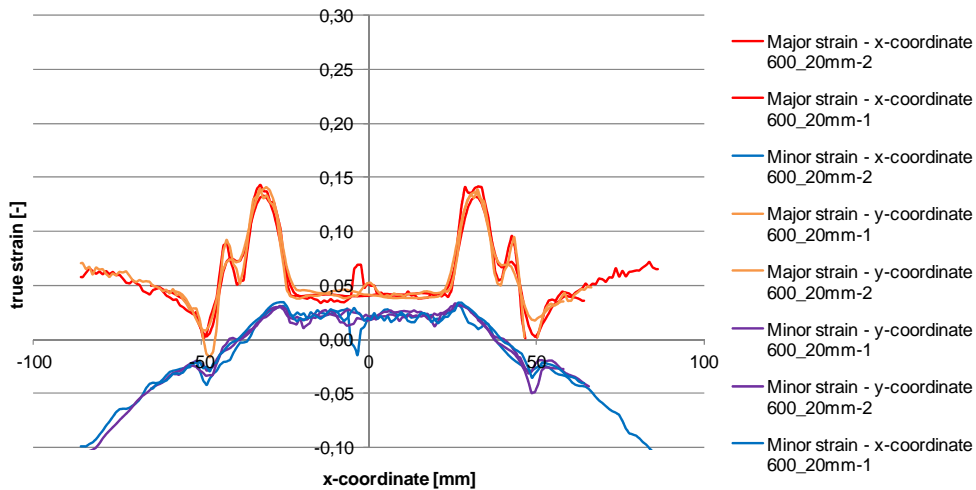


Figure 2.8.9: Major and minor strain of the square cup with 20 mm drawing depth

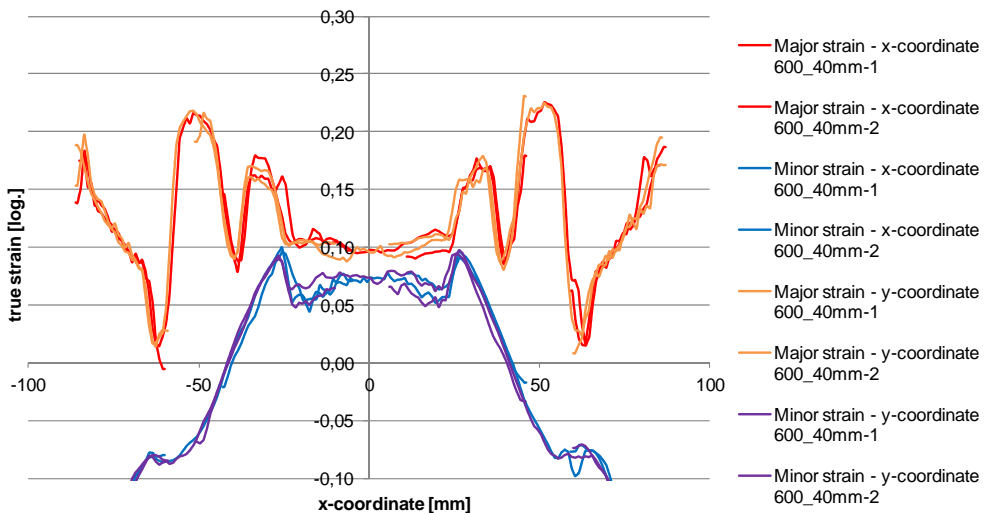


Figure 2.8.10: Major and minor strain of the square cup with 40 mm drawing depth

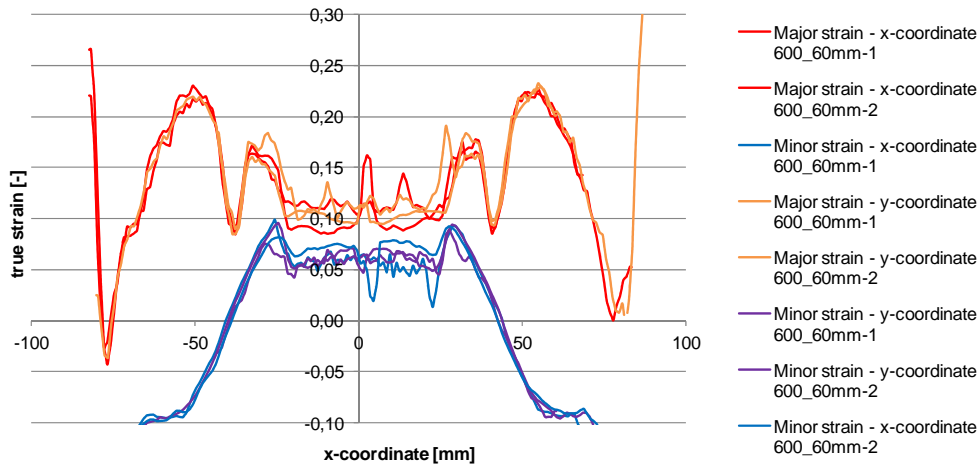


Figure 2.8.11: Major and minor strain of the square cup with 60 mm drawing depth

## 2.8.2 Simulation of experimentally evaluated forming processes and comparison with data obtained by simulation

The following forming experiments were considered to evaluate the TWIP4EU model: Tensile test, bulge test, Nakajima test and cup drawing test. The final parameters are given in Table 2.8.1. For comparison, the results from a simulation using a standard material model are also shown. The details of the used standard model (uniaxial flow curve + Hill48 yield locus) were given in Section 2.6.1.1.

### 2.8.2.1 Tensile test

For the simulation of the tensile tests, the specimen has been discretized by under-integrated hourglass stabilized shell elements with 5 integration points over the thickness. An element size of 1 mm was used. In Figure 2.8.12 – Figure 2.8.14 the true stress - true strain curves are shown in the three different directions with respect to the rolling direction. Since the tensile curve in rolling direction was used to adjust the hardening behavior, both models give a very good agreement. For the two other directions, the standard model gives a less accurate prediction of the experimental data. This is a well-known effect when this model is used: Using the flow curve in rolling direction and the three Lankford coefficients in 0, 45 and 90 degree for determination of the anisotropy parameter can lead to some deviations in the flow curve in 45 and 90 degree. Due to the more flexible description of the anisotropy of the TWIP4EU model, it can accurately describe the true stress - true strain curves in all three considered directions.

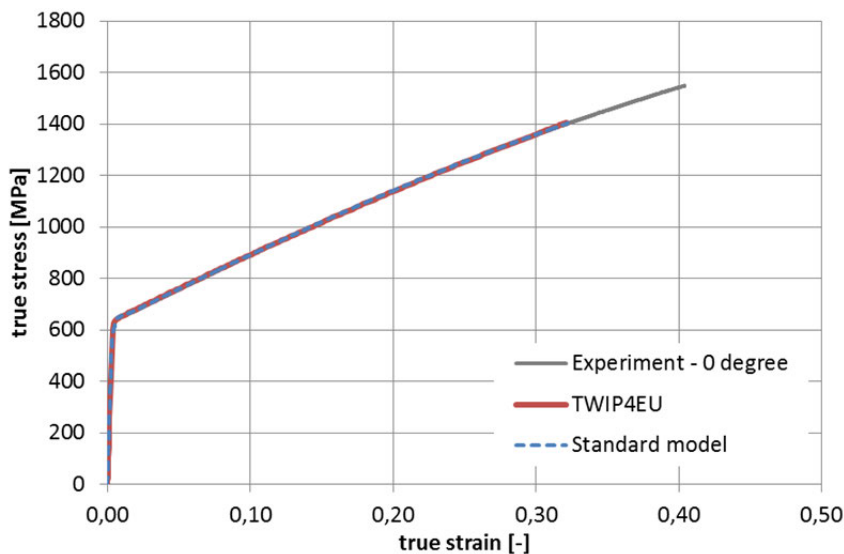


**Figure 2.8.12:** Tensile test in rolling direction

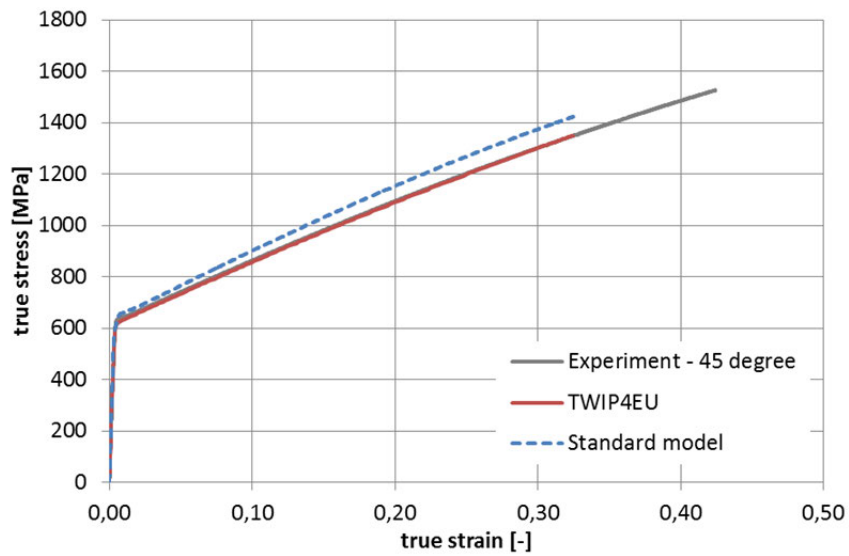


**Figure 2.8.13:** Tensile test in 45 degree to rolling direction

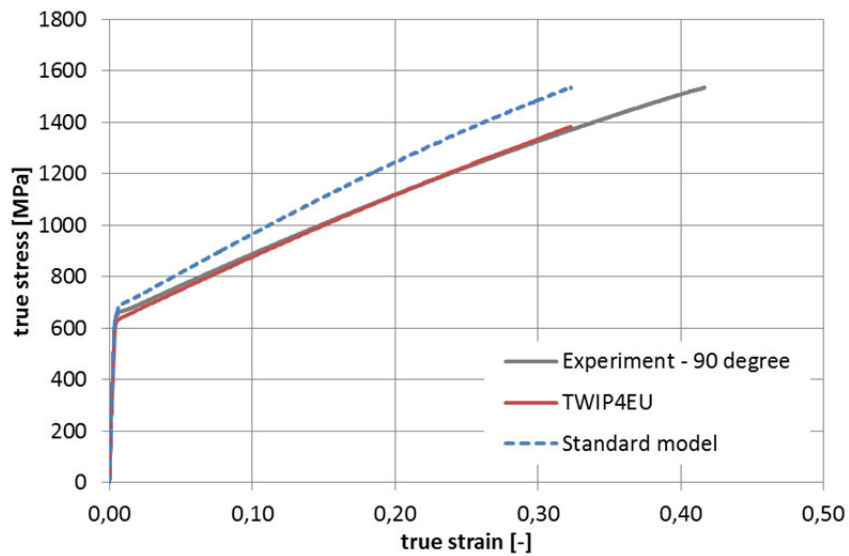


**Figure 2.8.14:** Tensile test in 90 degree to rolling direction

### 2.8.2.2 Bulge test

Details concerning the experimental set-up of the bulge test and some of the results are given in Section 2.4.1.3. In this section, the strain field and section cuts from simulations are compared with available experimental data. Figure 2.8.15 shows the major and minor strain distribution of the bulge specimen at an oil pressure of 230 bar. One can see that the shape of both strain fields can be well described with the TWIP4EU model.

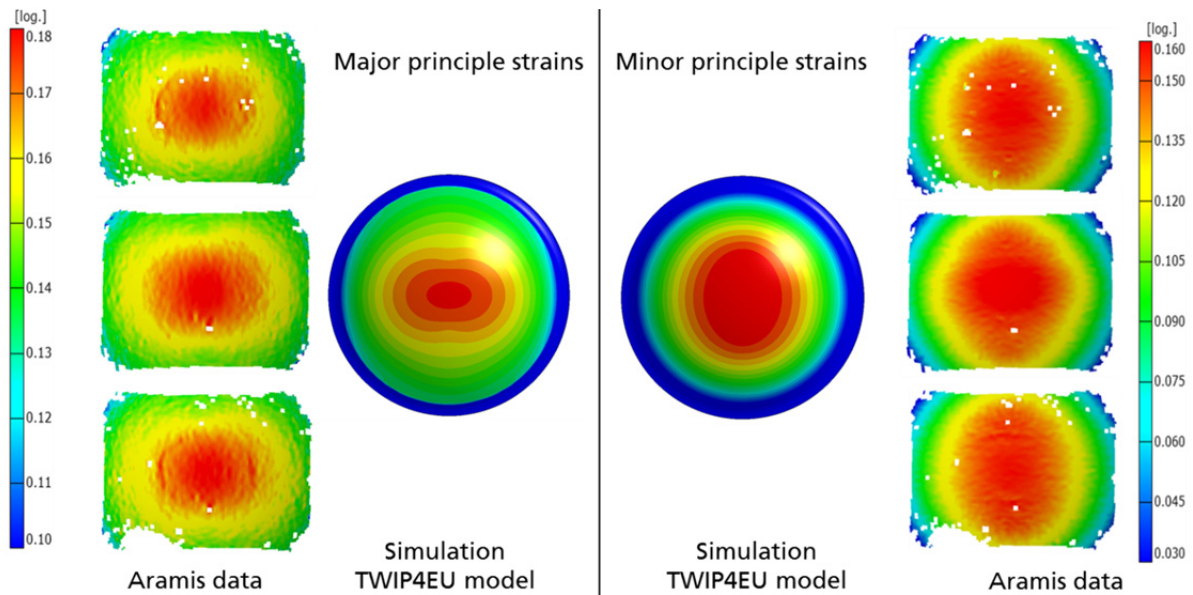


**Figure 2.8.15:** Bulge test - Comparison of the experimentally measure strain fields and the numerical results at an oil pressure of 230 bar.

In the Figures 2.8.16 - 2.8.19 the major and minor strains are plotted along a section cut parallel to the rolling direction and parallel to the transverse direction, respectively. The results of the TWIP4EU model as well as the results obtained from the standard model were compared to experimental data. The TWIP4EU model gives a good prediction of the maximum strains in the center of the specimen while the standard model overestimates the strains. Also, the shape of the curve is in a better agreement to the experimental data in case of the TWIP4EU model.

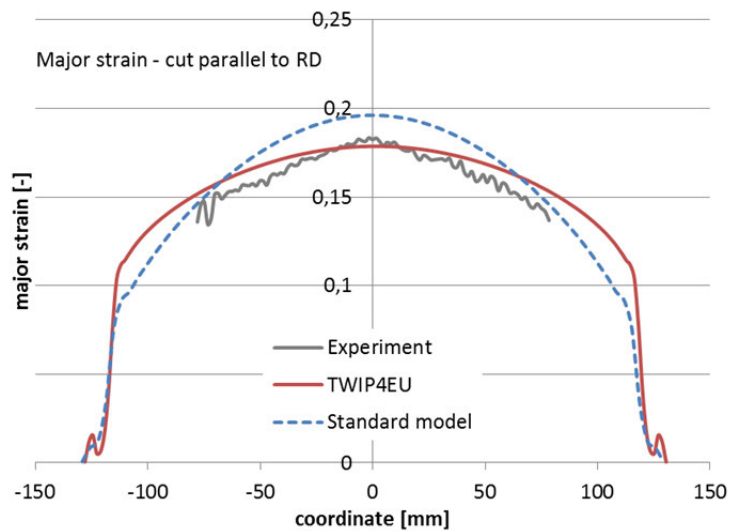


**Figure 2.8.16:** Bulge test – major strains in the cut parallel to the rolling direction. Comparison between experimental data and simulation

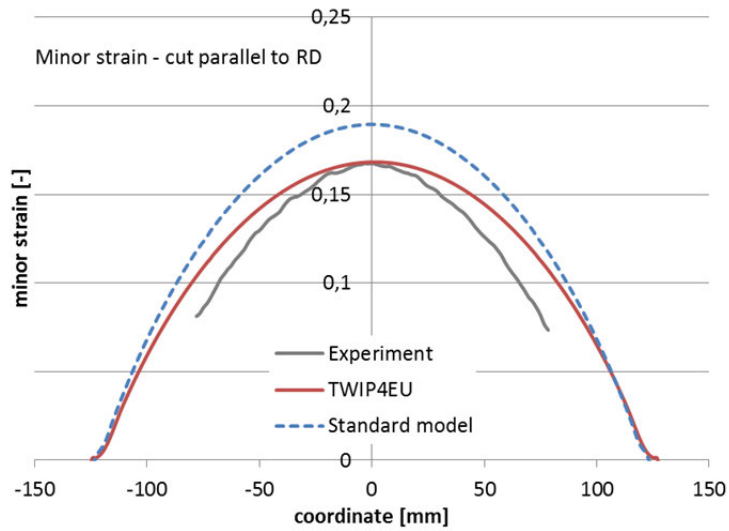


**Figure 2.8.17:** Bulge test – minor strains in the cut parallel to the rolling direction. Comparison between experimental data and simulation

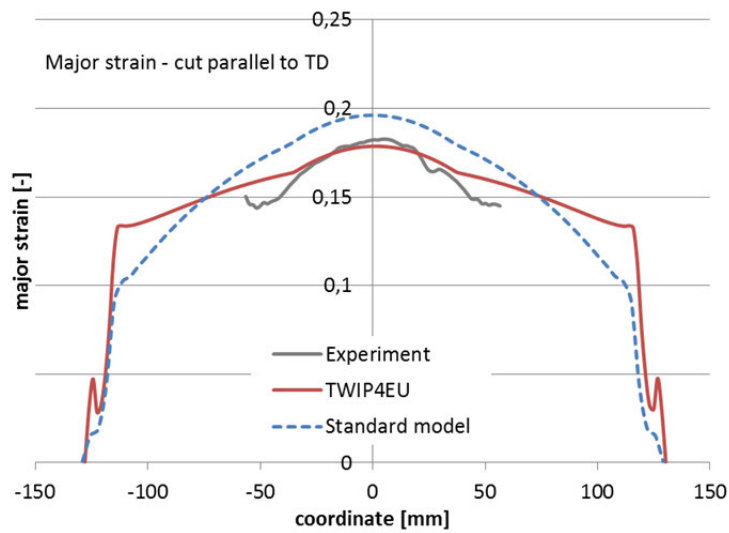


**Figure 2.8.18:** Bulge test – major strains in the cut parallel to the transverse direction. Comparison between experimental data and simulation

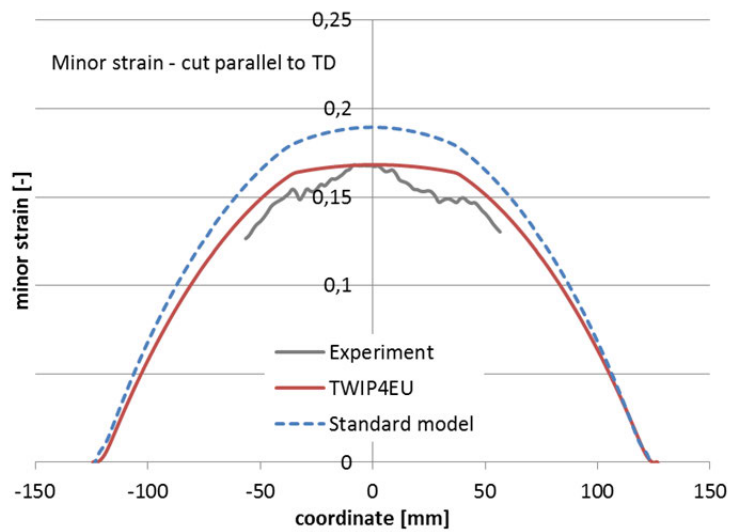


**Figure 2.8.19:** Bulge test – minor strains in the cut parallel to the transverse direction. Comparison between experimental data and simulation



The influence of the stress dependent hardening approach becomes visible in Figure 2.8.20. Here, two parameter sets of the TWIP4EU model are compared. Besides the TWIP4EU model using the standard parameter (see Table 2.8.1), an additional parameter set is considered that omits the effect of stress dependent hardening by setting  $m_s$  and  $m_c$  to zero. For all other parameter the standard values were used. Omitting the stress dependent hardening will predict to a softer material behavior and will overestimate the strains. This effect will increase with increasing strain level.

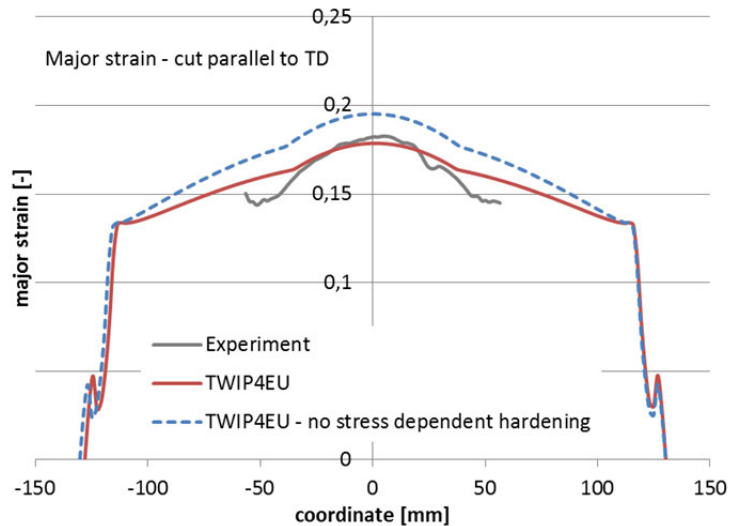


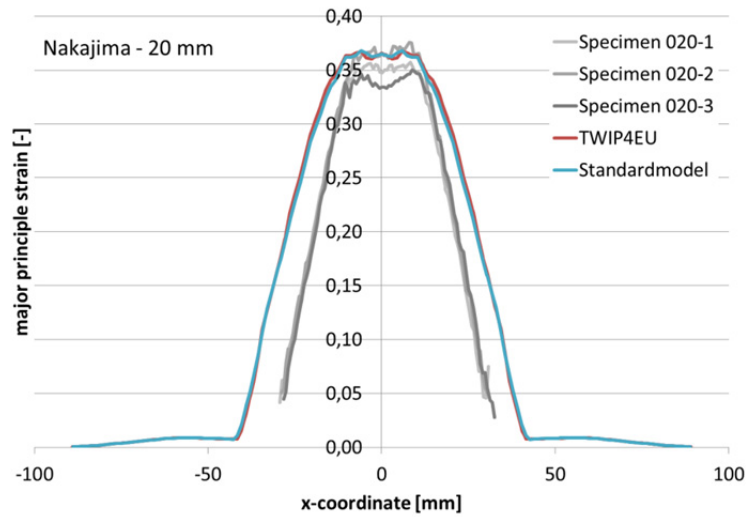
**Figure 2.8.20:** Bulge test – major strains in the cut parallel to the transverse direction. Comparison of the major strain obtained from TWIP4EU model considering the stress dependent hardening and without stress depending hardening.

### 2.8.2.3 Nakajima test

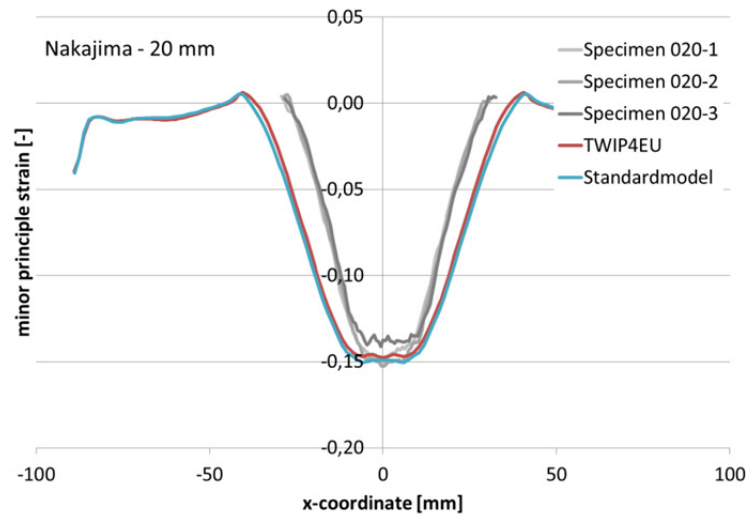
For the Nakajima-test, the results of the small 20 mm specimen (uniaxial tension), the 130 mm specimen (plain strain condition) and the round 200 mm specimen (biaxial tension) are presented in Figures 2.8.10 - 2.8.15. For the all specimens, the major and minor strains are shown along a section cut parallel to the rolling direction. Due to the tribological conditions in the experimental setup the friction was neglected, the friction coefficient  $\mu$  was set to zero.

For the 20 mm specimen the standard model as well as the TWIP4EU model shows a good agreement of the maximum strain level. The deviations can be explained by some differences in the evaluation of the data. In the case of the simulation, the developed view of the x-coordinate was used while the projection of the x-coordinate was given from experimental data.

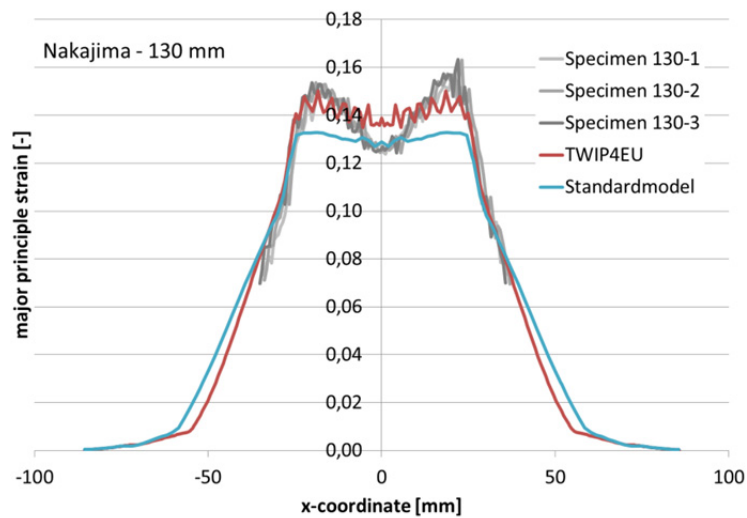
For the 130 mm specimen and the 200 mm specimen, the results of the TWIP4EU are in good agreement with the experimental data. The maximum strain values and also the shape of the curves can be well described. The prediction of the standard model shows some deviations in the strain level as well in the shape of the predicted strain curve along the cut.



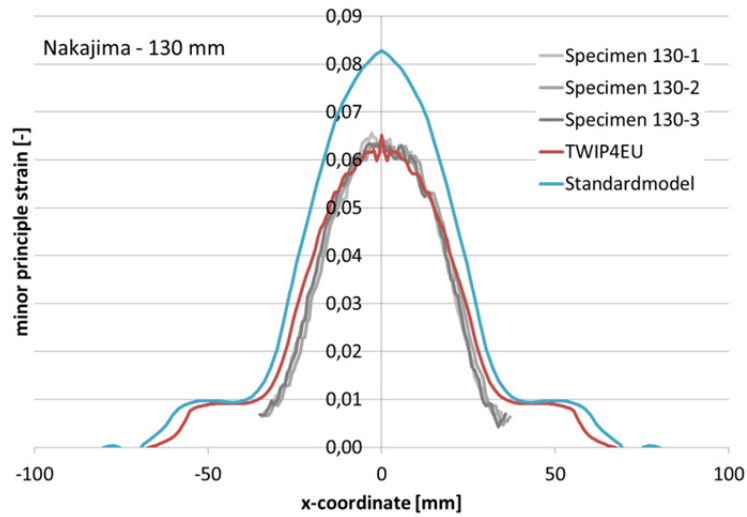
**Figure 2.8.21:** Major strain along a cut parallel to rolling direction for the 20 mm Nakajima specimen. Punch stroke 33.8 mm



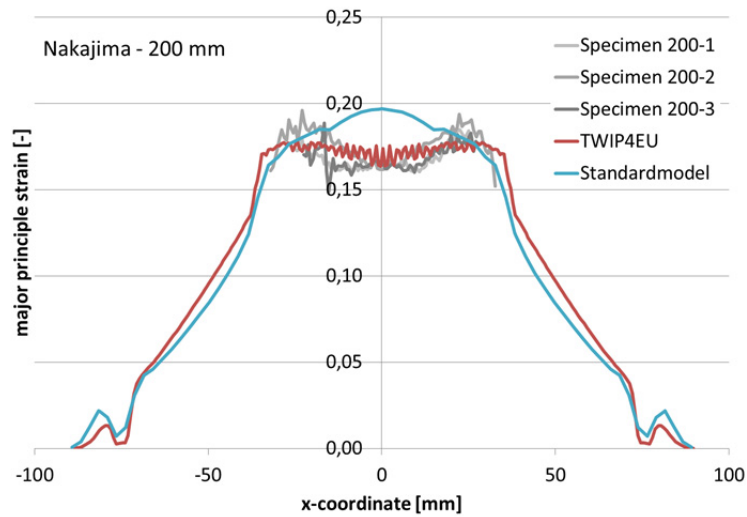
**Figure 2.8.22:** Minor strain along a cut parallel to rolling direction for the 20 mm Nakajima specimen. Punch stroke 33.8 mm



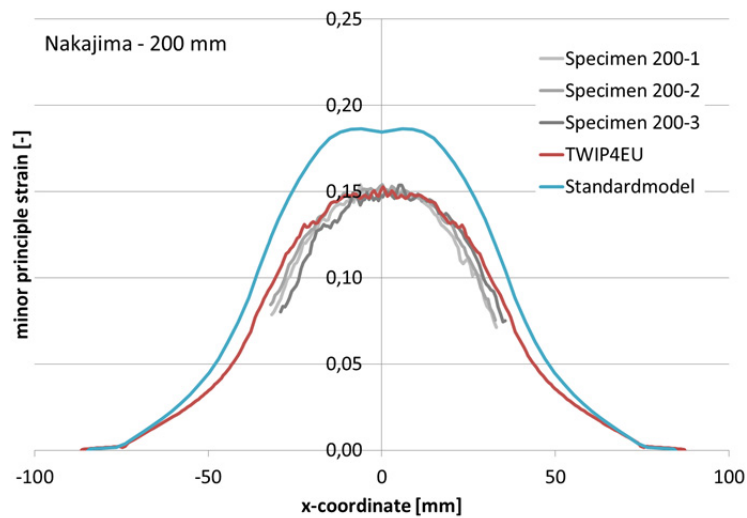
**Figure 2.8.23:** Major strain along a cut parallel to rolling direction for the 130 mm Nakajima specimen. Punch stroke 26.8 mm



**Figure 2.8.24:** Minor strain along a cut parallel to rolling direction for the 20 mm Nakajima specimen. Punch stroke 26.8 mm



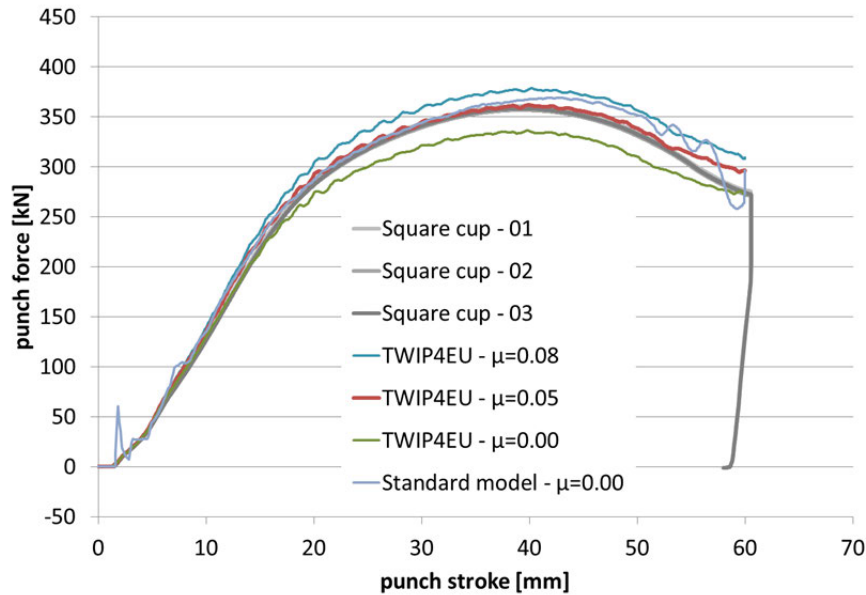
**Figure 2.8.25:** Major strain along a cut parallel to rolling direction for the 200 mm Nakajima specimen. Punch stroke 34.7 mm



**Figure 2.8.26:** Minor strain along a cut parallel to rolling direction for the 20 mm Nakajima specimen. Punch stroke 34.7 mm

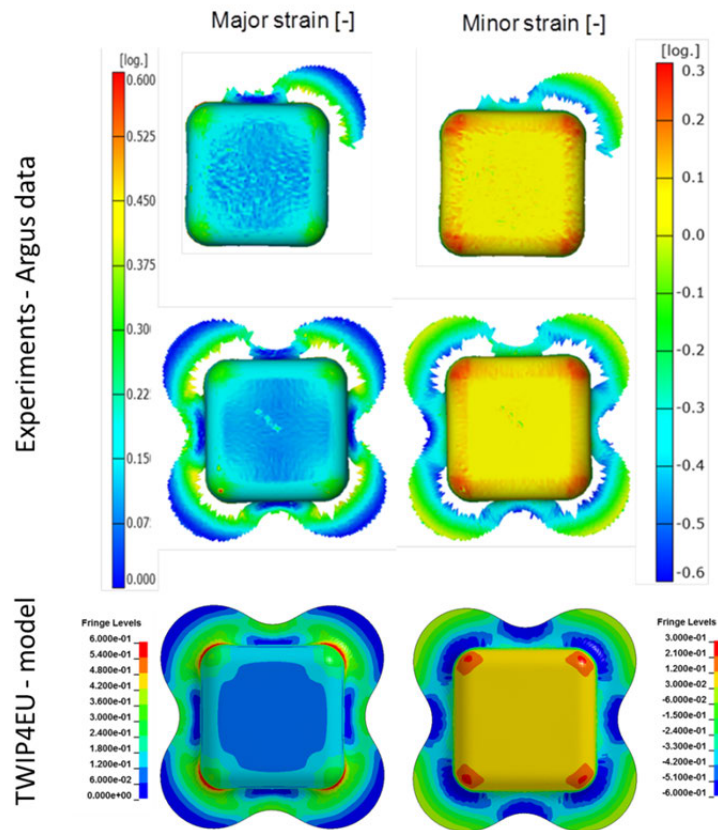
### 2.8.2.4 Cup drawing experiments

The drawing of a square cup was considered to evaluate the forming behavior of the TWIP-steel and to evaluate the material models under deep drawing conditions. The setup of the cup-drawing test was already described in Section 2.4.3.3. In this section, the experimental results will be compared with the numerical data using the standard material model and the TWIP4EU model, respectively. Figure 2.8.27 shows the force-displacement curve of the punch. A well-known issue in deep drawing simulations is the influence of the friction parameter on the resulting punch force. The influence of the friction coefficient is also illustrated in Figure 2.8.16. The force-displacement curve can be well described in the case of the TWIP4EU-model if a value of  $\mu=0.05$  is used. The standard model slightly overestimates the force-displacement curve even if no friction is assumed. For a more realistic friction coefficient  $\mu>0.00$ , the deviation becomes more pronounced.



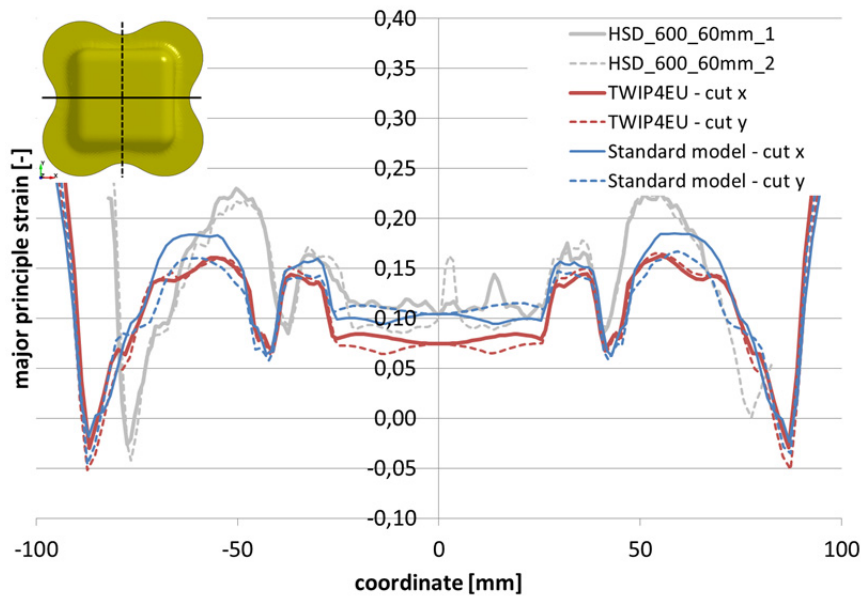
**Figure 2.8.27:** Force-displacement curve of the punch. Comparison of experiments and simulation.

Figure 2.8.28 shows the comparison between the strain fields (major and minor strains) evaluated from experiments using Argus measurement and the simulation results using the TWIP4EU model. Qualitatively, both results are in good agreement, the maximum and minimum values are predicted at the same position as in the experiment. It is noted, that the Argus measurement returns white pixels in regions where the mesh is destroyed during forming. For this reason the draw-in at the side of the cups appears larger as it is.



**Figure 2.8.28:** Force-displacement curve of the punch. Comparison of experiments and simulation.

The major and minor strains in a section cut parallel to the rolling direction and in diagonal direction are given in Figures 2.8.29 and 2.8.30, respectively. Compared the experiments, all simulations underestimate the extremal values of the strain in the section cut parallel to rolling direction, see Figure 2.8.18.



**Figure 2.8.29:** Major strains in a section cut parallel to the rolling direction

In the section cut in diagonal direction, the prediction of the maximum strain level fits better to the experimental data. However, to location of the maximum value is shifted along the coordinate.

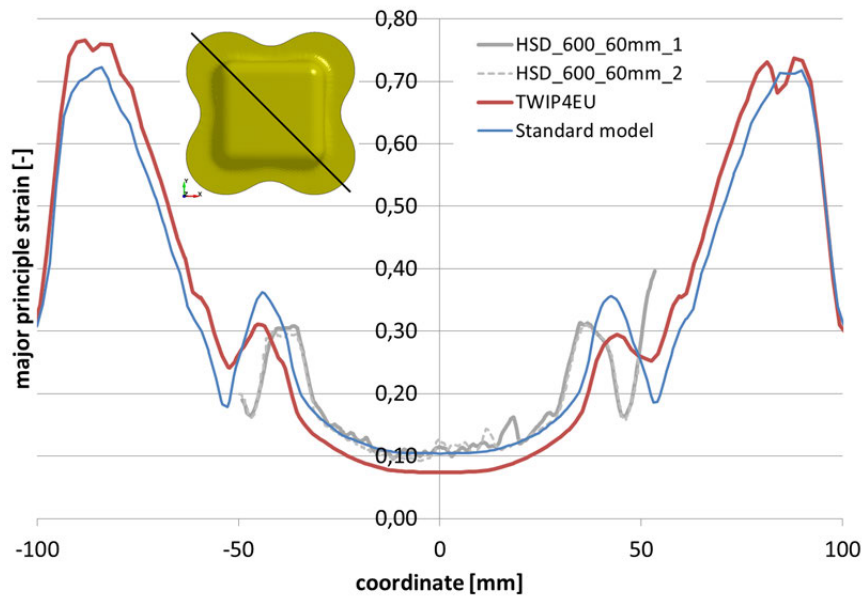


**Figure 2.8.30:** Major strains in a section cut in diagonal direction of the cup

### 2.8.3 Evaluation of spring back behavior of the formed specimen in simulations and experiment

The bending under tension test (BUT-test) was used to evaluate the spring back behavior of the TWIP-steel material, see Section 2.4.2.3. Depending on the chosen roll diameter and the applied back force, it is possible to realize different ratios of tension and bending. Six different combinations of roll diameter and back force are available from experiments and were used for comparison with simulation. The numerical model consists of three steps, see also Figure 2.8.31:

- **Step 1:** Application of the brake force on one end of the strip. In the initial configuration the strip is already bent over the roll in an angle of 90 degree.
- **Step 2:** The strip is pulled for a distance of 215 mm (displacement-controlled) while the brake force is still active
- **Step3:** Elastic spring back of the deformed strip. For step 3 an implicit solver was used, step 1 and step 2 were simulated with an explicit solver.

Some more details of the model are given in Figure 2.8.32. It was decided to use solid elements instead of shell elements since it is well known that also the stresses in thickness direction influence the spring back prediction. Since the anisotropic yield surface model YLD2000-2D (see Section 2.7.4) is limited to plane stress states, it is not available for solid element formulation. For this reason, the isotropic version (von Mises yield criterion) of the TWP4EU model is used in this case.

For comparison of the predicted shape of the strip after spring back, one overlay plot of the numerical and the experimental results is given in Figures 2.8.33 - 2.8.35. To correctly compare the shape of the strips, the size of the figures from simulation had to be adjusted. Therefore, the length of the lower, undeformed part of the strip was determined from numerical results. Then the figure was scaled to fit the determined length of the lower part of the strip with the ruler. In both figures, the red dot defines the starting point from which the strip is completely pulled over the roll, see also Figure 2.8.20. It is noted that the part of the strip between the upper end and the red dot cannot be compared with the experimental data.



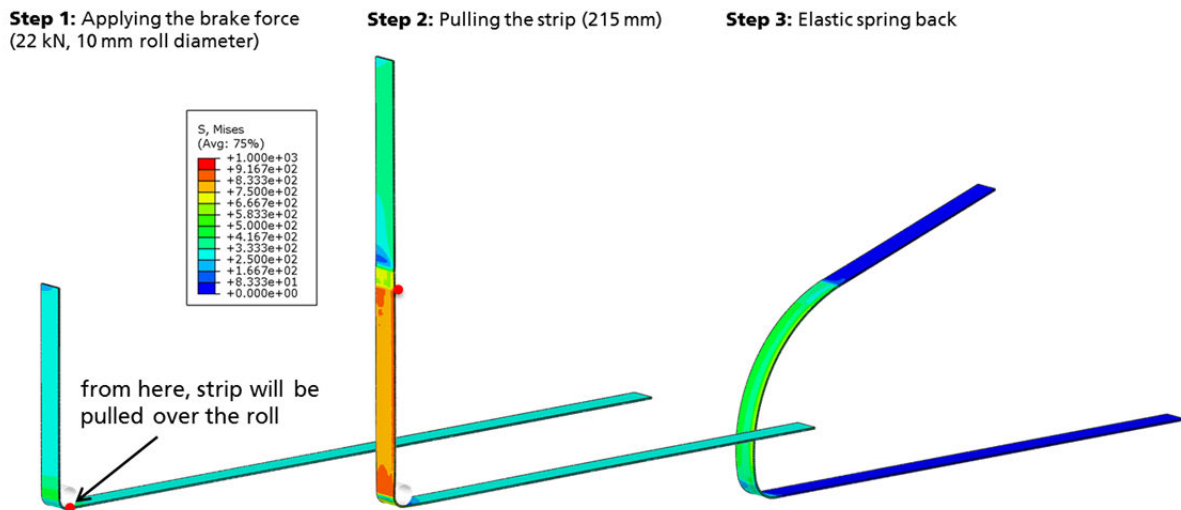


**Figure 2.8.31:** Simulation of the bending under tension test, divided into three steps.

- 8-node solid elements, reduced integration
- 5 Elements in thickness direction
- Element size: z-dir: 1,0 mm  
x-dir: 2,5 mm
- Symmetric boundary conditions in y-z-plane
- no friction between roll and strip (roll rotates in experiment)

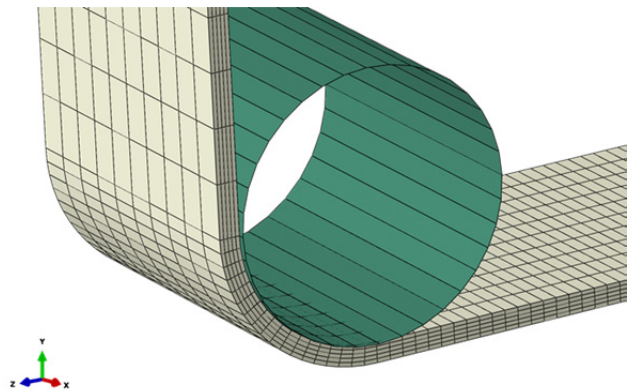


**Figure 2.8.32:** Numerical model for to simulation of the BUT-test.

From the deformed shape of the strips after spring back in Figure 2.8.33 it becomes clear that the TWIP4EU model overestimates the spring-back behavior of the strips. It is supposed that the portion of isotropic hardening might be too high. Figure 2.8.34 shows the results of the spring back simulation for a modified set of parameter with more pronounced kinematic hardening. In that case, the predicted spring back is less compared to Figure 2.8.33 but there are still some differences compared to the experiments. The consideration of two back-stress components (see Section 2.6.3.2) gives a spring-back prediction which is close to the experimental data, as illustrated in Figure 2.8.35.



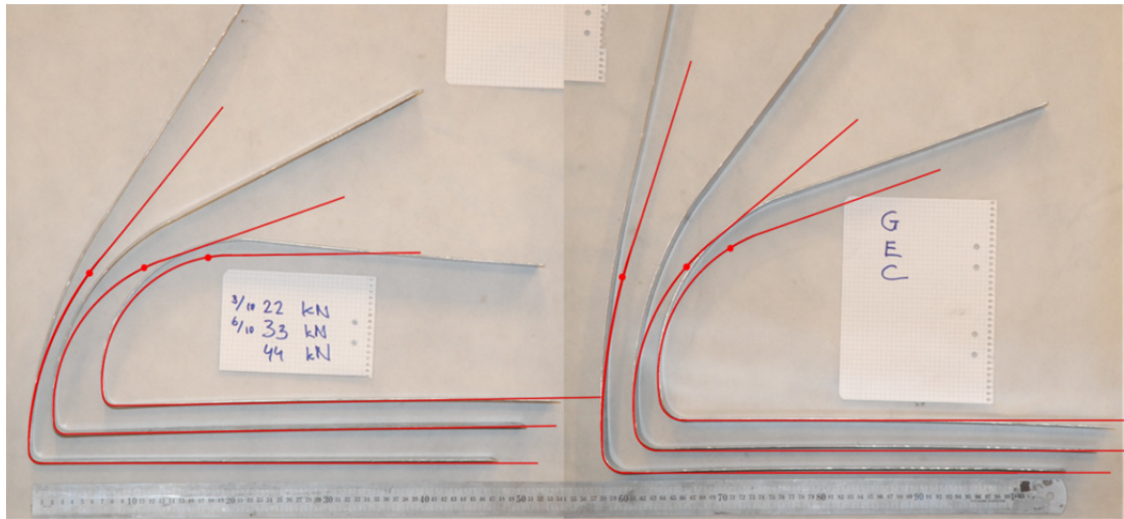


**Figure 2.8.33:** Comparison between the numerical prediction and the experimental data of the BUT-test.

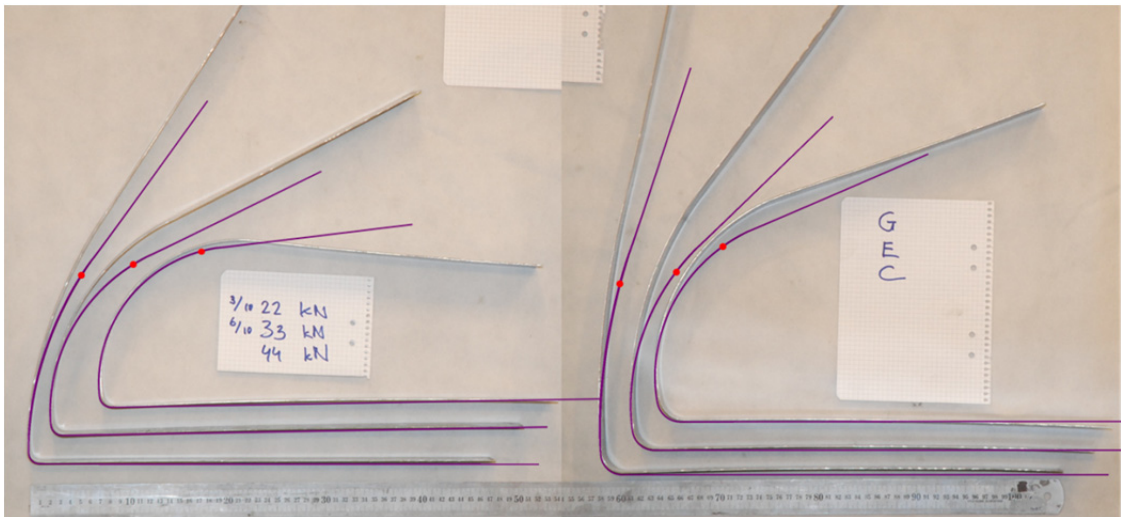


**Figure 2.8.34:** Comparison between the numerical prediction and the experimental data of the BUT-test with modified parameter set.

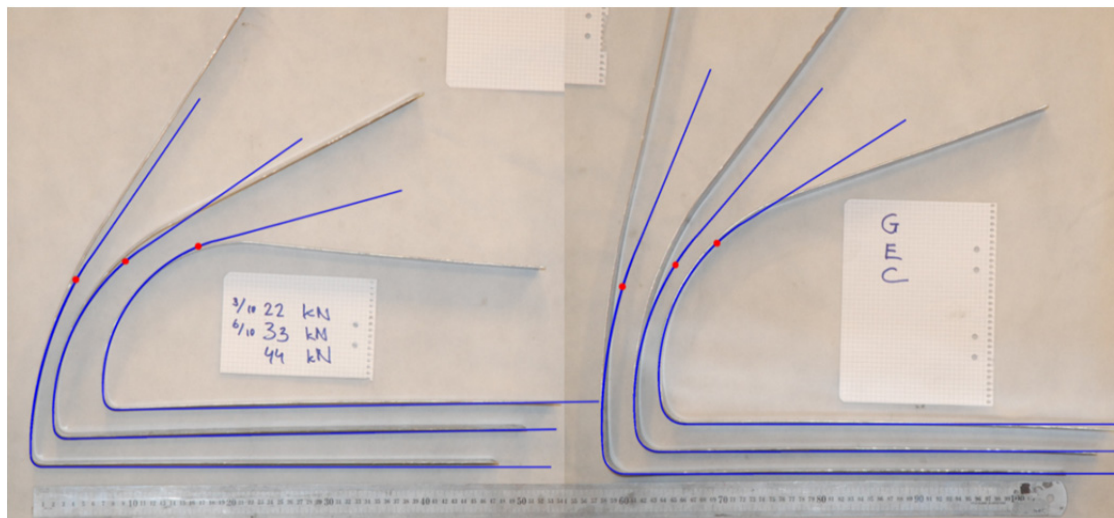


**Figure 2.8.35:** Comparison between the numerical prediction and the experimental data of the BUT-test: TWIPEU model including Chaboche-type extension.

## 2.8.4 Formulation of guidelines for usage of the new constitutive framework for forming simulations

The developed model considers different features to account for the experimentally observed material behavior. Based on the available results, the following procedure is proposed to identify the parameters of the TWIP4EU material model:

### 2.8.4.1 Uniaxial hardening

Needed data:

- Flow curve from uniaxial tensile test in rolling direction
- Information about the evolution of the twin volume fraction is helpful, but not obligatory.

The parameters needed to describe the monotonic hardening are given in Table 2.8.1:

- For the parameter  $E$ ,  $\nu$ , *density* and  $\mu$  data from macroscopic measurements were used.
- Standard values from literature were considered for  $b$  and  $M$
- If information about the evolution of the twin volume fraction as function of the plastic strain is available, these data can be used to determine the parameter  $F_0$ ,  $\beta$ ,  $m$ . The value for  $e$  is directly obtained from TEM measurement.  
If no TEM data are available the values defined in Table 2.8.1 can be used for this steel grade.
- The parameter  $\alpha$ ,  $k$ ,  $f$ ,  $\sigma_0$ ,  $n_0$  and  $\lambda$  are identified via inverse simulation of the stress-strain-curve of the uniaxial tensile test.
- The values for  $\varepsilon_{init}$  and  $\rho_0$  are assumed to be zero.

### 2.8.4.2 Anisotropic initial yield surface

If the anisotropic yield function Barlat YLD2000-2D is used for the description of the initial yield surface, the following procedure according state-of-the-art is proposed:

Needed data:

- Initial yield strength in 0, 45 and 90 degree with respect to rolling direction
- Lankford coefficients (r-values) in 0, 45 and 90 degree with respect to rolling direction
- Bulge-test: ratio of strains in rolling direction and in transverse direction to determine the  $r_b$ -value, initial yield strength

With these data, the initial yield locus of the YLD2000 model can be determined. Although it is state of the art to choose the yield function exponent  $M=8$  for fcc crystal structure (which is the case for TWIP-steel), a value  $M=6$  is recommended since it leads to a good prediction of the forming experiments. The values for  $\alpha_1$  to  $\alpha_8$  are determined by a least square fit of the observed yield stress values and the Lankford coefficients to the Barlat YLD2000 yield surface.

### 2.8.4.3 Stress dependent hardening

Needed data:

- Bulge test

As described in Section 2.7.1. different functions were implemented to account for the stress dependent hardening. The simplest approach is a linear function of the stress triaxiality, but this seem to no rather unphysical. In general it is possible to define two different slopes of the function  $k_{TWIN}$ : One slope  $m_t$  for positive triaxiality and one slope  $m_c$  for negative stress triaxiality. The value of  $m_t$  can be calibrated by inverse simulation of the pressure-displacement curve of the bulge test or on the strain field data. It is noted that the uniaxial tensile test is not influenced by variation of  $k_{TWIN}$ , see Section 2.6.3.2.

As long as no sufficient experimental data are available, it is reasonable to assume symmetric stress dependence, thus  $m_c = m_t$ . According to Figure 2.7.4, case 2 with equal values for the parameters  $m_t$  and  $m_c$  is recommended. A refined adjustment can be done, if experimental data for additional loading conditions and sufficient strain levels are available. It is also possible to omit the effect of stress dependent hardening if the values for  $m_t$  and  $m_c$  are set to zero.

#### 2.8.4.4 Parameter set

The set of parameters for the TWIP4EU model given in Table 2.8.1 was used for all simulations which were shown in this Section 2.8.2 and in Section 2.9.4 if not indicated otherwise.

Notation	Value	Unit	Physical meaning
$E$	175000	MPa	Young's Modulus
$\nu$	0,3	---	Poisson's Ratio
Density	7,40E-09	tone/mm <sup>3</sup>	Material density
<b><i>TWIP4EU uniaxial hardening</i></b>			
$\beta$	2,26	---	Fitting coefficient
$b$	2,50E-07	mm	Burgers vector
$M$	3,06	---	Taylor factor
$\alpha$	0,296	---	Mean dislocation strength parameter
$\lambda$	3,165E-04	mm	Mean spacing between slip bands
$k$	0,03	---	Forest (latent) hardening parameter
$f$	1,295	---	Parameter of dynamic recovery of dislocations
$m$	1,95	---	Parameter of stacking fault energy (SFE)
$d$	3,00E-03	mm	Grain size
$e$	2,20E-05	mm	Twin mean thickness
$F_{\max}$	0,36	---	Maximum volume fraction of twins
$\varepsilon_{\text{init}}$	0,00E+00	---	The critical strain at which twinning begins (assumption)
$\rho_0$	0,00E+00	mm <sup>-2</sup>	The initial dislocation density (assumption)
$\sigma_0$	592,1	MPa	The initial yield radius
$n_0$	1,0	---	The max. number of dislocation loops at the boundaries
<b><i>Stress dependent hardening</i></b>			
$m_t$	1,30	---	Slope of $k_{\text{TWIN}}$ -function in tension
$m_c$	1,30	---	Slope of $k_{\text{TWIN}}$ -function in compression
case	2	---	Selection of stres dependent hardening case (1 - 3)
<b><i>Anisotropy - YLD2000-2D</i></b>			
$\alpha_1$	0,810	---	YLD2000-2D anisotropy parameter
$\alpha_2$	1,168	---	YLD2000-2D anisotropy parameter
$\alpha_3$	1,192	---	YLD2000-2D anisotropy parameter
$\alpha_4$	1,027	---	YLD2000-2D anisotropy parameter
$\alpha_5$	0,993	---	YLD2000-2D anisotropy parameter
$\alpha_6$	0,815	---	YLD2000-2D anisotropy parameter
$\alpha_7$	1,023	---	YLD2000-2D anisotropy parameter
$\alpha_8$	1,066	---	YLD2000-2D anisotropy parameter
$m$	6	---	YLD2000-2D exponent

**Table 2.8.1:** Overview over model parameters to be identified. The colors indicate how the parameters were determined. Green: Macroscopic measurements. Orange: Literature. Blue: Calibrated on twinning evolution, red: Calibrated on macroscopic uniaxial flow curve, black: other.

## 2.9 WP9: Prototype production and validation

The following main objectives were defined for WP9:

- Formulate design specifications for the automobile component and fabrication of the prototype component under controlled conditions in a laboratory
- Characterization of the formed part using optical strain analysis and advanced mapping techniques
- Model creation and forming simulation of the prototype component
- Comparison of the prototype simulation with measured data obtained from experiments: strain distribution, spring back, sheet thickness

### 2.9.1 Formulation of design specifications and fabrication of the prototype component

The aim of this task is to define a demonstrator part with a complex 3D geometry with borderline critical behavior in a deep drawing step that demonstrates the superior formability of TWIP-steels in comparison with other high strength steels. A list of requirements on the demonstrator part has been set up:

- Specific demands on the chosen component
  - Part should be relevant in the automotive industry
  - Prototype and serial tools should be available in Faurecia
  - CAD tool data should be available
  - First stamping simulations should indicate critical behavior
  - A digitalization of the tool must be possible
- Specific demands with respect to the available material
  - Material: preseries TWIP-steel with  $R_{p0.2}$  600 MPa
  - Material thickness 1.5 mm
  - Maximum blank dimensions: 300 mm x 1000 mm

According to the requirements as mentioned above a backrest sidemember has been chosen as a suitable demonstrator part. Here, a prototype tools available at Faurecia Seating was used. The reasons for this decision are explained below.

#### 2.9.1.1 Relevance of a backrest side member as a demonstrator part

The beneficiary Faurecia sells seat frames for 17,5 million car sets each year. The seat frame illustrated in Figure 2.9.1 is a crucial element of passive safety requirements defined by legislative authorities and OEMs. As a load-bearing part directly positioned in the flow of forces, the backrest side member must provide a high degree of energy absorption during a potential car crash, while still maintaining a high degree of form stability. These demands suggest a broad field of application of TWIP-steels.

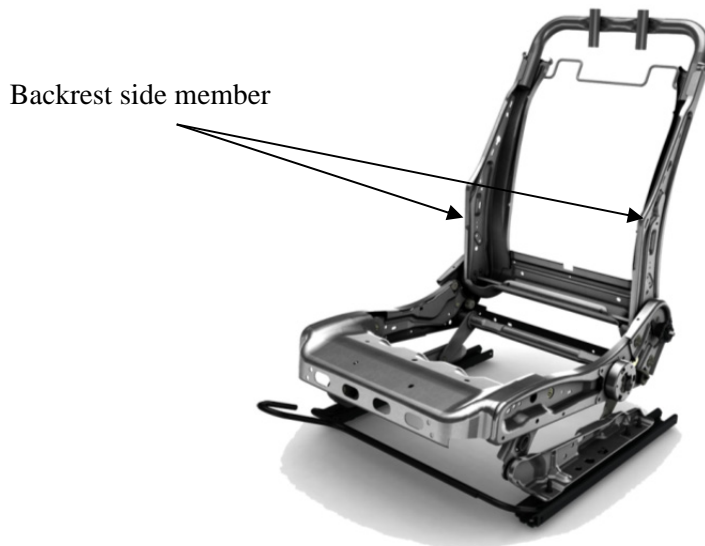


**Figure 2.9.1:** Seat Frame

### 2.9.1.2 Availability of existing prototype and serial tools

In order to limit possible tools, which should be taken into account, it should be checked, if the preseries TWIP-steel can be used in an existing prototype tool. Since the preseries material can only be delivered as rectangular blanks with 1,5 mm material thickness, a blank length of 1000 mm and a blank width of 300 mm, these dimensions of a potential demonstrator part must be taken into account while defining the prototype tool. Finally a prototype tool of a backrest sidemember have been chosen, because its blank dimensions match well with the blank dimensions of the preseries material. The CAD-model as well as the shape of the blank are illustrated in Figure 2.9.2.



**Figure 2.9.2:** CAD model of the backrest sidemember (left) and blank dimensions 272 mm x 679.9 mm x 1,5 mm (right)

After the definition of the prototype with dimensions matching to the pre-series material blank dimensions the availability of existing tools were checked. The lower part of the chosen prototype tool and the upper part of the serial tool are illustrated in Figures 2.9.3 and 2.9.4.





**Figure 2.9.3:** Lower part of the chosen prototype tool



**Figure 2.9.4:** Upper part of the chosen serial tool

### **2.9.1.3 Availability of CAD tool data**

CAD data of the tool geometry are necessary for the adaption of the existing tool geometries to the given material thickness of 1.5 mm and for the set-up of a temporary simulation model, which may help to find out, if the process limits can be reached during the prototype production.

By comparison between CAD geometry with real prototype tool geometry, it was necessary to rework the geometry of the punch of the prototype tool. Since the prototype tool was designed for a material thickness of 1.2 mm, it was necessary to remove 0.3 mm of the existing punch by a milling operation. The necessary NC data could be derived by an offset of the existing CAD data. After the milling operation it is necessary to determine the real part geometry of all tool parts in order to get accurate tool geometries in the simulation model. Since all parts of the chosen prototype part can easily be disassembled, a measurement with an optical measurement system like ATOS could be done very easily.

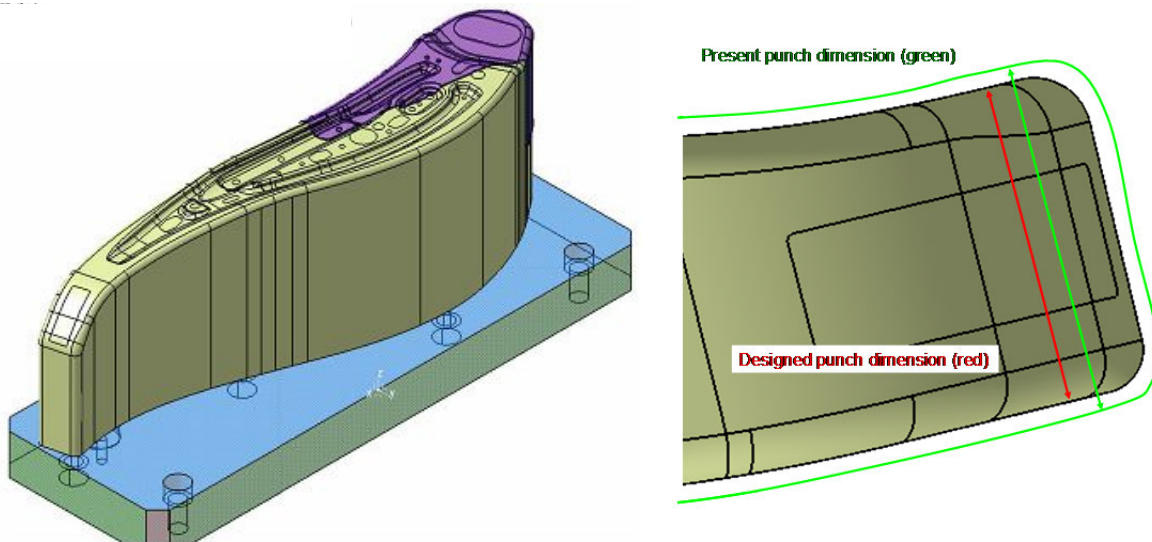


**Figure 2.9.5:** CAD model of the punch geometry (left). Definition of necessary adaption of existing tools to the sheet thickness of the pre-series TWIP-steel (right).

#### 2.9.1.4 Preparation of the prototype tool

As already mentioned, it had been necessary to rework the prototype tool by milling operations. Since the prototype tool was designed for deep drawing processes with a material thickness of 1.2 mm, it became necessary to adjust it for a material thickness of 1.5 mm according to the prototype material thickness. Therefore 0.3 mm of the material had to be removed circumferentially around the punch. As a consequence, it became necessary to check the gap between punch and other tool elements before starting the experiments with TWIP-steel. Thus, first experiments by use of DC04 material have shown that the gap between punch and other tool elements was locally differing from the foreseen value of 1.5 mm as shown in Figure 2.9.6. Furthermore, first experiments have shown that it was necessary to remove additional material at tool areas, where wrinkles of the blank material during the drawing process were expected. In order to adjust the tool gap in these areas it became necessary to manually re-mill the punch locally there and to repeat the first ATOS measurement of the punch that has been done, after the first milling of the punch, see Figure 2.9.7.

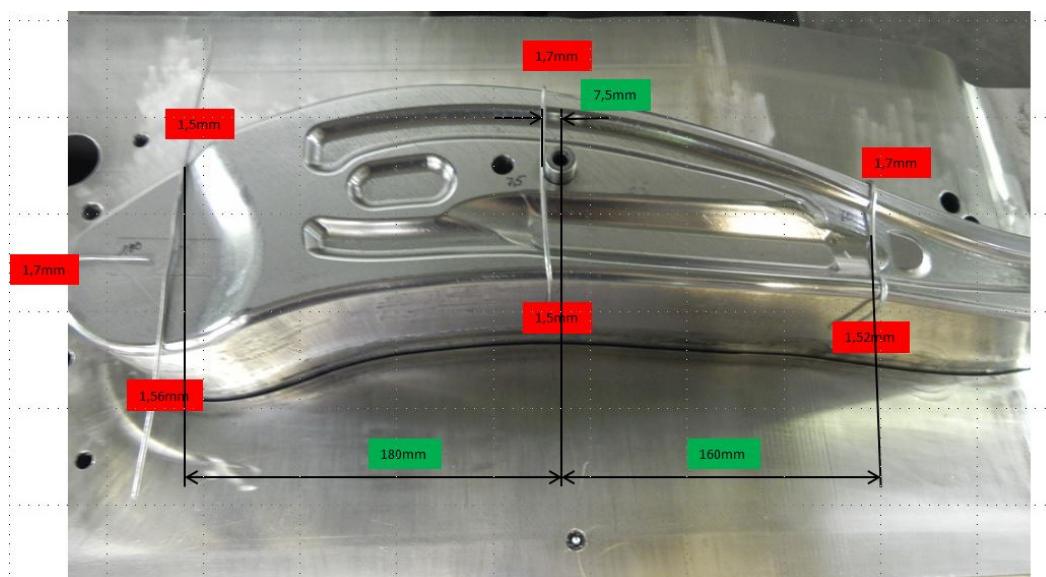


**Figure 2.9.6:** Gap between punch and tools after being re-milled.



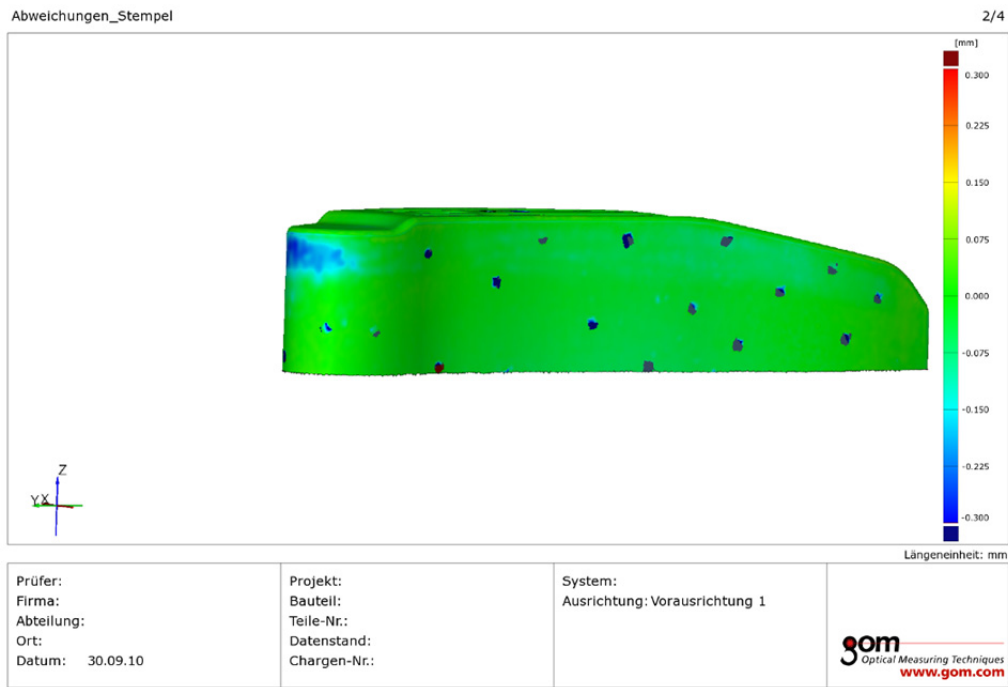


**Figure 2.9.7:** Deviations of punch shape between the first and the second manual rework. It can be seen that most of the second manual rework was done in the upper left area of the punch.

### 2.9.1.5 Definition of a demonstrator part shape by first simulations

One important objective of the work package WP9 is to fabricate a demonstrator part with a complex 3D geometry with borderline critical behavior in a drawing step that demonstrates the superior formability of TWIP-steels in comparison with other high strength steels. In order to define the demonstrator part geometry, it has been necessary to define a corresponding blank shape by simulation. The blank shape has to provide good part feasibility without cracks and wrinkles. At the same time the blank has to be big enough to provide surplus material that can be cut off after the drawing process in order to provide the exact part contour according to the CAD geometry.

Stamping simulations for blank shape definition have been done based on ideal CAD data and material data that have been delivered in other work packages. A first simulation has been done in order to determine the minimum blank shape that is absolutely necessary to form the complete contour of the demonstrator part (Figure 2.9.8), while a second stamping simulation has been done in order to define the maximum drawing depth of a closed profile in order to demonstrate the superior process limits of TWIP-steel (Figure 2.9.9). The two different blank shapes are illustrated in Figure 2.9.11. Blank type 1 refers to the minimum blank shape required; blank type 2 defines the blank shape to obtain a closed profile.

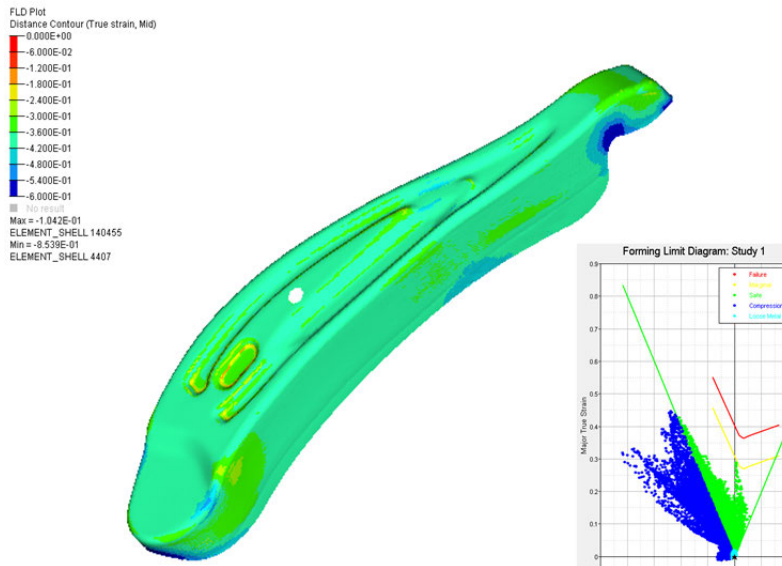


**Figure 2.9.7:** Definition of demonstrator part geometry by simulation to determine the minimum blank size (blank type 1, see Figure 2.9.11).

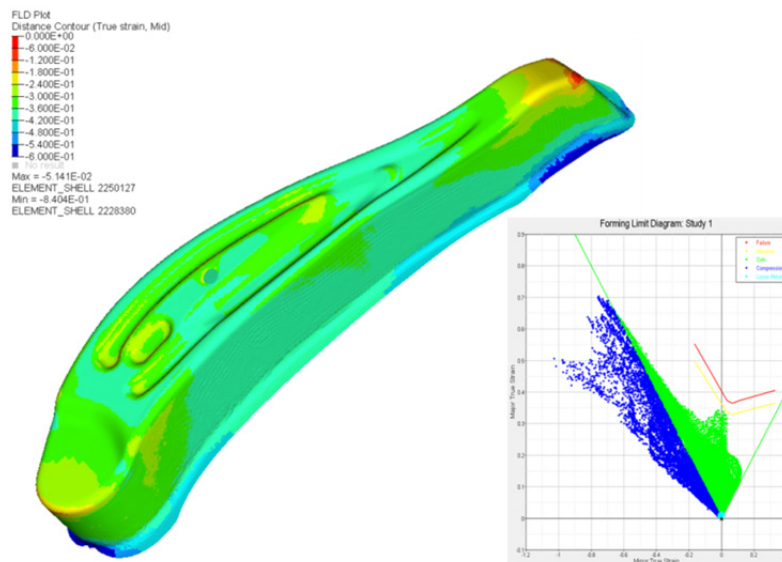


**Figure 2.9.8:** Definition of demonstrator part geometry by simulation to determine the maximum drawing depth of a closed profile (blank type 2, see Figure 2.9.11).

### 2.9.1.6 Fabrication of demonstrator parts

The fabrication of the prototype tools were done at the laboratory of the Salzgitter Mannesmann Forschung GmbH in Salzgitter. By use of the Faurecia prototype tool and the form blank with addendum, described in the previous section, demonstrator parts have been fabricated under controlled conditions. The lower part of the prototype tool installed in a tryout press is shown in Figure 2.9.10.

Before the drawing process a rectangular grating has been imprinted on the blank shape. By this measure an ATOS measurement could be done after the drawing process. The goal of the ATOS measurement was to determine the strain distribution within the part geometry that can later be compared to benchmark simulations in subsequent tasks. The realization of the ATOS measurements is described in Section 2.9.2. All process parameters such as description of blank shape, blank and tool positions at the beginning of the drawing process, punch velocity and binder force have been documented.



**Figure 2.9.10:** Lower part of the prototype tool installed in a tryout press at SZMF

As described in Section 2.9.1.5, two different blank shapes were used for forming of the prototype components, see Figure 2.9.11.:

- Blank type 1:
  - close to final part geometry
  - high spring back sensitivity
  - moderate forming demands
- Blank type 2:
  - circular flange,
  - low spring back sensitivity,
  - superior forming demands

Furthermore, two different drawing depths of 71 mm and 46 mm were realized with both blank shapes. Hence, four different variations of the prototype are available for comparison with simulation data, see Figures 2.9.12. The final prototype part made from TWIP-steel after trimming is shown in Figure 2.9.13

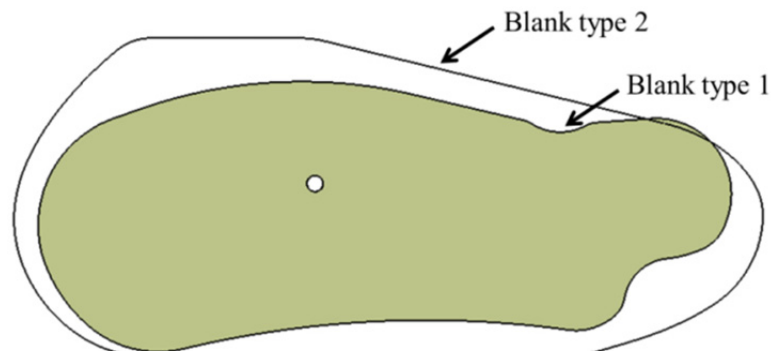
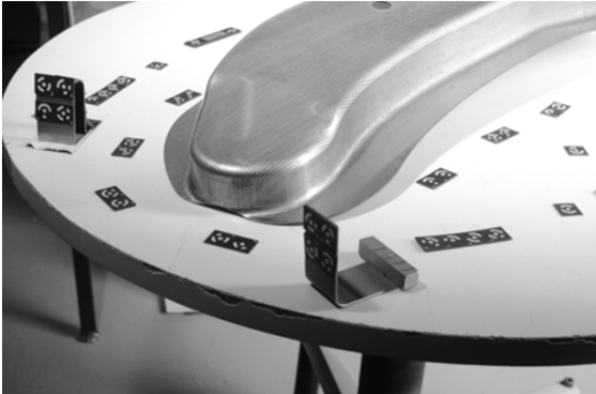
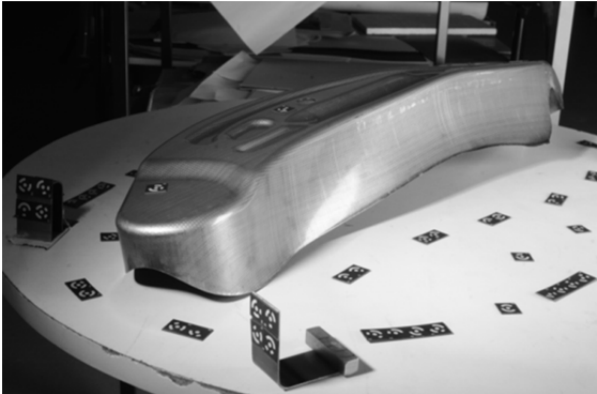


**Figure 2.9.11:** Comparison of the two considered blank shapes.

Blank type 1, half drawn



Blank type 1, half drawn



Blank type 2, half drawn



Blank type 2, full drawn

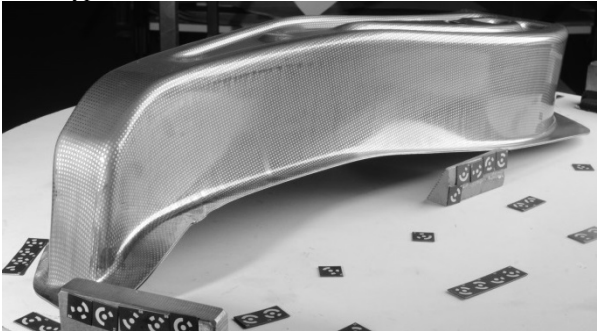


**Figure 2.9.12:** Different variations were considered for forming of the prototype.



**Figure 2.9.13:** Prototype component made of TWIP-steel. Top: blank type 1, centre: blank type 2, bottom: after laser cutting



## 2.9.2 Characterization of the formed part using optical strain measurements and advanced mapping techniques

The optical strain measurement system ARGUS was used to determine the strain distribution on the surface of the formed prototypes. Figure 2.9.14 shows a formed part and an overlay plot of one ARGUS measurement. Combining several ARGUS measurements from different angles leads to a complete strain field measurement. In Figure 2.9.15 and 2.9.16 the major strains from ARGUS measurement are illustrated for both considered blank types and for two drawing depths. For a better comparison of the strain fields, the same scale for the strain levels was used.

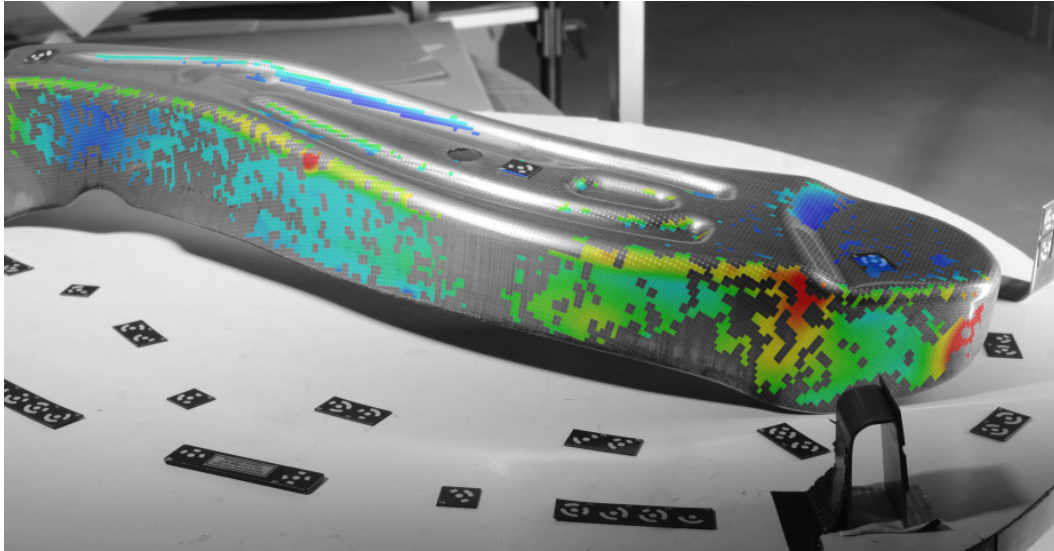


**Figure 2.9.14:** Formed part and overlay plot of one ARGUS measurement. Combining several ARGUS measurements from different angles gives a complete strain field.

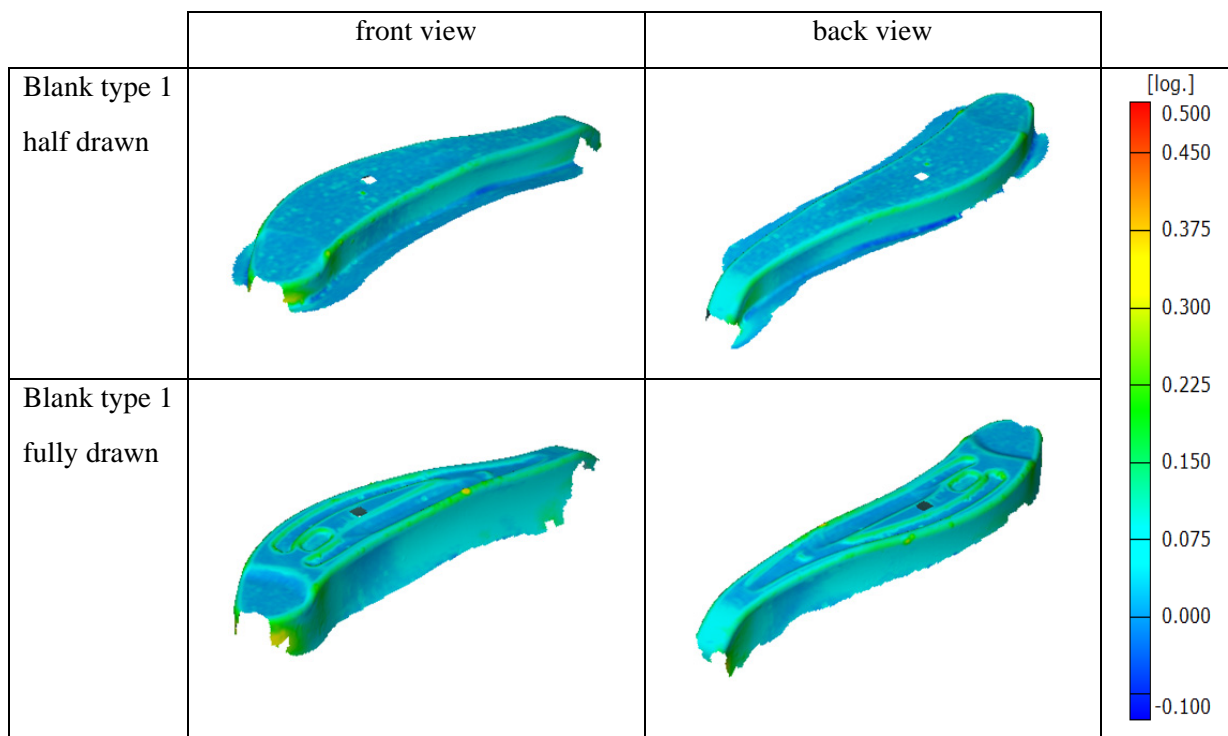


**Figure 2.9.15:** Major strain field of the formed prototype using **blank type 1**, evaluated from Argus measurement. The strain field was evaluated for two drawing depths.



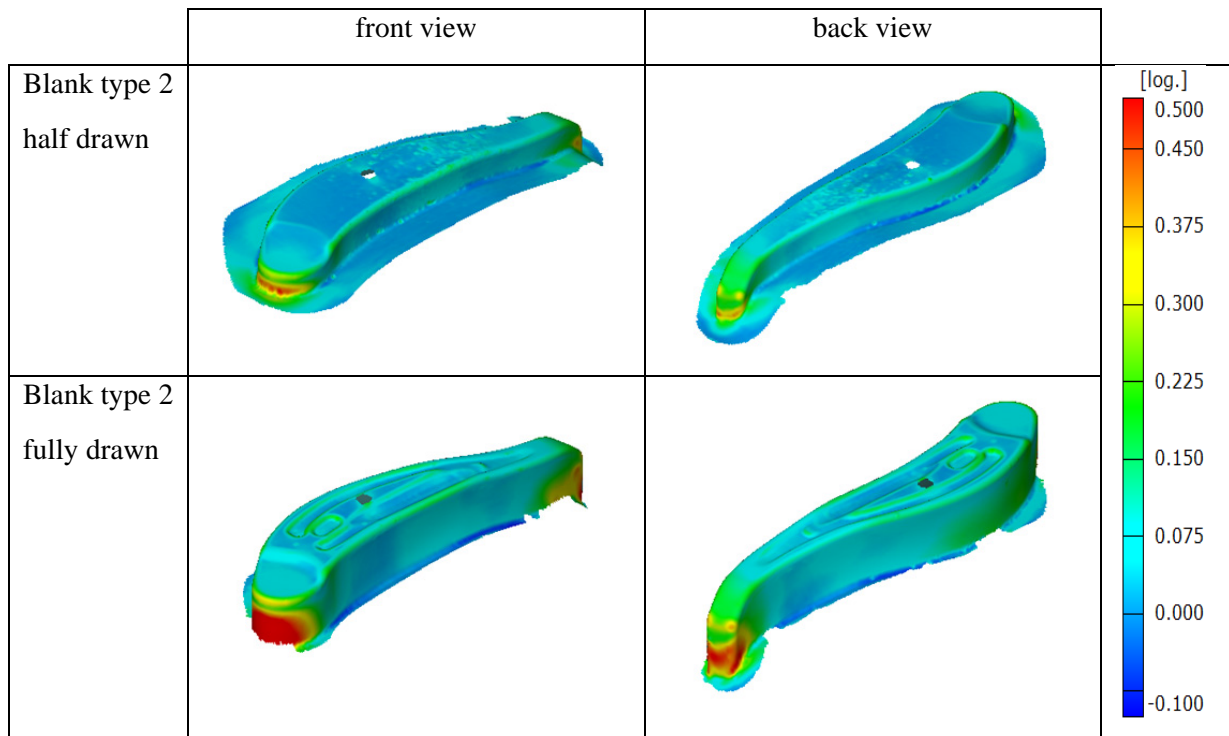


**Figure 2.9.16:** Major strain field of the formed prototype **using blank type 2**, evaluated from Argus measurement. The strain field was evaluated for two drawing depths.

In Figure 2.9.17 the scale of legend is refined for a better analysis of the strain field. Here, the major strain as well as the minor strain distribution is given. The section cut marked as black line was used to compare the results with different blank outlines and drawing depths.

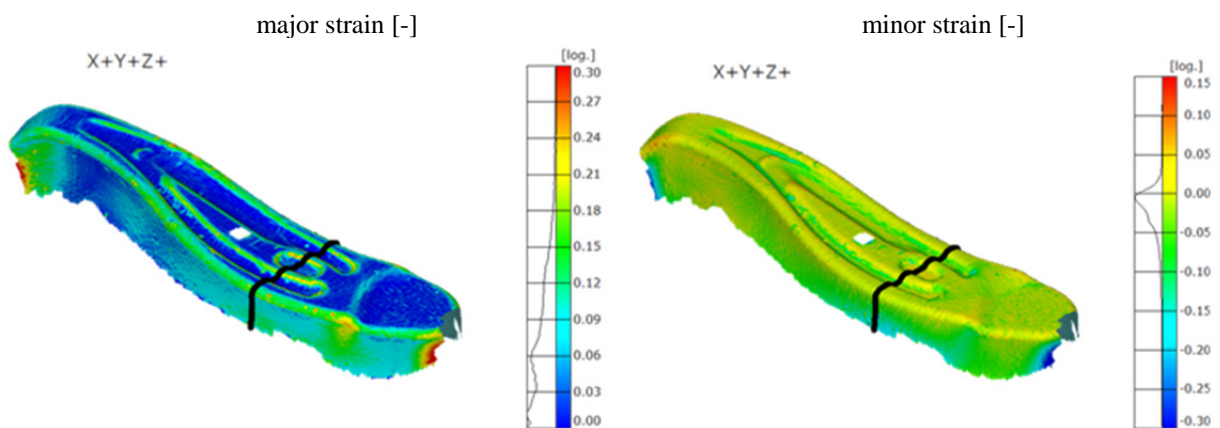


**Figure 2.9.17:** Major and minor strain distribution on the surface of one prototype (blank type 1, full draw)

To estimate the reproducibility of the prototype components, the results of three prototypes (blank type 1, full draw) which were produced with the same process parameter are shown in Figure 2.9.18. The strain fields and the FLC diagrams are in good agreement.

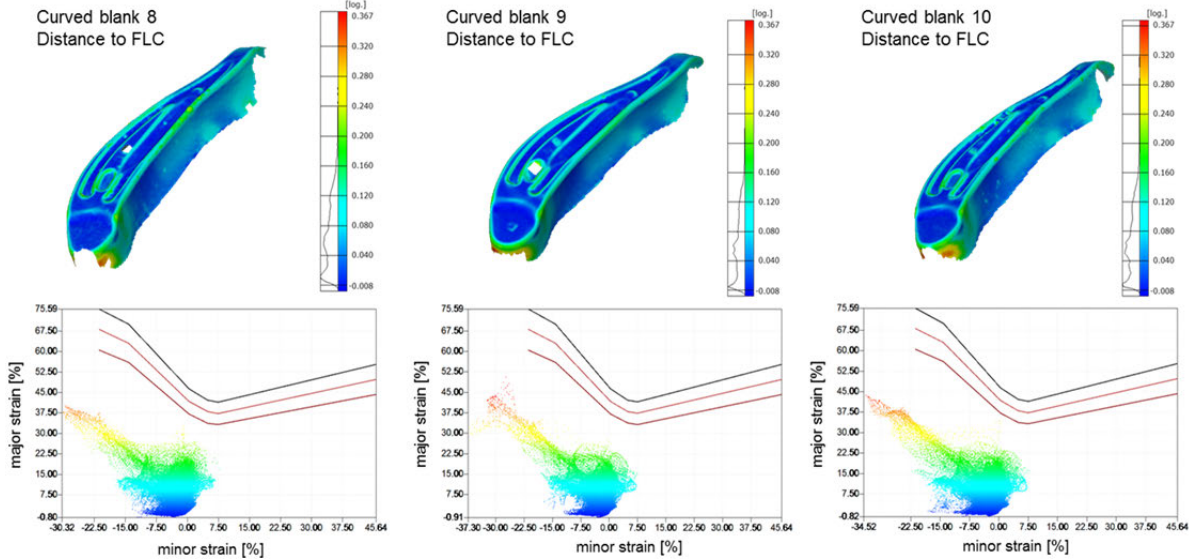


**Figure 2.9.18:** The comparison of the Argus measurements obtained from three prototypes show a good reproducibility of the strain field during forming.

Figure 2.9.19 shows the comparison of the shape and the major strain distribution of the prototypes given in Figure 2.9.12. The section cut which is evaluated is defined in Figure 2.9.17 as black line. Both results are in good agreement. As expected, some scattering can be observed in the major strains curves.

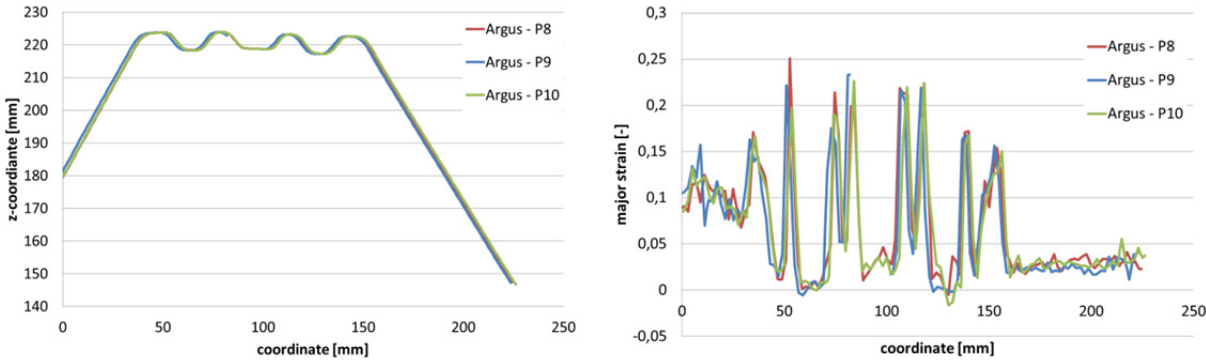


**Figure 2.9.19:** Shape of the deformed sheet (left) and major strain distribution (right) of section cut through 3 exemplary prototypes

## 2.9.3 Model creation and forming simulation of the prototype component

### 2.9.3.1 Model creation

A simulation model has been created based on the tool geometry of the prototype tool elements and the experimental parameters according to the prototype experiments at the laboratory of SZMF.

As it has already been described in Section 2.9.1.4, the geometry of the punch had to be reworked by a milling operation in order to provide a minimum tool gap of 1.5 mm, which corresponds to the material thickness of the prototype material, see Figure 2.9.20. Since the punch was first reworked by a milling operation in order to be adjusted to a material thickness of 1.5 mm and afterwards locally adjusted by manual grinding operations, there were significant differences between the ideal CAD geometry and the ATOS measurement. Therefore the ATOS geometry of the punch has been defined as the tool geometry. The example of the die geometry shows that in general there is a good fit between CAD data and ATOS data. Figure 2.9.21 shows the superposition of both geometries from top view. There are hardly any differences between CAD geometry at the lower end of the cross-member while small differences could be easily adjusted at the upper end.

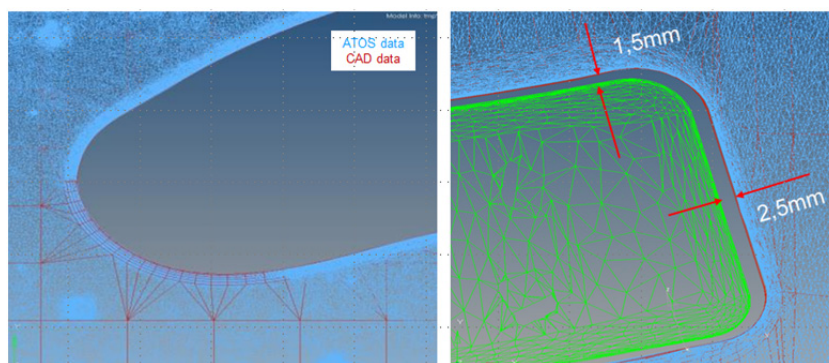


**Figure 2.9.20:** Superposition of CAD and ATOS geometry from top view

The side view shown in Figure 2.9.21 also shows a good fit between contact surface between the die and the binder and in the area of the bending radius. In contrast, the vertical flange could not be measured because of poor optical access of the ATOS laser in this particular area. Therefore in this area the CAD geometry was defined as tool geometry. A small deviation of the inclination of the binder surface between measured and CAD data was considered to be tolerable.

The outcome of similar considerations concerning the binder and support surfaces resulted in tool definitions according to the CAD geometry. The result of the tool set up is shown in Figure 2.9.22. The positioning of the tool elements and the definition of the tool kinematics were done in accordance to the experimental available. Figure 2.9.23 shows the schematic representation of the single steps of the forming simulation.

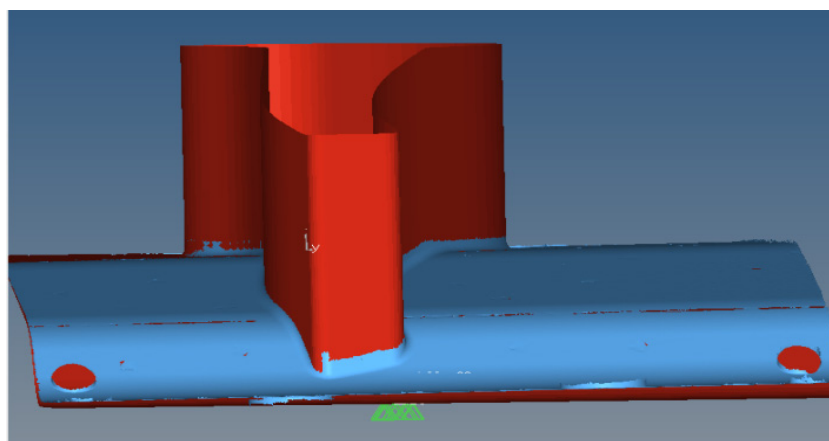


**Figure 2.9.21:** Superposition of CAD and ATOS geometry from side view

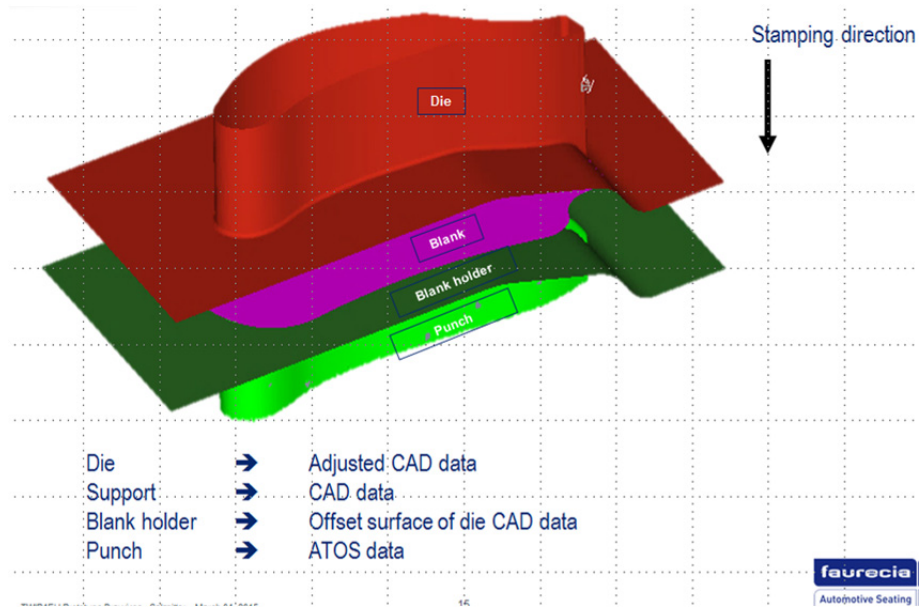


Figure 2.9.22: Final definition of FEM model

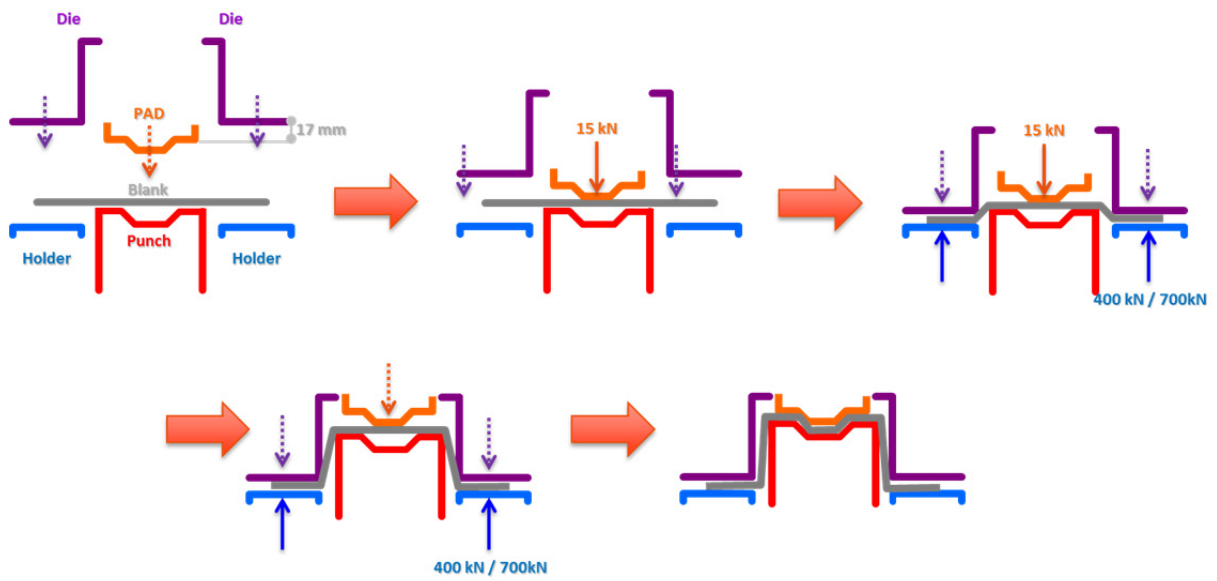
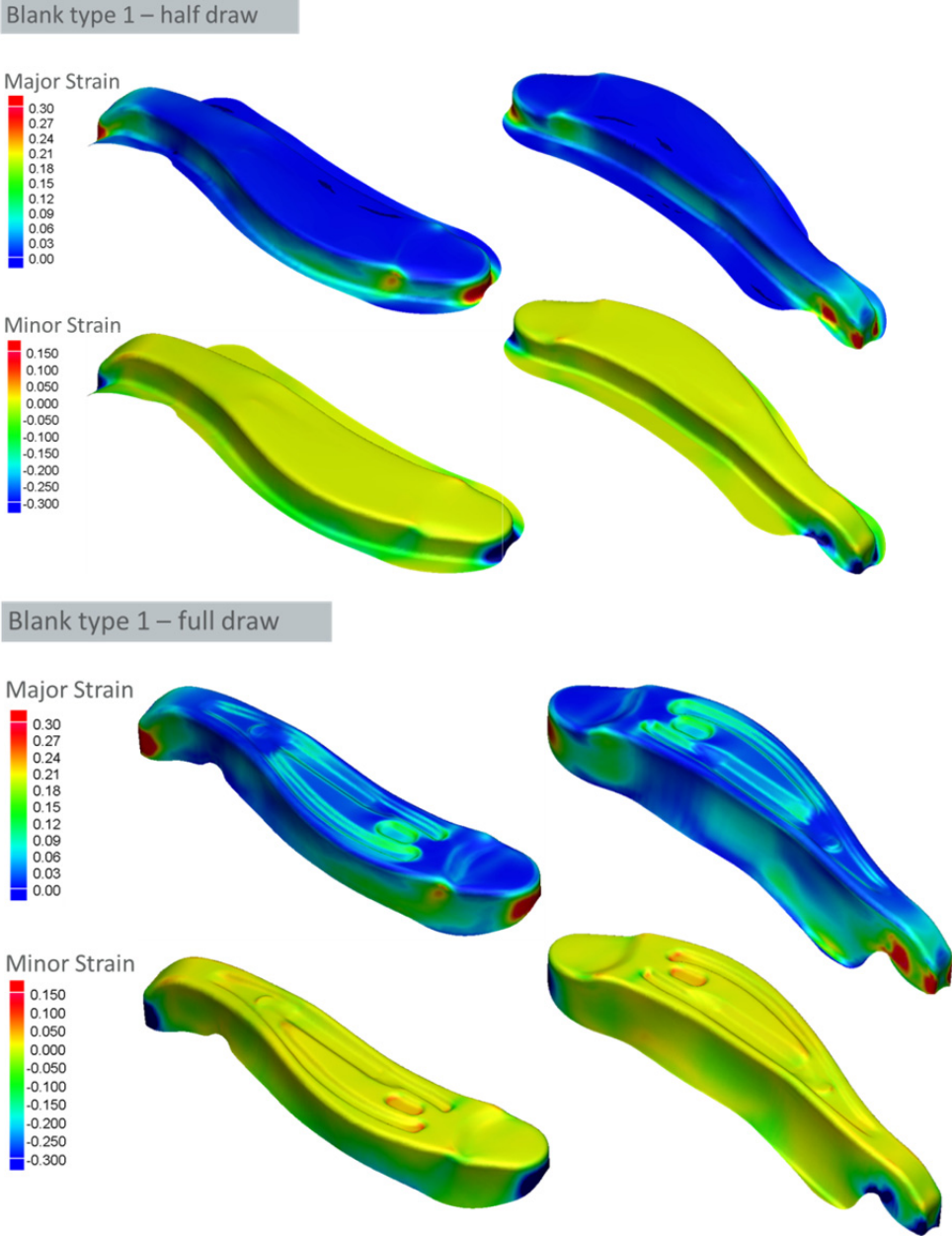


Figure 2.9.23: Modelling the sequence of the different steps of the forming process.

### 2.9.3.2 Simulation of the prototype component

The forming of the prototype components could be successfully simulated with the developed TWIP4EU model. The Figures 2.9.24 and 2.9.25 show the PAM-STAM results of the simulated prototype. The simulation results are shown for both blank types and for two drawing depths. For the simulation a friction coefficient of 0.125 was used which is within the range of typically used values for sheet metal forming.

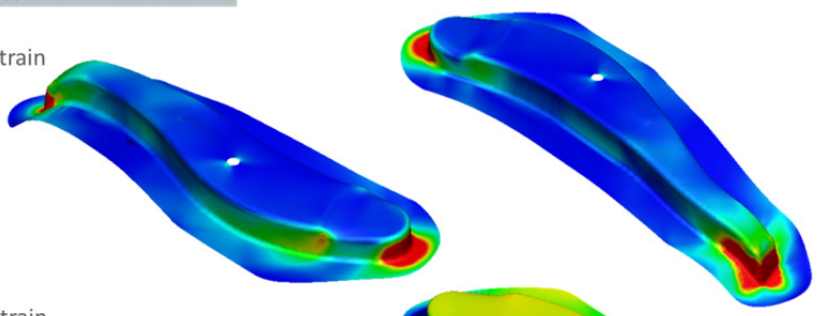
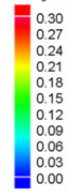


**Figure 2.9.24:** Simulation of the prototype component using blank type one. The results of the half drawn sheet and the full drawn sheet are illustrated.

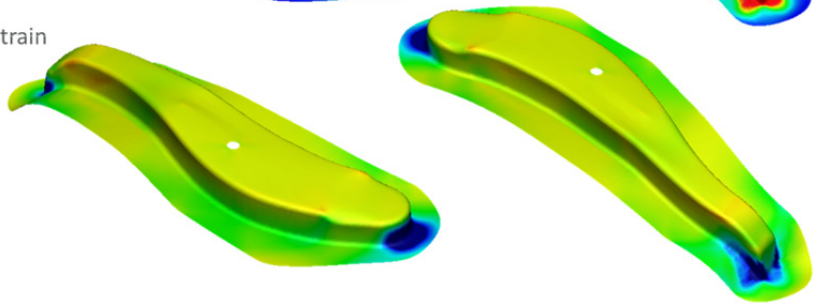
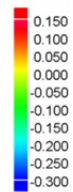


Blank type 2 – half draw

Major Strain

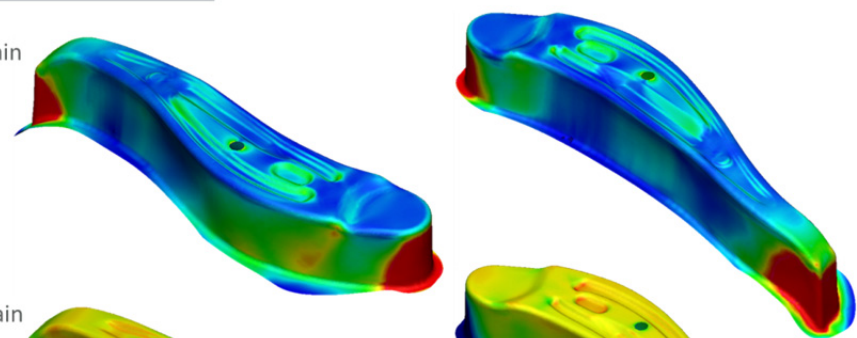
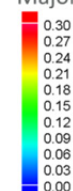


Minor Strain



Blank type 2 – full draw

Major Strain



Minor Strain

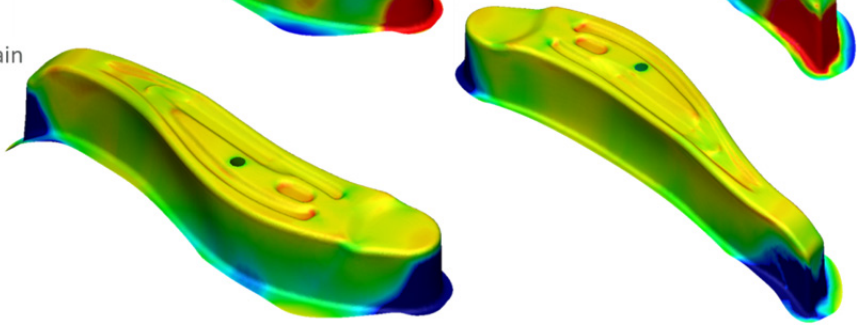
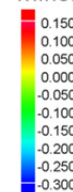


Figure 2.9.25: Simulation of the prototype component using blank type two. The results of the half drawn sheet and the full drawn sheet are illustrated.



## 2.9.4: Comparison prototype simulation with measured data from experiments

### 2.9.4.1 Strain field

A comparison of the major and minor strain field is given in Figure 2.9.26. There is a good agreement between the strain fields from experiment and the strain fields from simulation with the TWIP4EU model. The regions where the highest strains are measured are correctly predicted with the model.

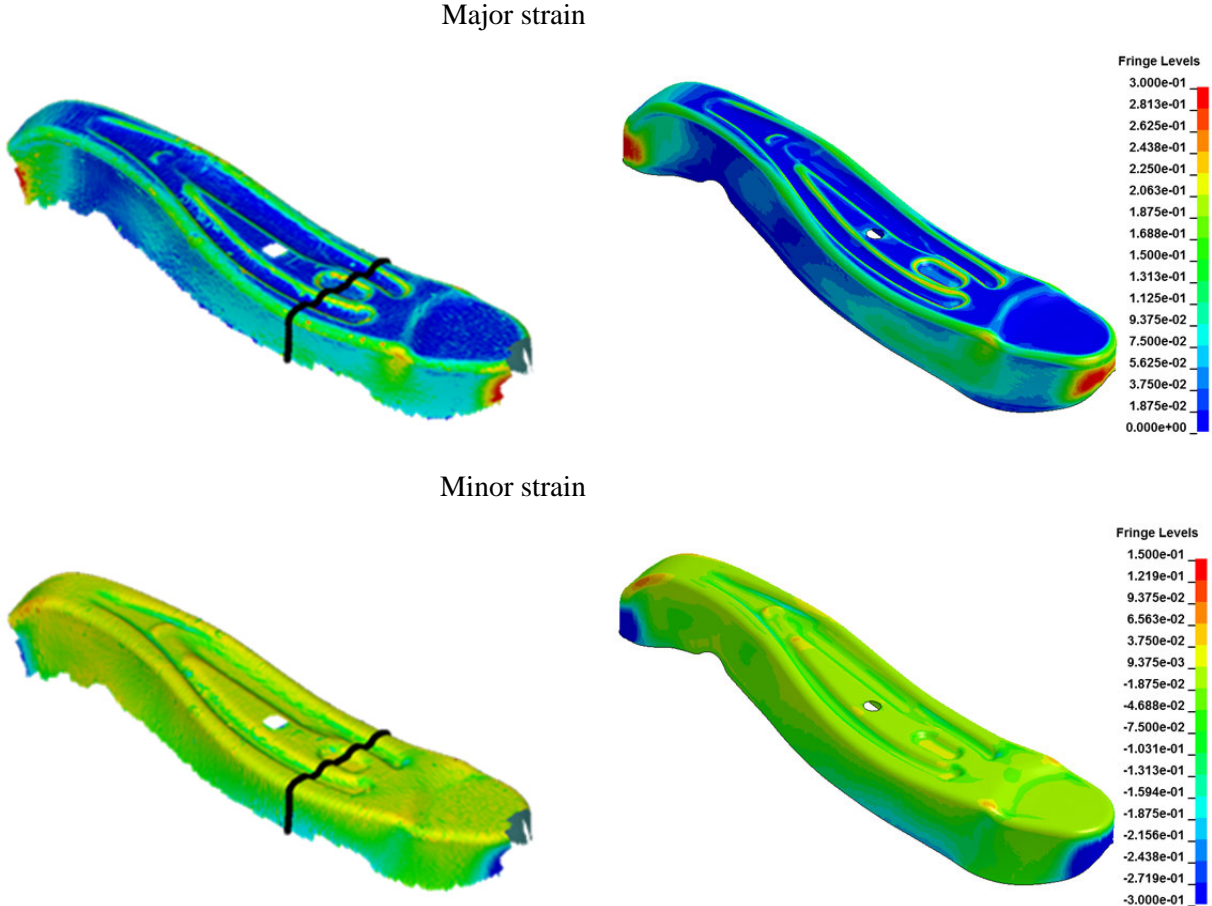


**Figure 2.9.26:** Comparison between the experimental data (left) and the simulation results with the TWIP4EU-model (right). The color scale of the legend is the same for experiment and simulation.

Further, strain data from the section cut through the prototype geometry which was already illustrated in Figure 2.9.17 were compared with simulation results. In Figures 2.9.27 and 2.9.28 the major and minor strain along the given section cut are compared for the fully drawn prototype with blank type 1. In both case there is a good agreement between the experiments and the simulation. It is noted that the absolute values of peaks should be carefully considered, since these values strongly depend on the discretisation of the ARGUS grid as well as on the finite element mesh.

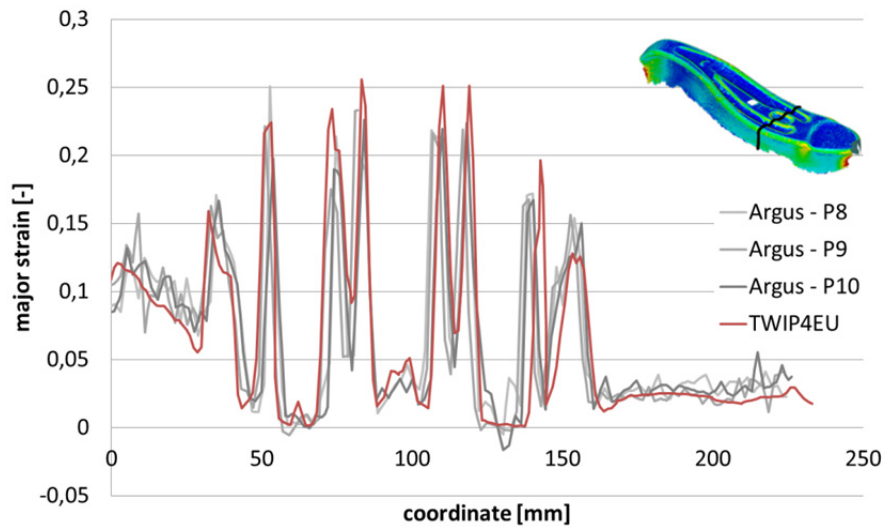


**Figure 2.9.21:** Major strains along the given section cut. Comparison between experimental data and simulation

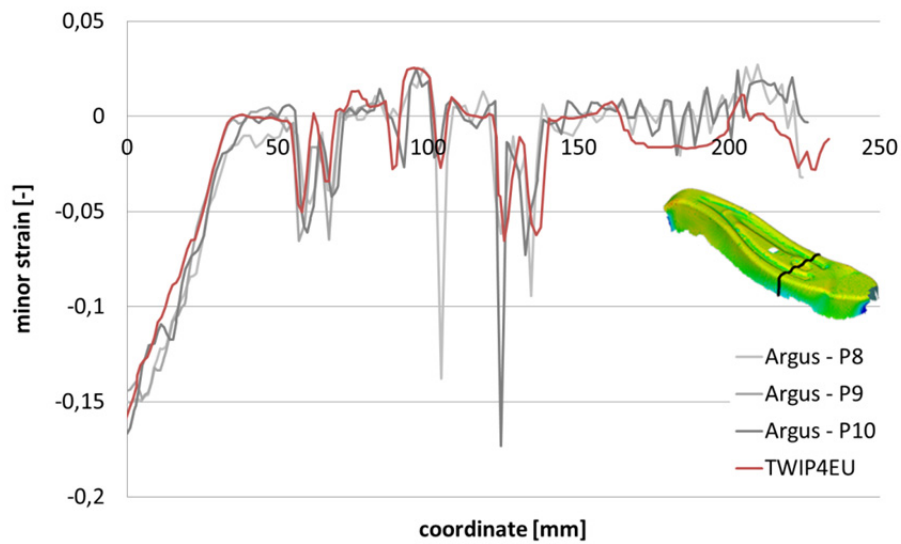


**Figure 2.9.22:** Minor strains along the given section cut. Comparison between experimental data and simulation

### 2.9.4.2 Spring back

For sheet metal forming simulations the prediction of the spring back after forming is an important aspect. The fully drawn prototype with blank type 1 was considered for this analysis since the strongest spring back effect was observed for this part. It was found that the TWIP4EU model overestimates the experimentally observed spring back, which corresponds to the results discussed in Section 2.8.3. Therefore it was analyzed whether the prediction of spring back behavior of the prototype can be improved if the parameter set of the material model is slightly modified. A comparison is given in Figure 2.9.29. For the simulation of TWIP4EU-Parameterset-2 the same hardening parameters were used as in the BUT-test simulation reported in Figure 2.8.34. As one can see, the maximum value of the resultant displacement and also the spring back decreases for both cases of the modified parameters.

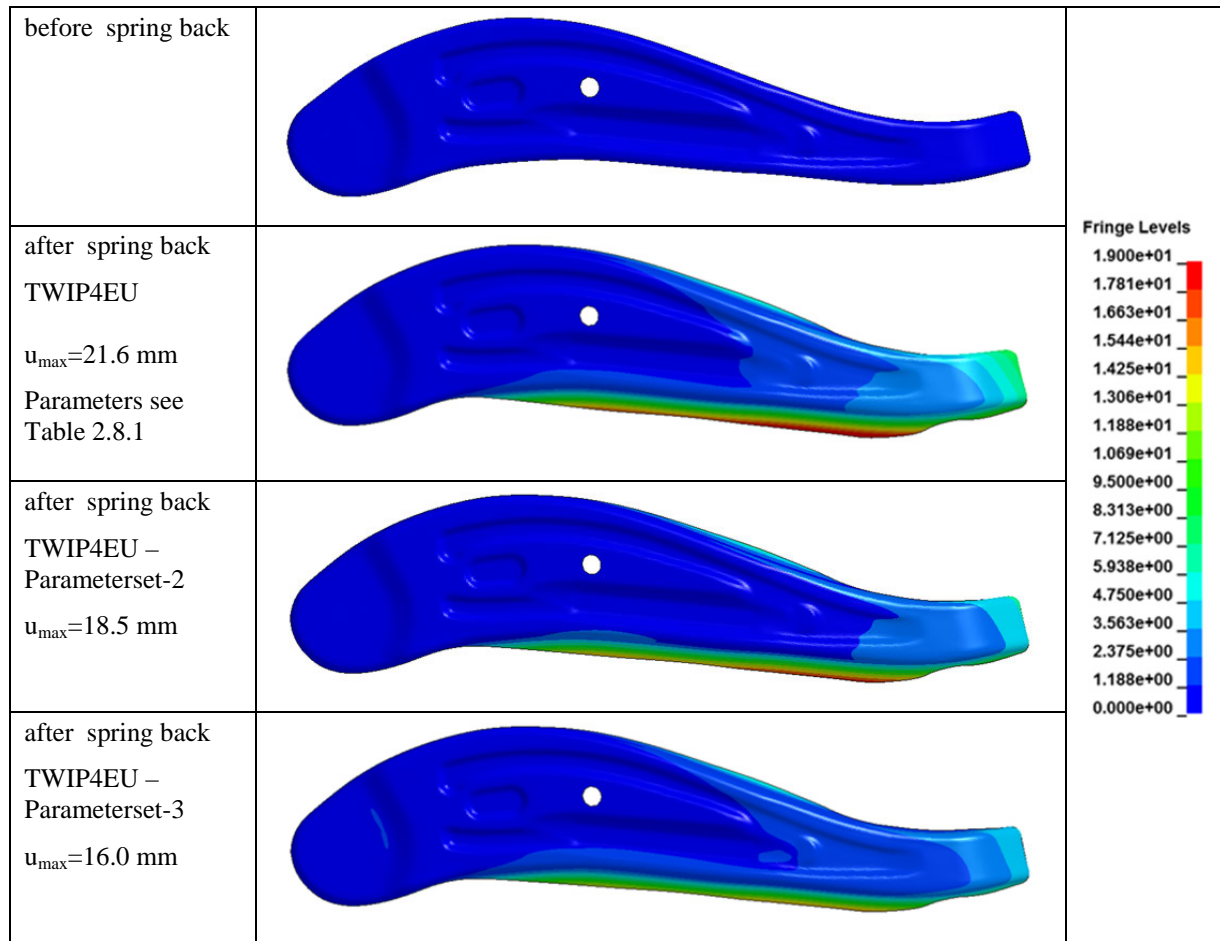


**Figure 2.9.29:** Simulation results of prototype using blank type 1. Resultant displacement after spring back. The result of standard model is compared with two simulations with slightly modified hardening approach. The shape before spring back is also shown (top figure).

A more quantitative comparison of the spring back prediction is given in Figure 2.9.30. Based on the ARGUS measurement the 3D surface information was exported as an STL-net. For comparison with simulation data, the geometries from ARGUS measurement and simulation were automatically aligned to each other with the aim to minimize the average distance between both geometries. The comparison of five different section cuts after alignment is illustrated in Figure 2.9.30 for the simulation using Parameterset-3. A good agreement can be obtained for all the section cuts. The deviations in section cut D are a slightly larger compared to the other cuts but still in an acceptable range. In section cut D it seems that the simulation slightly underestimates the spring-back. Thus, it is expected that the use of Parameterset-2 is also be applicable for spring-back simulation.

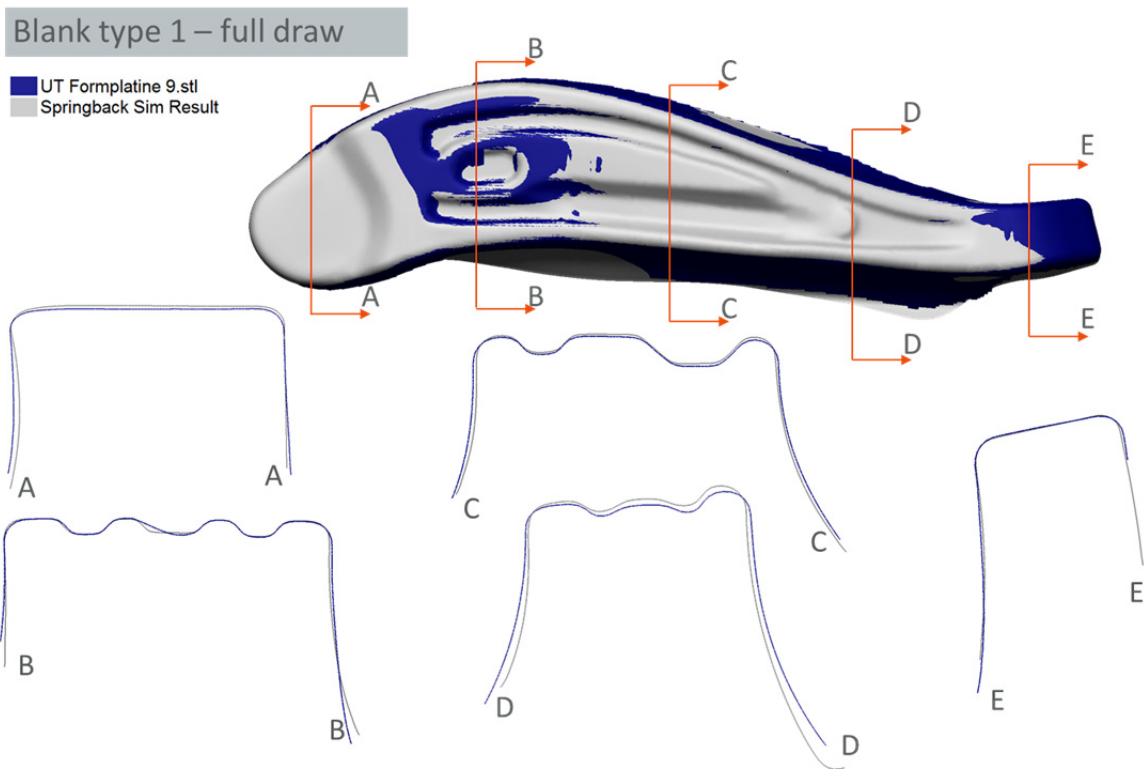


**Figure 2.9.30:** Comparison of the predicted spring back behavior (TWIP4EU-Parameterset-3) with experimental data for five chosen section cuts along the prototype.

### 2.9.4.3 Development of twin volume fraction

Figure 2.9.31 shows the development of the twin volume fraction for different stages of the deep drawing process. Here, blank type 1 is considered. The maximum twin volume fraction is 0.22 at the front region of the prototype. For a better comparison of the intermediate forming states, the legend in Figure 2.9.31 is scaled to a maximum value of 0.15.

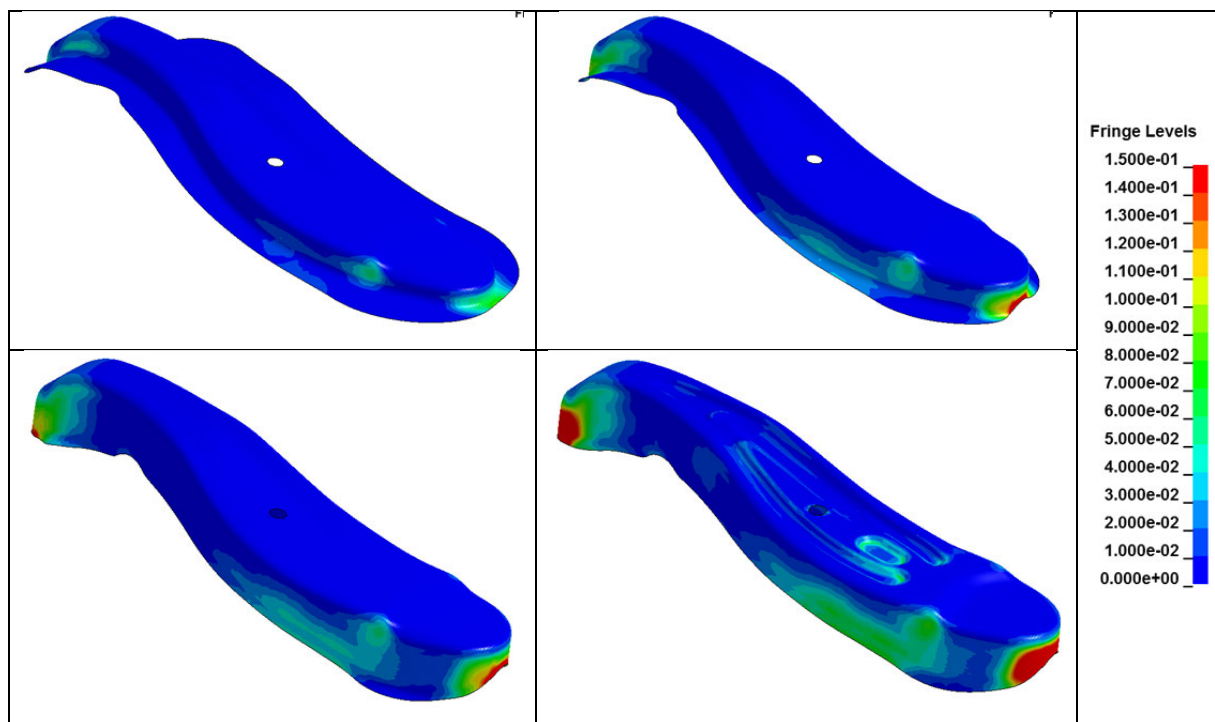


**Figure 2.9.31:** Twin volume fraction at different stages of the deep drawing of the prototype.

## 2.9.5 Hardness measurement on fabricated prototype component

While the work in WP3 is focused on the analysis of the initial state of the material and pre-defined deformation states, this task should analyse the material state after typical sheet forming processes accompanied with complex loading history. Initially it was planned to analyse the twin volume fraction within selected regions of the formed prototype. Based on work done in WP3 it has to be pointed out, that TEM analysis of an industrial part would cause a very high effort but would deliver rather low directly useable information. Therefore a micro hardness mapping was done as alternative and more efficient investigation. The analysis of the hardness measurement was done on prototypes which have also be analysed with the optical strain measurement system. This allows a correlation of strain and hardness distribution. Figure 2.9.32 shows the location of the analysed sections. A fully drawn prototype component produced with blank type 2 was considered for the hardness measurement.

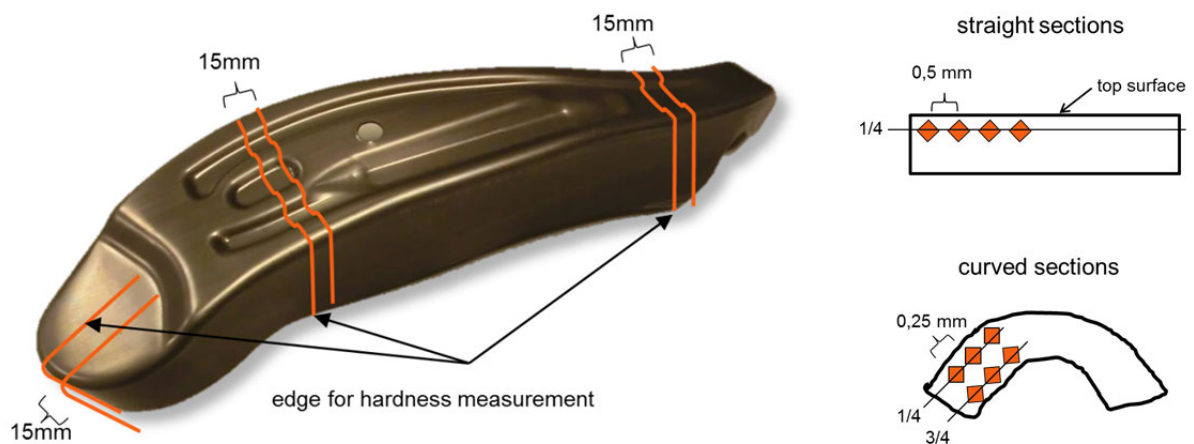


**Figure 2.9.32:** Definition of section cuts for micro hardness mapping (left) and the position of the indents in thickness direction of the sheet (right)

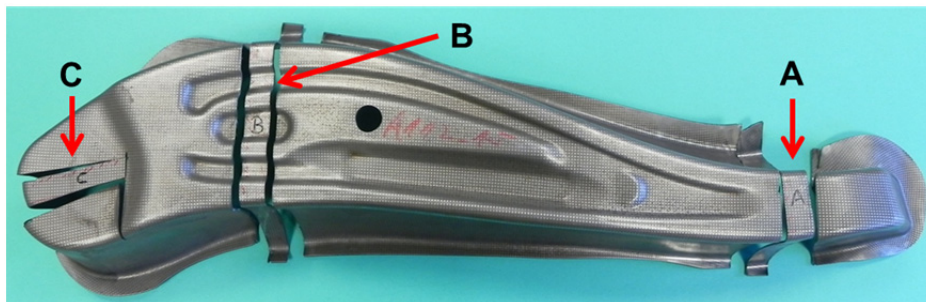


**Figure 2.9.33:** Specimens for micro hardness mapping cut out from a fully drawn prototype component (blank type 2)



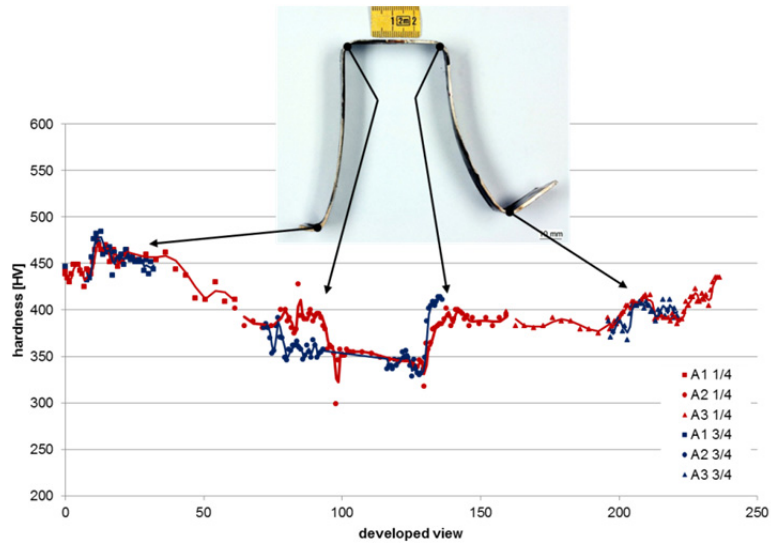


Figure 2.9.34: Results of micro hardness mapping in section cut A

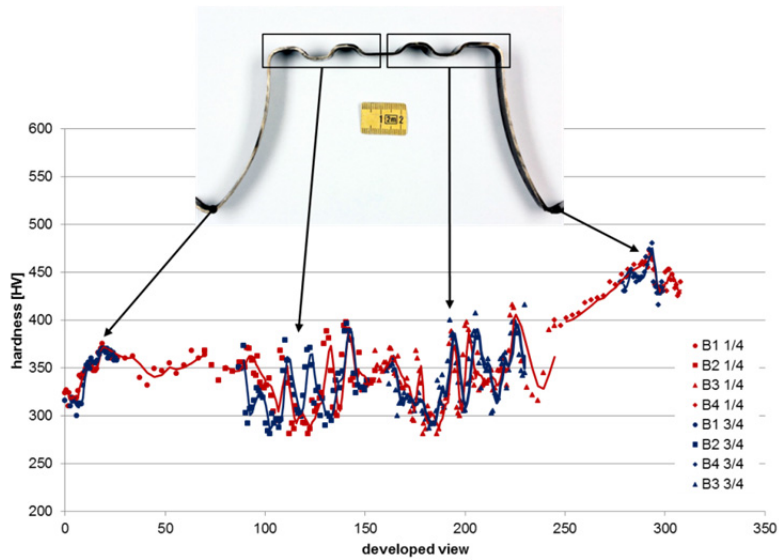


Figure 2.9.35: Results of micro hardness mapping in section cut B

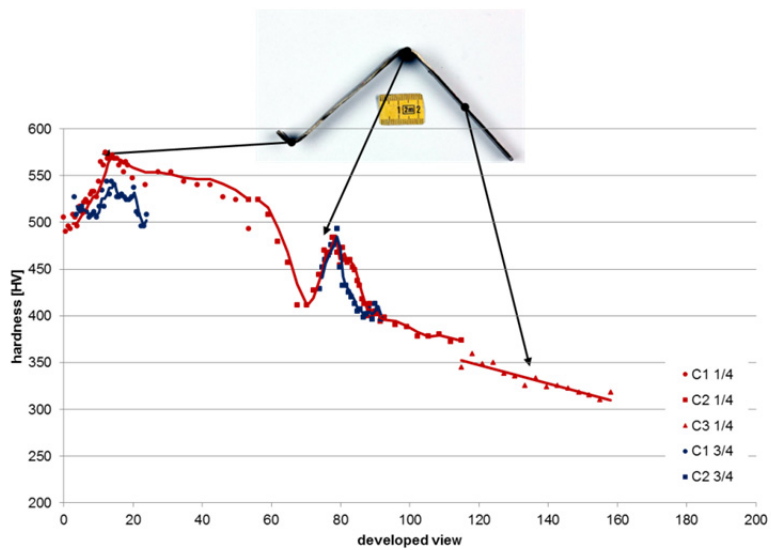


Figure 2.9.36: Results of micro hardness mapping in section cut C



## 2.10 Conclusions

A material model that captures the main characteristics of TWIP-steels has been successfully developed and implemented into two commercial finite element software packages. Thus, the main objective of the project was reached. The developed material model is able to describe the experimental observations with good accuracy. The typical standard tests like tensile test, bulge test and Nakajima test can be reproduced with better accuracy compared to a standard model (flow curve and Hill48 yield locus). Some deviations can be observed for the bending under tension test and for the cup drawing test. Since kinematic hardening plays a more significant role in these tests, it is expected that a more precise description of the Bauschinger effect could further improve the current model approach. The simulation of the prototype could be successfully realized with the new TWIP4EU material model. Here, the strain fields are in good agreement with the experiments. This shows that the TWIP4EU material model is also applicable for industrial forming simulations. It is noted, that this model has more parameters which have to be identified in comparison to a standard model. On the other hand, this gives more flexibility to adjust the model to the complex forming behavior of modern TWIP-steels. A procedure for the identification of the model parameter is proposed.

A detailed experimental test program was carried out to analyse different aspects of the material behavior on microscale and on macroscopic level, e.g. the evolution of twins, stress dependent hardening or Bauschinger effect. These analyses give a valuable insight into the forming behavior and also a better general understanding of the material. The results were used to develop the macroscopic model, to identify the model parameter and finally to validate the TWIP4EU-model.

As prototype component, a back rest side member was chosen and successfully produced. To demonstrate the very high formability of TWIP-steel, different blank shapes were used to form the part. The chosen prototype shows a typical application of TWIP-steels where high strength and high formability are desired at the same time.

## 2.11 Exploitation and impact of the research results

The project results are applicable to support the introduction of TWIP-steels for European automotive application. The core part of the project was the development of new material model (TWIP4EU-model) for the simulation of sheet metal forming processes of TWIP-steel. A detailed description of the developed model and the corresponding algorithmic treatment for the implementation into finite element software packages is documented and available. Thus, one of the main objectives of this project could be achieved. Within the project, the material model was already implemented into test versions of two commercial software packages. The availability of the TWIP4EU model for commercial use is currently under consideration. The final decision of the software companies will depend on the demand of the TWIP4EU model from industrial customers.

The extensive experimental characterization of the TWIP-steel material gives a detailed insight into the behavior of the analyzed TWIP-steel on both the microscale and on macro scale. The experimental results are available for further use. Based on these results, a parameter set for accurate simulation of typical forming processes is provided for the considered TWIP-steel grade.

The chosen demonstrator part represents a typical application of TWIP steel in automotive industry since it combines the needs for high strength and high formability. It clearly shows the applicability of this class of advanced high strength steels for sheet metal forming. TWIP-steels offer a high light weight potential through reduced material usage due to the combination of strength and ductility and a lower density (-5%) compared to conventional steels.

The dissemination of the results is ensured by the project consortium which includes two software companies, a steel producer and an automotive supplier. The obtained results were presented at several national and international conferences and workshops. Several publications are available in conference proceedings and also in industry related journals. An overview is given in Section 2.1.3. Finally, the project was presented at the *Blechexpo* trade fair 2015 in Stuttgart by Fraunhofer IWM. Figure 2.10.1 shows the TWIP4EU demonstrator part and the corresponding information board.



**Figure 2.10.1:** TWIP4EU demonstrator part at the *Blechexpo* trade fair 2015 in Stuttgart. Bottom right: Corresponding information board

## **List of Abbreviations**

BSE: Back-scattered electrons

EBSD: Electron backscatter diffraction

EELS: Electron energy loss spectroscopy

ND: Normal direction (perpendicular to plane of the sheet)

RD: Rolling direction

SEM: Scanning electron microscope

TD: Transverse direction

TEM: Transmission electron microscopy

TWIP: Twinning induced plasticity



## List of Figures

<b>Figure 1.2.1:</b> Seat frame including the backrest side member which was chosen as prototype component .....	5
<b>Figure 1.2.2:</b> Engineering stress-strain-curves from uniaxial tensile tests for three different directions	7
<b>Figure 1.2.3:</b> Prototype component made of TWIP-steel.....	13
<b>Figure 1.2.4:</b> Major strain field after forming. Comparison between the experimental data (left) and the simulation results with the TWIP4EU-model (right). The color scale of the legend is the same for experiment and simulation. ....	14
<b>Figure 2.1.1:</b> Work package overview .....	16
<b>Figure 2.2.1:</b> Engineering stress-strain curves of the pre-strained TWIP-steel from initial characterization .....	20
<b>Figure 2.2.2:</b> Belt casting plant to be installed in Peine .....	20
<b>Figure 2.3.1:</b> EBSD analysis on the initial material using two different set-ups, inverse pole figure map. Left: One with larger step size (0.25 $\mu\text{m}$ ) to cover a larger area and get texture information as well as grain size statistic. Right: A one with a finer step size (0.05 $\mu\text{m}$ ) to characterize twins and fine details in the microstructure. ....	22
<b>Figure 2.3.2:</b> SEM/BSE images of the microstructure.....	22
<b>Figure 2.3.3.:</b> Texture analysis from EBSD measurement. The extensive analyses showed that texture was similar on both sides and that there were small differences between surface (15% depth) and centre (35% depth). The texture was a weak retained fcc rolling texture. ....	23
<b>Figure 2.3.4.:</b> Left: Diffraction pattern from a crystal grain showing the spots from matrix respectively twin lattices. The (111) plane is the twinning habitus plane and is here close to parallel to the electron beam. Right: Dark field image showing bend twins by using the (200) reflection as indicated in the diffractogram above. Deformation degree was 25 % (engineering strain). The diagram below represents the intensity along the indicated line .....	25
<b>Figure 2.3.5.:</b> Intensity diagram showing the intensity from the (200) spot along the red line in the dark field shown in Figure 2.3.4.....	25
<b>Figure 2.3.6:</b> Twin volume fraction [%] as functions of strain .....	26
<b>Figure 2.3.7:</b> Mean twin spacing in nm as function of the applied strain .....	26
<b>Figure 2.3.8:</b> The specimens used for in-situ tensile test and shear test.....	27
<b>Figure 2.3.9:</b> Texture of the TWIP-steel after different degrees of tensile deformation. The first set of pole-figures was without any deformation. The second set was collected after 8% plastic deformation and the third set after 26% plastic deformation (elongation in X direction as measured on the specimen). ....	27
<b>Figure 2.3.10:</b> Texture of the TWIP-steel after different degrees of shear deformation.....	28
<b>Figure 2.3.11:</b> Major and minor strain in the 3 bulge tests (OBS scales are different in the strain bars) .....	29
<b>Figure 2.3.12:</b> Pole figures for the starting material and the 3 bulge tests at different strains. Not deformed (a), 15% (b), 25% (c), and 40% (d).The step during EBSD analysis was 2.5 $\mu\text{m}$ and the matrix was 489*366 pixels (1.2*0.9 mm). ....	30
<b>Figure 2.3.13:</b> Bulge test: EBSD orientation maps with colours according to IPF colouring in the rolling direction. Not deformed (top left), 15% (top right), 25% (bottom left), and 40% (bottom right).The step during analysis was 0.5 $\mu\text{m}$ and the matrix was 432*361 pixels. The scale bar is 100 $\mu\text{m}$ . ....	31
<b>Figure 2.3.14:</b> Example of specimen with clear stripes; Specimen 4-03, tensile specimen from macroscopic test. The fractured surface was dominated by shear, mostly flat surfaces with $\mu$ -dimples. The final (residual) rupture surface was small. The surface contained large dimples and visible inclusions/large particles .....	32
<b>Figure 2.4.1:</b> Test specimen used for the tensile testing in TWIP4EU .....	34
<b>Figure 2.4.2:</b> Engineering stress-strain-curves from uniaxial tensile tests for three different directions .....	35
<b>Figure 2.4.3:</b> Flow-curves from uniaxial tensile tests for three different directions. ....	35
<b>Figure 2.4.4:</b> Lankford coefficients (r-values) for three different directions. ....	36
<b>Figure 2.4.5:</b> Tensile tests under several different strain rates. ....	36

<b>Figure 2.4.6:</b> Tensile tests under several different strain rates. The three lower curves for the highest strain rates are from testing in a different machine where strain measurement was made with a laser extensometer. The scatter can be attributed to the difficulties in measuring the strain at these rates. ...	37
<b>Figure 2.4.7:</b> Temperature increase as function of applied deformation for three different strain rates .....	37
<b>Figure 2.4.8:</b> Test principle bulge test [Vucetic2012].....	38
<b>Figure 2.4.9:</b> Pressure-displacement curves of the center of the bulge specimen. ....	39
<b>Figure 2.4.10:</b> Displacement in z-direction for different pressure levels, cut parallel to the rolling direction.....	39
<b>Figure 2.4.11:</b> True strain - true thickness strain curves of 3 different TWIP-steel batches .....	40
<b>Figure 2.4.12:</b> Major and minor strain distribution of three different bulge tests for the standard TWIP-steel material at a pressure of 230 bar. ....	40
<b>Figure 2.4.13:</b> Strain states achieved by the bulge tests for different pressure levels .....	41
<b>Figure 2.4.14:</b> Comparison of the flow curves from uniaxial tensile test and bulge test. ....	41
<b>Figure 2.4.15:</b> Comparison of major and minor strains at the dome of the bulge specimen as function of the dome height. ....	42
<b>Figure 2.4.16:</b> Development of the major strain as function of the minor strain at the centre of the bulge specimen. ....	42
<b>Figure 2.4.17:</b> The first part of tensile tests. The mean Young's modulus is 182150 MPa with a mean deviation of 7191 MPa. The moduli are extracted from true stress-strain data.....	43
<b>Figure 2.4.18:</b> The mean Young's modulus for all these load-unloading sequences is 173650 MPa with a mean deviation of 5778 MPa. There is no apparent reduction due to plastic deformation. ....	44
<b>Figure 2.4.19:</b> The instantaneous tangent modulus of every loading-unloading sequence. The mean value represents each level of plastic deformation in Table 2.4.1. To the right the direction of the x-axis in the left figure is shown.....	44
<b>Figure 2.4.20:</b> The apparent moduli from the measurements presented in Figures 2.4.17 and 2.4.18. The points show the modulus at increasing plastic deformation.....	45
<b>Figure 2.4.21:</b> The three measurements of the apparent Young's moduli. The two first are values for the initial modulus. The last one represents the mean average apparent moduli from Figure 2.4.17. ...	45
<b>Figure 2.4.22a:</b> Results of cyclic tension-compression tests with different strain amplitudes. ....	47
<b>Figure 2.4.22b:</b> Results of cyclic tension-compression tests after several cycles. The strain amplitude is $\pm 1\%$ .....	47
<b>Figure 2.4.23:</b> Stress-strain curves from the pre-strained specimens .....	48
<b>Figure 2.4.24:</b> The Bending Under Tension (BUT) machine.....	49
<b>Figure 2.4.25:</b> The shape of the strips after they have been drawn in the BUT machine. The curvature of the strip is a measure for spring-back. ....	49
<b>Figure 2.4.26:</b> The curvature is evaluated in a continuous row of points. When a locally accepted deviation is reached the set of points all contribute to a global radius with a least square approach....	50
<b>Figure 2.4.27:</b> Schematic forming limit curve .....	51
<b>Figure 2.4.28:</b> FLCs determined by means of cross section method and time dependent linear best fit method.....	52
<b>Figure 2.4.29:</b> Comparison of 3 parallel specimen – 20 mm .....	53
<b>Figure 2.4.30:</b> Comparison of 3 parallel specimen – 130 mm .....	53
<b>Figure 2.4.31:</b> Comparison of 3 parallel specimen – 200 mm .....	54
<b>Figure 2.4.32:</b> Comparison of all nine specimens. It is noted that the plotted strains states are evaluated for defined punch displacements which do not represent the onset of failure. ....	55
<b>Figure 2.4.33:</b> Tools for forming experiment.....	55
<b>Figure 2.4.34:</b> Major and minor strain distribution of a square cup with 60 mm drawing depth.....	56
<b>Figure 2.4.35:</b> Strain states experimentally achieved by forming of square cups with three different drawing depths. ....	56
<b>Figure 2.4.36:</b> Global punch force vs. punch stroke of the formed square cups. ....	57
<b>Figure 2.5.1:</b> Typical hardening curve of a slip system and interpretation of the material parameter according to Equation 2.5.5.....	59
<b>Figure 2.5.2:</b> Detailed description of the hardening matrix $h_{\alpha\beta}$ .....	60
<b>Figure 2.5.3:</b> Procedure for creating the microstructure model and the parameter identification. ....	60



<b>Figure 2.5.4:</b> Comparison between the experimentally measured texture and texture with reduced number of orientations to be used as input for the microstructure model (left) Illustration of the discrete orientations (right). The orientations are projected in the RD-TD-plane of the sheet. ....	61
<b>Figure 2.5.5:</b> Results of the first pre-study of the stress-strain curve (left) and the twin volume fraction evolution (right) for different combinations of hardening parameter.....	63
<b>Figure 2.5.6:</b> True stress strain curve in rolling direction. Comparison between experimental data and the prediction of the microstructure model. ....	64
<b>Figure 2.5.7:</b> Lankford coefficients in rolling direction (0 deg.) and transverse direction (90 deg). Comparison between experimental value at 20 % strain and the prediction of the microstructure model.....	64
<b>Figure 2.5.8:</b> Development of the twin volume fraction. Comparison between experimental data obtained from WP3 and from the simulation of the microstructure model.....	65
<b>Figure 2.5.9:</b> Comparison of the initial yield surface based on the Barlat YLD2000-2D model and some initial yield points based on micromechanical simulations.....	65
<b>Figure 2.6.1:</b> Yield locus for the TWIP-steel (left) and true plastic strain - true stress curves from experiment and simulation (right).....	68
<b>Figure 2.6.2:</b> Comparison of the flow curve in rolling direction and in transverse direction: Measurement versus simulation. ....	68
<b>Figure 2.6.3:</b> Major strain on section cuts through Nakajima specimen with width of 20 mm .....	69
<b>Figure 2.6.4:</b> Major strain on section cuts through Nakajima specimen with width of 200 mm .....	69
<b>Figure 2.6.5:</b> Major strain on section cuts through bulge test at low pressure.....	70
<b>Figure 2.6.6:</b> Major strain on section cuts through bulge test at high pressure.....	70
<b>Figure 2.6.7:</b> Major strain on section cuts through square cup with 20 mm drawing depth .....	71
<b>Figure 2.6.8</b> Major strain on section cuts through square cup with 60 mm drawing depth.....	71
<b>Figure 2.6.9</b> Illustration of the dynamical Hall-Petch effect [De Cooman2012]. Mechanical twins are formed due to the low stacking fault energy. They gradually reduce the effective glide distance of dislocations, resulting in the very high strain hardening observed in TWIP-steel. ....	72
<b>Figure 2.6.10</b> Tensile behaviour of TWIP-steels with coarse grains (between 20 $\mu\text{m}$ and 40 $\mu\text{m}$ ) for a wide range of carbon and manganese contents [Bouaziz2011].....	73
<b>Figure 2.6.11</b> Identified evolution of the maximum number of dislocations stored at twin boundaries and the lattice friction stress [Bouaziz2011] .....	76
<b>Figure 2.6.12:</b> Summary of the twip-steel material model considering the extension from 1d formulation to a 3d tensorial formulation.....	77
<b>Figure 2.6.13:</b> Factor $k_{\text{TWIN}}$ to account on stress state dependent twinning.....	78
<b>Figure 2.6.14:</b> Influence of triaxiality on the twin volume fraction. ....	78
<b>Figure 2.6.15:</b> Cyclic test (left) and tensile test (right): Experiments and simulations with Chaboche extension (green curves) and within the standard formulation (red curves) .....	79
<b>Figure 2.6.16:</b> Extended TWIP-steel material model.....	80
<b>Figure 2.7.1:</b> Elastic trial step for the TWIP4EU von Mises based material model.....	83
<b>Figure 2.7.2:</b> Radial return for the TWIP4EU von Mises based material model. ....	83
<b>Figure 2.7.4:</b> Implemented versions for stress state dependent twinning.....	86
<b>Figure 2.7.5:</b> Stress return algorithm for the TWIP4EU-Barlat-YLD2000 version. ....	87
<b>Figure 2.7.6:</b> Iterative procedure for the plane stress condensation of the constitutive law.....	87
<b>Figure 2.7.7:</b> Stress-strain behavior in tensile test: 1D-hardening model Bouaziz vs. 3D-von Mises based TWIP4EU implementation in LS-DYNA (top right), and evolution of internal variables (below). ....	89
<b>Figure 2.7.8:</b> Load-displacement curve 90°-tensile test (left): Experimental results vs. TWIP4EU-model implemented in LS-DYNA (red), implemented in PAM-STAMP (green), IWM-Abaqus implementation (violet), geometry (middle), discretization of an eighth of the specimen with solid elements (right). ....	90
<b>Figure 2.7.9:</b> Shear Test (KIMAB): Load-relative Displacement curve experimental results vs. TWIP4EU-Model implemented in LS-DYNA: von Mises version vs. Barlat YLD2000-2D version..	91
<b>Figure 2.7.10:</b> Solid vs. shell discretization of a tensile test .....	92
<b>Figure 2.7.11:</b> Deformed tensile specimen and equivalent plastic strain: Solid vs. shell formulation.	92
<b>Figure 2.7.12:</b> Load-Displacement curve solid vs. shell .....	92

<b>Figure 2.7.13:</b> Twinning evolution of the considered TWIP-steel under uniaxial tension. The experimental data correspond to the data given in Table 2.3.2 .....	94
<b>Figure 2.7.14:</b> Numerical model for the simulation of the tensile test. Discretization of the specimen with shell elements, an element size of 1 mm was used. ....	94
<b>Figure 2.7.15:</b> Tensile test 0°: Stress-strain behavior: Experimental vs. simulation results (TWIP4EU-model based and 3-Parameter Barlat in combination with a hardening curve).....	94
<b>Figure 2.7.16:</b> Biaxial flow curve of bulge test vs. TWIP4EU-model hardening curve under biaxial loading for varying stress dependence parameters $m_i$ . ....	95
<b>Figure 2.8.1:</b> Specimen with an electrochemically etched pattern (left). Improved pattern with laser beam applied (right). ....	96
<b>Figure 2.8.2:</b> Major strain data from section cut of 20 mm Nakajima specimen .....	97
<b>Figure 2.8.3:</b> Minor strain data from section cut of 20 mm Nakajima specimen.....	97
<b>Figure 2.8.4:</b> Major strain data from section cut of 130 mm Nakajima specimen .....	98
<b>Figure 2.8.5:</b> Minor strain data from section cut of 130 mm Nakajima specimen.....	98
<b>Figure 2.8.6:</b> Major strain data from section cut of 200 mm Nakajima specimen .....	98
<b>Figure 2.8.7:</b> Minor strain data from section cut of 200 mm Nakajima specimen.....	99
<b>Figure 2.8.8:</b> Major and minor strains of the bulge test performed with 240 bar.....	99
<b>Figure 2.8.9:</b> Major and minor strain of the square cup with 20 mm drawing depth .....	100
<b>Figure 2.8.10:</b> Major and minor strain of the square cup with 40 mm drawing depth .....	100
<b>Figure 2.8.11:</b> Major and minor strain of the square cup with 60 mm drawing depth .....	101
<b>Figure 2.8.12:</b> Tensile test in rolling direction .....	102
<b>Figure 2.8.13:</b> Tensile test in 45 degree to rolling direction .....	102
<b>Figure 2.8.14:</b> Tensile test in 90 degree to rolling direction .....	102
<b>Figure 2.8.15:</b> Bulge test - Comparison of the experimentally measure strain fields and the numerical results at an oil pressure of 230 bar. ....	103
<b>Figure 2.8.16:</b> Bulge test – major strains in the cut parallel to the rolling direction. Comparison between experimental data and simulation.....	103
<b>Figure 2.8.17:</b> Bulge test – minor strains in the cut parallel to the rolling direction. Comparison between experimental data and simulation.....	104
<b>Figure 2.8.18:</b> Bulge test – minor strains in the cut parallel to the transverse direction. Comparison between experimental data and simulation.....	104
<b>Figure 2.8.19:</b> Bulge test – minor strains in the cut parallel to the transverse direction. Comparison between experimental data and simulation.....	104
<b>Figure 2.8.20:</b> Bulge test – major strains in the cut parallel to the transverse direction. Comparison of the major strain obtained from TWIP4EU model considering the stress dependent hardening and without stress depending hardening. ....	105
<b>Figure 2.8.21:</b> Major strain along a cut parallel to rolling direction for the 20 mm Nakajima specimen. Punch stroke 33.8 mm.....	106
<b>Figure 2.8.22:</b> Minor strain along a cut parallel to rolling direction for the 20 mm Nakajima specimen. Punch stroke 33.8 mm.....	106
<b>Figure 2.8.23:</b> Major strain along a cut parallel to rolling direction for the 130 mm Nakajima specimen. Punch stroke 26.8 mm.....	106
<b>Figure 2.8.24:</b> Minor strain along a cut parallel to rolling direction for the 20 mm Nakajima specimen. Punch stroke 26.8 mm.....	107
<b>Figure 2.8.25:</b> Major strain along a cut parallel to rolling direction for the 200 mm Nakajima specimen. Punch stroke 34.7 mm.....	107
<b>Figure 2.8.26:</b> Minor strain along a cut parallel to rolling direction for the 20 mm Nakajima specimen. Punch stroke 34.7 mm.....	107
<b>Figure 2.8.27:</b> Force-displacement curve of the punch. Comparison of experiments and simulation. ....	108
<b>Figure 2.8.28:</b> Force-displacement curve of the punch. Comparison of experiments and simulation. ....	109
<b>Figure 2.8.29:</b> Major strains in a section cut parallel to the rolling direction .....	109
<b>Figure 2.8.30:</b> Major strains in a section cut in diagonal direction of the cup .....	110
<b>Figure 2.8.31:</b> Simulation of the bending under tension test, divided into three steps.....	111
<b>Figure 2.8.32:</b> Numerical model for to simulation of the BUT-test.....	111

<b>Figure 2.8.33:</b> Comparison between the numerical prediction and the experimental data of the BUT-test. ....	112
<b>Figure 2.8.34:</b> Comparison between the numerical prediction and the experimental data of the BUT-test with modified parameter set. ....	112
<b>Figure 2.8.35:</b> Comparison between the numerical prediction and the experimental data of the BUT-test: TWIPEU model including Chaboche-type extension.....	112
<b>Figure 2.9.1:</b> Seat Frame .....	116
<b>Figure 2.9.2:</b> CAD model of the backrest sidemember (left) and blank dimensions 272 mm x 679.9 mm x 1,5 mm (right) .....	116
<b>Figure 2.9.3:</b> Lower part of the chosen prototype tool.....	117
<b>Figure 2.9.4:</b> Upper part of the chosen serial tool.....	117
<b>Figure 2.9.5:</b> CAD model of the punch geometry (left). Definition of necessary adaption of existing tools to the sheet thickness of the pre-series TWIP-steel (right).....	118
<b>Figure 2.9.6:</b> Gap between punch and tools after being re-milled. ....	118
<b>Figure 2.9.7:</b> Deviations of punch shape between the first and the second manual rework. It can be seen that most of the second manual rework was done in the upper left area of the punch.....	119
<b>Figure 2.9.7:</b> Definition of demonstrator part geometry by simulation to determine the minimum blank size (blank type 1, see Figure 2.9.11). ....	120
<b>Figure 2.9.8:</b> Definition of demonstrator part geometry by simulation to determine the maximum drawing depth of a closed profile (blank type 2, see Figure 2.9.11). ....	120
<b>Figure 2.9.10:</b> Lower part of the prototype tool installed in a tryout press at SZMF.....	121
<b>Figure 2.9.11:</b> Comparison of the two considered blank shapes. ....	121
<b>Figure 2.9.12:</b> Different variations were considered for forming of the prototype. ....	122
<b>Figure 2.9.13:</b> Prototype component made of TWIP-steel. Top: blank type 1, centre: blank type 2, bottom: after laser cutting.....	123
<b>Figure 2.9.14:</b> Formed part and overlay plot of one ARGUS measurement. Combining several ARGUS measurements from different angles gives a complete strain field. ....	124
<b>Figure 2.9.15:</b> Major strain field of the formed prototype using <b>blank type 1</b> , evaluated from Argus measurement. The strain field was evaluated for two drawing depths.....	124
<b>Figure 2.9.16:</b> Major strain field of the formed prototype <b>using blank type 2</b> , evaluated from Argus measurement. The strain field was evaluated for two drawing depths.....	125
<b>Figure 2.9.17:</b> Major and minor strain distribution on the surface of one prototype (blank type 1, full draw).....	125
<b>Figure 2.9.18:</b> The comparison of the Argus measurements obtained from three prototypes show a good reproducibility of the strain field during forming.....	126
<b>Figure 2.9.19:</b> Shape of the deformed sheet (left) and major strain distribution (right) of section cut through 3 exemplary prototypes.....	126
<b>Figure 2.9.20:</b> Superposition of CAD and ATOS geometry from top view.....	127
<b>Figure 2.9.21:</b> Superposition of CAD and ATOS geometry from side view .....	127
<b>Figure 2.9.22:</b> Final definition of FEM model .....	128
<b>Figure 2.9.23:</b> Modelling the sequence of the different steps of the forming process. ....	128
<b>Figure 2.9.24:</b> Simulation of the prototype component using blank type one. The results of the half drawn sheet and the full drawn sheet are illustrated.....	129
<b>Figure 2.9.25:</b> Simulation of the prototype component using blank type two. The results of the half drawn sheet and the full drawn sheet are illustrated.....	130
<b>Figure 2.9.26:</b> Comparison between the experimental data (left) and the simulation results with the TWIP4EU-model (right). The color scale of the legend is the same for experiment and simulation. ....	131
<b>Figure 2.9.21:</b> Major strains along the given section cut. Comparison between experimental data and simulation .....	132
<b>Figure 2.9.22:</b> Minor strains along the given section cut. Comparison between experimental data and simulation .....	132
<b>Figure 2.9.29:</b> Simulation results of prototype using blank type 1. Resultant displacement after spring back. The result of standard model is compared with two simulations with slightly modified hardening approach. The shape before spring back is also shown (top figure).....	133
<b>Figure 2.9.30:</b> Comparison of the predicted spring back behavior (TWIP4EU-Parameterset-3) with experimental data for five chosen section cuts along the prototype.....	134

<b>Figure 2.9.31:</b> Twin volume fraction at different stages of the deep drawing of the prototype.....	134
<b>Figure 2.9.32:</b> Definition of section cuts for micro hardness mapping (left) and the position of the indents in thickness direction of the sheet (right).....	135
<b>Figure 2.9.33:</b> Specimens for micro hardness mapping cut out from a fully drawn prototype component (blank type 2).....	135
<b>Figure 2.9.34:</b> Results of micro hardness mapping in section cut A.....	136
<b>Figure 2.9.35:</b> Results of micro hardness mapping in section cut B.....	136
<b>Figure 2.9.36:</b> Results of micro hardness mapping in section cut C.....	136
<b>Figure 2.10.1:</b> TWIP4EU demonstrator part at the BlechExpo trade fair 2015 in Stuttgart. Bottom right: Corresponding information board.....	138

## References

- [Allain2004] Allain, S., Chateau, J.-P., Bouaziz, O., Migot, S., Guelton, N. Modeling of mechanical twinning in a high manganese content austenitic steel. *Materials Science and Engineering A* 387-389 (2004) 158-162.
- [Armstrong1966] Armstrong, P.J., Frederick, C.O. A mathematical representation of the multiaxial Bauschinger effect, CEGB Report RD/B/N731, Berkeley, UK (1966).
- [Baiker2014] Baiker, M., Helm, D., Butz, A.: Determination of Mechanical Properties of Polycrystals by Using Crystal Plasticity and Numerical Homogenization Schemes. *Steel Research International* 2014, DOI: 10.1002/srin.201300202.
- [Banabic2010] Banabic D. Sheet metal forming processes. Springer-Verlag Berlin-Heidelberg 2010.
- [Barlat2003] Barlat, F. et al.: Plane stress yield stress yield function for aluminum alloy sheets – part1, Theory, *International Journal of Plasticity*, 19 (2003), 1-23.
- [Barlat1989] Barlat, F.; Lian, J.: Plastic behaviour and stretchability of sheet metals (Part I) A yield function for orthotropic sheet under plane stress conditions, *Int. J. Plasticity* 5 (1989) 51–56.
- [Bouaziz2011] Bouaziz, S. Allain, C.P. Scott, P. Cugy, D. Barbier. High manganese austenitic twinning induced plasticity steels: A review of the microstructure properties relationships. *Current Opinion in Solid State and Materials Science* 15 (2011) 141–168.
- [Bouaziz2001] Bouaziz O, Guelton N. Modelling of TWIP effect on work-hardening. *Material Science and Engineering A* 319–321 (2001) 246–249
- [Chaboche1983], J.L, Rousselier, G. On the plastic and viscoplastic constitutive equations, Parts I and II, *Journal of Pressure Vessel and Piping* 105 (1983) 453–164
- [De Cooman2012] De Cooman, B. C., Kwon, O., Chin, K.-G. State-of-the-knowledge on TWIP-steel. *Materials Science and Technology* 28 (2012) 513-527.
- [DIN EN ISO 12004-2] DIN EN ISO 12004-2: Metallische Werkstoffe – Bleche und Bänder - Bestimmung der Grenzformänderungskurve – Teil 2: Bestimmung von Grenzformänderungskurven im Labor
- [Eisenlohr2008] Eisenlohr, P, Roters, F.: Selecting a set of discrete orientations for accurate texture reconstruction. *Computational Materials Science*, 2008, Vol. 42, 670-678.
- [GOM2014] GOM: ARAMIS - Determination of Forming Limit Curves, webinar, January 2014
- [Guitierrez2011] I. Guitierrez-Urrutia and D. Raabe, Dislocation and twin substructure evolution during strain hardening of an Fe-22% Mn-0.6 wt%C TWIP-steel observed by electron channeling contrast imaging. *Acta Materialia*, 29, 2011
- [Hill1948] Hill, R.: A theory of the yielding and plastic flow of anisotropic metals. *Proc. Roy. Soc. London A* 193 (1948) 281-297.
- [Hutchinson1970] J. W. Hutchinson, *Proc. R. Soc. A Math. Phys. Eng. Sci.* 1970, 319(1537), 247.
- [Kim2013] Jinkyung Kim, Yuri Estrin, and Bruno de Cooman, Application of a Dislocation-Based Constitutive Model to Al-Alloyed TWIP-steels, *Metallurgical and Materials Transactions A*, Vol. 44A, 2013, pp. 4168-4182
- [Mandel1973] J. Mandel, *Plasticite Classique et Viscoplasticite*, CISM Inter, Springer, New York 1973.
- [Mecking1981] Mecking, H., Kocks, U.F. Kinetics of flow and strain-hardening. *Acta Metallurgica* 29 (1981) 1865-1875.

- [Miehe1999] Miehe, C.; Schröder, J.; Schotte, J.: Computational Homogenization Analysis in Finite Plasticity. Simulation of Texture Development in Polycrystalline Materials Computational Methods in Applied Mechanics and Engineering, 1999, Vol. 171, 387-418
- [Prakash2009] Prakash, A.; Weigand, S.M.; Riedel, H.: Modeling the evolution of texture and grain shape in Mg alloy AZ31 using the crystal plasticity finite element method. Computational Material Science, 2009, Vol. 45, 744-750.
- [Rémy1978] Rémy, L. Kinetics of f.c.c. deformation twinning and its relationship to stress-strain behaviour. Acta Metallurgica 26 (1978) 443-451.
- [Renard2012] Renard, K., Idrissi, H., Schryvers, D., Jacques, P.J. On the stress state dependence of the twinning rate and work hardening in twinning-induced plasticity steels. Scripta Materialia 66 (2012) 966-971
- [Roters2010] Roters, F.; Eisenlohr, P.; Hantcherli, L.; Tjahjanto, D. D.; Bieler, T. R. & Raabe, D. Overview of constitutive laws, kinematics, homogenization and multiscale methods in crystal plasticity finite-element modeling: Theory, experiments, applications. Acta Materialia, 2010, Vol. 58, 1152-1211
- [Simo1998] Simo, J.C., Hughes, T.J.R. (1998): "Computational Inelasticity", Springer-Verlag, New York.
- [Steinmetz2013] Steinmetz, D.R., Jäpel, T., Wietbrock, B., Eisenlohr, P., Gutierrez-Urrutia, I., Saeed-Akbari, A., Hickel, T., Roters, F., Raabe, D. Revealing the strain-hardening behavior of twinning-induced plasticity steels: Theory, simulations, experiments. Acta Materialia 61 (2013) 494-510.
- [Vucetic2012] M. Vucetic, S. Hübner, I. Peshekhodov and B.-A. Behrens: Influence of Strain Rate on Biaxial True Stress – True Strain Curves from the Bulge Test, IDDRG 2012, pp.232]



## HOW TO OBTAIN EU PUBLICATIONS

### Free publications:

- one copy:  
via EU Bookshop (<http://bookshop.europa.eu>);
- more than one copy or posters/maps:  
from the European Union's representations ([http://ec.europa.eu/represent\\_en.htm](http://ec.europa.eu/represent_en.htm));  
from the delegations in non-EU countries ([http://eeas.europa.eu/delegations/index\\_en.htm](http://eeas.europa.eu/delegations/index_en.htm));  
by contacting the Europe Direct service ([http://europa.eu/eurodirect/index\\_en.htm](http://europa.eu/eurodirect/index_en.htm)) or  
calling 00 800 6 7 8 9 10 11 (freephone number from anywhere in the EU) (\*).

(\*). The information given is free, as are most calls (though some operators, phone boxes or hotels may charge you).

### Priced publications:

- via EU Bookshop (<http://bookshop.europa.eu>).

The aim of TWIP4EU is to promote the introduction of modern twinning induced plasticity (TWIP) steels as candidate material for production of lightweight automobile components. To introduce a new steel grade like high strength and ductility TWIP-steel for large scale applications in industrial practice, a thorough validation of the material behavior with useable material laws implementable in commercial finite element codes must be available since numerical simulations are used all along the production process of car body parts. For this purpose, this project proposes a novel and advanced approach towards modelling the deformation and forming behavior of new TWIP-steels.

The project comprises a comprehensive experimental plan combined with the development of a constitutive framework motivated from micromechanical quantities to describe the deformation behaviour of TWIP-steels. Based on the results from microstructure analyses, macroscopic test and forming experiments the material was extensively characterized. The experimental results were taken into consideration for the development of the constitutive framework. The developed TWIP4EU material model was implemented into two commercially available finite element software packages. Prototype components were successfully produced out of TWIP-steel material. The superior formability of TWIP-steel could be demonstrated. The numerical results which are obtained from simulation using the developed material model are in good agreement with the experimental findings.

